EXPERIMENTAL AND NUMERICAL INVESTIGATION OF THE QUASI-STATIC AND HIGH STRAIN RATE CRUSHING BEHAVIOR OF SINGLE AND MULTI-LAYER ZIG-ZAG 1050 H14 AL TRAPEZOIDAL CORRUGATED CORE SANDWICH STRUCTURES

A Thesis Submitted to
the Graduate School of Engineering and Sciences of
İzmir Institute of Technology
in Partial Fulfilment of the Requirements for the Degree of

DOCTOR OF PHYLOSOPHY

in Mechanical Engineering

by
Cenk KILIÇASLAN

July 2014
İZMİR

We approve the thesis of **Cenk KILIÇASLAN**

Examining Committee Members:

Prof. Dr. Mustafa GÜDEN
Department of Mechanical Engineering, İzmir Institute of Technology

---

Prof. Dr. Bülent YARDIMOĞLU
Department of Mechanical Engineering, İzmir Institute of Technology

---

Prof. Dr. Ramazan KARAKUZU
Department of Mechanical Engineering, Dokuz Eylül University

Prof. Dr. Hasan YILDIZ
Department of Mechanical Engineering, Ege University

Assist. Prof. Dr. Selçuk SAATÇİ
Department of Civil Engineering, İzmir Institute of Technology

10 July 2014

Prof. Dr. Mustafa GÜDEN
Supervisor, Department of
Mechanical Engineering
İzmir Institute of Technology

Assoc. Prof. Dr. Alper TAŞDEMİRCİ
Co-Supervisor, Department of
Mechanical Engineering
İzmir Institute of Technology

Prof. Dr. Metin TANOĞLU
Head of the Department of
Mechanical Engineering

Prof. Dr. R. Tuğrul SENGER
Dean of the Graduate School of
Engineering and Sciences

ACKNOWLEDGEMENTS

Firstly, I would like to thank to my supervisor Professor Mustafa Güden for accepting me to his research team, all of his wisdoms, endless support and brilliant ideas during the dead end times of my studies and great contributions to my writing skills.

Secondly, thank you to my co-supervisor Assoc. Professor Alper Taşdemirci for his supports and Mr. Cumhur Akar for providing corrugated aluminum core sheets and brazed sandwich samples.

My greatest regards go to my research team mate İsmet Kutlay Odacı, DTM team; Ali Kara, Kıvanç Turan, Metin Çakırcalı, Selim Şahin, Atacan Yücesoy, the Lab145 team; Doğuş Zeren, Yiğit Attila and Umut Savacı, and heat & mass transfer laboratory team; Tümcan Şen and Hasan Çelik for their endless support and association.

Lastly, I gratefully thank to my wife, Buse Kılıçaslan, for her full support and patience during my graduate career.

ABSTRACT

EXPERIMENTAL AND NUMERICAL INVESTIGATION OF THE QUASI-STATIC AND HIGH STRAIN RATE CRUSHING BEHAVIOR OF SINGLE AND MULTI-LAYER ZIG-ZAG 1050 H14 AL TRAPEZOIDAL CORRUGATED CORE SANDWICH STRUCTURES

The quasi-static and dynamic crushing behavior of single, double and multi-layer zig-zag 1050 H14 Al trapezoidal corrugated core sandwich structures in 0°/0° and 0°/90° core orientations and with and without interlayer sheets were investigated both experimentally and numerically at varying impact velocities. The numerical simulations were conducted using the finite element code of LS-DYNA. The effect of fin wall imperfection was assessed through the fin wall bending and bulging. The numerical homogenization of the single layer corrugated structure was performed using MAT26 honeycomb material model. The buckling stress of single- and double-layer corrugated sandwich structures increased when the strain rate increased. The increased buckling stresses were ascribed to the micro inertial effects. The initial buckling stress at quasi-static and high strain rate was numerically shown to be imperfection sensitive. Increasing the number of core layers decreased the buckling stress and increased the densification strain. The panels tested with spherical and flat striker tips were not penetrated and experienced slightly higher deformation forces and energy absorptions in 0°/90° corrugated layer orientation than in 0°/0° orientation. However, the panels tested using a conical striker tip were penetrated/perforated and showed comparably smaller deformation forces and energy absorptions, especially in 0°/90° layer orientation. The homogenized models predicted the low velocity compression /indentation and projectile impact tests of the multi-layer corrugated sandwich with an acceptable accuracy with reduced computational time.

ÖZET

TEK VE ÇOK KATMANLI ZİKZAK 1050 H14 AL İKİZKENAR YAMUK DALGALI GÖBEKLİ SANDVİÇ YAPILARIN YARI-STATİK VE DİNAMİK GERİNİM HIZLARDAKİ EZİLME DAVRANIŞININ DENEYSEL VE NÜMERİK İNCELENMESİ

Tek, çift ve çok katmanlı zikzak 1050 H14 Al ikizkenar yamuk dalgalı göbekli, 0°/0° ve 0°/90° göbek yönelimli, ara plakalı ve ara plakasız sandviç yapıların yarı-statik ve dinamik özellikleri değişen darbe hızlarında deneysel ve nümerik olarak incelenmiştir. Nümerik simülasyonlar sonlu elemanlar kodu LS-DYNA kullanılarak yapılmıştır. Kanat duvarı kusurunun etkisi kanat duvarı eğilmesi ve şişmesi göz önüne alınarak incelenmiştir. Tek katmanlı dalgalı yapının nümerik olarak homojen hale getirilmesi MAT26 bal peteği malzeme modeli kullanılarak gerçekleştirilmiştir. Tek ve çift katmanlı dalgalı sandviç yapıların burkulma gerilmesi gerinim hızı arttıkça atmıştır. Artan burkulma gerilmesi mikro atalet etkisine bağlanmıştır. Yarı-statik ve dinamik gerinim hızlarındaki ilk burkulma gerilmesinin kusura duyarlı olduğu nümerik olarak gösterilmiştir. Göbek katman sayısının arttırılması burkulma gerilmesini azaltmış ve yoğunlaşma gerinimini arttırmıştır. Küresel ve düz vurucu uçları ile test edilen paneller delinmemiş ve paneller 0°/90° göbek yöneliminde 0°/0° göbek yöneliminden daha yüksek deformasyon kuvvetleri ve enerji sönümleme özelliği göstermişlerdir. Ancak konik vurucu uçlu ile test edilen paneller delinmiş ve özellikle 0°/90° göbek yöneliminde çok düşük deformasyon kuvvetleri ve enerji sönümleme miktarı göstermiştir. Homojen modeller çok katmanlı dalgalı sandviç yapıların düşük hızlı basma/batma ve projektör çarpışma testlerini yeterli doğrulukta daha az çözümleme zamanında tahmin etmiştir.

TABLE OF CONTENTS

LIST OF FIGURES

Figure **Page**

LIST OF TABLES

LIST OF SYMBOLS

$\dot{\varepsilon}_0$	Reference strain rate
$\dot{\varepsilon}$	Strain rate
A_0	Initial cross section area
A_B	Cross section area of bar
A_i	Instantaneous cross section area
A_s	Cross section area of specimen
C_B	Elastic wave speed of bar
c_{pl}	Plastic wave velocity
D	Cell wall size
E	Elastic modulus
E	Energy
G	Shear modulus
H	Height
I	Moment of inertia
l_0	Initial length of the specimen
l_f	Final length of the specimen
l_i	Instantaneous length
m	Mass
M_p	Plastic moment of the plastic hinge
P	Force
t	Cell wall thickness
T	Compressive pulse
t	Time
T_m	Melting temperature
T_r	Room temperature
v	Element volume
V	Relative volume
V_0	Initial velocity
v_f	Fully compacted element volume
ε	Strain
ε_d	Densification strain

ε_I	Incident strain
ε_R	Reflected strain
ε_T	Transmitted strain
ε_t	True strain
θ	Deviation angle
ν	Poisson's ratio
ρ	Relative density
ρ^*	Density of foam
ρ_s	Density of cell wall material
σ	Stress
σ^*	Collapse strength
σ_c	Crushing strength
σ_{pl}	Plateau stress
σ_t	True stress
σ_{ys}	Yield stress of cell material
ω	Inclination angle

CHAPTER 1

SANDWHICH AND LIGHT-WEIGHT CORE STRUCTURES

1.1. Sandwich Structures

A sandwich structure consists of stiff, thin face sheets and a light weight core (Figure 1.1). The face sheet is selected from the materials of high resistance to bending and stretching loads. The front and back face sheets are usually constructed from the same material with the same thickness. However, different face sheet materials or thicknesses may also be used in a single sandwich structure in the presence of specific loading conditions. Core material is considered to be the most critical part, as it greatly affects the overall performance of a sandwich structure. The crushing strength of sandwich structures is directly related to the resistance of the core to the applied loads in through thickness direction. The core structure is also required to withstand transverse loads that can cause core buckling/bending. Cores are usually selected between the light-weight or low density materials or structures such as balsa wood, metallic and synthetic foams, honeycomb and corrugated structures. The core and face sheets are bond to each other using a thin layer of adhesive. An additional weight is generally applied to sandwich structure to create an uninterrupted contact between face sheets and core and the whole structure is cured. During curing process, a stiff resin creates a strong bonding between core and face sheets. The selected adhesive has also significant effects on the mechanical performance of sandwich structure. Adhesive material has to be stiff enough to carry bending and shear loads without leading to any separation between sandwich components. A variety of metallic core materials have been investigated, particularly aiming at improving the impact resistance of sandwich structures, including aluminum foams [1-9] and honeycombs [10-15].

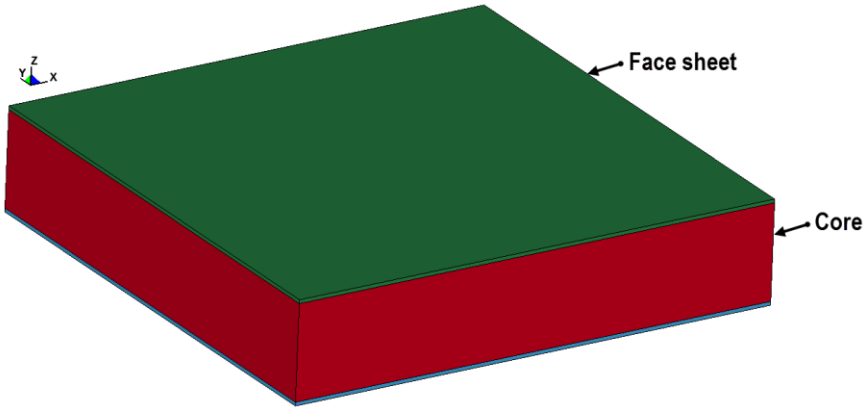

Figure 1.1. Schematic of a sandwich structure: face sheets and core.

1.2. Metallic Foams

Foam refers to the dispersion of gas bubbles in a liquid [16]. When the liquid phase is a molten metal, the foam retains its cellular structure in solid state upon rapid solidification. The solidified cellular metal structures constitute a group of materials known as *foamed metal* or *foam metal*. Metallic foams have the potentials of extensive applications for light-weight constructions due to their low density and relatively good energy absorbing and heat and sound insulating properties as outlined in Figure 1.2. The density of metallic foams may be ten times lower than that of the metal they are made of. They crush at a relatively low stress but nearly at the same stress level until about large strains, leading to relatively high energy absorption capacity and efficiency. Metallic foams are generally preferred as the core material in sandwich structures for the protection against blast and impact. Any metal can be practically foamed but commercially available metallic foams are usually made of aluminum metal because of relatively low density and meting temperature of aluminum. Since aluminum is foamed easily in the molten state even in the processes starting from aluminum powder, the cells are inherently closed by the cell walls. Currently, aluminum closed-cell foams are commercially produced through three different routes: the foaming aluminum melts by gas injection, the foaming aluminum melts with a foaming/blowing agent and the foaming aluminum powder compacts [16].

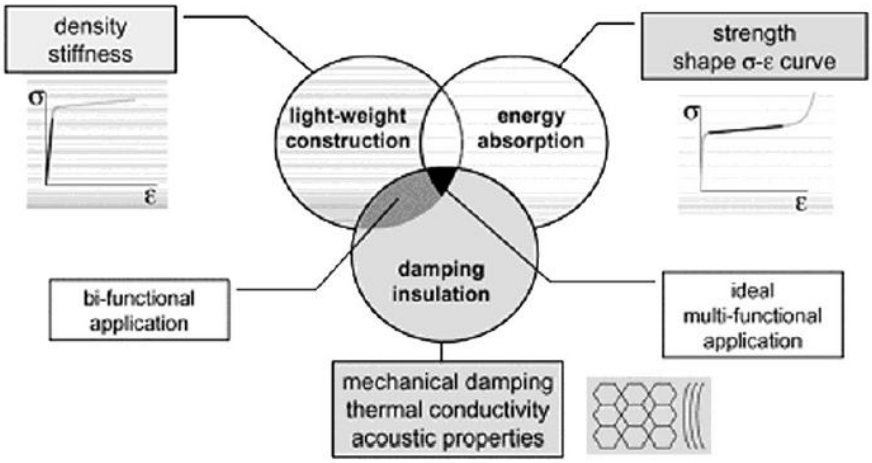

Figure 1.2. Mechanical and physical properties of metallic foams [17].

Foaming melts by gas injection method was developed by ALCAN International Limited [18, 19]. In this process, a gas (air or nitrogen) is injected into the molten aluminum or aluminum alloy to create gas bubbles (Figure 1.3). To stabilize the gas bubbles, ceramic particles, usually SiC, are added to the melt. The stabilized gas bubbles are collected from the surface of the melt and then solidified. The foaming aluminum melts with a foaming/blowing agent method is based on adding a blowing or foaming agent into molten metal, then the agent releases gas upon heating. At the first stage of this process, 1.5 wt% calcium is added to increase the viscosity of liquid aluminum to allow stable gas bubble formation (Figure 1.4(a)). When desired viscosity of the molten metal is reached, foaming agent TiH_2 (1.6 wt%) is added and the liquid solution is mixed (Figure 1.4(b)). The decomposion of foaming agent releases hydrogen gas which drives the foaming of liquid aluminum (Figure 1.4(c)). In a final stage, the liquid foam is solidified (Figure 1.4(d)). The foaming powder compacts method begins with mixing metal and foaming agent powders (Figure 1.5) [16]. Then, the mixture is compacted to attain a relative density of 99%. Finally, the compact is heated to a temperature close to the melting point of aluminum. The decompositon of foaming agent results in the expansion of the compact in liquid or partially liquid state.

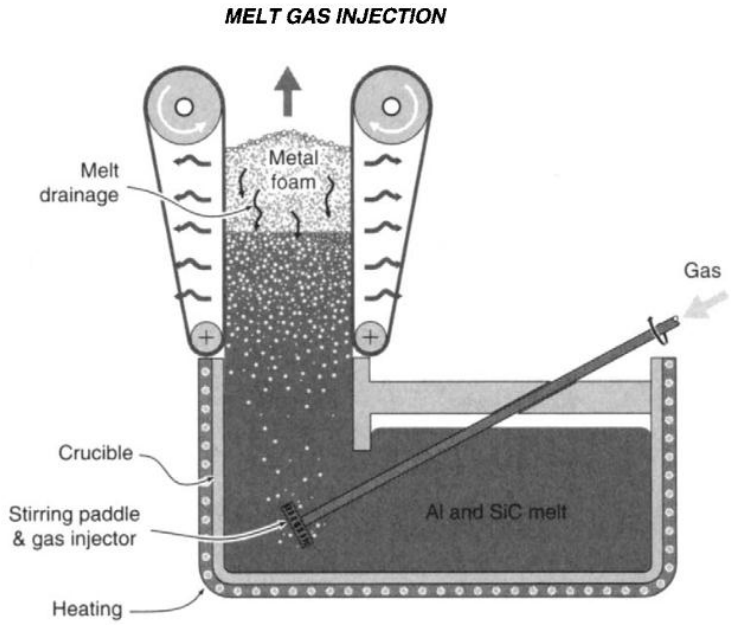

Figure 1.3. Foaming melts by gas injection method [20].

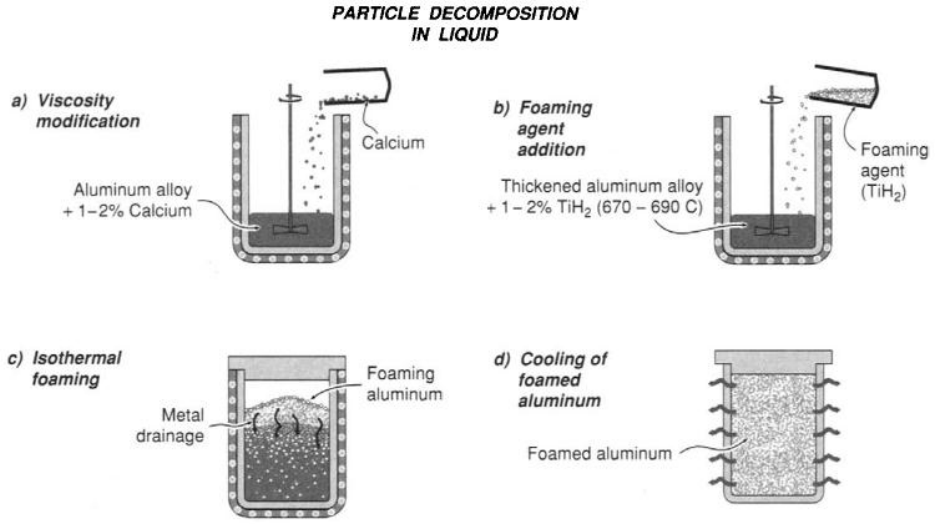

Figure 1.4. The foaming aluminum melts with a foaming/blowing agent method [20].

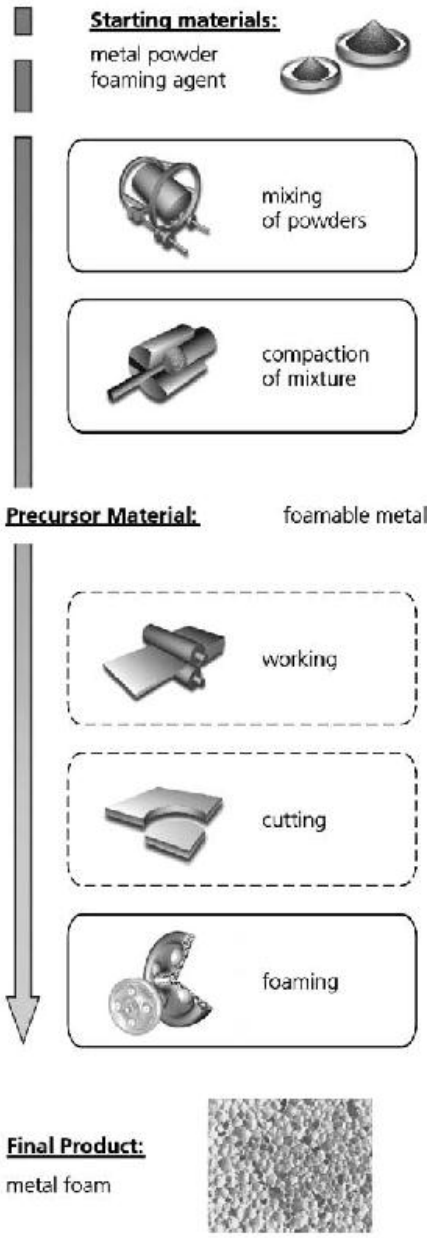

Figure 1.5. The foaming powder compacts method [16].

The mechanical properties of metallic foams depend on the properties of the metal which they are made of, the relative density and cell topology [20]. The experimental and idealized quasi-static compression stress-strain curve of a closed-cell aluminum foam is presented in Figure 1.6. As marked in Figure 1.6, the compression stress-strain curve is composed of mainly three distinct regions: 1- linear elastic region, 2- plateau region and 3- densification region. The linear region is represented with an elastic modulus (E), the plateau region with a collapse strength (σ^*) or plateau stress (σ_{pl}) and the densification region with a densification strain (ε_d). In the elastic region, cell walls are subjected to bending and stretching loads. In the plateau region, cell walls

collapse plastically and experiences large amount of deformation energy absorption through cell wall buckling, crushing and tearing [21]. Lastly, cell walls are completely compressed at the densification strain and the stress increases sharply in this region. Almost all metallic foam structures show somewhat similar compression stress-strain behavior and deformation characteristics with those of aluminum foams explained above.

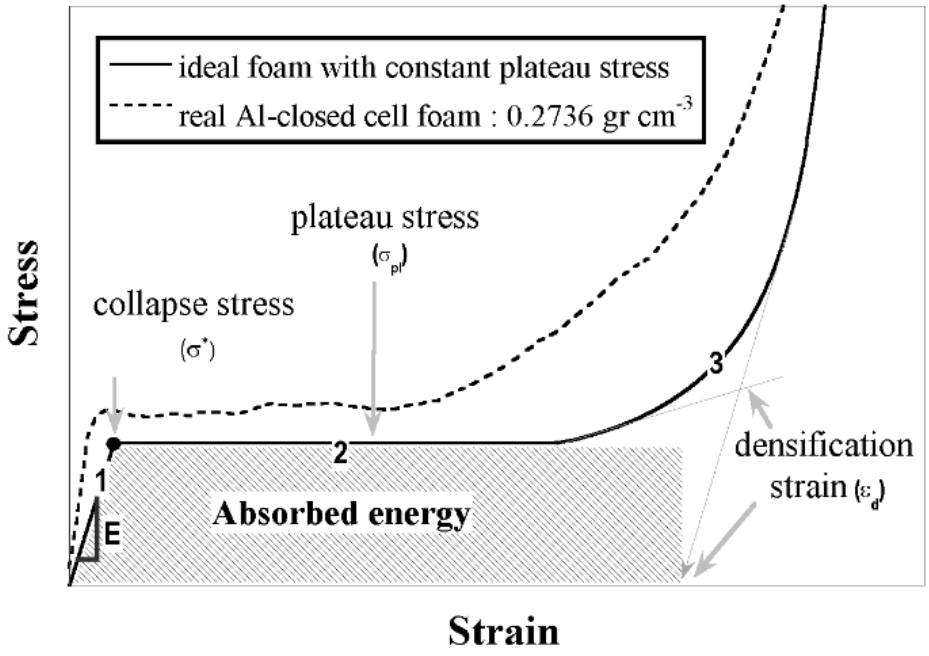

Figure 1.6. Typical compressive stress-strain curve of a closed-cell metallic foam [21].

The elastic moduli of ideal open and closed-cell metallic foams can be calculated from the cell edge bending deflection and the stretching of the planar cell faces and are given sequentially by the following relations [22],

$$\frac{E^*}{E_s} = c_1\rho^2 \tag{1.1}$$

and

$$\frac{E^*}{E_s} = c_2\rho^2 + c_3\rho \approx c_4\rho \tag{1.2}$$

where E^* and E_s are the elastic modulus of foam and cell wall material, respectively and c_1, c_2, c_3 and c_4 are the constants and ρ is the relative density calculated as,

$$\rho = \frac{\rho^*}{\rho_s} \tag{1.3}$$

where ρ^* and ρ_s are the density of foam and cell wall material, respectively.

The collapse stress or plateau stress is an indication for the progressive inelastic and inhomogeneous deformation of the cell. For ideal open and closed-cell foams, the plastic collapse is expected to occur by the plastic hinges at the bent cell edges and cell wall stretching in a direction perpendicular to compression axis. The plateau stresses for ideal open-cell and tetrakaidecahedron closed-cell foams are given sequentially by the following relations [22],

$$\frac{\sigma_{pl}}{\sigma_{ys}} = 0.3\rho^{3/2} \tag{1.4}$$

and

$$\frac{\sigma_{pl}}{\sigma_{ys}} = 0.33\rho^{2} + 0.44\rho \tag{1.5}$$

where, σ_{ys} is the yield strength of the cell wall material. By including material distribution between cell edges and cell walls the following relation is proposed for a closed-cell foam plateau stress [23],

$$\frac{\sigma_{pl}}{\sigma_{ys}} = 0.3(\phi\rho)^{3/2} + (1-\phi)\rho \tag{1.6}$$

where, ϕ is the volume fraction of the solids contained on the plateau borders. The first term in Eqn.1.6 corresponds to plastic hinge formation and the second to the membrane stretching of the cell walls. Eqn. 1.6 predicts the collapse stress of open-cell and closed-cell foam when ϕ=1 and ϕ=0, respectively.

1.3. Honeycombs

Honeycombs are the replicas of structures created by honeybees. Honeycomb structures are composed of repeated unit cells along in plane directions. The topologies of these unit cells can be hexagonal, square or triangular, depicted in Figures 1.7 (a-c). These are closed-cell structures either made from metallic or plastic sheets. The repeated unit cells along in plane directions lead to high stiffness and excessive load bearing capacity [24]. As with foamed metals, honeycombs resemble light-weight structures with relatively high energy absorbing capabilities [25]. A honeycomb structure is highly anisotropic and represented by three principal directions: longitudinal (L), width (W) and transverse (T) as shown in Figure 1.8.

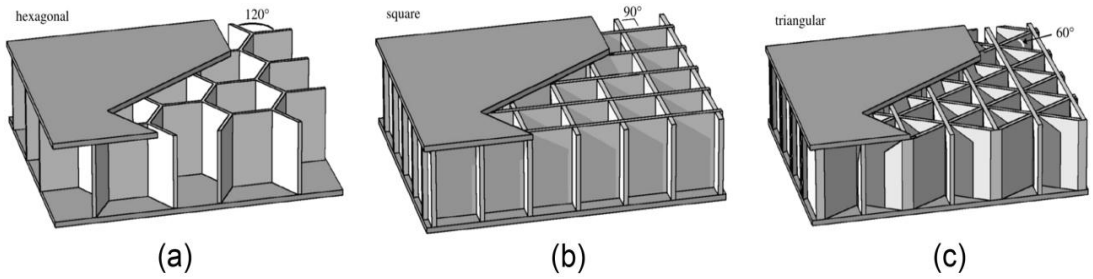

Figure 1.7. Different honeycomb core topologies: (a) hexagonal, (b) square and (c) triangular [26].

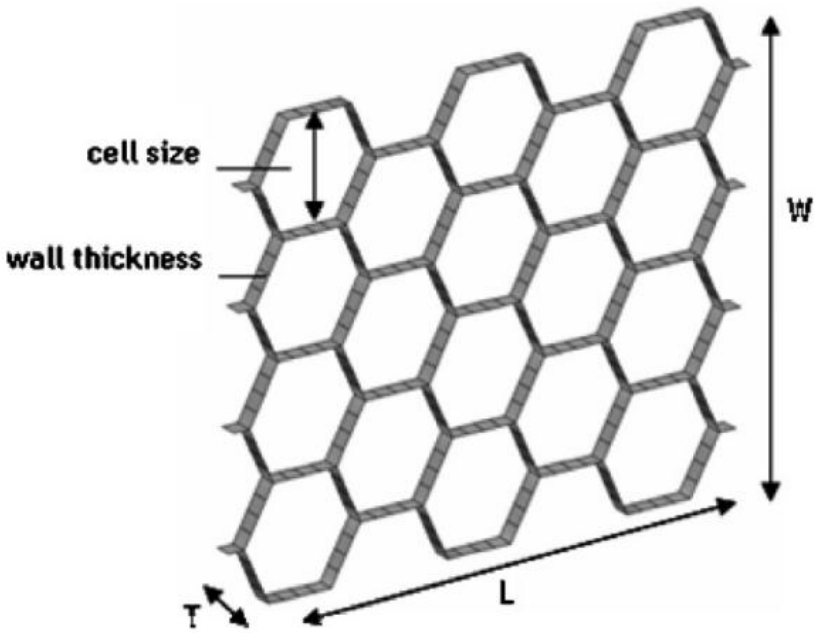

Figure 1.8. Principle directions of honeycomb structure [27].

The simplified steps of honeycomb processing are shown schematically in Figure 1.9. The method is based on the sheet metal forming process. At the first stage, the aluminum sheets are sliced into desired dimensions and then bent using the dies. The bent layers are bonded to each other with a strong adhesive or laser welding to form HOBE. HOBE is then sliced into desired dimensions and subjected to the stretching perpendicular to its thought thickness direction. This leads to stretch bended layers to form honeycomb geometry.

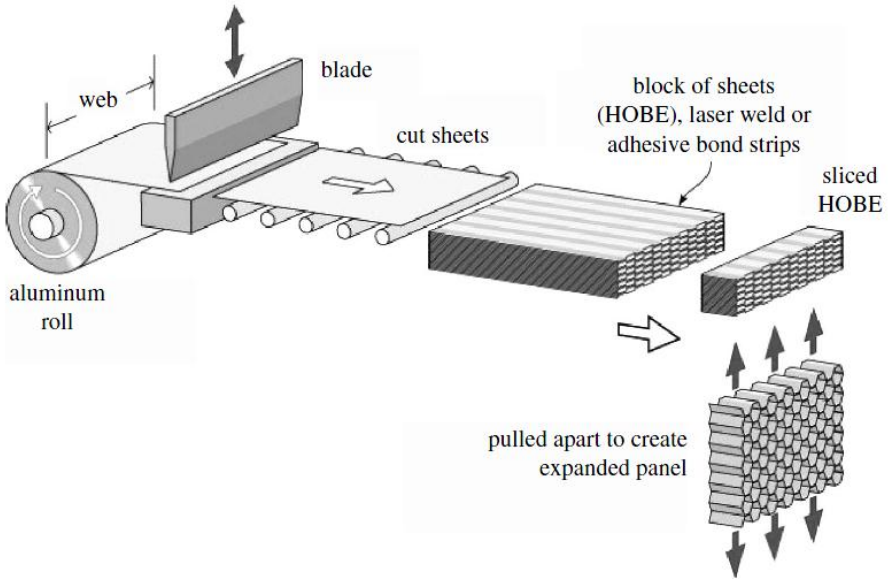

Figure 1.9. Honeycomb manufacturing process [26].

The mechanical properties of honeycomb structures, as expected, depend on loading directions, base material properties and the size and the thickness of hexagonal walls. The compression mechanical strength of honeycomb is lowest in the longitudinal (through length) and lateral (through width) directions as result of bending of cell walls and highest through thickness. Through thickness direction, the honeycomb cells crush through cell wall folding. Typical load-displacement and energy absorption-displacement curves of an aluminum honeycomb structure subjected to axial compression through thickness direction are shown in Figure 1.10. Following to the initial peak load (the point a in Figure 1.10), the cell walls crush under compressive loads. The initial peak load is usually used to calculate the compressive strength [25]. Upon the start of the cell wall bending/folding, load decreases sharply to the point b. After that point, fluctuations in load occurs as honeycomb cells fold/buckle. The crushing behavior is progressive; starting from one of the ends and proceeds to other

end of the test sample. The average load from the point b to the densification point is defined as the crushing load of honeycomb. The energy absorption increases almost linearly with displacement as depicted in Figure 1.10.

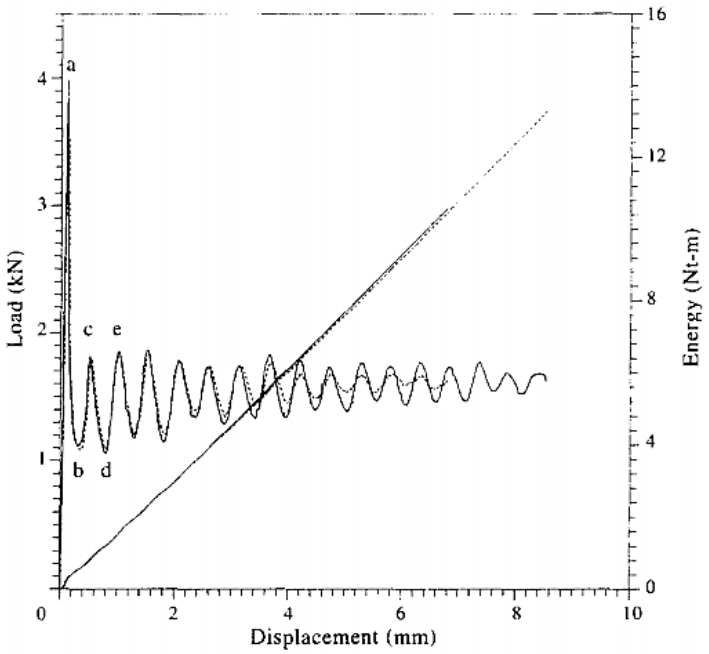

Figure 1.10. Load-displacement and energy absorption-displacement curves of an aluminum honeycomb structure under quasi-static compression [25].

The crushing strength of a metallic honeycomb structure can be approximated theoretically as [28],

$$\sigma_c = 16.56\sigma_{ys}\left(\frac{t}{D}\right)^{5/3} \tag{1.7}$$

where, σ_c, t and D are the crushing strength, the cell-wall thickness and the cell size, respectively.

1.4. Corrugated Structures

Corrugated structures are relatively new groups of materials, which offer overall strength and mechanical performances comparable with those of metal foams and honeycombs. Corrugated structures can be made of paper [29-33], composite [34-41]

and metallic materials [42-50]. Corrugated sandwich paper board shown in Figure 1.11 is an example for a corrugated structure and used to protect the products against impact loading during handling and transportation. The core between the liners, also called fluting, provides cushioning to the structure to be protected. The processing route for corrugated structures enables them to be manufactured in intricate geometries with relatively homogeneous macro-structures [51]. The most widely investigated topologies include V-type [49, 52], U-type [50, 53], X-type (diamond) [54] and Y-type [46, 47, 49]. The schematics of various corrugated topologies including straight, trapezoidal, V-type and curvilinear are shown sequentially in Figures 1.12(a-d).

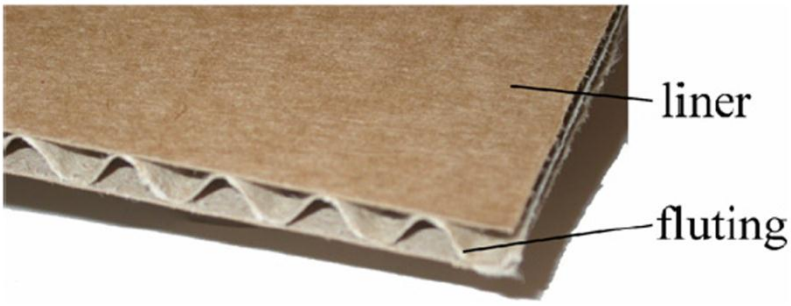

Figure 1.11. A picture of a corrugated paper board [55].

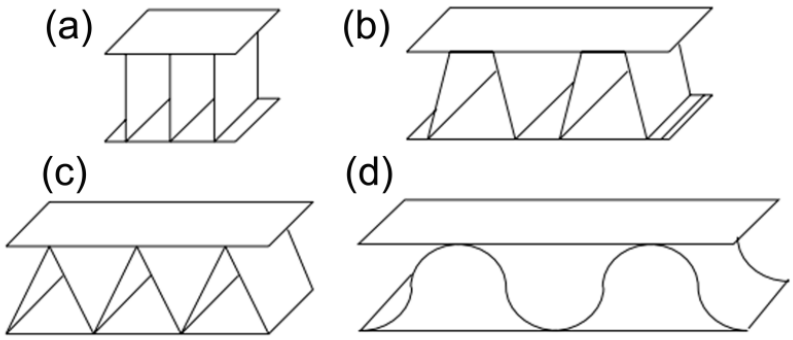

Figure 1.12. Corrugated topologies; (a) Straight, (b) hat (trapezoidal), (c) triangular (V- type) and (d) curvilinear [56].

The manufacturing process of metallic corrugated structures is thoroughly based on the sheet metal forming technology. The metal sheet shown in Figure 1.13 is continuously deformed, as it moves, into corrugated sheet form between the pair of upper and lower dies; then, each corrugated layer is cut into desired dimensions. In a final step, the corrugated layers are bonded to each other by using an adhesive or applying welding/brazing.

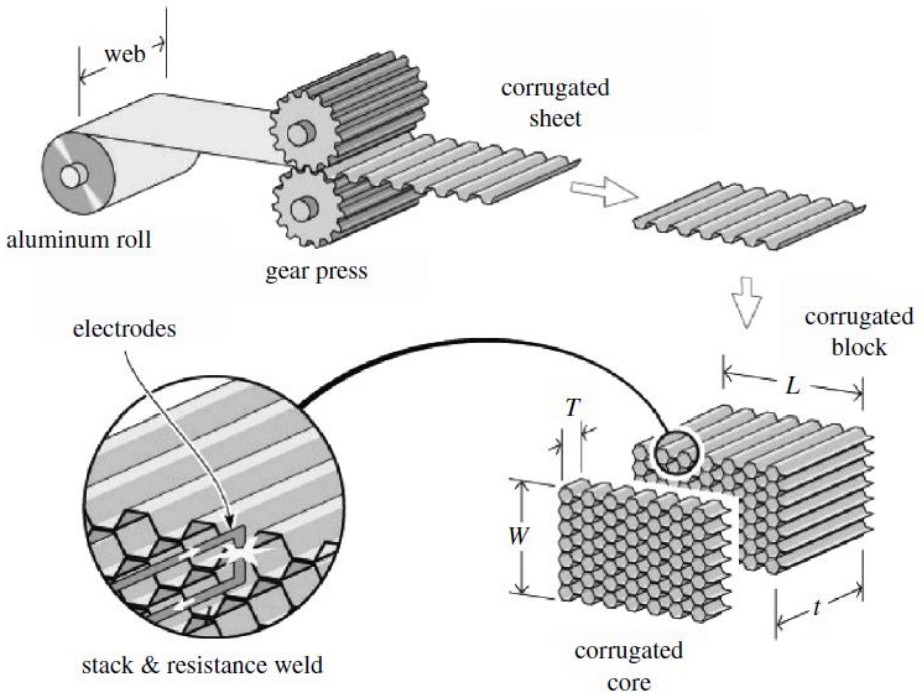

Figure 1.13. Corrugation process [26].

A typical stress-strain curve of a unit aluminum triangular corrugated structure subjected to quasi-static axial compression is shown in Figure 1.14. Upon initial elastic loading of the structure, a maximum peak stress appears at the point II in Figure 1.14. This initial peak stress is usually taken as the crushing strength of the structure. As the loading progresses, the core walls buckle, leading to fluctuations in stress values. Similar to foamed metal, a densification region occurs at the final stage of the deformation at a densification strain (point IV in Figure 1.14).

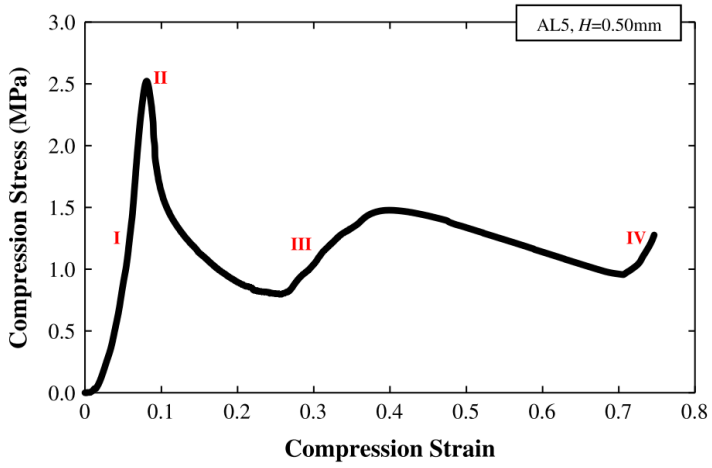

Figure 1.14. Stress-strain curve of an aluminum triangular corrugated structure under compression [37].

1.5. Lattice Truss Structures

Lattice trusses are extremely light, open-cell multi-functional structures [57]. Energy absorption capacity of such structures is also noted to be relatively high. These structures are considered as alternative to honeycombs and metallic foams in the applications designed for the mitigation of the stress waves resulting from the blast or impact loading. The most widely investigated topologies include tetrahedral [57-60], pyramidal [51, 61, 62] and kagome [59, 63-65] shown in Figure 1.15. The formation of tetrahedral lattice structure is based on the perforations of metal sheets using pairs of punches (Figure 1.16). In a final stage, the perforated sheet is folded to form regular tetrahedrons. The manufacturing process of pyramidal lattice is composed of three stages: slitting/expanding (Figure 1.17(a)), rolling (Figure 1.17(b)) and folding (Figure 1.17(c)). Kagome lattice cores are more complex in structure and processing than 2D truss cores. Various manufacturing process are available for Kagome lattice cores including injection molding, rapid 3D prototyping or extrusion based deposition modeling [64]. Three dimensions Kagome lattice can also be constructed using a simplified technique known as wire bending (Figures 1.18(a-d)). The wires either metal or fiber are bent into trapezoidal shape and weaved sequentially together.

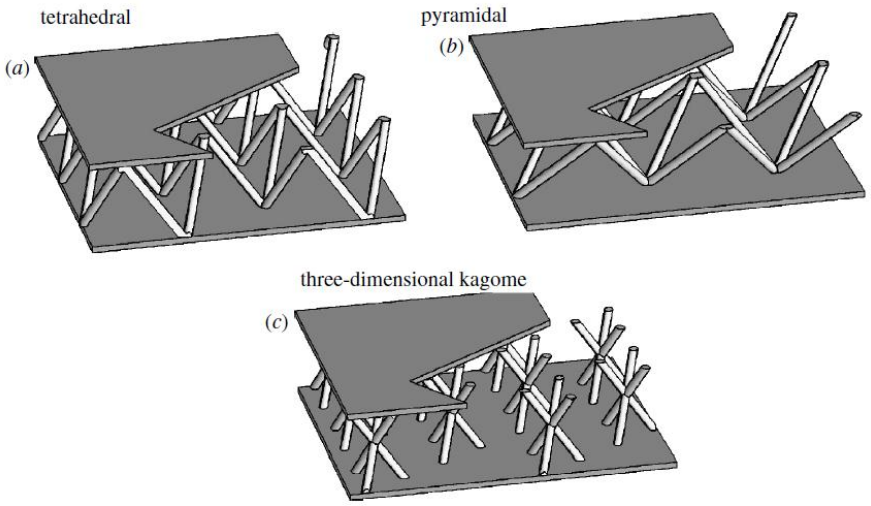

Figure 1.15. Lattice truss structures: (a) tetrahedral, (b) pyramidal and (c) kagome [26].

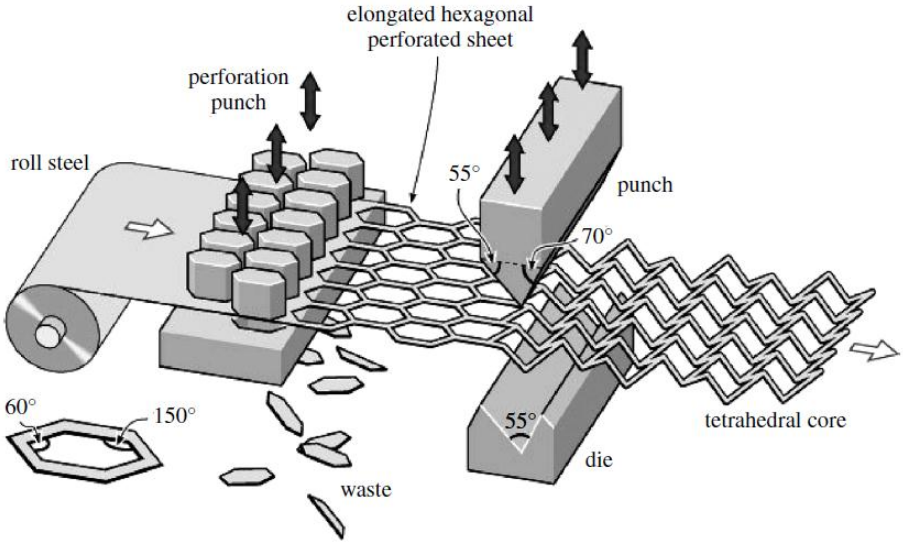

Figure 1.16. Forming steps of tetrahedral lattice core [26].

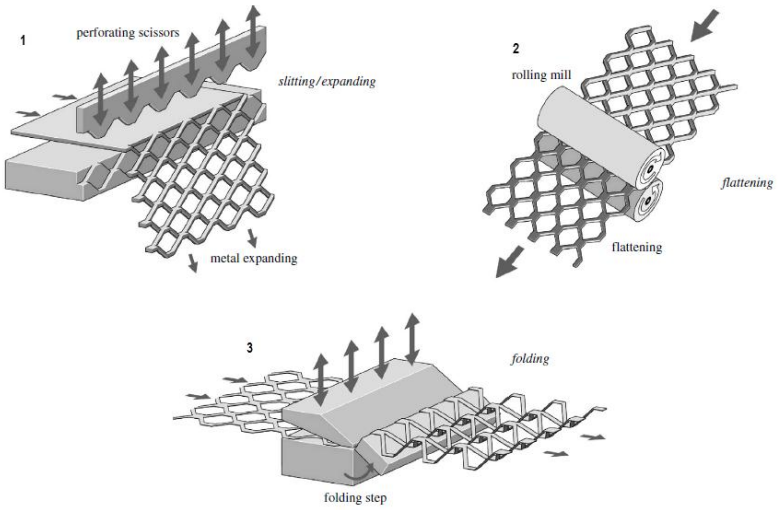

Figure 1.17. Forming steps of pyramidal lattice core [26].

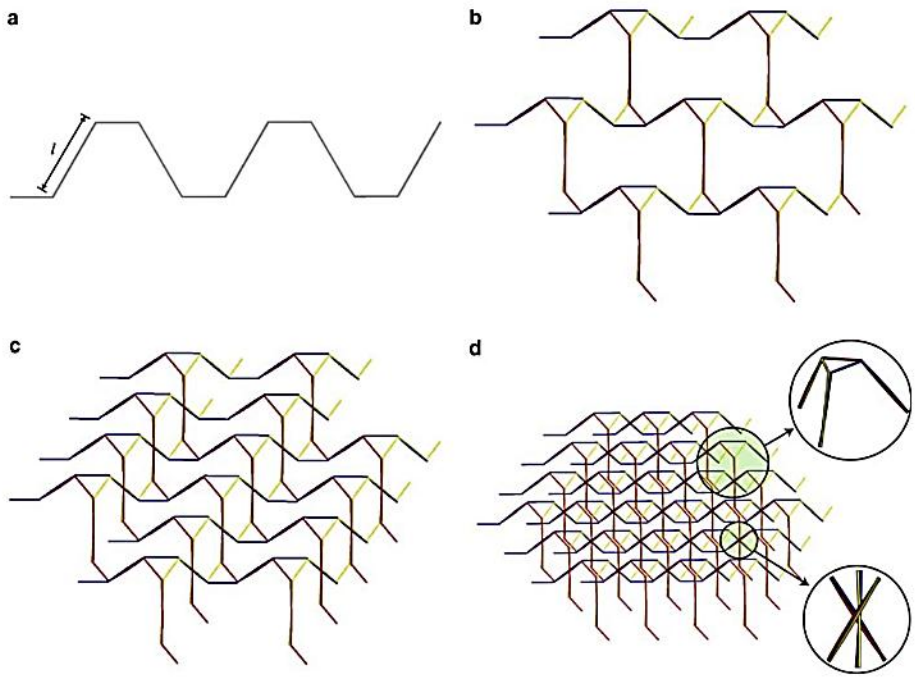

Figure 1.18. Manufacturing steps of kagome truss core using wires [59].

Pyramidal truss cores deform through bending/buckling of trusses under compressive loads. The quasi-static and dynamic compressive stress-strain of a unit stainless steel pyramidal truss core is shown in Figure 1.19. At both loading rates, following the initial peak stress, the stress values drop gradually due to the collapse of trusses, a deformation behavior similar to that of honeycombs and corrugated structures. The quasi-static compression load-displacement curve of a Kagome sandwich panel is shown in Figure 1.20. As similar to other topologies, an initial peak load occurs in the load-displacement curve. After this point, the force suddenly decreases and fluctuates as a result of buckling of the Kagome core walls.

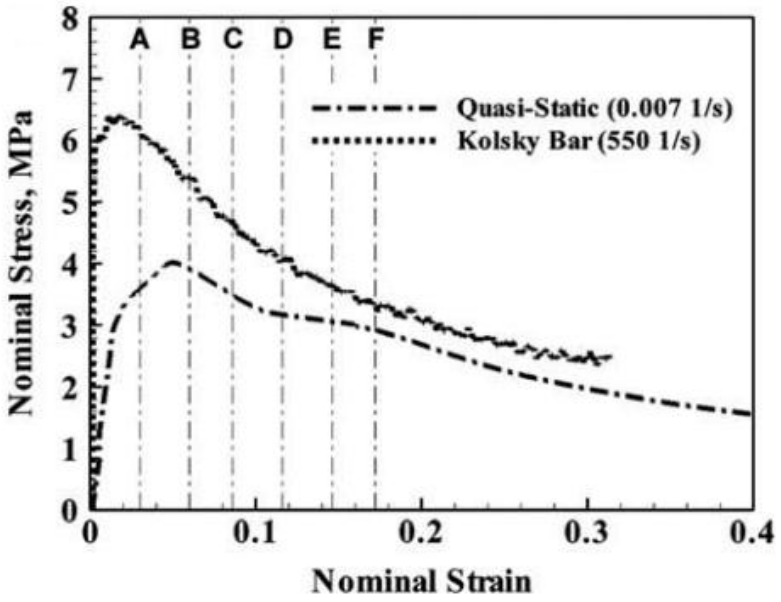

Figure 1.19. Compression stress-strain curve of a stainless steel pyramidal truss [61].

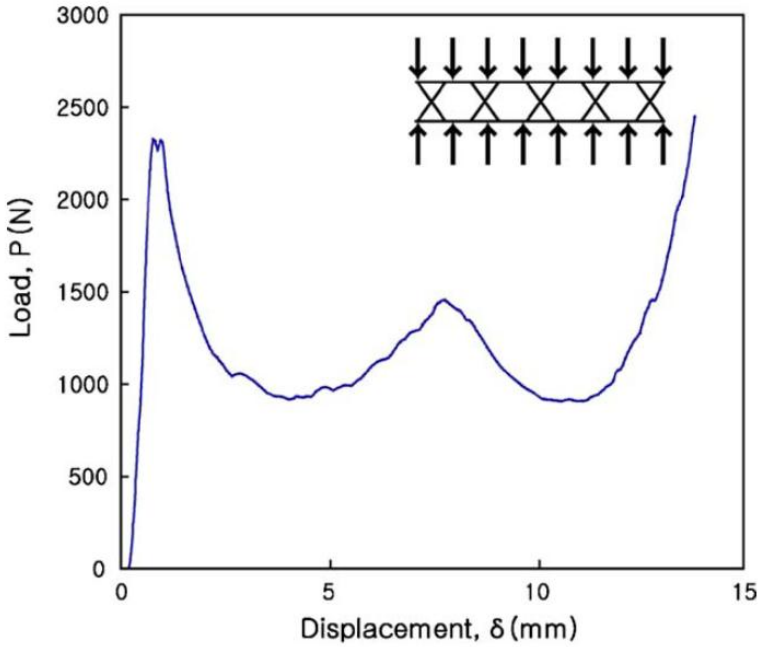

Figure 1.20. Compression load-displacement curve of a Kagome truss sandwich panel [59].

1.6. Comparison of Core Structures

Wadley et al. [26] compared the strength of various types of cellular structures. The comparison was based on the normalized strength (strength of cellular

solid/strength of bulk metal) versus relative density as shown in Figure 1.21. It is noted in the same figure that corrugated, lattice truss and honeycombs structures exhibit higher normalized strength than open cell foams and pyramidal solid lattice structures are the lightest structures with relatively low normalized strength. At the similar relative densities, the strength of pyramidal hollow structures is approximately three times higher than that of pyramidal solid lattice structures. At moderate relative densities, square/diamond hollow and square solid lattice truss structures exhibit the similar strength with square honeycombs. Corrugated structures lie somewhat between honeycomb and open cell foams in terms of normalized strength. Finally, it should be noted that the strength data shown in Figure 1.21 is only for triangular corrugated structures.

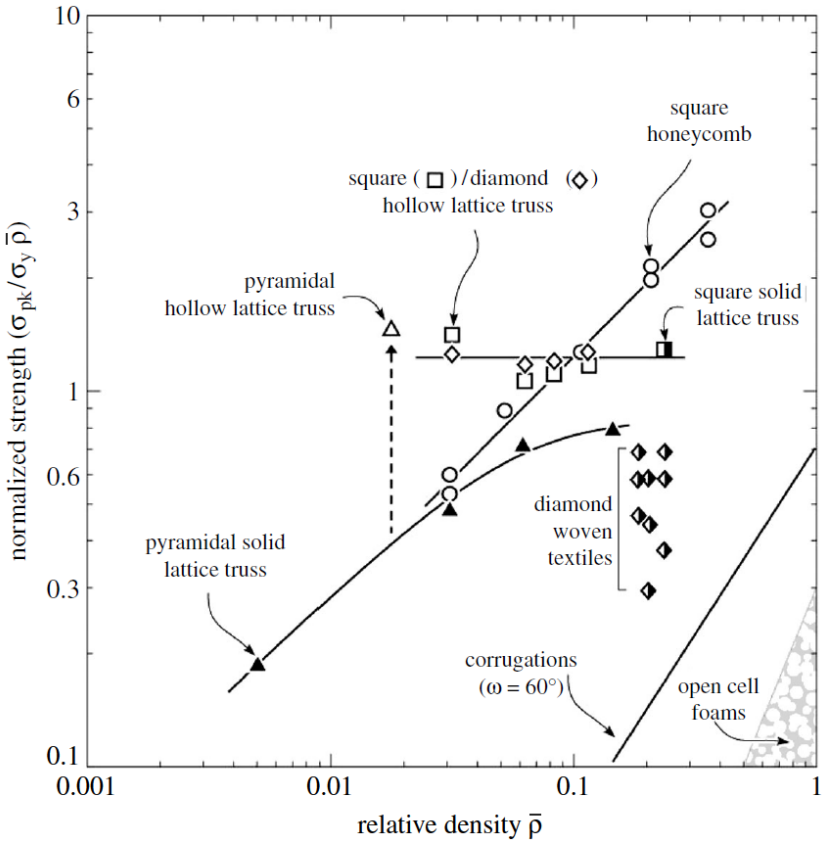

Figure 1.21. Normalized strength versus relative density of periodic cellular structures [26].

CHAPTER 2

A LITERATURE SURVEY: THE MECHANICAL BEHAVIOR OF LIGHT-WEIGHT STRUCTURES

2.1. Truss Cores

Kooistra et al.[57] investigated the compressive behavior of brazed AA6061 Al alloy tetrahedral truss lattice sandwich structures with the core relative densities ranging 0.02-0.083. The initial peak stress of sandwich panels was found highly dependent on the applied heat treatment. Annealing decreased the initial peak stress while aging increased the peak stress considerably (Figure 2.1(a) and (b)). The initial peak stress was almost doubled with age-hardening as the yield strength of aluminum alloy increased with age hardening. Tetrahedral truss lattice sandwich structures was shown to exhibit similar energy absorptions with pyramidal truss lattices and woven textiles per volume base (Figure 2.2 (a)), while it showed higher energy absorption than pyramidal truss lattices and woven textiles per mass base (Figure 2.2 (b)).

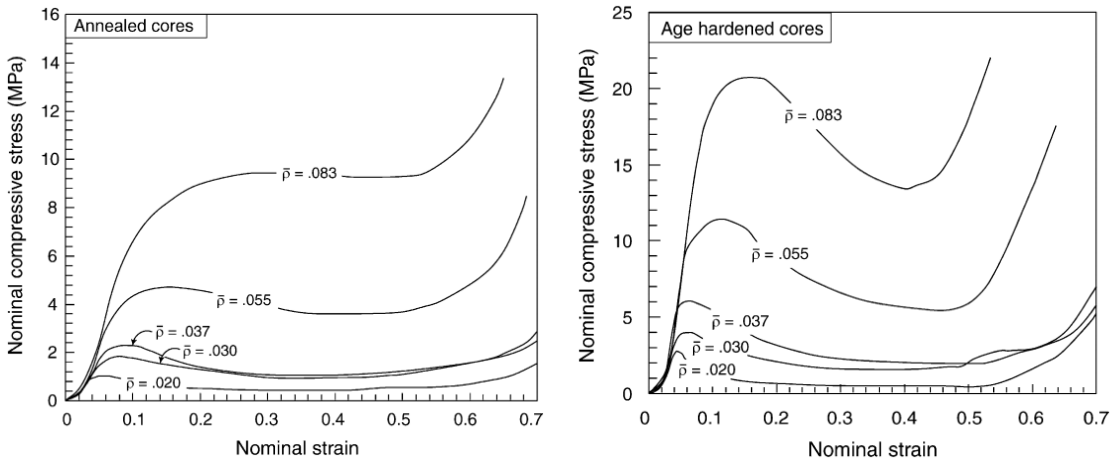

(a) (b)

Figure 2.1. Nominal compressive stress-strain curves of (a) annealed and (b) age-hardened AA6061 truss cores [57].

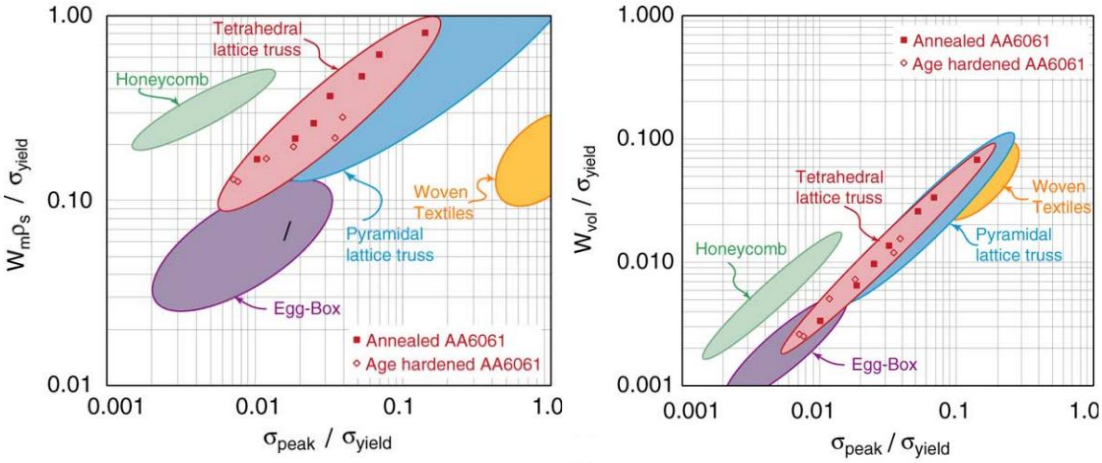

(a) (b)

Figure 2.2. Energy absorption of tetrahedral lattice trusses as compared with conventional core topologies: (a) per unit volume and (b) per unit mass ($W_m=W_v/\bar{\rho}\rho_{alloy}$) [57].

Queheillat et al. [66] investigated the quasi-static compression responses of 316L stainless steel solid and hollow pyramidal lattice structures assembled through brazing (Figures 2.3(a) and (b)). Both types of cores exhibited similar compressive stress-strain behavior and deformation mechanisms under compressive loads: following an initial peak stress, truss members buckled plastically and formed a plateau region (Figure 2.4). However, hollow pyramidal lattice core exhibited two times higher initial peak and plateau stress than solid truss structure. The use of hollow trusses as the ligaments of pyramidal lattice truss structures was reported to increase the inelastic buckling resistance of hollow tubes. The radius of gyration, ($\sqrt{\frac{I}{A}}$; I: moment of inertia and A: area of truss) increased by a factor 2 in hollow truss compared to solid truss, which increased the column resistance to buckling.

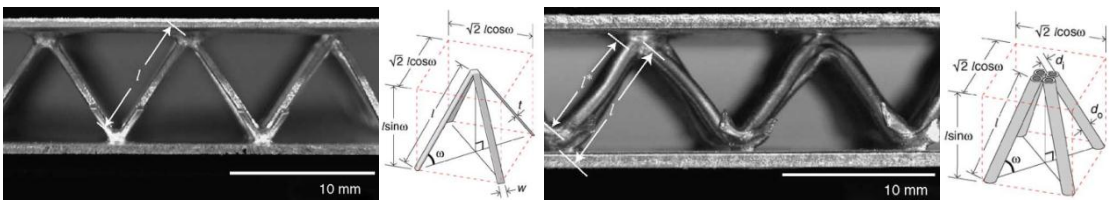

(a) (b)

Figure 2.3. Pyramidal lattice structures: (a) solid and (b) hollow trusses [66].

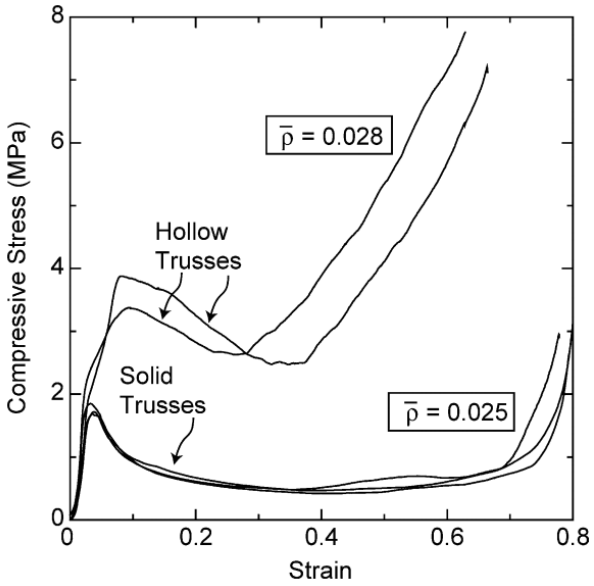

Figure 2.4. Compressive stress-strain curves of solid and hollow pyramidal trusses [66].

Tang et al. [67] investigated the dynamic crushing responses of AA6061 T6 and over aged AA6061 OA aluminum alloy tetrahedral truss sandwich structures as a function of core material, impact velocity and temperature. The tests were conducted in a SHPB set-up at the impact velocities between 23.6 and 11.3 m s^{-1} and at temperatures between 27 and -170 °C. It was shown that over aging and increasing testing temperature reduced the crushing stresses (Figure 2.5).

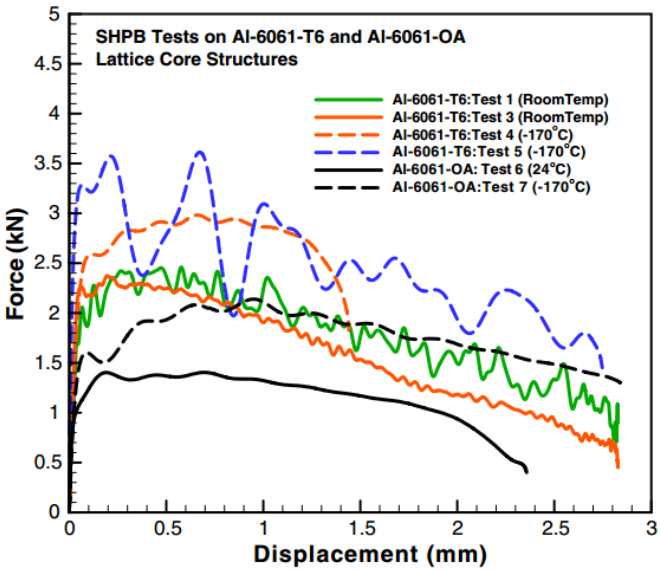

Figure 2.5. SHPB test results of Al 6061 T6 and Al 6061 OA tetrahedral truss cores at room and -170 °C temperature [67].

Lee et al. [61] investigated both experimentally and numerically the quasi-static ($8x10^{-5}$ m s^{-1}) and dynamic (2.5-6.4 m s^{-1} and 84.5-115 m s^{-1}) compression behavior of a unit metallic pyramidal truss core (Figure 2.6). Dynamic tests were conducted using a SHPB bar and gas gun test system. The specimen was placed either at the front of transmitter bar (forward impact test) or striker bar (reverse impact test) (Figure 2.7). The Hopkinson Pressure Bar test peak stresses were 60% higher than quasi-static test peak stresses and the peak stresses in the gas gun tests were 3-4 times higher than those in the quasi-static tests (Figure 2.8). The increased compressive stress at increasing strain rates was attributed to the strain rate sensitive flow stress behavior of stainless steel and inertial effects. The tested unit core was reported type II structure, experiencing inertia-induced rate effects. Initial imperfections were given to numerical models. The numerical model with perfect core could not capture the experimental densification strain (Figures 2.9(a) and (b)). The imperfections were shown to determine the direction of core wall buckling.

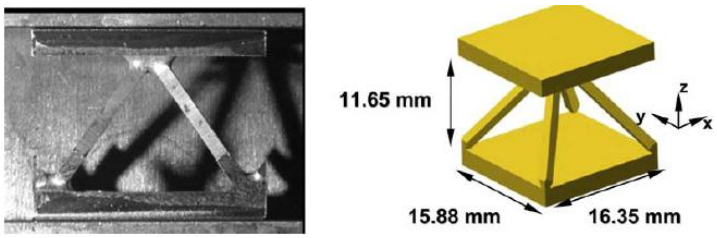

Figure 2.6. Unit stainless steel pyramidal truss core [61].

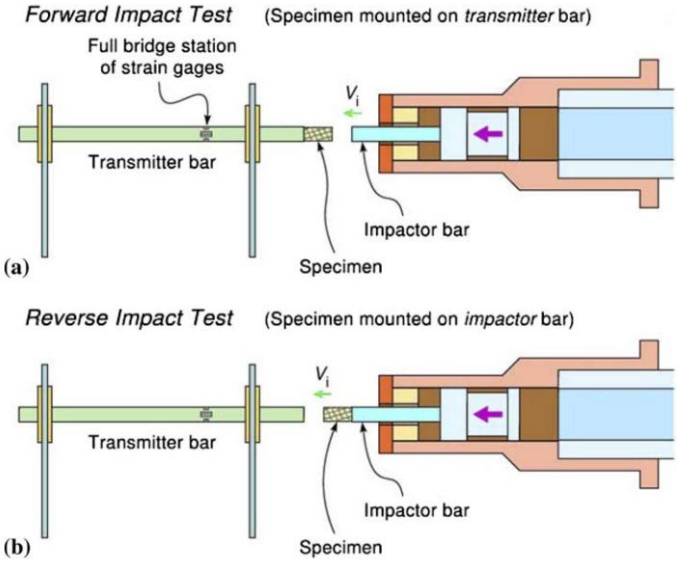

Figure 2.7. Gus gun tests: (a) forward and (b) reverse impact tests [61].

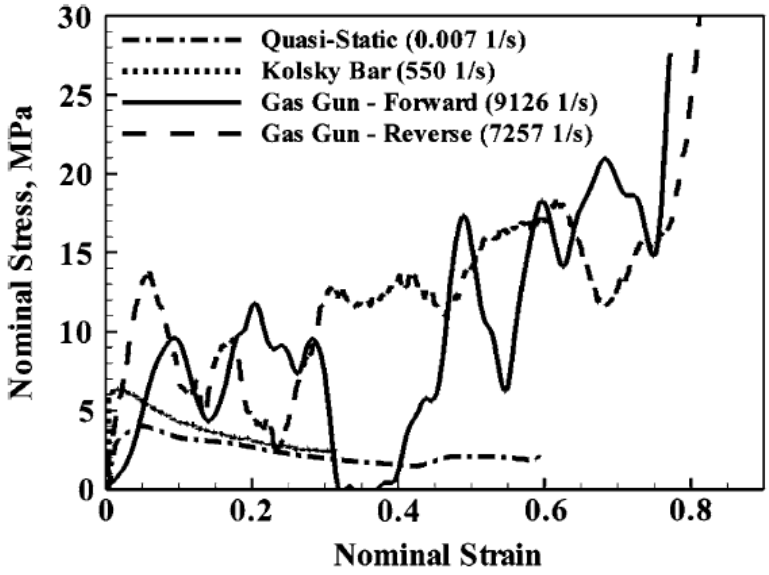

Figure 2.8. Compression stress–strain curves of pyramidal truss core crushed at different strain rates [61].

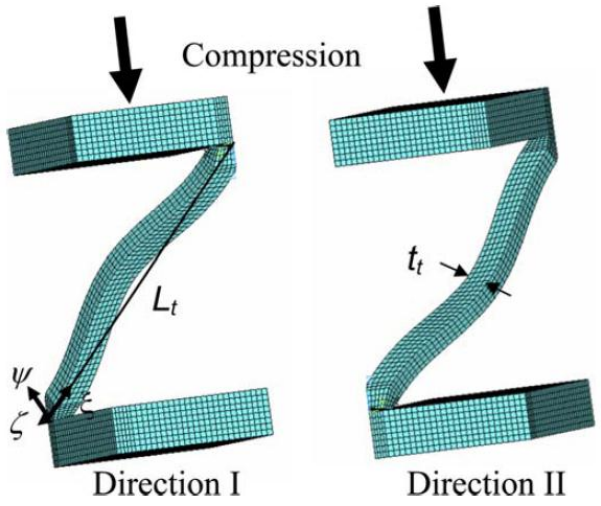

(a)

Figure 2.9. (a) The numerical imperfections on the core walls and (b) the effect of imperfection on the behavior of truss core at the quasi-static strain rate [61].

(cont. on next page)

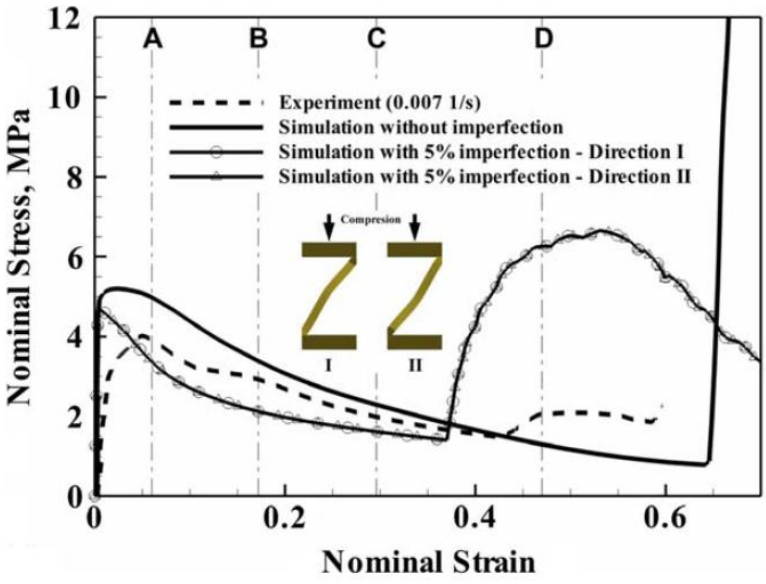

(b)

Figure 2.9 (cont.)

Mori et al. [68] investigated the underwater blast performance of pyramidal truss and honeycomb sandwich structures of identical core density using an experimental setup called fluid-structure interaction (Figure 2.10). A projectile was fired using a piston to generate pressure like blast loading to the sandwiches. The sandwich panels experienced 30% less back face deflection than monolithic plate. The back face deflections of both sandwiches were also shown to be very similar with each other (Figure 2.11(a) and (b)).

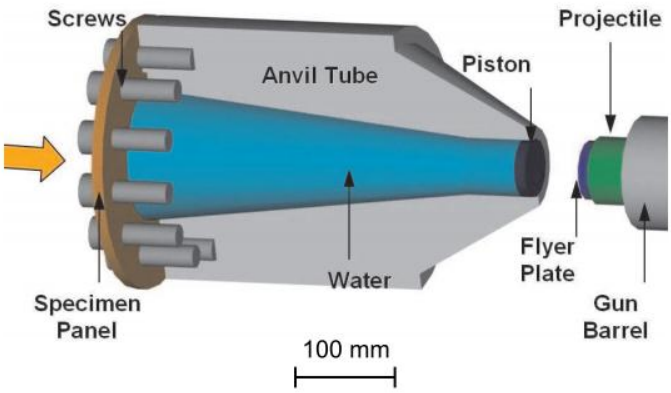

Figure 2.10. Fluid-structure interaction test system [68].

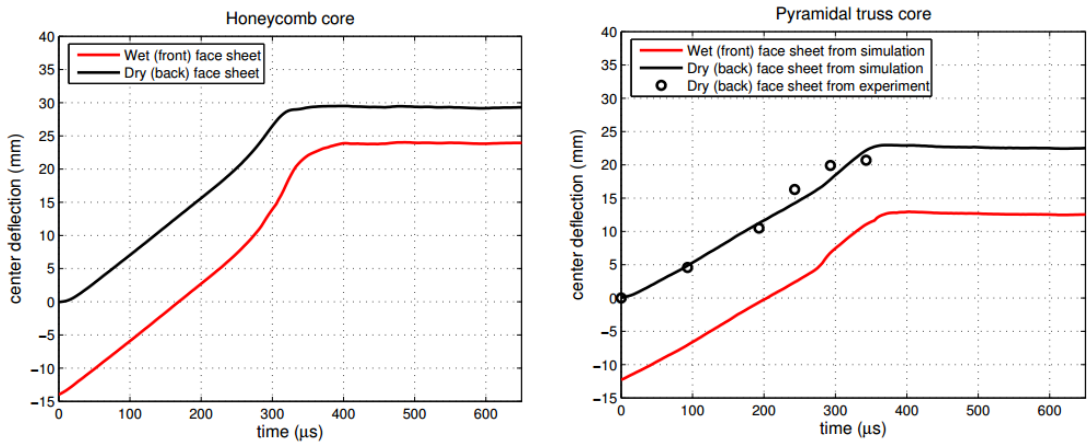

(a) (b)

Figure 2.11. Maximum center deflections of (a) honeycomb and (b) pyramidal truss core sandwich panels [68].

Yungwirth et al. [62] investigated the ballistic performance of 304 L stainless steel and 6061 T6 aluminum pyramidal lattice core panels. The tests were conducted using a spherical steel projectile at impact velocities between 250 and 1300 m s^{-1}. The results showed that aluminum lattice core panels exhibited higher energy absorption than stainless steel lattice panels (Figure 2.12(a)). However, the energy absorption of stainless steel lattice core panels and monolithic steel plates were found very similar at equal mass (Figure 2.12(b)).

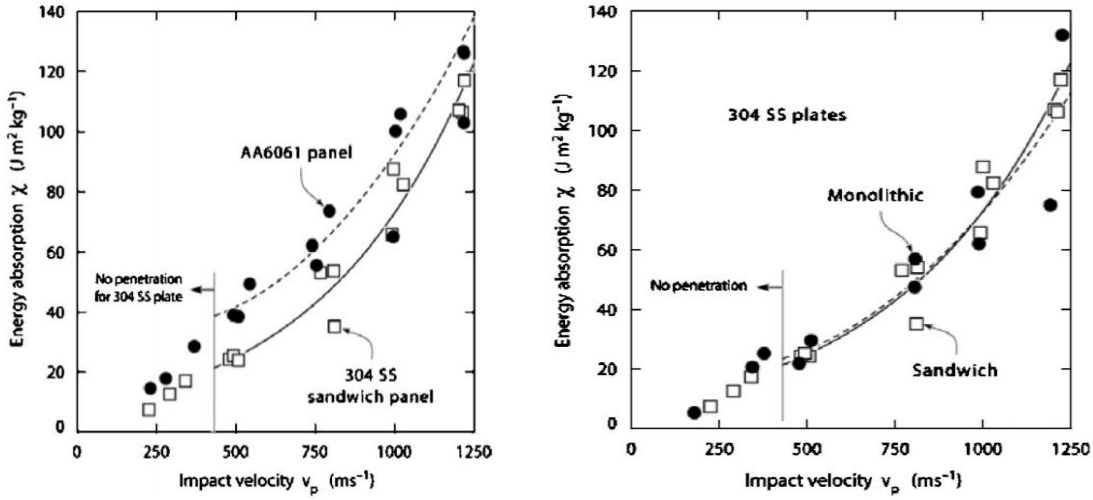

(a) (b)

Figure 2.12. Energy absorption-impact velocity curves of (a) 304 stainless steel and 6061 T6 aluminum sandwich and (b) 304 L stainless steel monolithic panels [62].

Wadley et al. [69] investigated the water shock response of multi-layered 304L stainless steel pyramidal lattice panels (Figures 2.13(a) and (b)) using a laboratory scale blast loading test system (Figure 2.14). The panels were prepared through brazing in a vacuum furnace. After brazing process, panels were cut into cylindrical test samples of 203 mm in diameter (Figure 2.13(b)). In water shock experiments, the test panels were inserted between hardened plates with a central opening and strain gages were placed on specimen holder columns to measure the transmitted pressures. Impulse was generated by a detonator in a water tank. The quasi-static compression behavior of the blast tested pyramidal lattice panels was very similar to that of metallic foams; exhibiting nearly a flat plateau region (Figure 2.15). Small stress peaks occurred in the plateau region due to the buckling of truss members. The developed numerical model captured the experimental compression curve of panels. In dynamic shock loading, the pyramidal lattice panels was shown to reduce the peak pressure transmitted to the back face as compared with the equivalent monolithic plate (Figures 2.16 (a) and (b)). The pyramidal lattice panels also increased the impulse duration transferred to the backing plate.

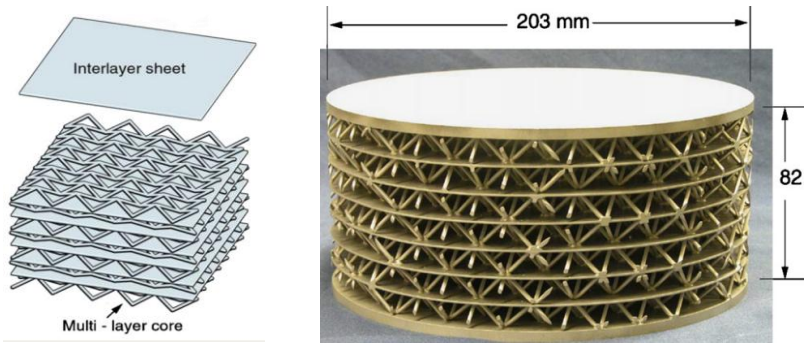

(a) (b)

Figure 2.13. (a) Multi-layer pyramidal lattice panel and (b) the tested panel [69].

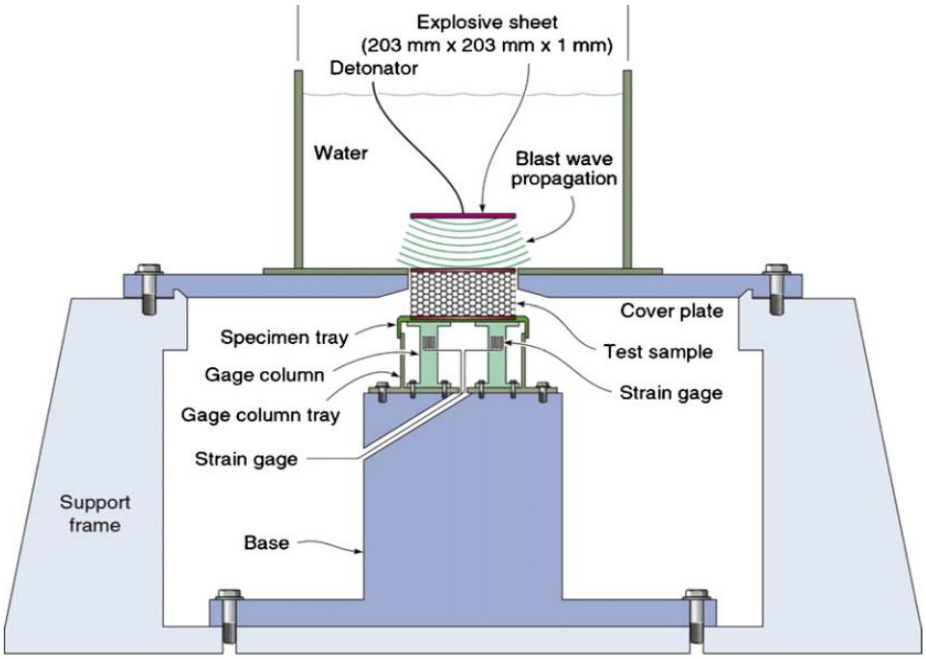

Figure 2.14. Water shock test set-up [69].

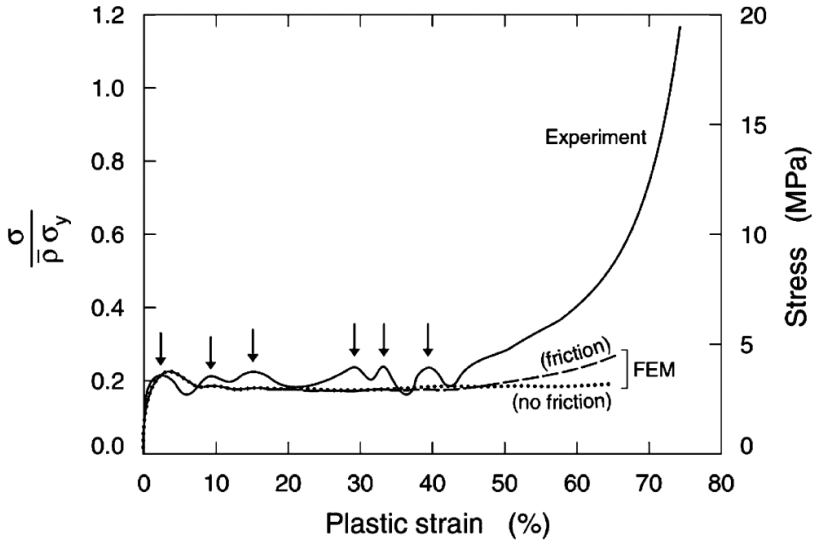

Figure 2.15. Experimental and numerical quasi-static compression response of multilayered pyramidal lattice structure [69].

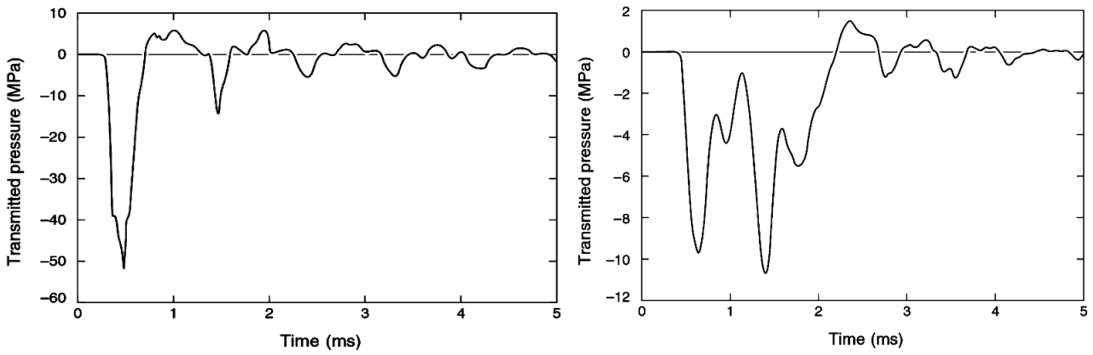

(a) (b)

Figure 2.16. Transmitted pressure to the back face for (a) monolithic solid plate and (b) pyramidal truss panel [69].

Jiang et al. [70] investigated the residual stresses generated and the effects of forming variables including punching angle and length on the deformation of a brazed stainless steel pyramidal lattice sandwich structure using finite element (FE) analysis. The results showed that large residual stresses were generated on the brazed joints between lattice core and face sheets. Two different deformations were detected; the thickness reduction of trusses and the shrinkage of filler brazing material. The punching angle was found to be very effective on the residual stresses and thickness reduction while punching length did not show a significant effect on the residual stresses. Both forming variables were seen to have imperceptible effect on the filler shrinkage.

Dharmasena et al. [71] investigated experimentally and numerically the response of stainless steel pyramidal lattice core sandwich panels subjected to air blast. The responses of the panels were compared with those of the monolithic solid plates of equivalent areal density. The panels were tested by the detonation of a 150 g spherical C-4 explosive (Figure 2.17) and Con-Wep blast algorithm was used in the FE simulations. The pyramidal core sandwich panels exposed to air blast loading exhibited only slightly reduced back face reflection compared to equivalent mass solid plate (Figure 2.18). The simulations also showed that the pyramidal core sandwich panels transmitted significantly lower vertical forces to the support than the monolithic plate (Figures 2.19(a) and (b)).

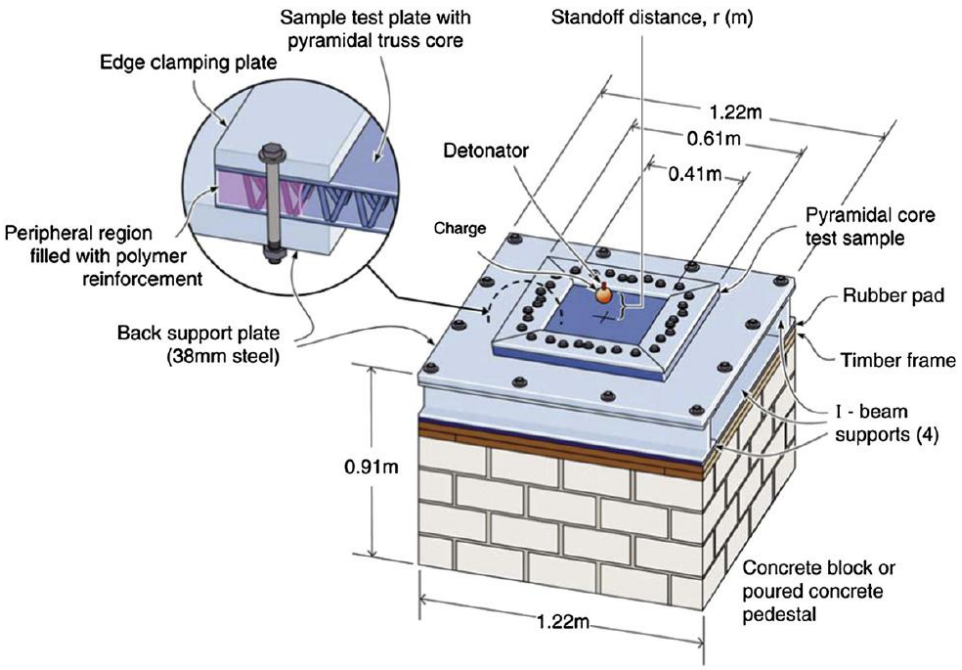

Figure 2.17. Experimental set-up of the air blast test [71].

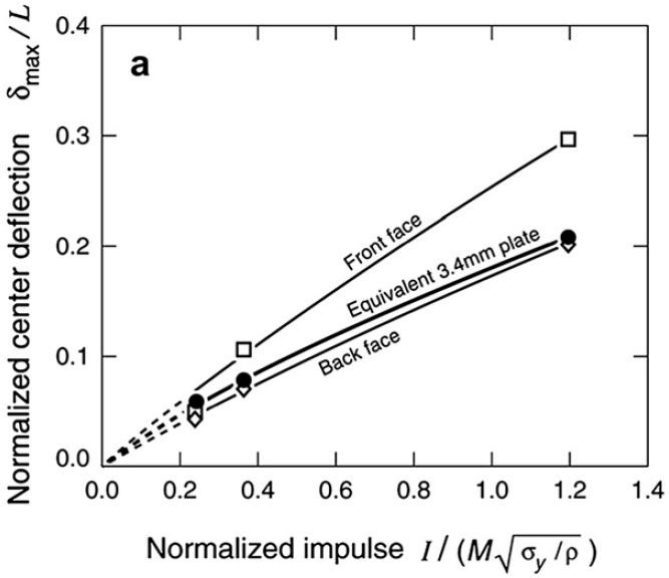

Figure 2.18. Normalized center deflections of pyramidal core sandwich panel and solid plate [71].

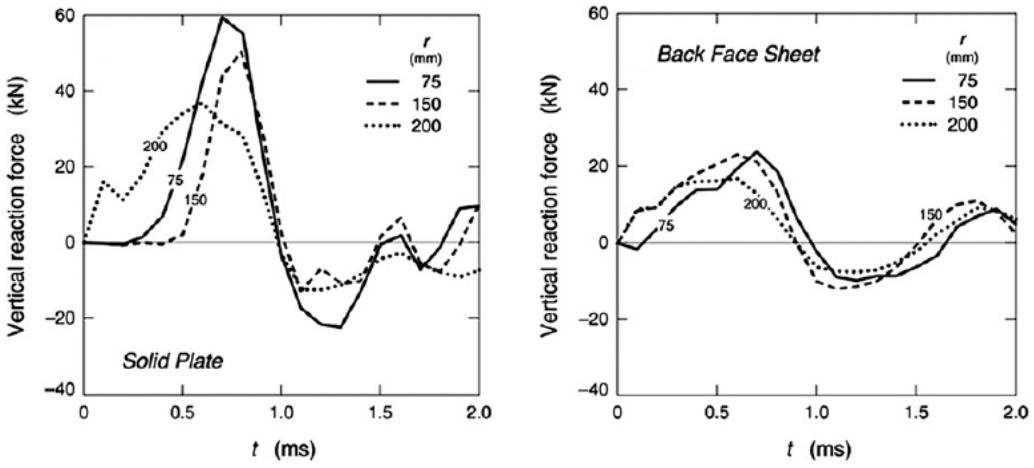

(a) (b)

Figure 2.19. Vertical reaction forces transmitted to supports as a function of time for the three standoff distances: (a) solid plate and (b) back face sheet of pyramidal core sandwich panel [71].

2.2. Corrugated Cores

In an earlier study in 2001, Liang et al. [52] investigated the optimum weight designs of metallic corrugated core structures in transverse and axial directions. The most effective parameters on the face sheet axial stress were reported to be corrugation length and face sheet thickness, while all other geometrical parameters equally affected the core axial stress (Figure 2.20).

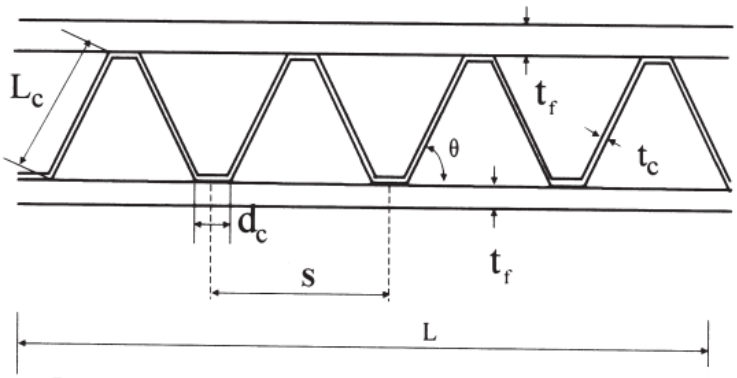

Figure 2.20. Geometrical parameters of corrugated sandwich [52].

Armentani et al. [29] developed a nonlinear FE model of the corrugated paper boards under compressive loads. The effects of full geometrical corrugated layer modeling (Figure 2.21(a)) and solid core modeling (Figure 2.21(b)) on the compression behavior were investigated. Paper was assumed orthotropic and linear elastic in the numerical models. The numerical analysis showed that the simplified solid core modeling and full geometrical model resulted in similar load values until about 5 mm displacement at which the buckling of core layers started (Figure 2.22). After that, the load-displacement curve of solid core model and full geometrical model deviated from each other in post-buckling region. The deviation, however, were reported to be acceptable, when the computation time was considered.

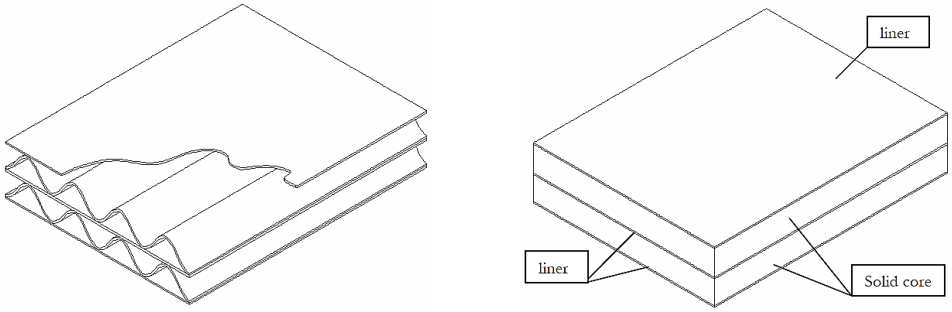

(a) (b)

Figure 2.21. Double corrugated board sandwich: (a) the full geometrical model and (b) simplified solid core model [29].

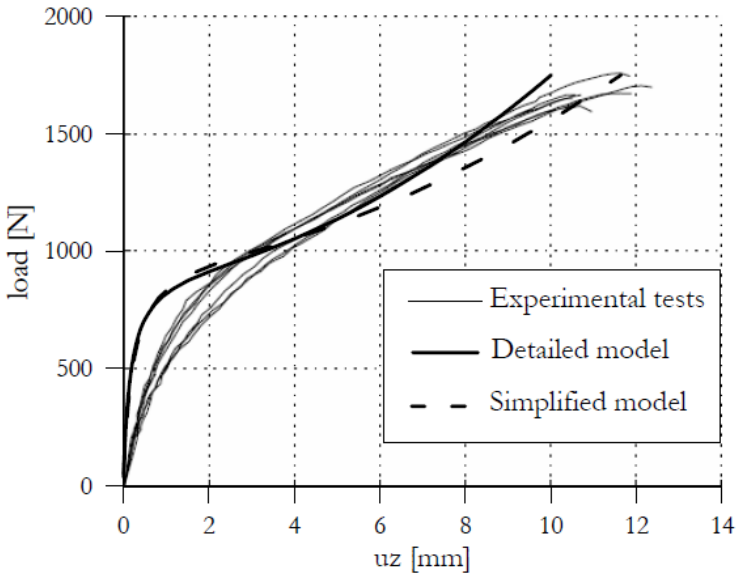

Figure 2.22. Experimental and numerical load-displacement curves of paper board sandwich structure [29].

Radford et al. [51] conducted projectile impact tests using aluminum foam projectiles on stainless steel triangular corrugated (Figure 2.23(a) and pyramidal truss (Figure 2.23(b)) core plates. The pyramidal and corrugated core exhibited similar compressive peak stresses at quasi-static strain rate (Figure 2.24). The mid-span deflections of monolithic plates were found to be higher than those of pyramidal and corrugated core sandwich beams at all initial projectile momentum as shown in Figure 2.25.

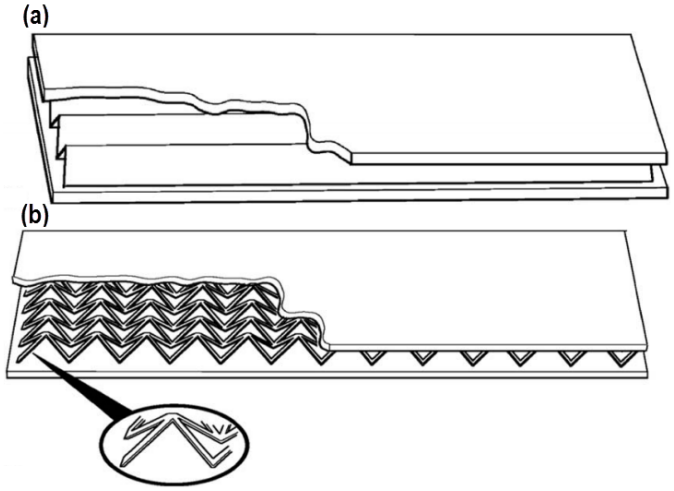

Figure 2.23. Sandwich plates with (a) triangular corrugated and (b) pyramidal truss cores [51].

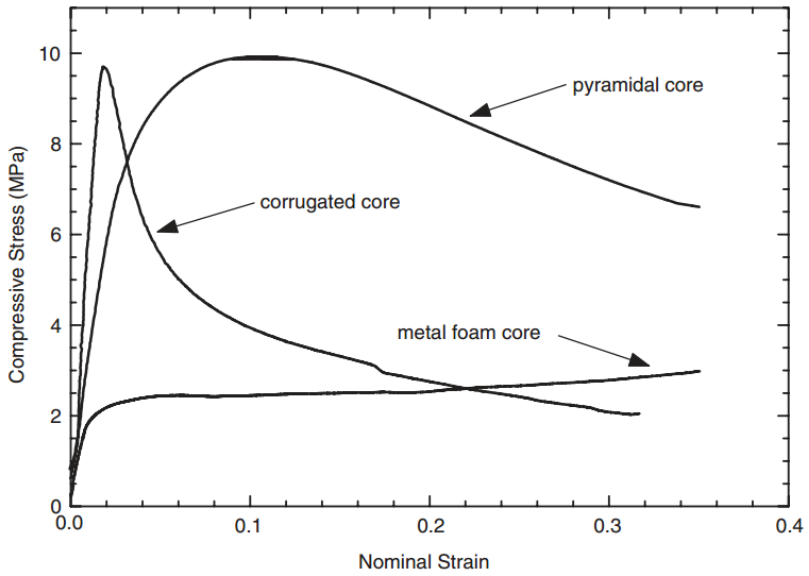

Figure 2.24. Compressive stress-nominal strain curve of corrugated, pyramidal and metal foam cores [51].

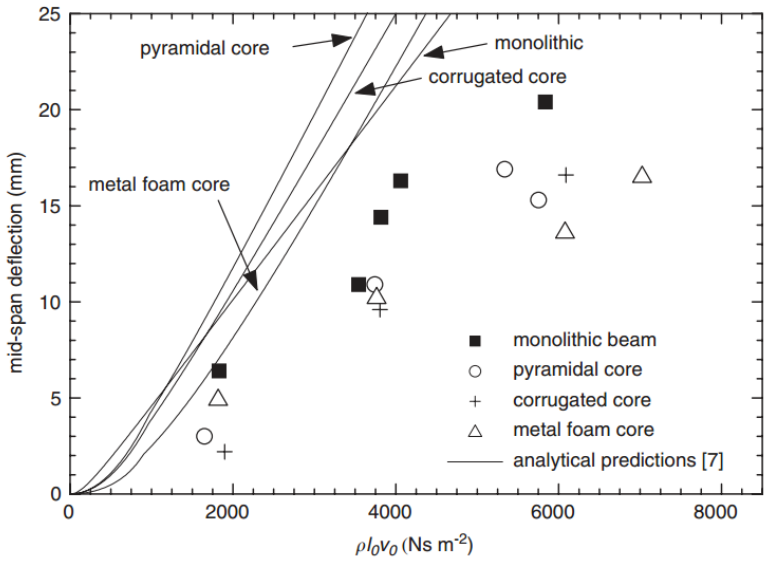

Figure 2.25. Mid-span deflection of monolithic plates and sandwich beams versus initial projectile momentum [51].

Cote et al. [54] determined the compressive, transverse and longitudinal shear responses of sandwich panels with stainless steel triangular corrugated ($0.03<\overline{\rho}\leq 0.06$) and diamond lattice ($0.08<\overline{\rho}\leq 0.25$) cores (Figures 2.26 (a) and (b)). The crushing strength and energy absorption capabilities of the cores were further compared with those of the square honeycomb and pyramidal cores. It was found that the corrugated and diamond cores under transverse shear and out-of-plane compressive loadings exhibited lower energy absorptions than the square honeycomb and pyramidal cores (Figure 2.27(a) and (b)), while the energy absorptions of the cores were shown to be close to those of square-honeycomb core under longitudinal shear (Figure 2.27(a)).

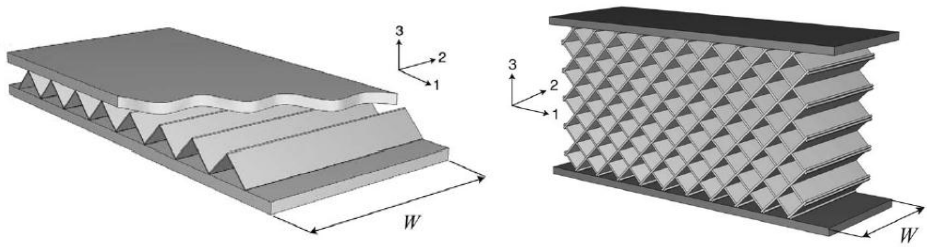

(a) (b)

Figure 2.26. Isometric view of (a) corrugated and (b) diamond core models [54].

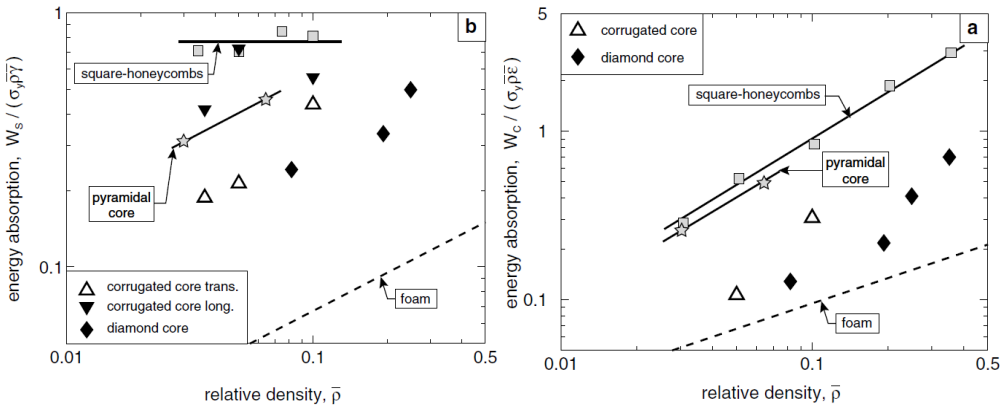

(a) (b)

Figure 2.27. Energy absorption-relative density curves of (a) transverse and longitudinal shear loading and (b) out-of-plane compression [54].

McShane et al. [72] investigated the projectile impact response of clamped circular AL 6XN stainless steel pyramidal (Figure 2.28 (a)) and AISI 304 stainless steel square-honeycomb (Figure 2.28(b)) sandwich plates using metal foam projectiles. The mid spans back face deflections and the core deformations of the plates were measured as function of projectile momentum. Pyramidal and square-honeycomb plates showed smaller blackface deflections than monolithic plates of equivalent mass, while the square-honeycomb plates exhibited the smallest back face deflection (Figure 2.29).

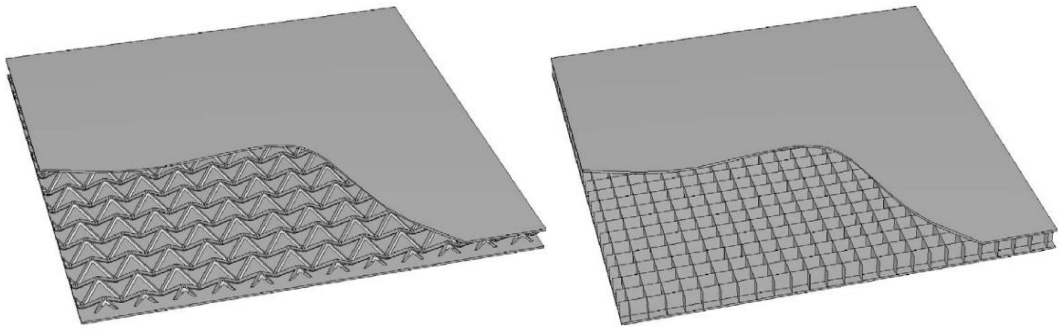

(a) (b)

Figure 2.28. Sandwich structures with (a) pyramidal and (b) square honeycomb core [72].

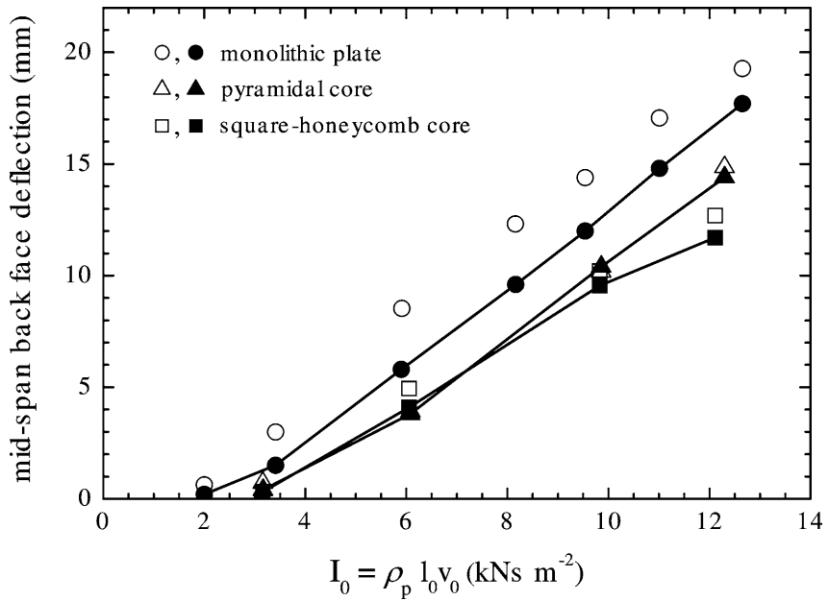

Figure 2.29. Mid-span back face deflection versus projectile momentum [72].

Tilbrook et al. [49] investigated the quasi-static (v_o=0.022 mm s^{-1}) and dynamic (v_o=2-200 m s^{-1}) compression deformation behavior of AISI 304 stainless steel triangular corrugated and Y-frame core sandwiches. The dynamic tests were performed using a modified SHPB test apparatus in two different testing protocols. In the first, the sample inserted at the front of the striker bar was directly impacted to the end of the incident bar (Figure 2.30(a)). In the second protocol, the sample placed at the end of the incident bar was impacted by the striker bar (Figure 2.30(b). It was shown that stresses generated at the front and rear faces were similar at low impact velocities ($v_o \leq 60$ m s^{-1}) for both corrugated and Y-frame core sandwiches as shown (Figures 2.31(a) and (b)). This was attributed to the inertial stabilization of webs against buckling. The corrugated structure was also found to be more inertia sensitive than Y-frame core (Figure 2.31(a) and (b)). At high impact velocities ($60 \leq v_o \leq 200$ m s^{-1}), the front face stress was found to increase with increasing impact velocity while rear face stress remained almost constant in Y-frame and corrugated sandwich cores (Figure 2.32 (a) and (b)), which was attributed to the plastic wave effects within the core members.

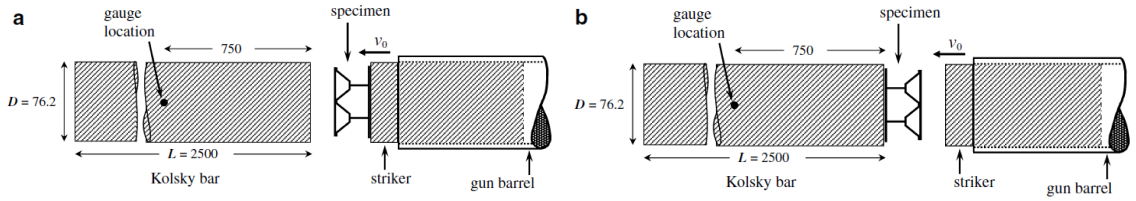

Figure 2.30. SHPB test configurations of the corrugated bar: (a) front face and (b) rear face testing [49].

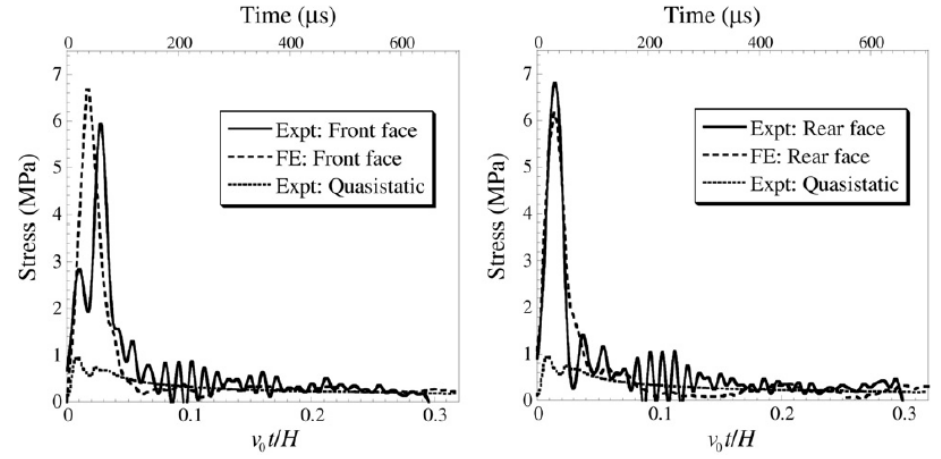

(a)

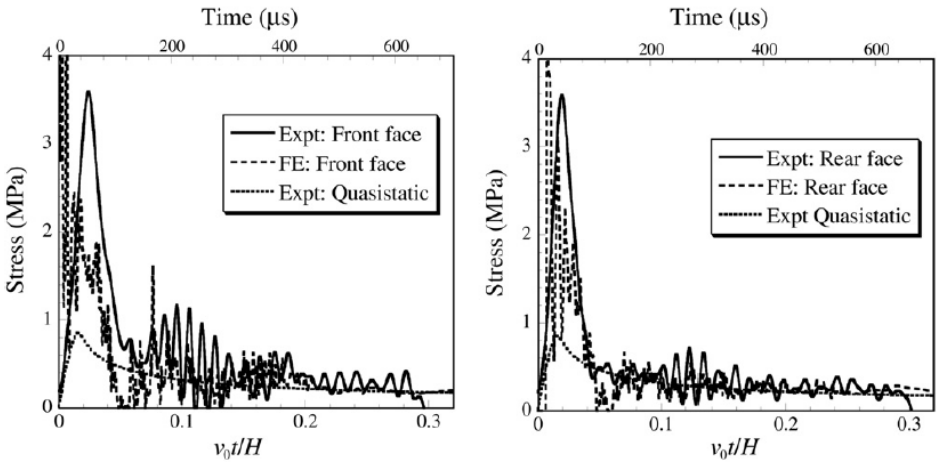

(b)

Figure 2.31. The experimental and FE stresses of sandwich specimens tested at 0.022 mm s^{-1} and 10 m s^{-1}: (a) the front and rear face of corrugated core and (b) the front and rear face of Y-frame core [49].

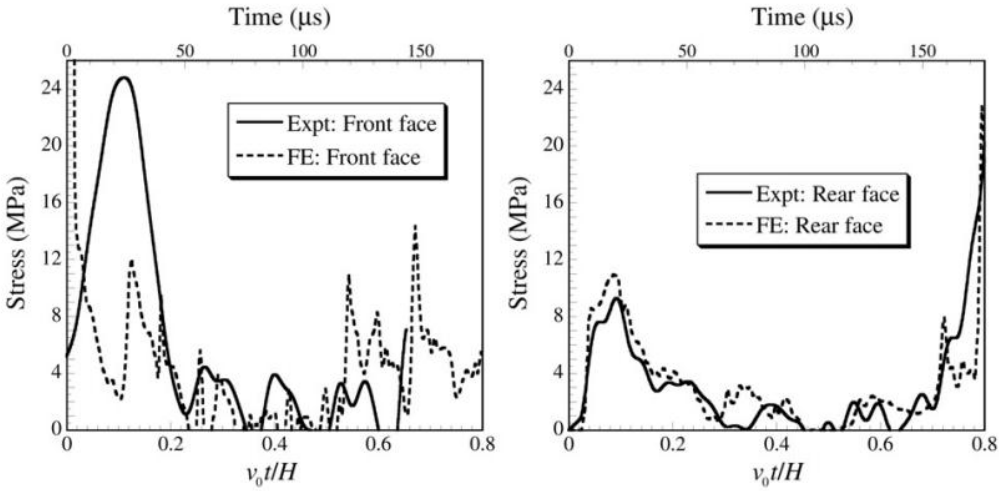

(a)

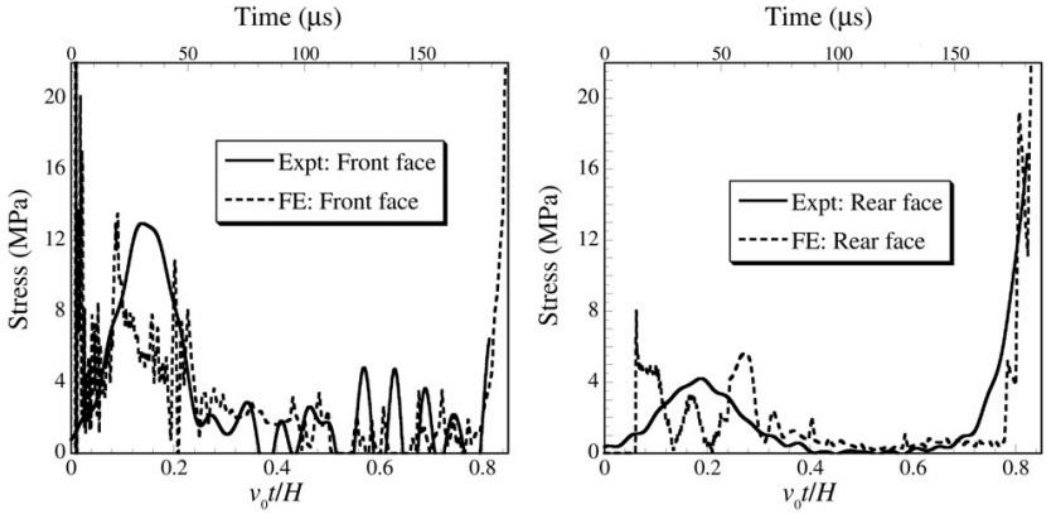

(b)

Figure 2.32. The experimental and FE stresses of sandwich specimens tested at 100 m s ^{1}: (a) the front and rear face of corrugated core and (b) the front and rear face of Y frame core [49].

Rubino et al. [46] investigated experimentally and numerically the impact response of end-clamped AISI 304 stainless steel Y-frame and corrugated core sandwich beams using aluminum foam projectiles (Figure 2.33(a)). Longitudinal and transverse core alignments were used in sandwich beams (Figure 2.33(b)). The sandwich beams with transverse core had the similar back face deflections with the monolithic beam (Figures 2.34(a) and (b)), while the sandwich beams with longitudinal core configuration showed smaller back face deflection than the equal mass monolithic beam (Figure 2.35).

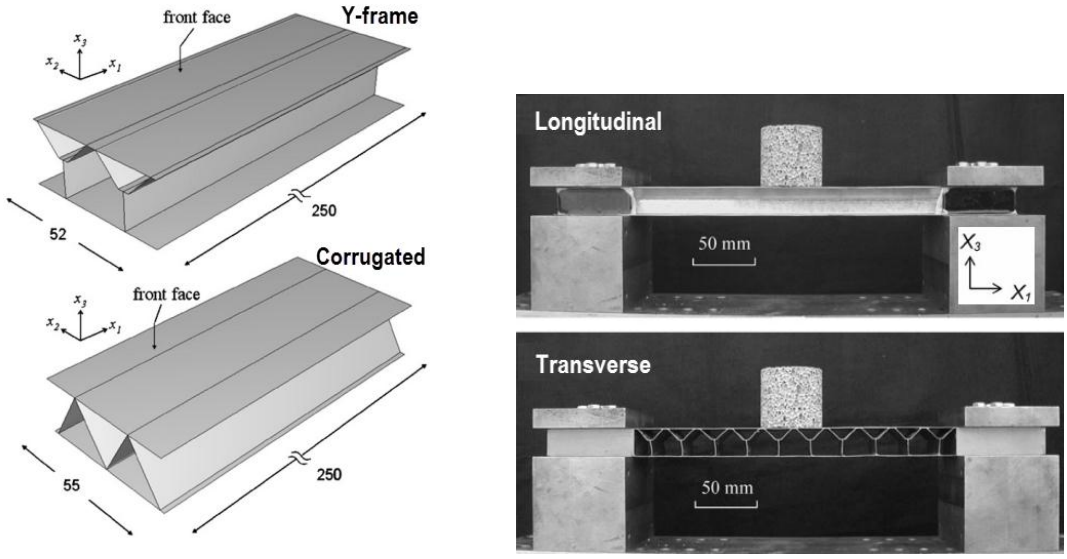

(a) (b)

Figure 2.33. (a) Y-frame and corrugated core sandwich beams and (b) longitudinal and transverse core alignments [46].

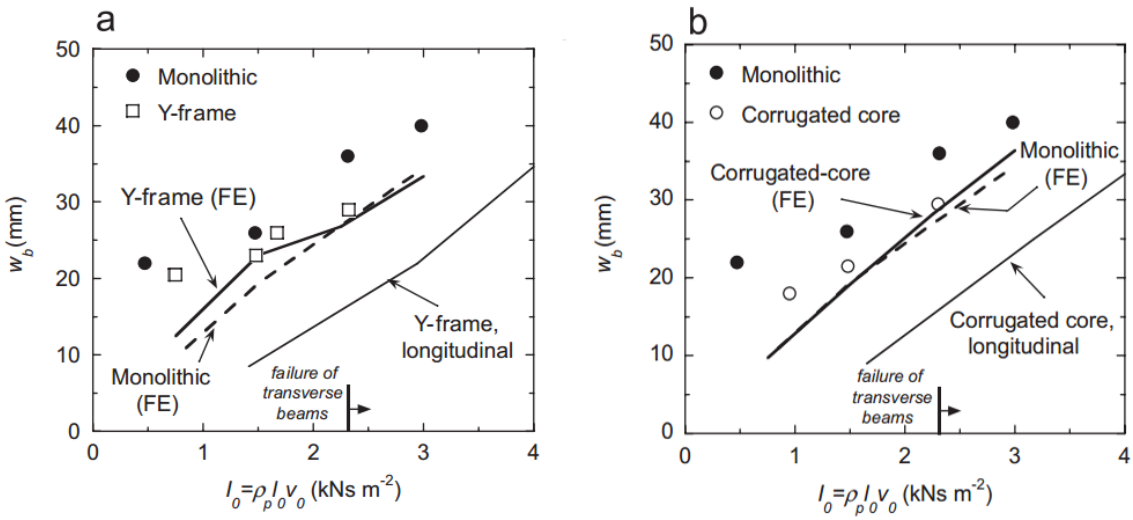

Figure 2.34. Rear face deflections of sandwich beams with transverse core arrangements as function of projectile momentum (I_0): (a) Y-frame core and (b) corrugated core [46].

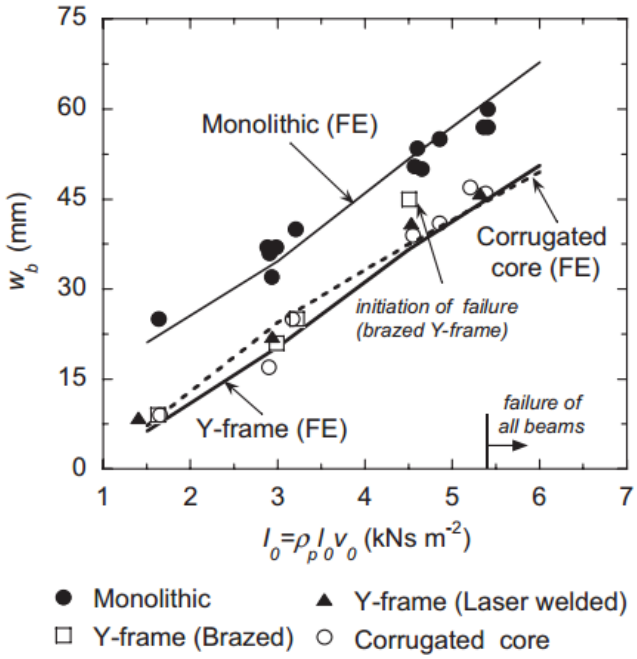

Figure 2.35. Rear face deflections of sandwich beams with longitudinal core arrangements as function of projectile momentum (I_0) [46].

Rubino et al. [47] investigated the projectile impact response of clamped AISI 304 stainless steel Y-frame and corrugated core sandwich plates using aluminum foam projectiles. The results showed that plates deflected less than beams and the ratio of permanent deflection of sandwich plates to monolithic plates increased with increasing impulse. However, the face sheets of sandwich plates failed at lower impulse as compared with monolithic plates.

Seong et al. [73] studied the bending responses of mild steel sandwich panels with uni-directionally and bi-directionally corrugated cores (Figure 2.36(a) and (b)). Bi-directionally corrugated cores were found to increase the bending resistance of face sheets and reduced the anisotropic bending behavior of sandwich structures.

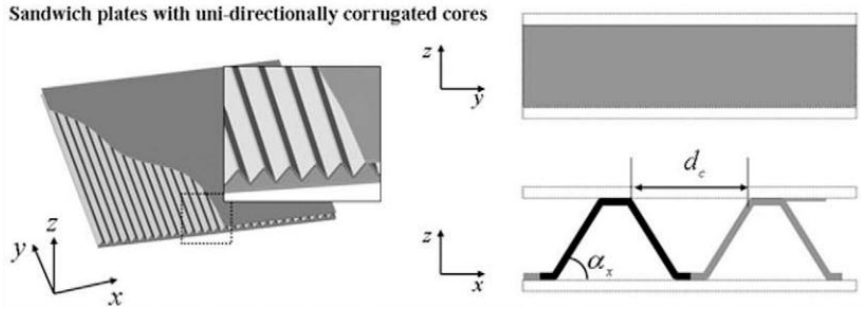

(a)

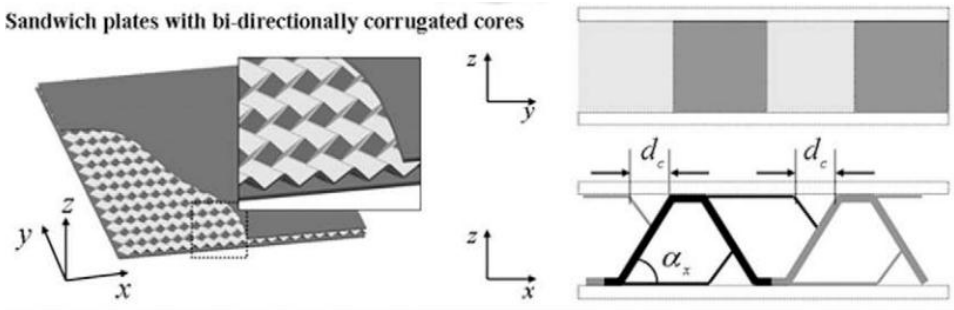

(b)

Figure 2.36. Sandwich plates with (a) uni-directionally and (b) bi-directionally corrugated cores [73].

Zhang et al. [50] compared the quasi-static crushing behavior of V, U, X and Y-type corrugated core sandwich panels both experimentally and numerically (Figure 2.37(a-d)). Quasi-static compression tests were conducted at 0.16 mm s^{-1} loading rate, while the numerical analyses were implemented at 2 m s^{-1} impact velocity. Experiments and numerical analysis showed that all core topologies had excellent crushing response except Y-frame corrugated structure. The core walls of Y-frame corrugated structure deformed in bending mode (Figure 2.38). The experimental and numerical studies also revealed that V-shape corrugated core exhibited the highest crushing strength and energy absorption capacity. The deviations between the experiments and models were attributed to the imperfections induced in the core structures during welding.

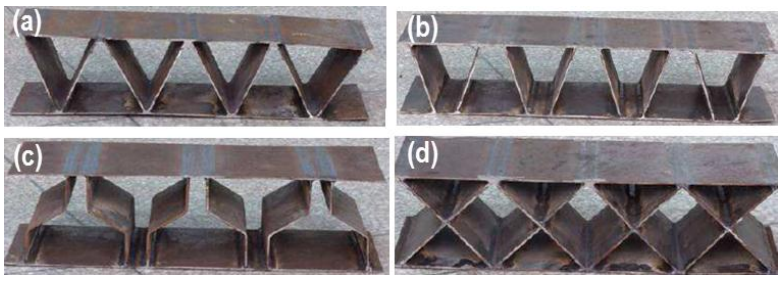

Figure 2.37. Corrugated cores: (a) V-shape, (b) U-shape, (c) Y-shape and (d) X-shape [50].

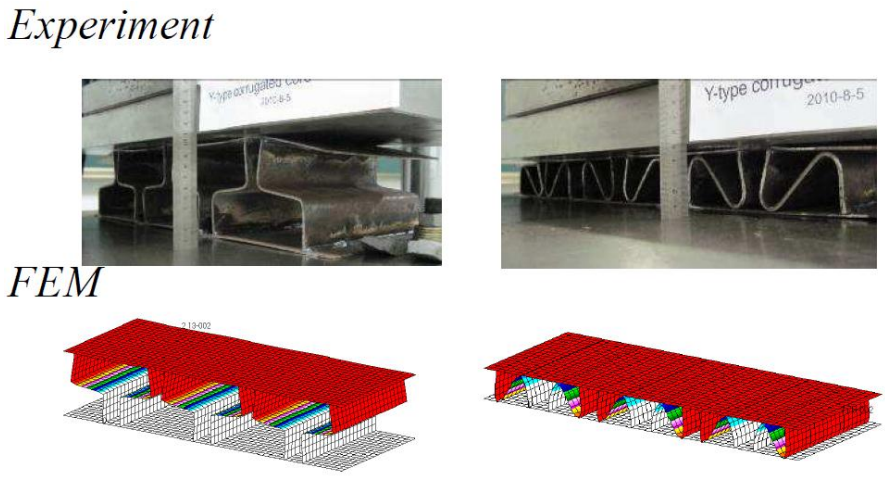

Figure 2.38. Experimental and numerical deformation of Y-shape sandwich panels [50]

McShane et al. [74] investigated the quasi-static and dynamic compression behavior of a 304 stainless steel triangular metallic corrugated core sandwich structure (Figure 2.39(a) and (b)). Numerical analyses were also performed to determine the effects of strut geometry on the compression behavior. The geometrical parameters of unit cell model included length *(L)*, width (*a)* and inclination angle (ω). In the model, *L/a* was taken as 20 and 60 and ω taken as 45°. The non-dimensional front face sheet velocity (V_0/c_{pl} sinω, $c_{pl:}$ plastic wave velocity) was used to define compression rate. The value of V_0/c_{pl} sinω ranged $8x10^{-3}$-1.7, equivalent to 1-200 m s^{-1}. The reaction forces were found similar to each other for quasi-static and dynamic tests for the strut with *L/a*=20 (Figure 2.40(a)). The struts deformed plastically at both loading rates. However, deformation was elastic at quasi-static rate and plastic at dynamic rate for the strut with *L/a*=60 (Figure 2.41(a)). It was also seen that buckling mode was similar at quasi-static and dynamic rates for the strut with *L/a*=20 while buckling direction was opposite in dynamic case for the strut with *L/a*=60. When V_0/c_{pl} sinω increased to 0.5 (Figure 2.40(b) and Figure 2.41(b)), the front and back reaction forces were not similar with each other for the strut with *L/a*=20 and 60 due to the impact of buckled strut to the front face. The contact of the strut to the face sheet was defined as stubbing. For V_0/c_{pl} sinω was equal to 1.3, the front and back face reaction forces almost stayed constant for the strut with *L/a*=20 and 60 (Figure 2.40(c) and Figure 2.41(c)). This phenomenon was attributed to the generation of only stubbing and no plastic buckling on the strut. As a general conclusion, the plastic buckling occurred when the wavelength was equal to strut length as in the quasi-static loadings. At higher impact loadings, wavelength was smaller than strut length resulting in plastic buckling and stubbing.

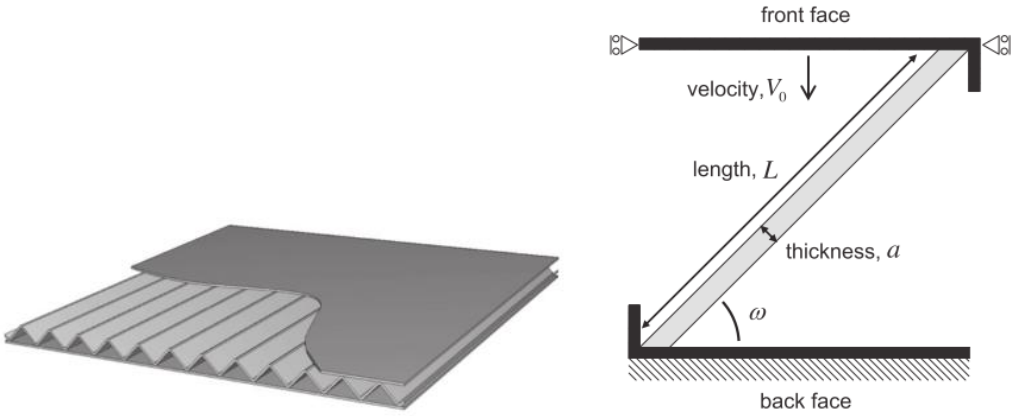

(a) (b)

Figure 2.39. (a) Triangular corrugated sandwich structure and (b) strut geometry [74].

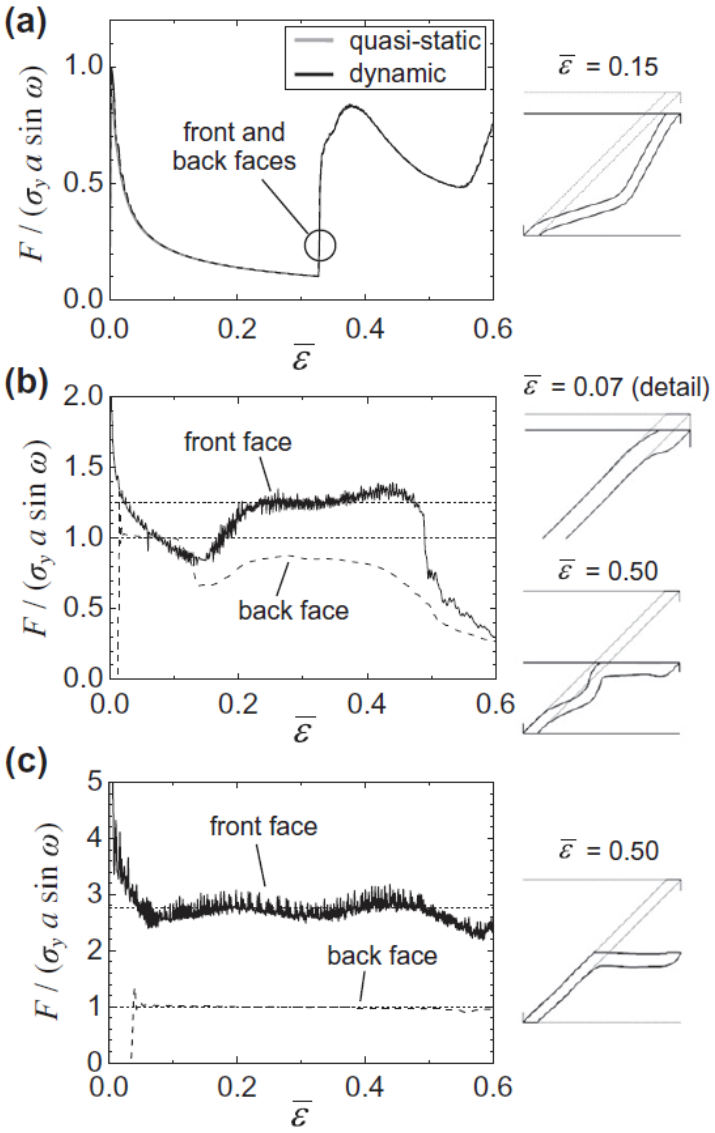

Figure 2.40. The face sheet reaction force versus strain for corrugated core with L/a=20 for V_0/c_{pl} sinω: (a) 0.0083, (b) 0.5 and (c) 1.3 [74].

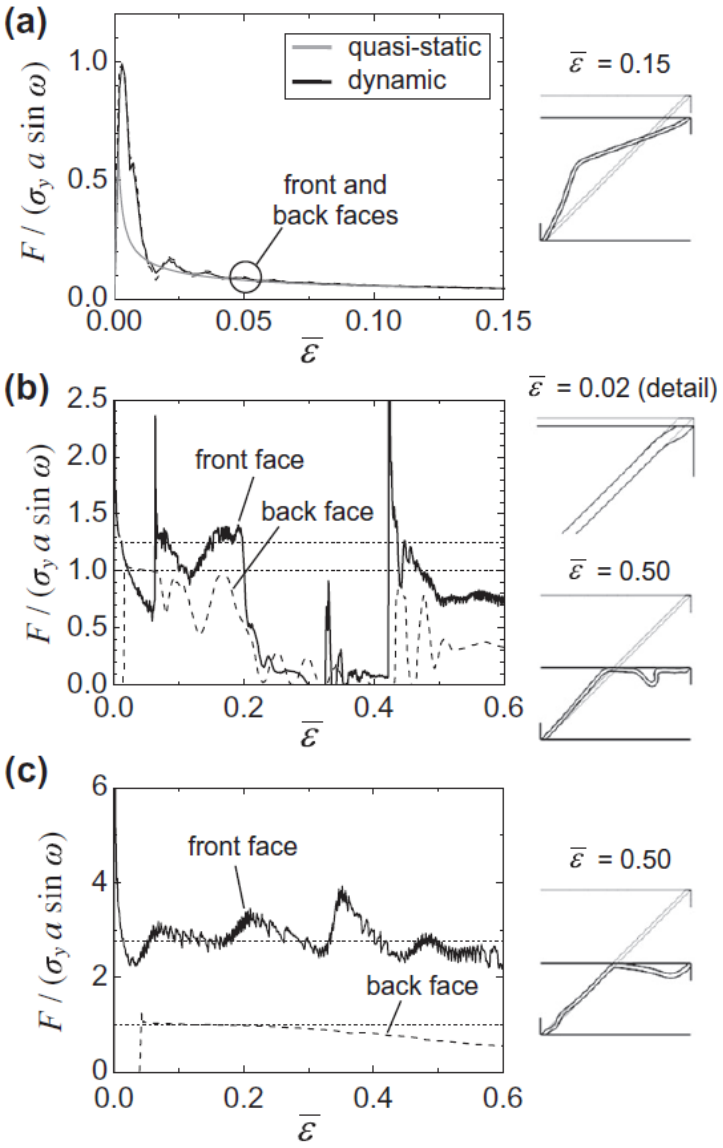

Figure 2.41.The face sheet reaction force versus strain for corrugated core with L/a=60 for V_0/c_{pl} sinω: (a) 0.0083, (b) 0.5 and (c) 1.3 [74].

Hou et al. [75] determined the quasi-static crushing and low velocity localized and planar impact behavior of 2024 Al alloy trapezoidal (Figure 2.42(a)) and triangular (Figure 2.42(b)) corrugated core sandwich panels both experimentally and numerically. Numerical simulations captured experimental curves reasonably except the densifications points for both core topologies (Figures 2.43(a) and (b)). The deviation in the stress-strain curves at the densification was attributed to the presence of epoxy adhesive layer in real specimens which delayed the buckling of core walls. It was shown that the shape of unit core had no significant effect on the impact response when the localized impact loading was present (Figure 2.44(a)). However, under the planar impact condition, the shape of unit core becomes relatively crucial (Figure 2.44(b)).

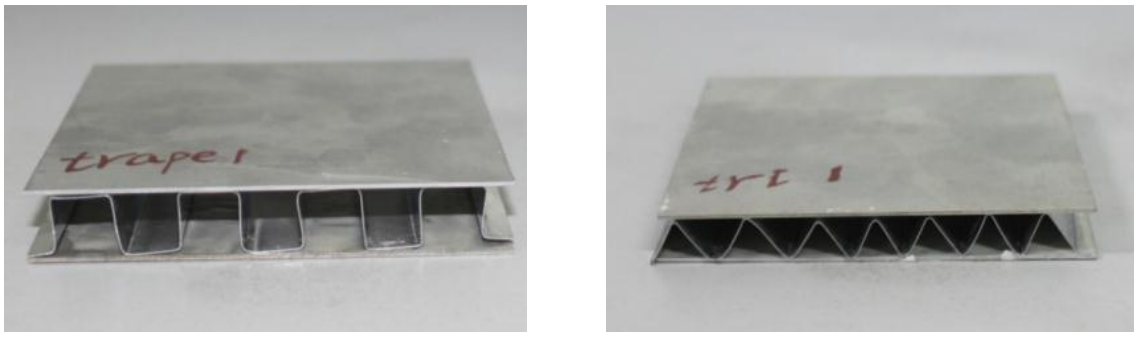

(a) (b)

Figure 2.42. Corrugated specimens: (a) trapezoidal and (b) triangular core [75].

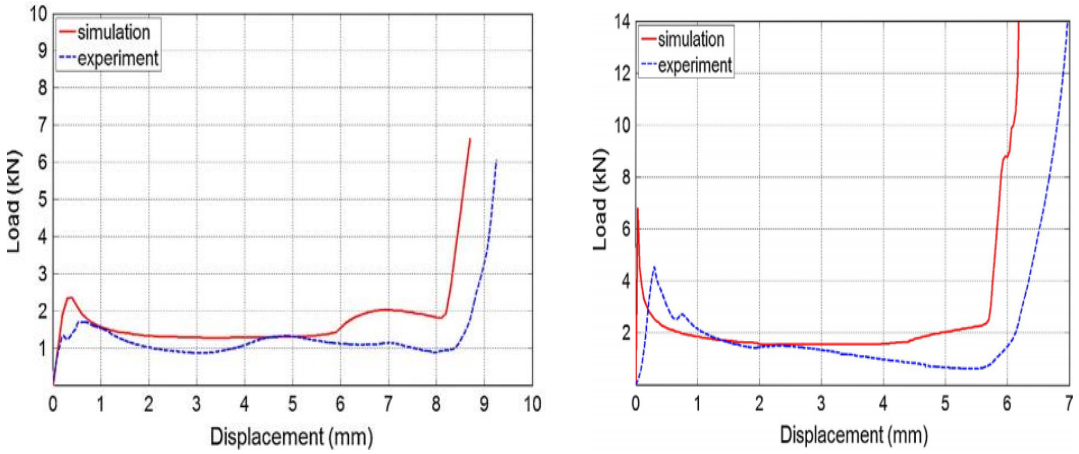

(a) (b)

Figure 2.43. Experimental and numerical quasi-static force-displacement curves of (a) trapezoidal and (b) triangular sandwich structures [75].

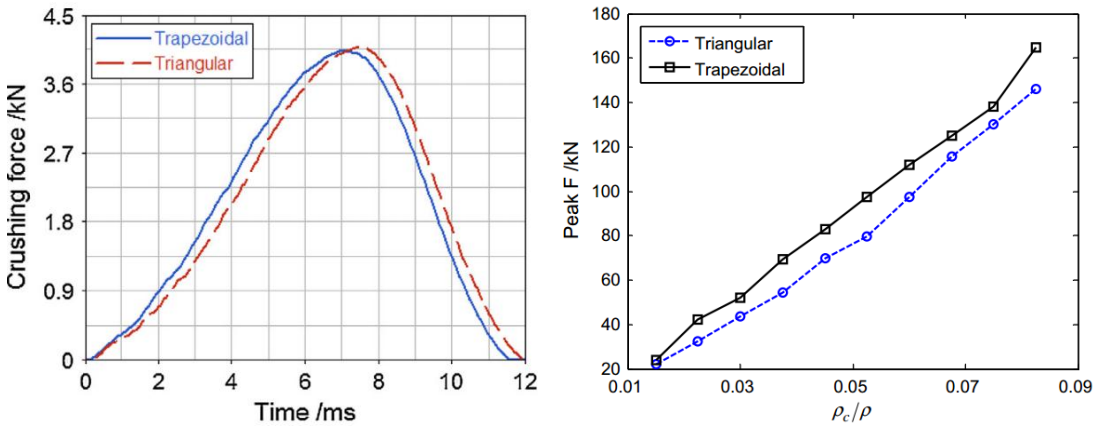

(a) (b)

Figure 2.44. Force-time curves of trapezoidal and triangular sandwiches for localized impact and (b) peak crushing forces for planar impact [75].

Rejab et al. [37] investigated, both experimentally and numerically at quasi-static loading rate (1 mm min^{-1}), the crushing responses of triangular corrugated sandwich structures made of 2024-O Al alloy, glass fibre reinforced plastic (GFRP) and carbon fibre reinforced plastic (CFRP) (Figures 2.45(a)-(c)). Aluminum 2024-O alloy triangular corrugated deformed through core wall bending (Figure 2.46(a)), whereas, CFRP and GFRP corrugated cores showed fiber delamination, fracture and debonding (Figure 2.46(b)). CFRP composite corrugated core had higher crushing strength than aluminum and GFRP composite corrugated core (Figure 2.47). The study also showed that the crushing strength of aluminum honeycombs can be reached using thick CFRP composite corrugated cores (Figure 2.47).

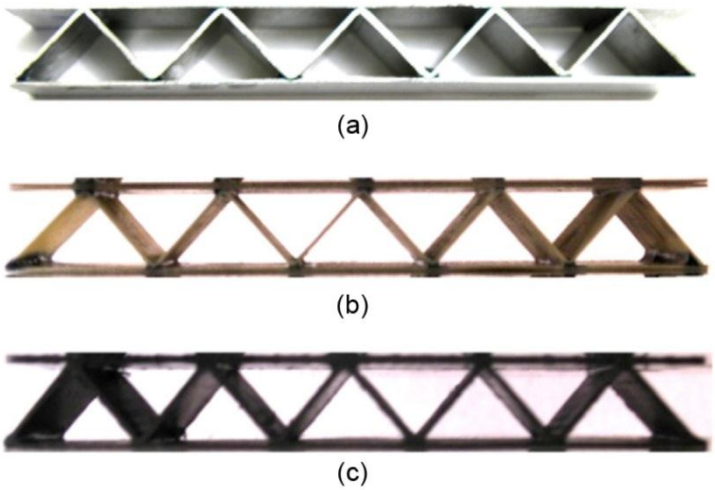

Figure 2.45. Triangular corrugated sandwiches: (a) 2024-O Al, (b) glass fibre reinforced plastic (GFRP), and (c) carbon fibre reinforced plastic (CFRP)[37].

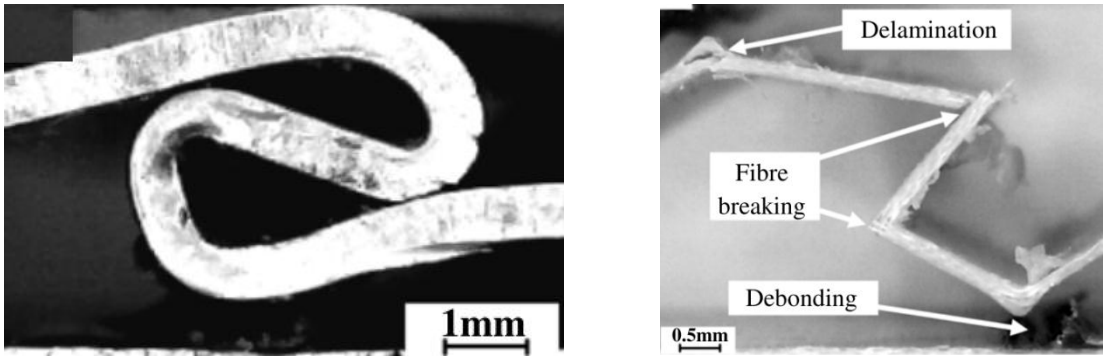

(a) (b)

Figure 2.46. Deformation modes of corrugated cores: (a) 2024-O Al, and (b) carbon fibre reinforced plastic (CFRP) [37].

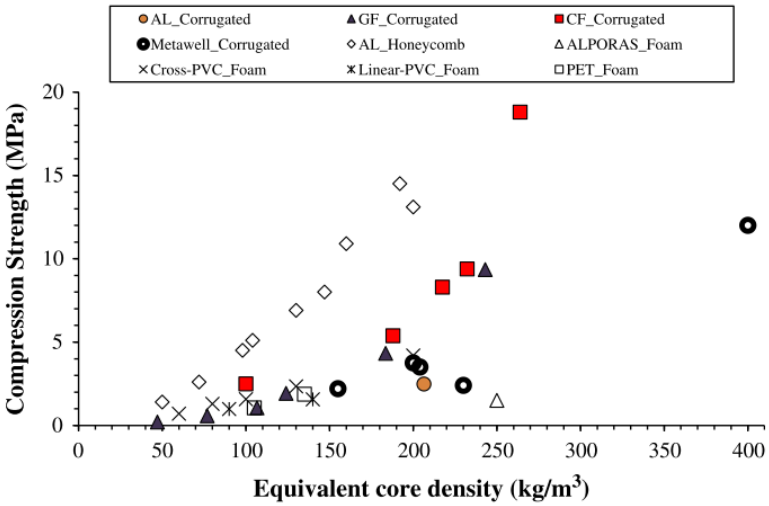

Figure 2.47. Compression strength versus equivalent core density [37].

2.3. Micro-Inertia Effects and Type I and Type II Structures

The type of the deformation of the structures subjected to impact loadings is essential to achieve high energy absorption capacity. At quasi-static strain rates, structures collapse under steadily increasing loads and deformation type is not complicated. However, in dynamic loading rates collapse mechanisms are more complicated due to two main factors [76]: the strain rate sensitivity of flow stress of material and the mode of the deformation affected by inertia forces. The yield stress of some materials increases at high strain rates which results an increase in the resistance of the structure against buckling. Inertia effect delays the buckling of column at dynamic loading rates, so that critical buckling load becomes higher than the one in quasi-static loading rates.

Calladine and English [76] classified structures in energy absorbing situations as type I and type II structures. Type I structures show a flat-topped load-displacement curve as shown in Figure 2.48. Examples of type I structures include laterally loaded cylinders (Figure 2.49(a)). The force-displacement curve of type II structures shows an initial peak following a softening behavior as shown in Figure 2.48. The axial loading of columns is an example to type II structures (Figure 2.49(b)). Type-II structures are more sensitive to impact velocity than type I structures [76]. This is attributed to large initial rotation rate of plastic hinges and high transverse accelerations under dynamic loading [77].

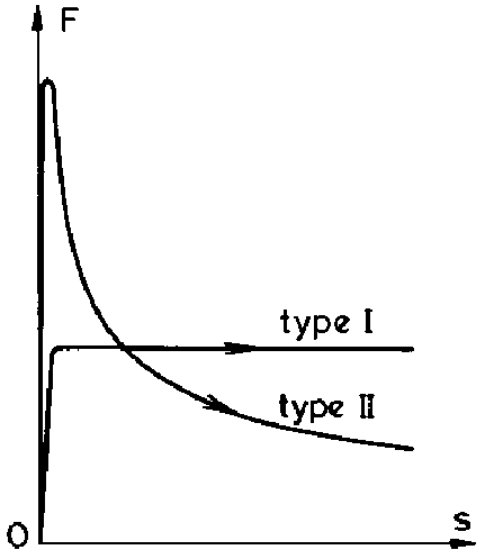

Figure 2.48. Force-displacement curves of type I and type II structures [76].

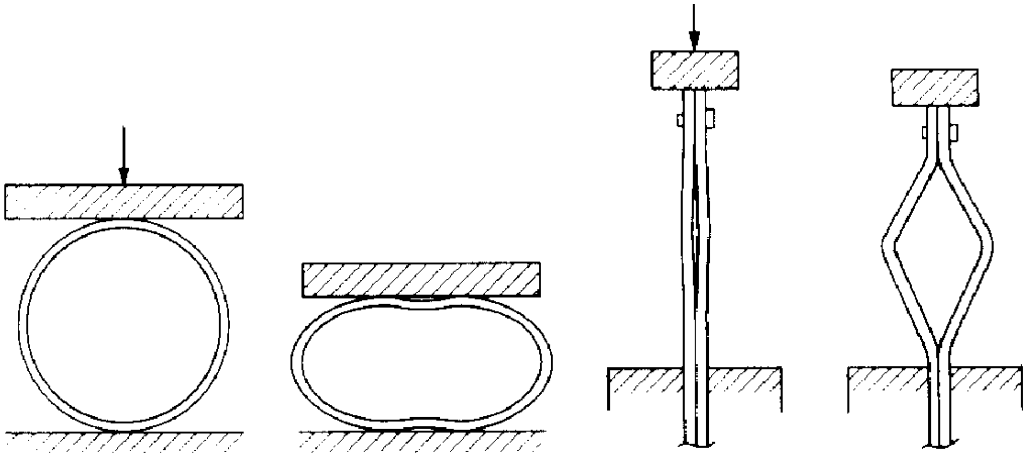

Figure 2.49. Deformation of (a) type-I and, (c) type-II structures [76].

The energy absorption in type I structures increased linearly (Figure 2.50) mainly resulting from the rotation of plastic hinges, while it increases non-linearly in type II structures [77]. A large amount of energy was absorbed during the initial loading in type II structures as a result of endwise shortening of the rod which included a central hinge (Figure 2.51).

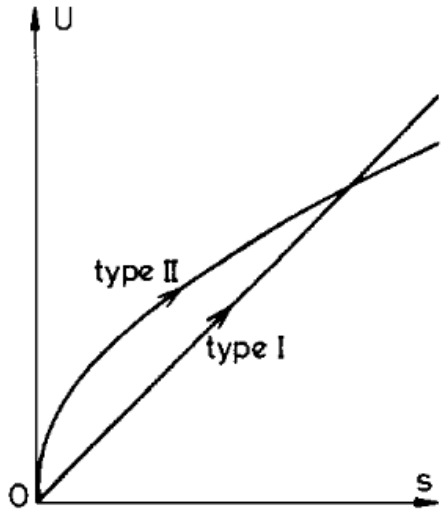

Figure 2.50. Energy-displacement curves of type I and type II structures [76].

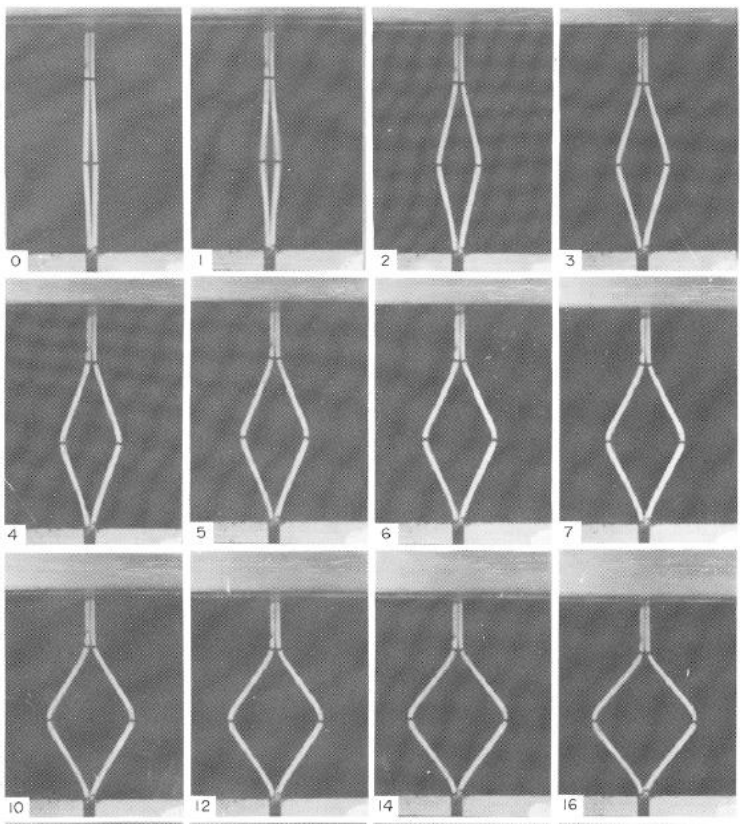

Figure 2.51. Deformation of type II specimen; impacted at 4.8 ms^{-1}
(the interval between successive frames is 0.2 ms.) [77].

Zhao and Abdennaher [78] outlined a mathematical model of type II deformation of bars. The mathematical model included two massless rigid bars linked

by a plastic hinge with a concentrated mass in the middle as shown in Figure 2.52. In this model, the change in length of bars are defined as,

$$\delta v = -L \sin\theta d\theta \tag{2.1}$$

The bar will collapse when the maximum moment generated by applied force (F) becomes greater than the fully plastic moment of the plastic hinge ($M_p = bt^2\sigma_s / 4$),

$$F = M_p \left| \frac{2\delta\theta}{2\delta v} \right| = \frac{\sigma_s bt^2}{4L \sin\theta} \tag{2.2}$$

where, *b*, *t* and *L* are width, thickness and length of the bar and σ_s is the yield strength of bar material. The angle θ is deviation angle and it is also used to define the initial imperfection. If the angle θ is relatively small, the buckling force will be approximately equal to yield stress of the bar material multiply its cross-sectional area. At higher impact speeds, the collapse of the system depends on the acceleration of the concentrated mass in the middle as shown in Figure 2.52,

$$m\ddot{x} = 2N \sin\theta \tag{2.3}$$

where the force N is limited by the yield stress of the bar material. The maximum acceleration of the mass is given as,

$$m\ddot{x} \le 2\sigma_s bt \sin\theta \tag{2.4}$$

When the system is loaded dynamically, more time is needed to reach the velocity of the concentered mass to the impact velocity as depicted in Eqn. (2.4). During this time, the rotation of bars is so small and crushing mostly occurs as compression of bars instead of buckling. Therefore, the buckling force will be higher in dynamic loading rates than in the static loading rates.

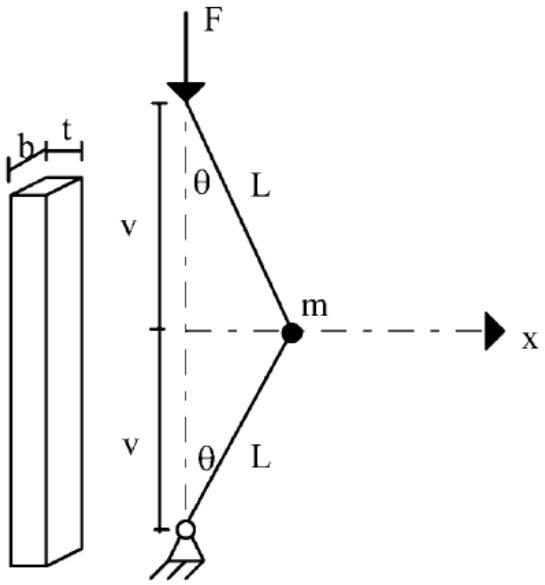

Figure 2.52. Mathematical model of plastic bars [78]

2.4. Motivation

The periodic cellular metal constructions encompass the group of materials with the various topologies such as corrugated and lattice trusses. These light weight periodic constructions have wide range of engineering applications and are often required multi-functionality [26]. Either in the form of single- or multi-layer form, the use of cellular metal constructions are certainly advantageous, partly due to their simple manufacturing routes and partly due to their mechanical properties which are comparable with those of commonly used light-weight cores such as metallic foams [51].

The recent experimental and numerical investigations on the periodic cellular metal constructions have biased toward the impact and blast loading. These studies have provided important information on the mechanical properties and operative deformation modes of the periodic cellular metal constructions at different impact velocity regimes. The dynamic buckling of the columnar structures may be considered in three different velocity regimes as outlined by McShane et al. [74]: low velocities, the plastic buckling is delayed by lateral inertia; intermediate velocities, the buckling occurs behind an axial shock wave propagating along the column and high velocities, the impact velocity exceeds the plastic wave. The increased crushing strengths of the cellular structures at increasingly high strain rates are ascribed to the micro-inertial effects. The increased deformation forces at increasing strain rates in the compression of aluminum

honeycomb structures through out of plane [79], metallic columnar structures [80], aluminum foams [79, 81] and balsa wood in the axial direction [82, 83] were reported to result from the micro-inertial effects. The inertia sensitive structures, classified as Type II structures by Calladine and English [76], are characterized with a strong softening after yielding at quasi-static strain rates. The lateral inertia forces lead to increased bending forces at increasing impact velocities. V-frame corrugated structures were shown to be more inertia sensitive than Y-frame, as the deformation in V-frame structure is the stretching-governed buckling, while in Y-frame core it proceeds with the bending of one of the legs [49]. It was also shown that U-, X- and V-frame cores exhibiting buckling mode of deformation showed higher crushing strengths and energy absorptions than Y-frame cores exhibiting the bending mode of deformation [50]. The sandwich panels constructed using the periodic cellular metal constructions with open structure are attractive both for the impact load mitigation such as blast loading where the large amount of blast energy is required to be absorbed by the progressive crushing of the core and for the heat exchange media, where the heat dissipation is request in a relatively small space [26] . The previous experimental and accompanying numerical investigations are also noted to be on the single layer corrugation: while, the effect of layering on the overall performance of multi-layer corrugated metal core sandwiches has not been investigated.

The focus of thesis is on the crushing responses of 1050 H14 aluminum trapezoidal zig-zag corrugated core sandwich structures at quasi-static and high strain rates. The investigated sandwich structure is different from the previously studied corrugated core sandwich plates in that the corrugated fin layers are currently used in the conventional heat exchangers. The zig-zag form facilitates the fluid flow and thermal conduction. The tested corrugated layer sandwich forms a closed-loop-system for a coolant to circulate within each layer. One of the potential applications with its current form is in the constructions of the ammunition store walls. In this application, the corrugated sandwich walls function in three ways upon an explosion. First, it absorbs the blast through the deformation of the corrugated layers. Second, it provides impact protection against debris by the interlayer sheets. And lastly, the structure supplies coolant to extinguish any fire. The effects of strain rate, zig-zag form and imperfection of the corrugation on the compression mechanical properties and deformation modes of single and multi-layer constructions were analyzed both experimentally and numerically.

The implementation of the full deformation models of the corrugated core sandwiches is noted to be challenging for several reasons. The core models eliminate the arbitrary selection of the element size that directly affects the accuracy of models [44]. The generated mesh size and mesh distribution can also affect the failure significantly [84]. Finally, the numerical core models oblige the use of intricate contact definitions between the individual cores as well as the core and face/interlayer sheets. All these increase the computational time of simulations significantly. The homogenized models are widely applied in order to shorten the computational time of the deformation models of the metallic cellular structures. The existent literature of the homogenized models is mostly on aluminum honeycomb and foam core sandwiches and the most widely used codes include MAT-126 [84], MAT-63 [85, 86] and MAT-26 [87, 88] in LS-DYNA, simplified orthotropic material model [89] and shell and macro-solid models in PAM-CRASH [90].

The homogenized solid models of the single layer (without face sheets) of 1050 H14 Al trapezoidal zig-zag corrugated core were also investigated for simulating the low velocity and dynamic deformation of a multi-layer trapezoidal aluminum corrugated core sandwich in LS-DYNA. Two approaches were adopted in the present study. In the first approach, the MAT-26 material model parameters of the single core layer were determined from the quasi-static compression tests on the single core layer specimen along three different axes. In the second approach, the model parameters were determined from the numerical full model compression testing of the single core layer along the same three different axes. The fidelities of the developed numerical models were further checked by comparing the results of the homogenized with those of the full model and experimental SHPB direct impact testing of the single-layer corrugated core sandwich and low velocity compression and indentation and projectile impact testing of the multi-layer corrugated core sandwich.

CHAPTER 3

QUASI-STATIC AND DYNAMIC TESTING METHODS

3.1. Quasi-Static Tension and Compression Tests

Tension test is a conventional test used to determine the stress-strain or flow curve and the mechanical properties including elastic modulus, yield strength, tensile strength and failure strain. In a tension test, test specimen is loaded under tensile load uniaxially until fracture by increasing the applied load gradually at a constant cross-head speed. Various types of tension tests specimens for different material geometries (plate, bar, sheet and etc.) are specified by the ASTM test standards. A picture of a dog-bone tension test specimen is shown in Figure 3.1. The diameter of the specimen is reduced in gage length section to confine the deformation in a narrow area (Figure 3.1).

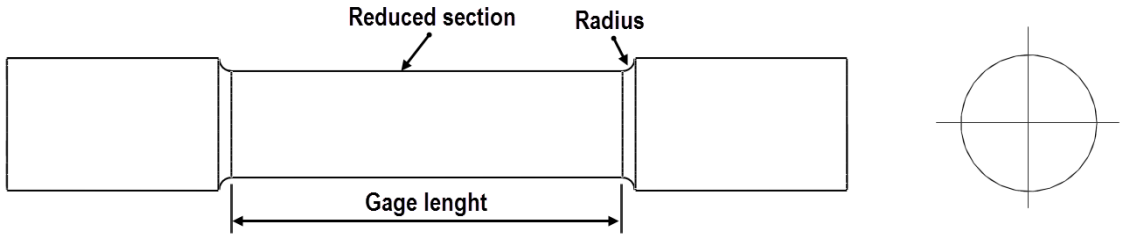

Figure 3.1. ASTM standard tension test specimen.

During tension test, as the specimen elongates, the load bearing cross section area decreases as depicted in Figure 3.2. The engineering tensile stress (σ) and engineering strain (ε) are determined using the following relations,

$$\sigma = \frac{F}{A_0} \tag{3.1}$$

and

$$\varepsilon = \frac{l_f - l_0}{l_0} = \frac{\Delta l}{l_0} \tag{3.2}$$

where, F, A_0, l_f and l_0 are the force and initial cross section area and final length and initial length of the specimen, respectively. The true stress (σ_t) and true strain (ε_t) are,

$$\sigma_t = \frac{F}{A_i} \tag{3.3}$$

and

$$\varepsilon_t = \ln \frac{l_i}{l_0} \tag{3.4}$$

where, A_i and l_i are the instantaneous cross section area and length of the specimen, respectively. The conversion equations of engineering stress and strain to true stress and strain are based on the homogeneous deformation of the sample along the gage length and provided by the following relations,

$$\sigma_t = \sigma(1+\varepsilon) \tag{3.5}$$

and

$$\varepsilon_t = \ln(1+\varepsilon) \tag{3.6}$$

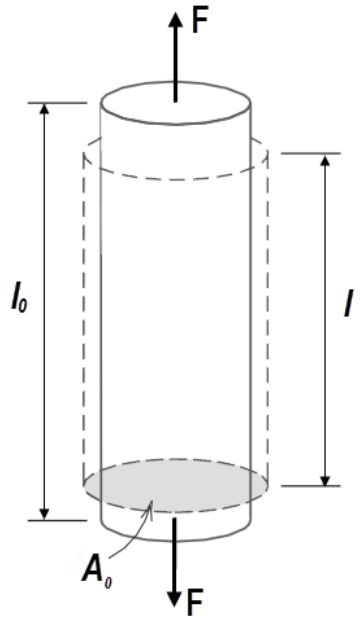

Figure 3.2. Geometrical changes in specimen during tension test.

A typical tensile engineering stress-strain curve of a metal is shown in Figure 3.3. In the initial region of the curve, the stress increases with strain linearly, showing the elastic region of Hooke's Law (Figure 3.3). The slope of this linear region simply gives the Elastic Modulus. The determination of the elastic modulus is generally not possible in a universal test machine as the test machine extents as much as the specimen at very low displacements. Special care should be taken to differentiate the machine displacement from the sample displacement. To calculate sample displacement, the machine displacement should be subtracted from the total displacement. Machine displacement can be calculated using the test machine stiffness which can be determined by conducting separate tests without sample. The stain gages mounted on the sample or video extensiometer attached to the sample measure the sample displacement directly. The yield stress (σ_y) can be determined using proportional limit or off-set method as shown in Figure 3.3. The point at which the stress-strain relation deviates from linearity is called proportional limit, which is presented by letter P_1 in Figure 3.3. In off-set method, a tangent line is drawn from an off-set strain (0.002) and the stress which crosses the tangent line is called yield stress, which is presented by letter P_2 in Figure 3.3. After yield point, plastic deformation starts and stress reaches a maximum point *M* as shown in Figure 3.3, which is called ultimate tensile strength. After point *M*, deformation becomes non-uniform and is localized in a region called necking. The fracture occurs at point *F* (Figure 3.3). It should be noted that Equations

3.5 and 3.6 are not valid after the necking for which the homogeneous deformation assumption is not valid any longer along the sample gage length. After point M, the strain should be calculated by measuring the reduction in area in neck region and the stress is tri-axial rather than uniaxial.

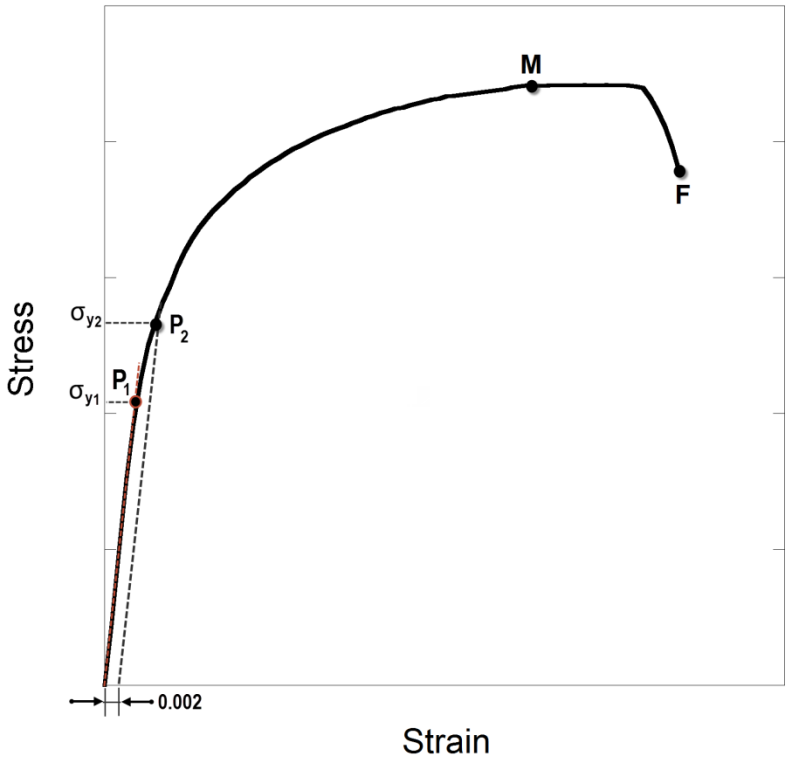

Figure 3.3. Typical tensile stress-strain curve of a metal.

The compression test is very similar with tension test, except the applied force is compressive as depicted in Figure 3.4. Here, cross section area increases while initial length decreases during loading. True stress and strain are calculated from engineering stress and strain as,

$$\sigma_t = \sigma(1-\varepsilon) \tag{3.7}$$

and

$$\varepsilon_t = \ln(1-\varepsilon) \tag{3.8}$$

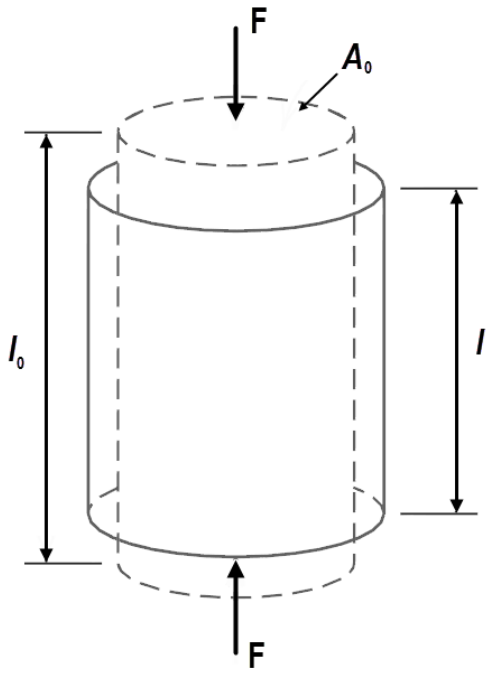

Figure 3.4. Geometrical changes in specimen during compression test.

3.2. Low Velocity Impact Tests

Low velocity impact (LCI) tests are usually conducted using drop weight impact towers at intermediate strain rate range. A typical drop weight impact tower consists of striker, adjustable weights, velocity sensors, and specimen fixtures (Figure 3.5). The striker is attached to the tip of a piezoelectric or strain-gaged force transducer. The adjustable weights are added to the system to reach the desired impact energy. The velocity of the impact is measured by velocity sensors which are placed in the path of the striker before the impactor strikes to the specimen. In a typical drop weight test, adjustable weights, impact velocity and impact energy may vary from 1 to 15 kg, 1 to10 m s^{-1}, and 1 to 150 J, respectively. The force-time history is started to be measured when the striker contacts the specimen and it stops when contact is lost.

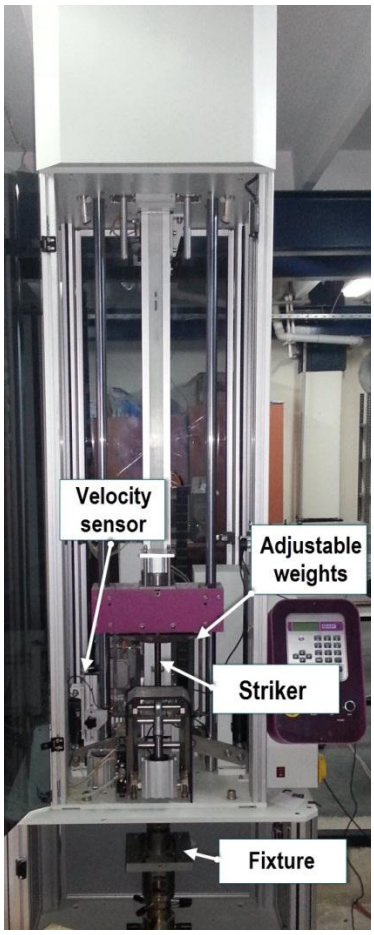

Figure 3.5. A schematic picture of drop weight test set-up.

Energy (E) is calculated from integration of the force-time signal as,

$$E = V_0 \int_0^t P dt \tag{3.9}$$

where, v_0, P and t are the initial velocity of the striker, load and time, respectively. Example of force-time and energy-time curve of a composite material tested in a drop weight tester is shown in Figure 3.6. When striker hits the specimen, the force increases suddenly to a maximum point, P_m. At the point of maximum load (P_m) and maximum energy (E_m), the striker experienced maximum penetration into the specimen and then it rebounds. After rebound, the contact between the striker and specimen is lost and force decreases to zero. The total energy absorbed by the specimen is represented by E_t.

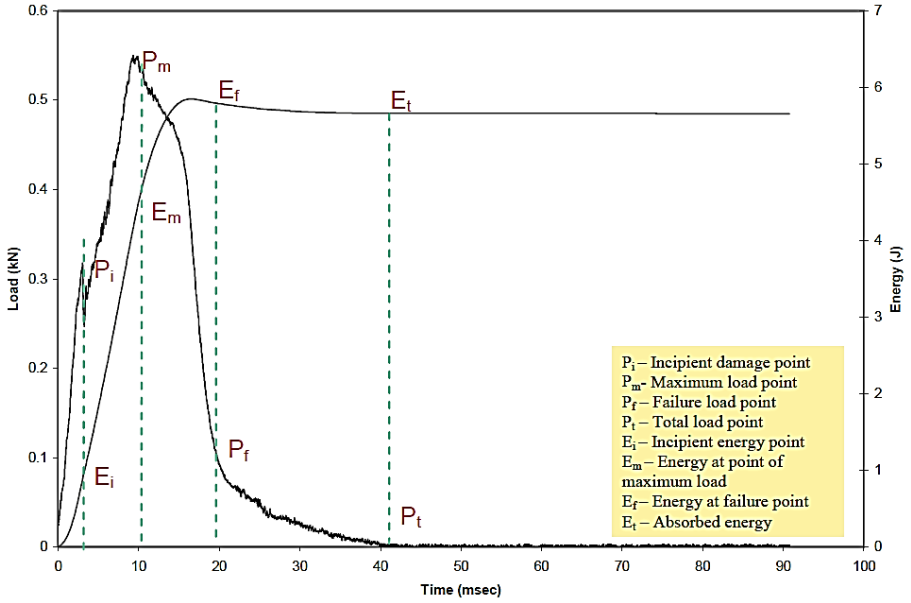

Figure 3.6. Typical force-time and energy-time curves of an impact test [91].

3.3. Split Hopkinson Pressure Bar Tests

Split Hopkinson Pressure Bar, developed by Kolsky in 1949 [92], is an experimental test system/set-up used to test materials at high strain rates. The strain rate reached in SHPB ranges 100 s^{-1}-10^4 s^{-1}. The schematic of a SHPB test system is shown in Figure 3.7. Main parts of SHPB test system are the striker launching system, bar components, data acquisition and recording system. Striker launching system includes gas gun and striker bar. Nitrogen gas is compressed in a gas gun tank. When the compressed gas is released, the striker bar is launched through incident bar. The velocity of the striker bar can be controlled by changing the pressure of compressed nitrogen gas. Bar components of a SHPB test system are incident bar and transmitter bar. All bars in the system are generally made of the same material with the same diameter. High strength steels and aluminum alloys are generally used as bar materials. The length of the incident bar must be at least twice as long as the striker bar towards overlapping between incident and reflected pulses [93]. The specimen is mounted between the incident and transmitter bar as shown in Figure 3.7. Data acquisition system includes strain gages and oscilloscope. Two strain gages are mounted on the each top and bottom surfaces of incident and transmitted bars. The voltage output taken from strain gages is amplified by pre-amplifiers and recorded in an oscilloscope.

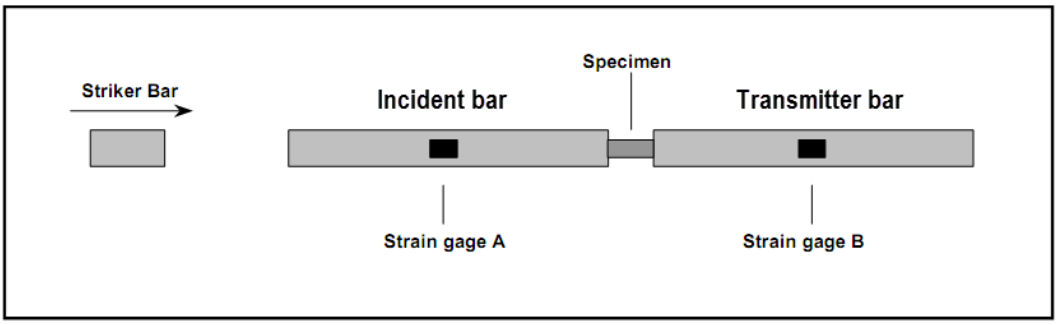

Figure 3.7. Components of a SHPB test system.

A typical SHPB test voltage-time curve is shown in Figure 3.8. When a striker bar is impacted on the incident bar, compression wave is generated and wave propagates though the incident bar. When the wave arrive the end surface of the incident bar, it is partially reflected and partially transmitted into the specimen. A portion of the incident wave is reflected back along the incident bar as a tensile wave. This reflected strain is also measured by the strain gage located on the incident bar. The transmitted wave propagates thought transmitter bar as a compression wave until it reaches the end of this bar.

Loading duration of incident compressive pulse (T) is;

$$T = \frac{2L}{C_B} \tag{3.10}$$

and C_B is represented as;

$$C_B = \sqrt{\frac{E_B}{\rho}} \tag{3.11}$$

where C_B, E_B and ρ are the elastic wave speed of striker bar, elastic modulus and density of striker bar, respectively.

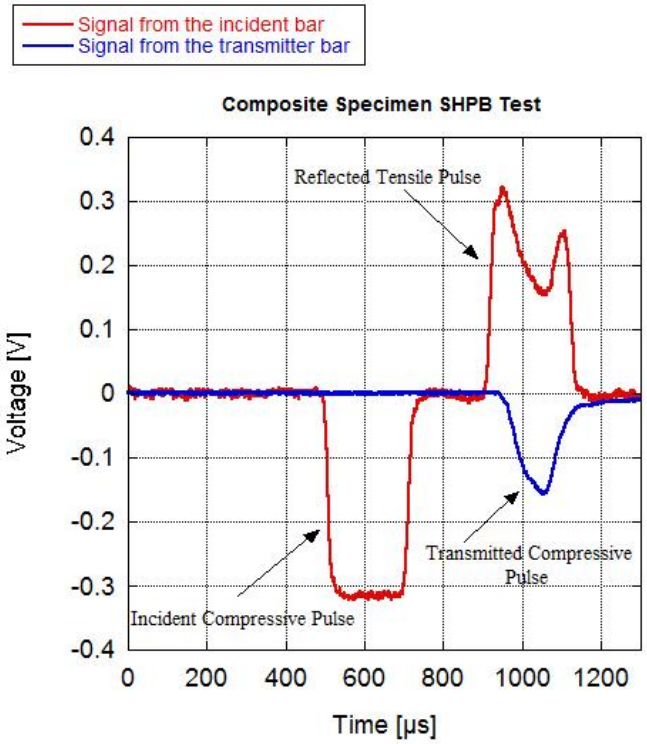

Figure 3.8. A typical voltage versus time curve of a SHPB test [94].

3.4. SHPB Theory

In SHPB test, it is assumed that stress waves propagate in the incident and transmitter bars without dispersion according to one dimensional wave theory. The particle velocity of specimen ends (Figure 3.9) is,

$$v_1 = C_B(\varepsilon_I - \varepsilon_R) \tag{3.12}$$

and

$$v_2 = C_B \varepsilon_T \tag{3.13}$$

where, v_1 and v_2 are the velocity of specimen ends. Subscripts I, R and T are the incident, reflected and transmitted pulses. The engineering strain and strain rate in the specimen are,

$$\varepsilon = \frac{v_1 - v_2}{L_s} = \frac{C_B}{L_s}\left(\varepsilon_I - \varepsilon_R - \varepsilon_T\right) \tag{3.14}$$

and

$$\dot{\varepsilon} = \int_0^t \varepsilon dt = \frac{C_B}{L_s}\int_0^t \left(\varepsilon_I - \varepsilon_R - \varepsilon_T\right) dt \tag{3.15}$$

where, L_s is the initial length of the specimen. Stress generated on the specimen ends are,

$$\sigma_1 = \frac{A_B}{A_s} E_B \left(\varepsilon_I + \varepsilon_R\right) \tag{3.16}$$

$$\sigma_2 = \frac{A_B}{A_s} E_B \varepsilon_T \tag{3.17}$$

where, A_B and A_s are the cross section areas of bar and specimen, respectively. The specimen is assumed to be in stress equilibrium as,

$$\sigma_1 = \sigma_2 \tag{3.18}$$

From equations (3.16) and (3.17), it is written as,

$$\varepsilon_I + \varepsilon_R = \varepsilon_T \tag{3.19}$$

Strain, strain rate, stress can be written by using Equations (3.14), (3.15) and (3.17) as,

$$\varepsilon = -2\frac{C_B}{L_s}\varepsilon_R \tag{3.20}$$

$$\dot{\varepsilon} = -2\frac{C_B}{L_s}\int_0^t \varepsilon_R dt \tag{3.21}$$

and

$$\sigma = \frac{A_B}{A_s} E_B \varepsilon_T \tag{3.22}$$

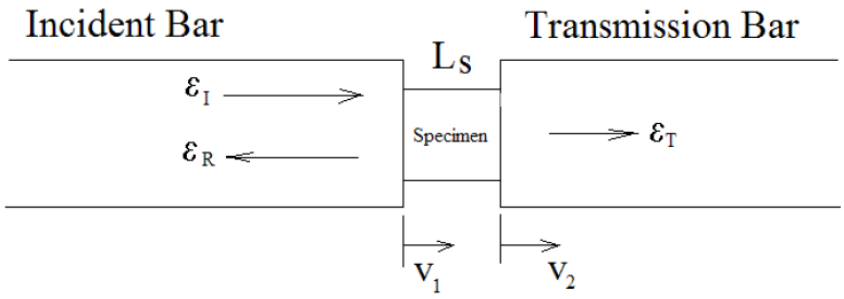

Figure 3.9. Schematic view of SHPB testing section.

CHAPTER 4

ZIG-ZAG TRAPEZOIDAL CORRUGATED CORES AND SANDWICHES

4.1. Zig-zag 1050 H14 Al Trapezoidal Corrugated Core Layers

The trapezoidal corrugated aluminum core layers used in the sandwich constructions were commercially produced by a local factory in specified fin geometry using a hydraulic press as shown in Figure 4.1. The hydraulic press was composed of hydraulic pressure unit, dies and machine frame. In this process, 1050 H14 Al alloy sheets with a thickness of 0.135 mm were punched and bent into a die cavity in which zig-zag form and trapezoidal shape were formed. The pictures of the forming machine and bottom die are shown in Figures 4.2(a) and (b), respectively.

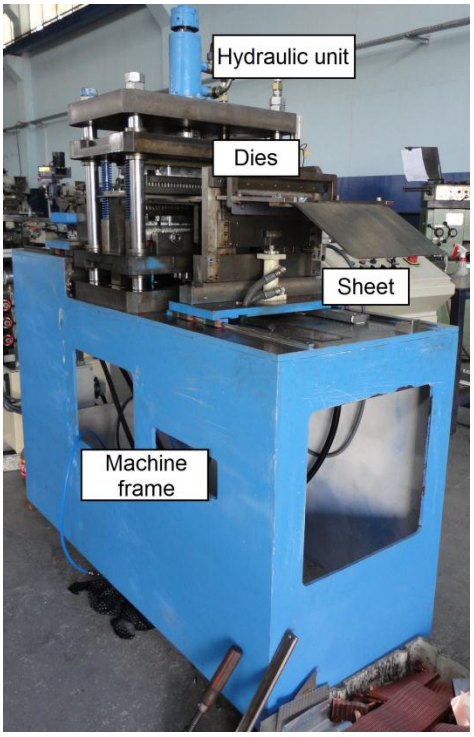

Figure 4.1. Hydraulic press used to form corrugated layers.

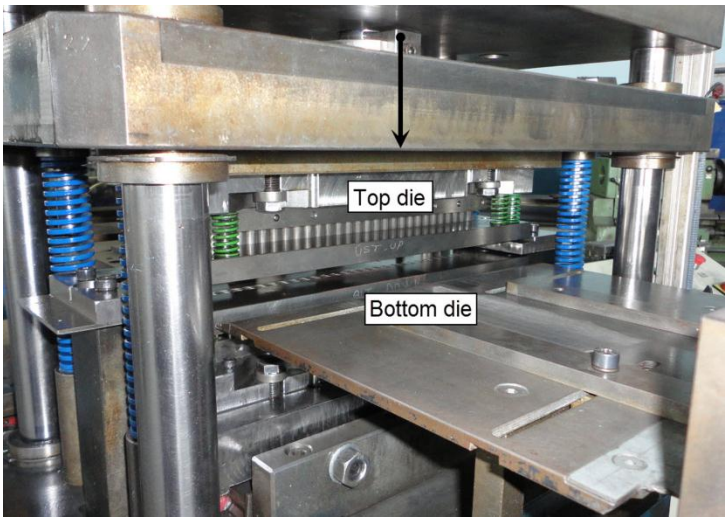

(a)

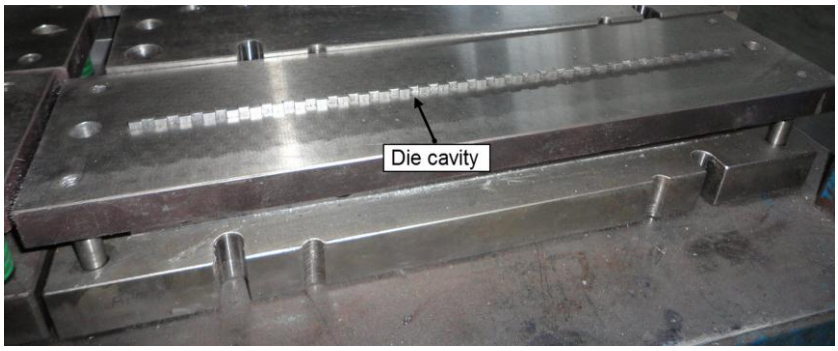

(b)

Figure 4.2. The pictures of (a) forming machine and (b) bottom die.

The picture and technical drawing of a zig-zag 1050 H14 Al trapezoidal corrugated core layer is shown sequentially in Figure 4.3(a) and (b). The height, width and thickness of the fin layer are sequentially 9, 5 and 0.135 mm and the fin wall is inclined with an angel of 83° from x-axis as shown in Figure 4.3(b). The density of the corrugated fin layer was 0.115 g cm^{-3}, corresponding to a relative density of 0.042.

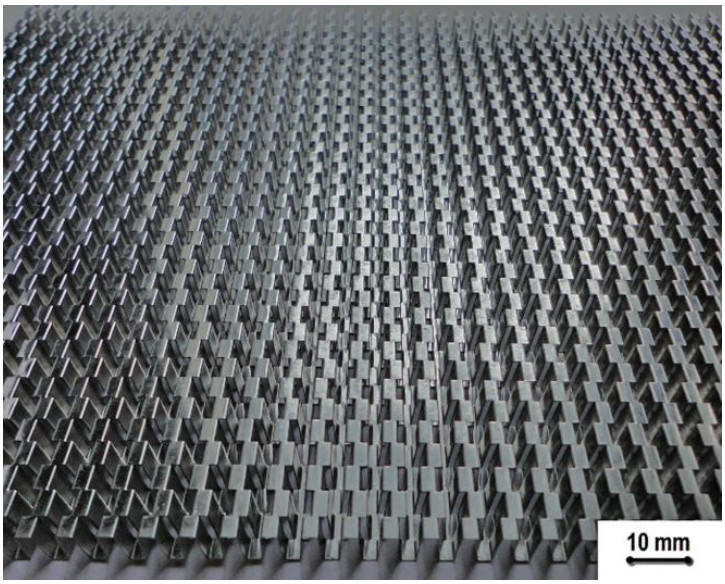

(a)

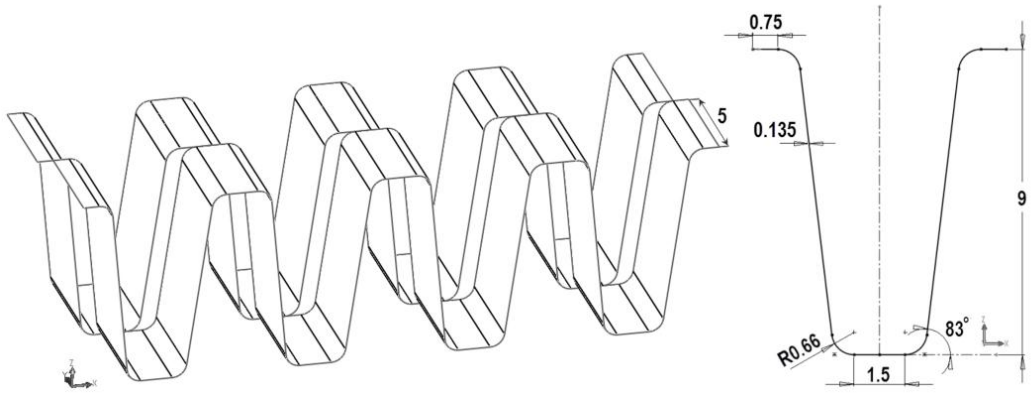

(b)

Figure 4.3. (a) The picture of corrugated aluminum fin layer and (b) 3D model of the fins and unit fin geometrical parameters.

4.2. Corrugated Sandwich Structures

The tested corrugated sandwich structures were prepared in three different configurations; single-layer, double-layer and multi-layer. Each corrugated core sandwich structures consisted of zig-zag 1050 H14 Al trapezoidal corrugated core layers, the face sheets, either 1050 H14 or 3003 Al alloy, and 1050 H14 Al interlayer sheets. The thicknesses of interlayer and face sheets are sequentially 0.5 mm and 1.5 mm.

The sandwich panel components were brazed in a furnace at 600 ^{o}C for 10 min under atmospheric pressure using a 4343 aluminum filler sheet (6.6-8.2 wt%), following

the cleaning and flux slurry spraying of the surfaces. In another route, the fin layers, aluminum interlayers and face sheets were assembled using a polyurethane adhesive (Henkel Thomsit R710). The panels were kept under a weight of 10 kg for 2 h after applying a thin adhesive layer on the surfaces of components.

4.3. Single and Multi-layer Corrugated Sandwich Structures

The single-layer configuration consisted of one core layer with two face sheets (Figure 4.4 (a)) and double-layer configuration consisted of two core layers with one interlayer sheet and two face sheets (Figure 4.4(b)). The square cross-sectioned single- and double-layer corrugated sandwiches were 25 mm in width and 12 and 22 mm in height, respectively. All components of sandwiches were adhesively bonded and made of 1050 H14 Al alloy. These specimens were used in direct impact SHPB tests.

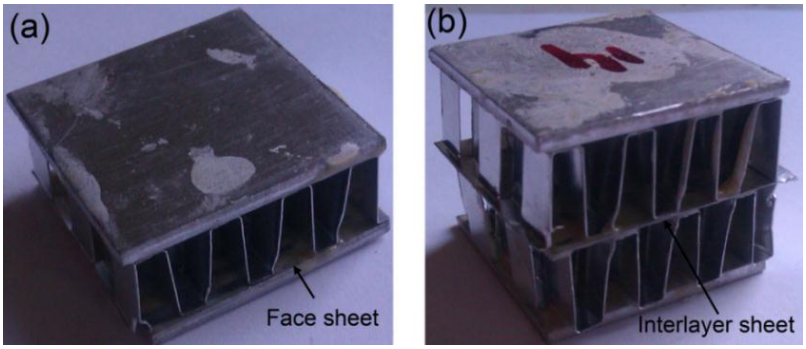

Figure 4.4. Pictures of (a) single- and (b) double-layer corrugated sandwich samples.

The multi-layer corrugated core sandwich specimens consisted of bonded/brazed seven corrugated fin layers, six interlayer sheets and two face sheets (Figures 4.5(a), (c) and (b)). As-received brazed panels, 500x500x70 mm in size, were sliced into desired test specimen sizes using an electric discharge machine.

In quasi-static and drop weight dynamic compression tests, bonded/brazed multi-layer corrugated sandwich panels were used. The square cross-sectioned multi-layer corrugated sandwiches were 50 mm in width and thickness and 70 mm in height, respectively (Figure 4.5(a), (b) and (c)). The prepared bonded/brazed multi-layer samples had 0°/0° fin layer orientation (Figure 4.5(a), (b)). Multi-layer samples without

interlayer sheets were also prepared in 0°/0° and 0°/90° fin layer orientations using only adhesive bonding (Figure 4.5(c)).

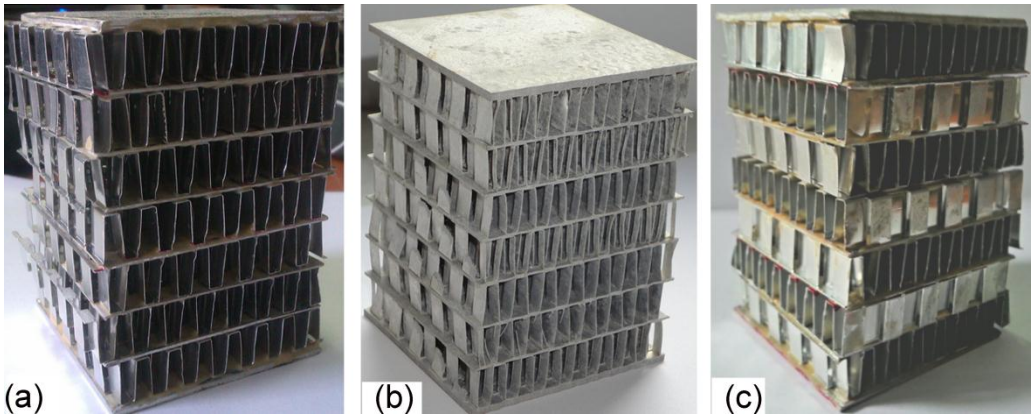

Figure 4.5. Multi-layer corrugated sandwich specimens: (a) bonded 0°/0° oriented, (b) brazed 0°/0° oriented and (c) bonded 0°/90° oriented.

In drop weight tests, multi-layer bonded/brazed 0°/0° Figure 4.6 (a) and bonded 0°/90° Figure 4.6 (b) oriented corrugated core sandwich specimens were used in size of 100 mm in length and width and 70 mm in height. The fin and interlayer sheets were made of 1050 H14 aluminum alloy and the face sheets are either 1050 H14 or 3003 aluminum alloy. The thicknesses of face sheets and interlayer sheets were the same with the compression test samples.

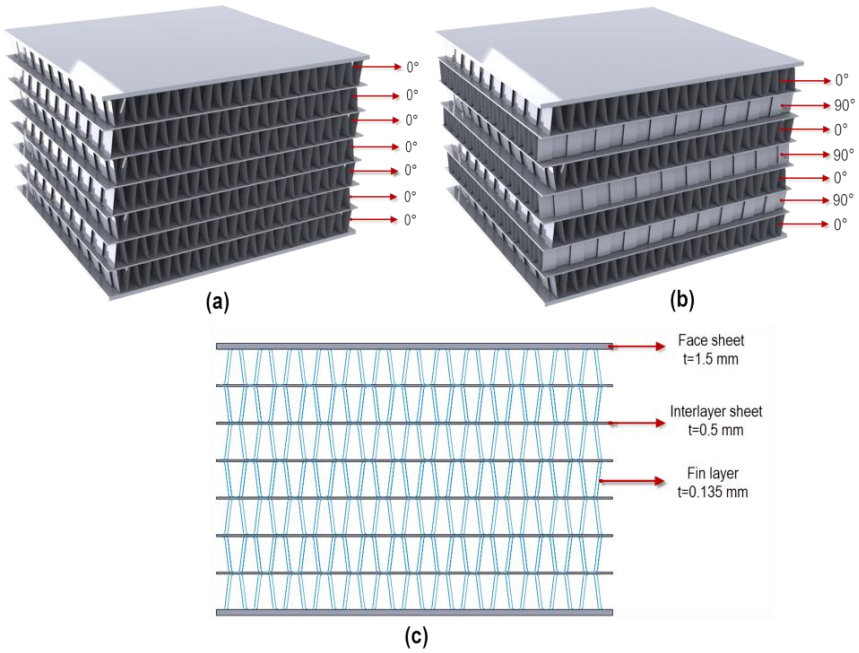

Figure 4.6. 3D model of (a) 0°/0° and (b) 0°/90° fin layer oriented sandwich panels and (c) 2D model of 0°/0° fin layer oriented sandwich panels.

In the projectile impact test, multi-layer bonded 0°/0° oriented corrugated core sandwich specimens were 200 mm in length and width and 70 mm in height as shown in Figure 4.7.

Figure 4.7. 0°/0° oriented corrugated core sandwich specimen for projectile impact test specimen.

The density of multi-layer corrugated sandwiches with interlayer sheets varied with the number of fin layers as shown in Figure 4.8. The density of adhesively bonded sandwiches reached almost a constant value of 0.35 g cm^{-3} after about 20 fin layers. The use of adhesive increased the density of multi-layer corrugated sandwich by 0.05 g cm^{-3}. The densities of tested brazed and polyurethane bonded sandwiches with interlayers were similar; ~0.39 g cm^{-3}, while the sandwiches without bonding layer were ~0.36 g cm^{-3}.

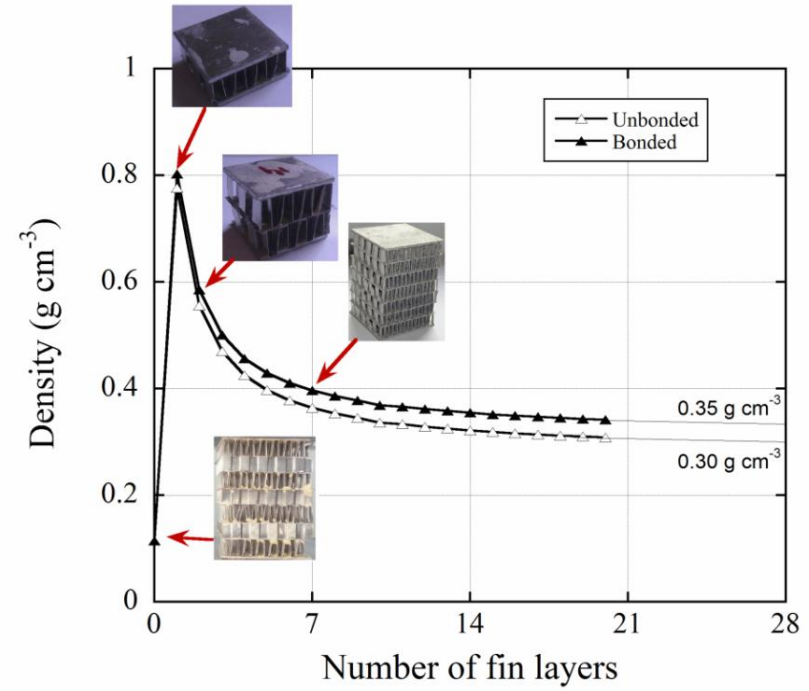

Figure 4.8. Density vs. number of fin layers of bonded and unbounded single- and multi-layer sandwiches.

CHAPTER 5

EXPERIMENTS

5.1 Quasi-static Tension and Compression Tests

5.1.1 Mechanical Characterization of 1050 H14 and 3003 Aluminum Alloys

The quasi-static tensile stress-strain behavior of 1050 H14 and 3003 Al alloys were determined at the strain rate of 10^{-3} s^{-1} using SHIMADZU universal testing machine. The tension test specimens, as shown in Figure 5.1(a) and (b), were prepared in accord with ASTM E8M-04 Standard [95]: the gage length and thickness were 60 and 1.5 mm, respectively (Figure 5.1(a)). A video extensometer synchronized with the mechanical testing machine was used to measure the displacement of the specimen.

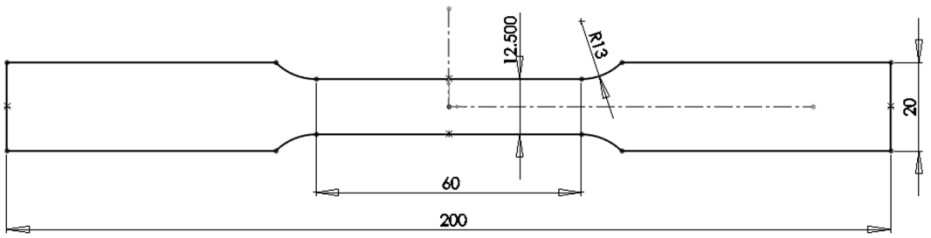

(a)

Figure 5.1. Tension test specimens: (a) technical drawing and (b) pictures.

(cont. on next page)

(b)

Figure 5.1 (cont.)

In order to determine the effect of brazing on the stress-strain behavior, few tension test specimens were passed through a heat treatment process in a furnace (Figure 5.2), the same with the one applied in the brazing. These specimens were heated from 200 °C to 600 °C in 13 min, hold at 600 °C for 2 min; then, cooled to ambient temperature in air.

Figure 5.2. The picture of furnace used in the heat treatment process of tension test specimens.

5.1.2. Quasi-static Compression Tests on Corrugated Sandwich Structures

The quasi-static compression tests on adhesively bonded single- and double layer sandwiches (25x25x12 and 22 mm) were conducted at the strain rates of 10^{-3}, 10^{-2} and 10^{-1} s^{-1}. The quasi-static compression tests on the adhesively bonded and brazed multi-layer corrugated sandwich specimens (50x50x70 mm) were conducted at 10^{-3} and 10^{-1} s^{-1}. The deformations of test samples were recorded using a high speed camera (Fastcam Photron) (Figure 5.3) with the frame rate of 50 fps (frame per second).

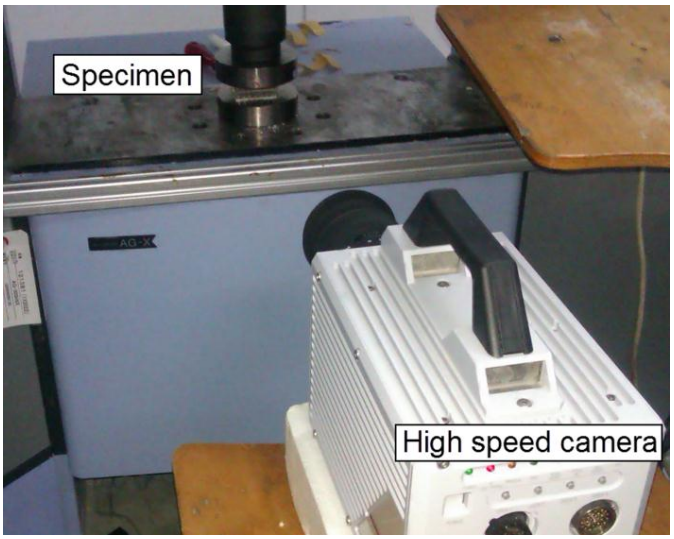

Figure 5.3. Quasi-static compression test set-up and high speed camera.

The constraint compression tests were performed on the adhesively bonded multi-layer corrugated sandwich specimens at the strain rate of 10^{-1} s^{-1} using a rectangular screwed closed-die shown in Figure 5.4. The sandwich specimen was placed inside the die and with a punch (Part no.5 in Figure 5.4) the specimen was axially compressed in the die. In order to reduce the friction between the die and test sample, the surfaces of die were lubricated using grease.

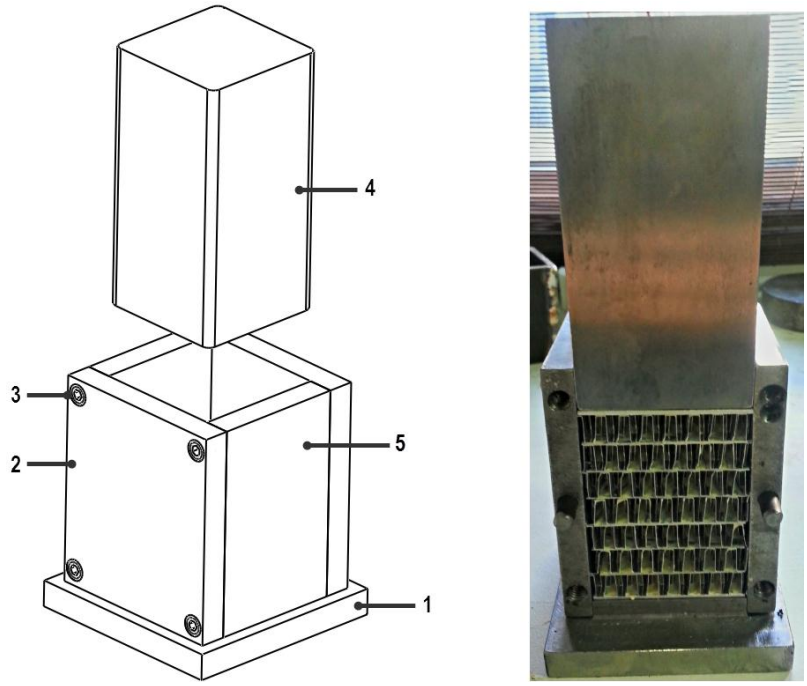

Figure 5.4. Constraint compression test die.

The quasi-static compression tests at the strain rate of 10^{-1} s^{-1} were performed on single-layer zig-zag trapezoidal corrugated core in x-, y- and z-axis as shown in Figures 5.5(a)-(c). These tests were conducted for the numerical homogenization of the corrugated core layers.

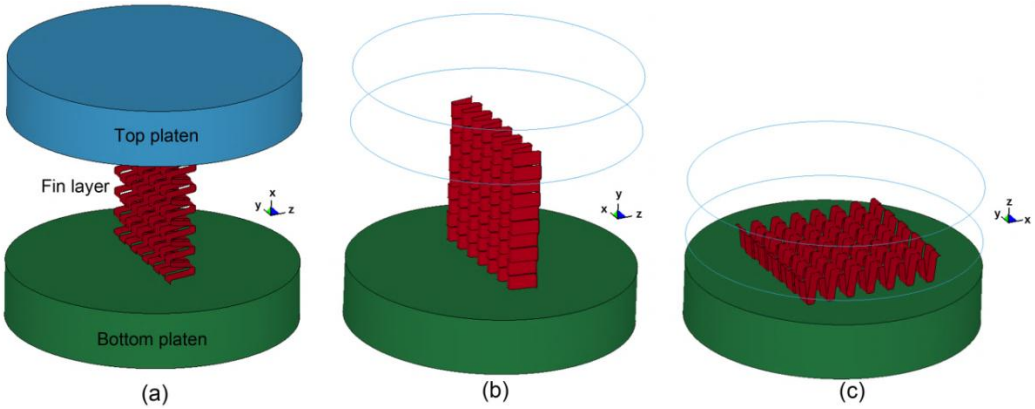

Figure 5.5. Geometrical representation of quasi-static compression tests on single core layer along: (a) x-axis, (b) y-axis and (c) z-axis.

The quasi-static indentation tests were conducted on adhesively bonded multi-layer corrugated sandwich specimens (100x100x70 mm) at the strain rate of 10^{-1} s^{-1} using a spherical ended striker as shown in Figure 5.6. Spherical indenter was made of

4340 heat-treated steel and attached to cross-head of SHIMADZU testing machine using a set of screws.

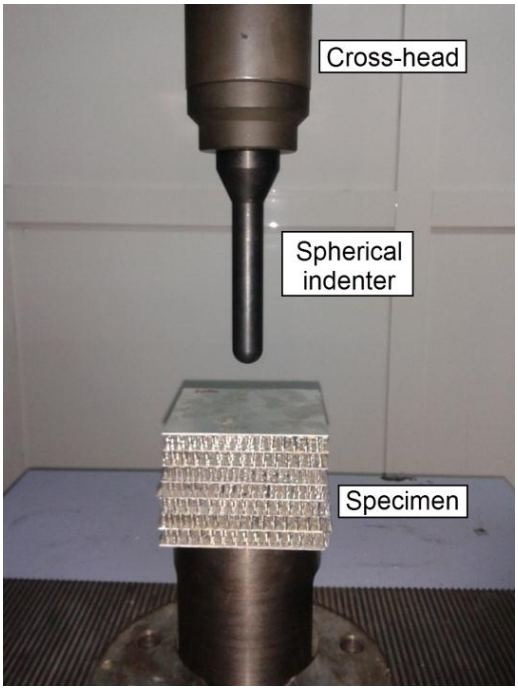

Figure 5.6. Quasi-static indentation test set-up with spherical tip.

5.2. Dynamic Tests

5.2.1. Direct Impact SHPB Tests

The high strain rate tests were performed on the single- and double-layer sandwiches using a strain-gaged direct impact SHPB set-up [49]. In these so-called modified SHPB tests, one of the faces of the sandwich specimen was attached to the end of the incident bar by using one layer of double stick tape and the gas chamber fired the striker bar on the specimen as depicted in Figure 5.7.

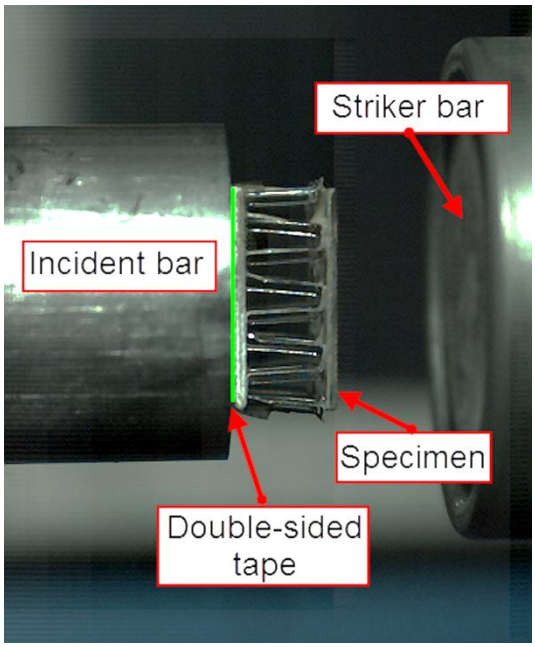

Figure 5.7. Position of specimen on direct impact SHPB test set-up.

Figure 5.8 shows the picture of direct SHPB test set-up. The SHPB set-up was made of 7075 T6 Al alloy bars (40 mm in diameter), with the striker bar length of 300 mm and incident bar length of 1000 mm. The elastic modulus and density of bar material were 71.7 GPa and 2810 kg m^{-3}, respectively.

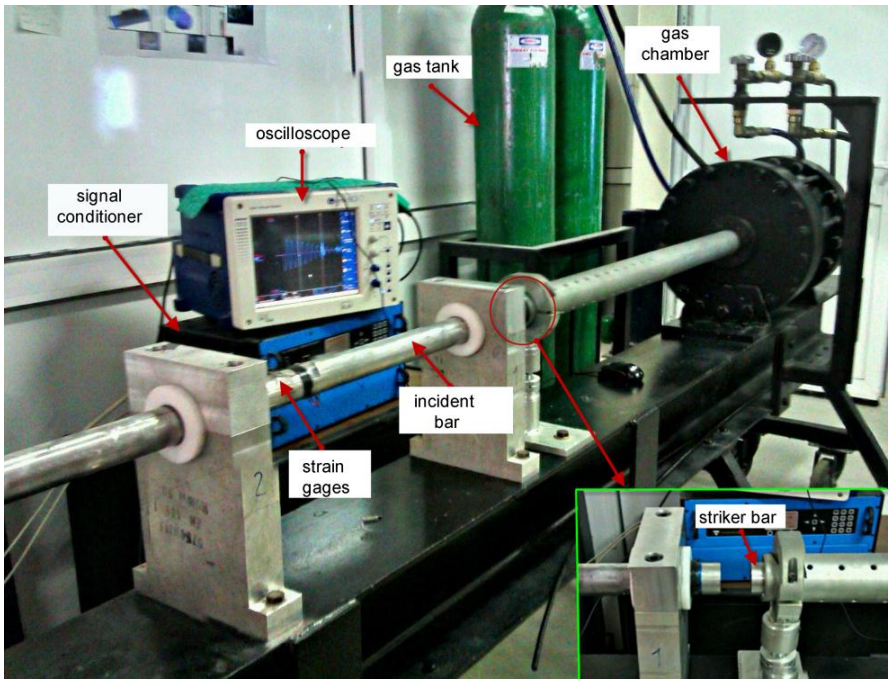

Figure 5.8. Direct impact SHPB test set-up.

The stress wave on the incident bar was measured by means of 350 Ω foil strain gages mounted on the incident bar in a full Wheatstone-bridge configuration. The bridge input voltage was provided with an amplifier/conditioner and an oscilloscope was used to record the output bridge voltage. In a typical test, the gas chamber (Figure 5.7) is filled with nitrogen gas and the release of the gas chamber fires the striker bar onto the incident bar end. The distance between the end of the incident bar and the location of the full-bridge was 500 mm. The loading of the specimen during the test was captured using a high speed camera at 20,000 fps. The velocity of the striker bar was adjusted by the chamber gas pressure and measured using laser-velocity gates located at the exit of the gun chamber barrel. The tests were performed at the striker velocity (v_o) of ~18 m s^{-1}. The stress (σ) in the impacted sample (transmitted to incident bar) was calculated as,

$$\sigma(t) = \frac{E_b A_b}{A_s} \varepsilon_t(t) \tag{5.1}$$

and the average strain (ε) and strain rate ($\dot{\varepsilon}$) in the sample was calculated as,

$$\varepsilon = \frac{v_0 t}{H} \tag{5.2}$$

$$\dot{\varepsilon} = \frac{v_0}{H} \tag{5.3}$$

where, E_b, A_b and A_s are the elastic modulus of the bar and sample and bar cross-sectional areas, respectively, H is the height of sample, ε_t is the strain measured on the incident bar and t is the time.

5.2.2. Drop Weight Compression Tests

The dynamic compression tests on the adhesively bonded and brazed multi-layer corrugated sandwich specimens were performed in FRACTOVIS drop weight tower at strain rate of 40 s^{-1}. The main parts of the drop weight tower test machine, striker,

platen, photocells and the bottom plate, are shown in Figures 5.9. The striker was attached to a 45 KN piezoelectric force transducer. The striker velocity was measured by the photocells of drop weight tower. In a typical test, the specimen is placed on the bottom plate and the striker with an initially attained velocity crushes the specimen. The total mass of impact system was 15.778 kg. The tests were performed at 3 m s^{-1} using a flat-end striker. The diameter of the striker end was 70 mm. The deformations of test samples were recorded using a high speed camera with the frame rate of 5000 fps.

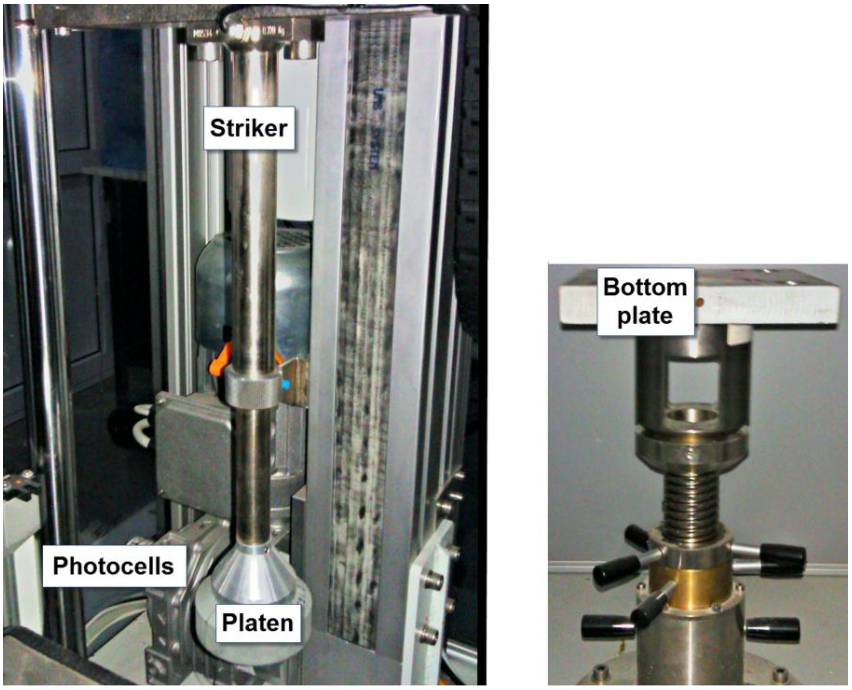

Figure 5.9. Components of drop weight tower test set-up.

5.2.3. Drop Weight Indentation Tests

Drop weight indentation tests were performed in FRACTOVIS drop weight tower. The striker was attached to a 90 KN piezoelectric force transducer. The geometrical details and sizes of the used striker tips are shown in Figures 5.10(a-c). The striker velocity was measured by the photocells of drop weight tower. The energy absorption was calculated by integrating force-displacement curves. In a typical test, the specimen is inserted between the bottom and top rings (Figure 5.10(c)); the bottom ring is clamped and the top ring exerted a clamping force to the specimen in order to prevent its motion. The clamping force should be as low as possible in order not to cause fin

wall buckling. An applied clamping force of 20 N was determined to be causing no fin wall buckling and prevent the specimen motion. The total mass of the impact system was 15.778 kg. The initial impact tests were performed at 3 and 6 m s^{-1} using spherical striker tip on brazed and adhesively bonded sandwich panels with 3003 aluminum face sheets. Later, the tests were conducted using flat and conical striker tips at 6 m s^{-1} on adhesively bonded sandwich panels with 1050 H14 aluminum face sheets.

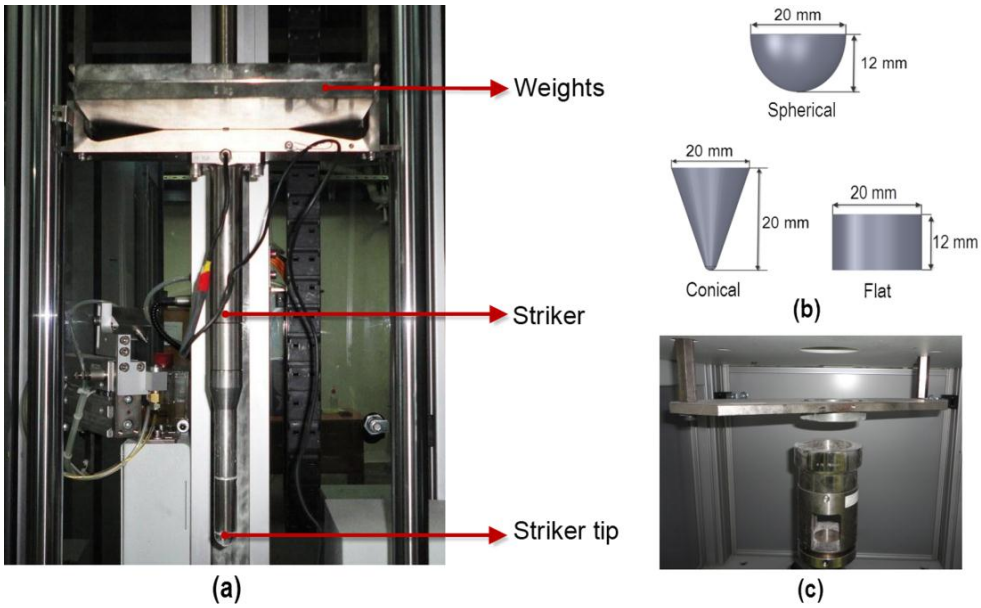

Figure 5.10. Drop weight indentation test system and parts: (a) impact set-up, (b) striker tips and (c) specimen holder rings.

5.2.4. Projectile Impact Tests

Projectile impact tests were performed in gas gun test set-up shown in Figure 5.11. The assembly consisted of pressure vessel, trigger, specimen holder and laser barriers which determined the initial and residual velocity of projectile (Figure 5.11). The projectile used in test was a hardened steel sphere, 30 mm in diameter and 110 g in weight. The projectile was guided with a polyurethane foam sabot (18 g) (Figure 5.11). The target panel was clamped into a steel frame using bolts. Two laser barriers measured the initial and residual velocity of the projectile.

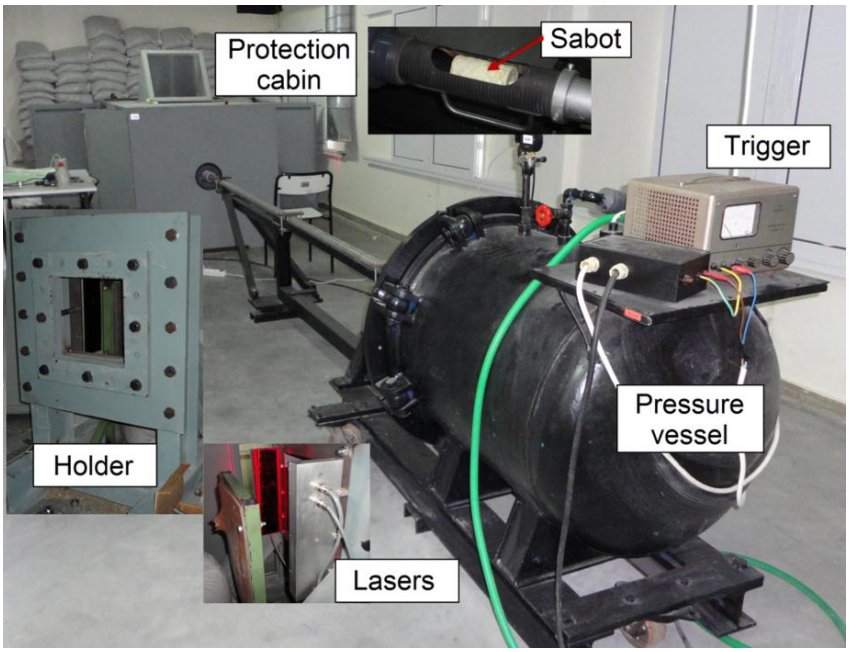

Figure 5.11. The gas gun test set-up.

CHAPTER 6

NUMERICAL MODELS

6.1. Geometry Modeling and Mesh Generation of Zig-zag Trapezoidal Corrugated Fin Layers

The full geometrical numerical models of the experiments were developed in non-linear explicit FE code LS-DYNA. Three dimensional models of corrugated fin layers were developed in Solidworks CAD software. Initially, a unit fin of a corrugated fin layer was modeled (Figure 6.1(a)). The created unit fin was duplicated in the direction of x- and y-axis to create zig-zag form and corrugation. However, "*Linear pattern"* option in Solidworks could not be used for this process due to duplicating-tolerance problem which directly affected the dimensions between unit fins in a single corrugated sheet. For this reason, complete corrugated core sheets were generated in Hypermesh software. The unit fin created in CAD software was meshed to predefined finite elements as shown in Figure 6.1(b). Then, generated mesh was duplicated in the direction of x-axis (Figure 6.1(c)). After that, whole structure was duplicated in y-axis and moved in the direction of x-axis simultaneously to create zig-zag form (Figure 6.1(d)).

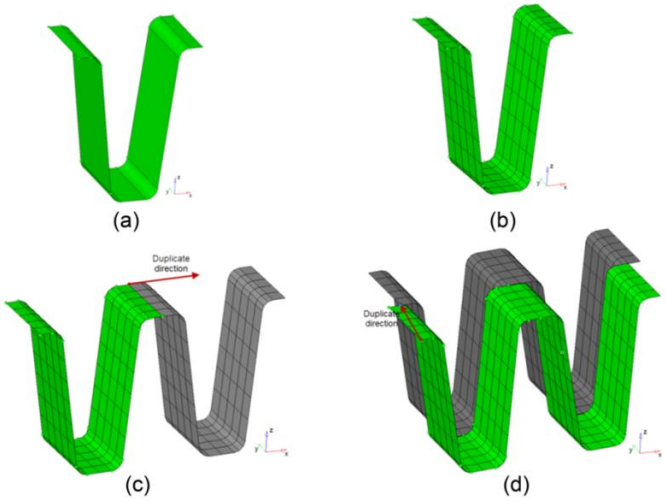

Figure 6.1. Mesh generation of a corrugated core sheet; (a) CAD geometry, (b) meshing, (c) duplication in x-axis and (d) duplication in y-axis.

6.2. Material Models

6.2.1. Johnson-Cook (JC) Material Model

MAT_SIMPLIFIED_JOHNSON_COOK material model, material type 98 in LS-DYNA, was used to model the flow stress of 1050 H14 and 3003 Al alloys in numerical simulations. Johnson and Cook (JC) flow stress model is given as [96],

$$\sigma = \left[A + B\varepsilon^{n} \right] \left[1 + c \ln\left(\frac{\dot{\varepsilon}}{\dot{\varepsilon}_0} \right) \right] \left[1 - \left(T^{*} \right)^{m} \right] \tag{6.1}$$

where σ, ε, $\dot{\varepsilon}$ and $\dot{\varepsilon}_0$, respectively, the effective stress, effective plastic strain, strain rate and reference strain rate; *A, B, n, c* and *m* are the model parameters. The last term T^* is expressed as,

$$T^{*} = \frac{T - T_r}{T_m - T_r} \tag{6.2}$$

where, T is the temperature and T_r and T_m are the reference and melting temperatures, respectively. Material type 98 does not take into account temperature effect expressed in the last bracket of Eqn. (6.1). As aluminum alloys are known to have negligible strain rate dependent flow stresses: the second bracket of Eqn. (6.1) is omitted in the material model.

6.2.2. Honeycomb Material Model

Numerical homogenization of single layer of zig-zag trapezoidal corrugated core was carried out using HONEYCOMB material model, mat26, in LS-DYNA. This model can represent the elasto-plastic anisotropic behavior of honeycomb and foam materials [97]. HONEYCOMB model is based on not compacted or fully compacted deformation states. In not compacted deformation state, normal and shear stresses are

fully uncoupled in all directions [98]. In this model, the normal compression stress-strain and shear stress-strain curves at three different loading axes must be defined separately.

The strain in not compacted state is the volumetric strain and represented as [97],

$$\varepsilon = 1 - V \,,\; V = \frac{v}{v_f} \tag{6.3}$$

where, V is the relative volume, v and v_f are the element volume and fully compacted element volume, respectively. Elastic and shear moduli in not compacted state are calculated as [97],

$$E_{ii} = E_{ii}^{un} + \beta\left(E^{com} - E_{ii}^{un}\right) \tag{6.4}$$

$$G_{ij} = G_{ij}^{un} + \beta\left(\frac{E^{com}}{2(1+\mu)} - G_{ij}^{un}\right) \tag{6.5}$$

where, superscripts *un* and *com* represents not compacted and compacted states, respectively. On Eqn. (6.5) μ is the Poisson's ratio and β is represented as following[97],

$$\beta = \max\left[\min\left(\frac{1-V}{1-v_f}, 0\right)\right] \tag{6.6}$$

Stresses for not compacted state can now be calculated as [97],

$$\sigma_{ii}^{n+1^{trial}} = \sigma_{ii}^{n} + E_{ii}\Delta\varepsilon_{ii} \tag{6.7}$$

$$\sigma_{ij}^{n+1^{trial}} = \sigma_{ij}^{n} + 2G_{ij}\Delta\varepsilon_{ij} \tag{6.8}$$

where σ_{ii} and σ_{ij} are trial normal and shear stresses, $\Delta\varepsilon_{ii}$ and $\Delta\varepsilon_{ij}$ strain increments and lastly n is the time increment.

6.3. Numerical Models of Compression of Single and Double-layer Corrugated Sandwiches

The handling of the fin layers and the applied weight during assemble of the sandwiches naturally induced imperfections on the fin walls. Two types of imperfections were detected: fin wall bending and fin wall bulge formation as shown by arrows in Figures 6.2(a) and (b).

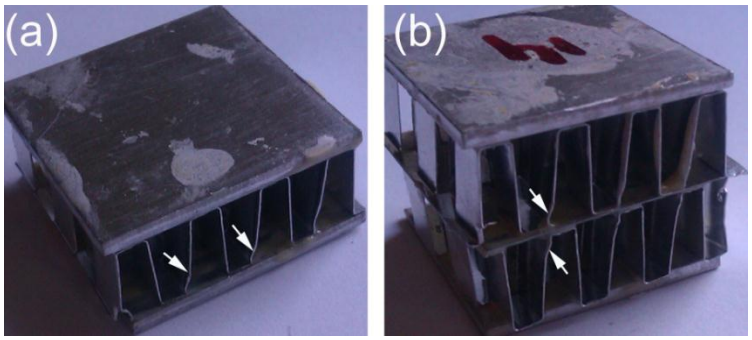

Figure 6.2. Imperfections on (a) single- and (b) double-layer corrugated sandwich samples.

The effect of induced fin wall imperfection was simulated by the implementation of imperfect models. In the imperfect model, bending type imperfection (9 mm in length) was introduced to the half of the fin walls, with a radius of 2 mm and an angle of 6.5° from the original fin wall (Figure 6.3(a)). The numerical imperfect models were implemented using the bending type imperfection, while the effect of the length of the imperfection was assessed by bulge type impaction with a radius of 1.7 mm and length of 1.5 mm as shown in Figure 6.3(b).

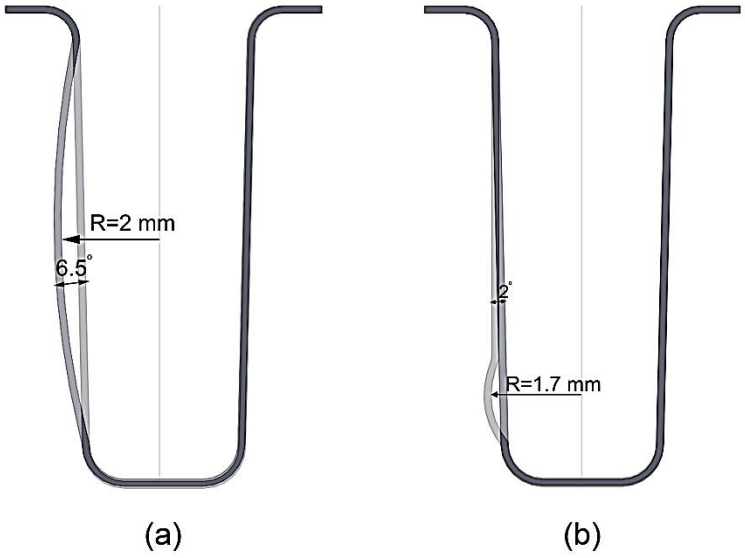

Figure 6.3. Numerical fin wall imperfections: (a) fin wall bending and (b) fin wall bulging.

The numerical perfect models of single-layer sandwiches with and without adhesive (polyurethane) layer and the double-layer sandwich without adhesive layer are sequentially shown in Figures 6.4(a-c). The corresponding imperfect models of the single- and double-layer sandwiches in Figures 6.4(a-c) are sequentially shown in Figures 6.4(d-f). The effect of the adhesive layer on the stress-strain behavior of the sandwiches was assessed with the implementation of the single-layer models with adhesive layers between the face sheets and corrugated fin layer (Figures 6.4(b) and (e)). The polyurethane adhesive layer was modeled using the MAT01_ELASTIC material model (E=69 MPa and υ=0.25). The thickness of the adhesive layer was taken as 0.2 mm. The contacts between core, adhesive layer, interlayer sheets and face sheets were assumed to be perfectly bonded and defined by TIED_NODES_TO_SURFACE contact algorithm. The self-contacting interfaces were defined by ERODING_SINGLE_SURFACE contact.

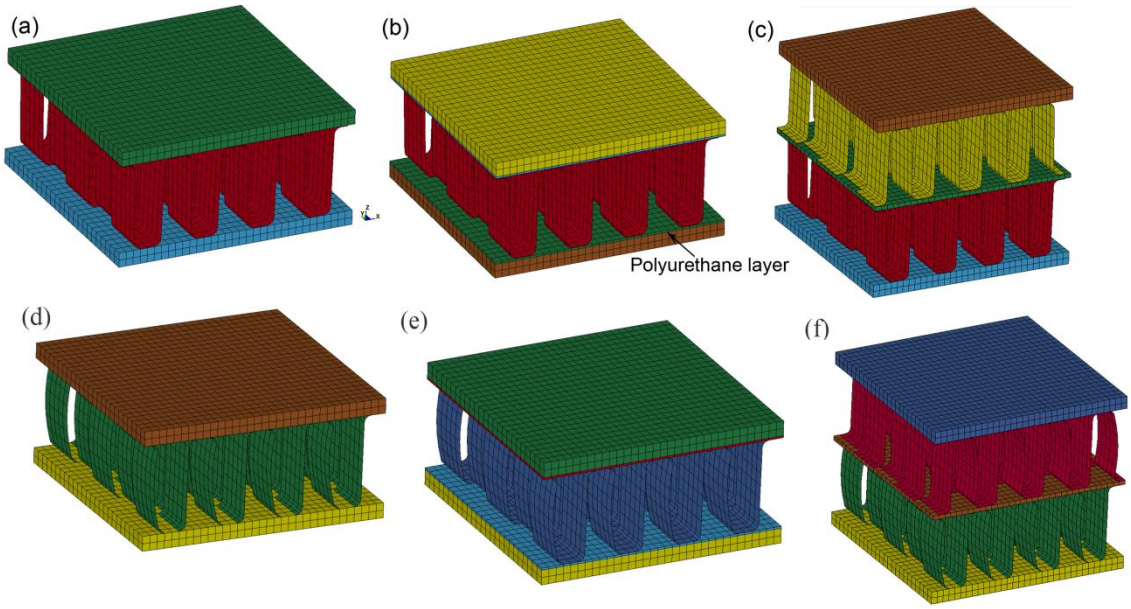

Figure 6.4. Perfect numerical models of (a) single-layer, (b) single-layer with polyurethane layers, (c) double-layer sandwiches and imperfect numerical model of (d) single-layer, (e) single-layer with polyurethane layers and (f) double-layer sandwiches.

The trapezoidal corrugated fin layers (Figure 6.5(a)) were meshed using Belytschko-Tsay shell elements with five integration points and the interlayer and face sheets were modeled using the constant stress solid elements. The increased number of integration points in the shell elements generally leads to prolonged CPU calculation times. On the other side, in order to increase the accuracy of the models, the number of integration points should be higher than two when the buckling is the dominant deformation mode [99]. In addition, the FE meshes of the corrugated fin layers and interlayer-face sheets have to coincide with each in order to be able to define tied contacts. This naturally limits the use of arbitrary-defined mesh distribution and element sizes. The effect of element size on the modeling results was assessed by implementing (i) a fine mesh model, comprising 10800 shell and 9900 solid elements, (ii) a medium mesh model, comprising 2800 shell and 3300 solid elements and (iii) a coarse mesh model, comprising 960 shell and 660 solid elements in the SHPB testing models of single-layer sandwich specimen. The quasi-static and high strain rate compression testing of the straight trapezoidal (Figure 6.5(b)) and triangular perfect corrugated (Figure 6.5(c)) single-layer sandwich structures were also modeled in order to determine the effect of fin geometry on the crushing strength.

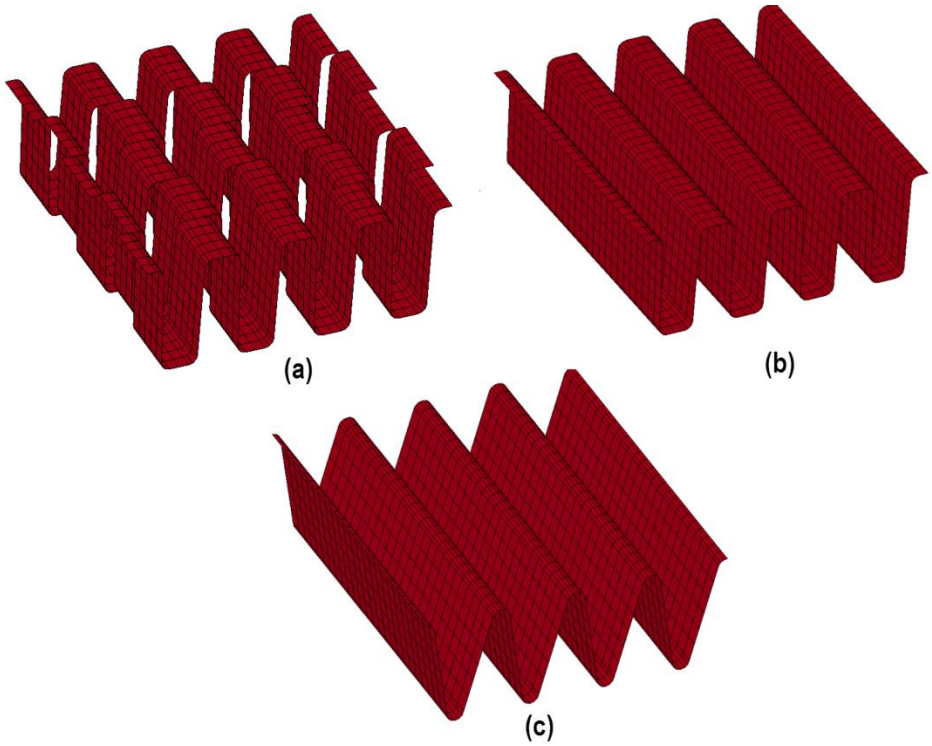

Figure 6.5. Perfect numerical models of corrugated fin layers: (a) zig-zag, (b) straight and (c) triangular.

Figure 6.6 shows the numerical model of quasi-static compression test set-up. The model consists of the top and bottom compression test platens and specimen. Each compression test platen was modeled using 19200 constant stress solid elements. The compression platens were modeled with MAT20_RIGID material model (E=210 GPa and υ=0.3). In the model, the rotations and the movement of the compression platens were fully constrained, except the axial motion of the top platen in the z-direction. The axial velocity of the top platen was kept constant, the same as the experiments and defined by PRESCRIBED_MOTION_RIGID card. The contact between compression test platens and specimen was defined by AUTOMATIC_SURFACE_TO_SURFACE contact. Since the total CPU time for the quasi-static test solutions are relatively long [100], the mass scaling was applied in the quasi-static simulations by defining a positive time step value in CONTROL_TIMESTEP card.

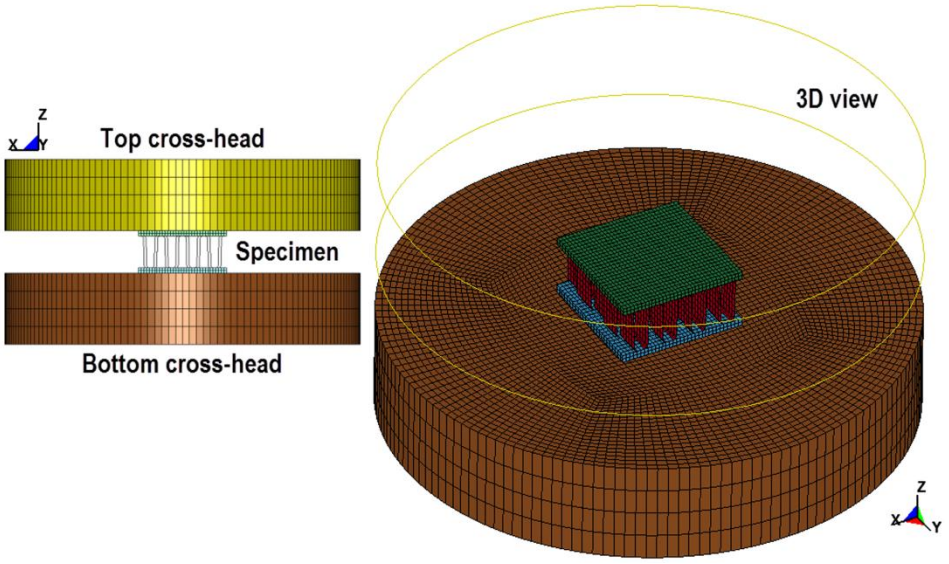

Figure 6.6. The numerical model of quasi-static compression test set-up.

The numerical model of the direct SHPB impact testing is shown in Figure 6.7. The contact area between the striker bar and the specimen was meshed with 2 mm size elements, while the rest of the length was meshed with 7 and 17 mm size elements. The incident bar was modeled with 20 mm size elements. The models of striker and incident bar consisted of 23660 and 33800 constant stress solid elements, respectively. The striker and incident bar deformations were modeled using MAT01_ELASTIC material model. The axial movement and the rotations of the striker and incident bars were constrained in all directions, expect the axial movement of the striker bar in the z-direction. The experimental striker bar velocity, 18 m s^{-1}, was defined in the model using VELOCITY_GENERATION in LS-DYNA. The contact between bars and specimen was defined by AUTOMATIC_SURFACE_TO_SURFACE contact. The bar contact during deformation was defined by AUTOMATIC_SINGLE_SURFACE. The static and dynamic friction coefficients were set to 0.3 and 0.2 in all contact definitions, respectively. The stress values on the incident bar were calculated on the bars from an element located at the same distance with the strain gages in the experiments.

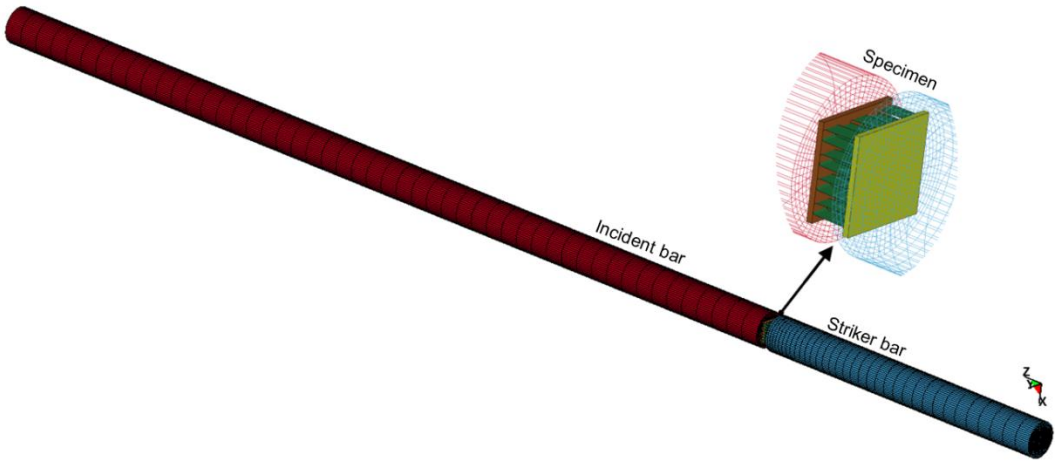

Figure 6.7. The numerical model of direct impact SHPB test set-up.

6.4. Numerical Models of Compression of Multi-layer Corrugated Sandwiches

The numerical models of 0°/0° fin layer orientated sandwich sample with interlayer sheets and 0°/0° and 0°/90° fin layer orientated samples without interlayer sheets are sequentially shown in Figures 6.8(a-c). Trapezoidal corrugated fin layers were meshed using Belytschko-Tsay shell elements with five integration points and the interlayer and face sheets were modeled using constant stress solid elements. The increased number of integration points in shell elements raise the CPU calculation times. In case buckling is the dominant deformation mode; however, the number of integration points should be higher than two in order to increase the accuracy of the models [99]. The FE meshes of corrugated fin layers and interlayer/face sheets have to coincide with each other in order to define tied contacts between them. This limits the implementations of arbitrary-defined mesh distribution and element sizes. The contacts between core, interlayer and face sheets were assumed to be perfectly bonded and defined by TIED_NODES_TO_SURFACE contact algorithm. The self-contacting interfaces were defined by ERODING_SINGLE_SURFACE contact type.

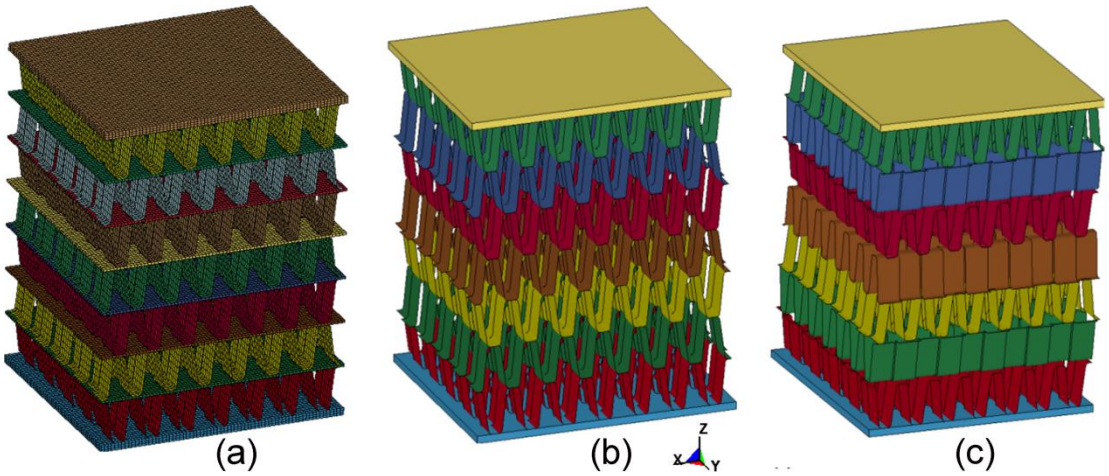

Figure 6.8. Numerical models of (a) 0°/0° core oriented sandwich and (b) 0°/0° and (c) 0°/90° core oriented sandwiches without interlayer sheets.

The developed full numerical models of quasi-static compression test system and drop weight test are shown in Figures 6.9((a) and (b)), respectively. The numerical model of quasi-static compression test comprised of top and bottom compression test platens and the specimen. Each platen model consisted of 19200 constant stress solid elements. Quasi-static simulations were performed at the strain rate of 10^{-1} s^{-1} in order to reduce CPU time. The flat-end of the striker, which was in direct contact with specimen, was meshed using 1 mm, while the rest was modeled using 10 mm element sizes. The striker was defined to move only in the z-direction and consisted of 106192 constant stress solid elements. The stationary bottom plate model comprised 5000 solid quad elements. The contact between the cross-head and the specimen was defined by AUTOMATIC_SURFACE_TO_SURFACE contact. Similar to the drop weight experiments, the initial velocity of the striker in the model was set to 3 m s^{-1}. In quasi-static simulations, the mass scaling was applied by defining a positive time step value in CONTROL_TIMESTEP card in LS-DYNA.

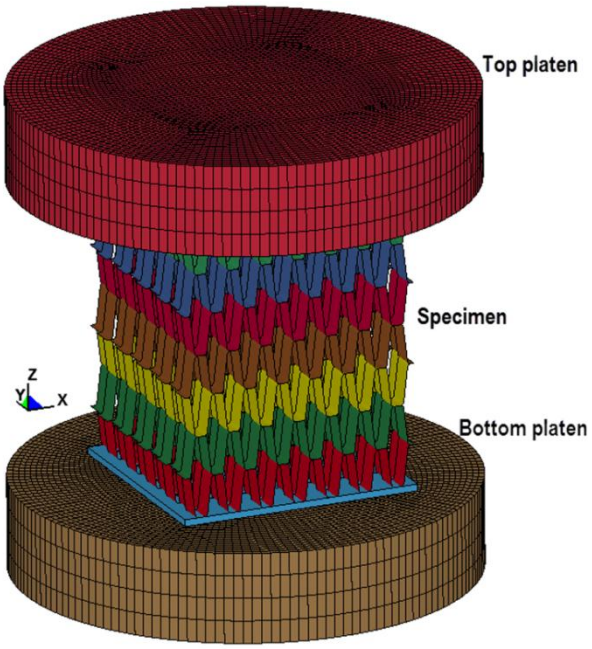

(a)

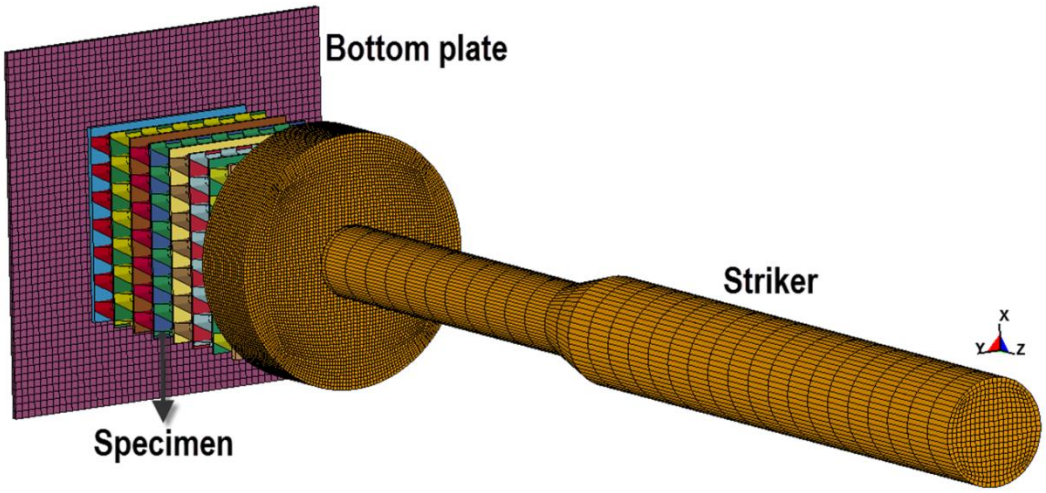

(b)

Figure 6.9. The numerical models of (a) quasi-static compression and (b) drop weight compression test.

6.5. Numerical Models of Indentation of Multi-layer Corrugated Sandwiches

The explicit full geometrical model of adhesively bonded 0°/0° oriented corrugated sandwich panels with 1050 H14 aluminum face sheets is shown in Figure 6.10(a)). The corrugated fin layers were meshed using quad Belytschko-Tsay shell elements with five integration points. This element formulation is capable of capturing

deformation modes with a reasonable CPU calculation time [99, 101]. As is seen in Figure 6.10(b), the FE meshes of the interlayers and fin layers coincide with each other in order to satisfy tied contact definition, which eliminates arbitrary element size selection option. The face sheets and interlayer sheets were meshed using quad solid elements. The effect of mesh size on the numerical results was assessed by implementing (i) a fine mesh model, comprising 254800 shell and 243704 solid elements, and (ii) a coarse mesh model, comprising 76440 shell and 115064 solid elements. In order to capture the deformation realistically, a uniform element distribution was preferred in sheet meshing as suggested in ref. [102].

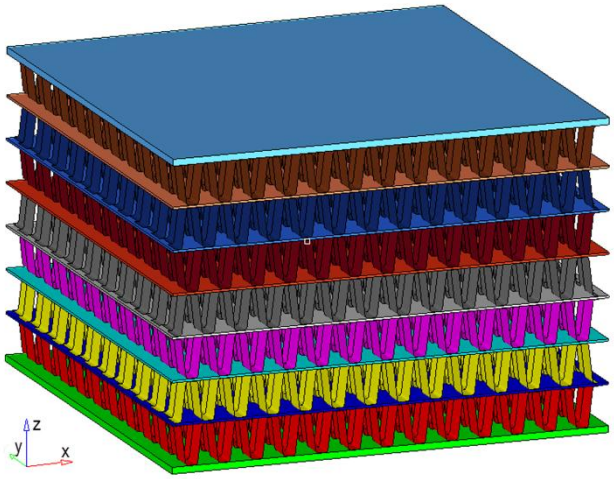

(a)

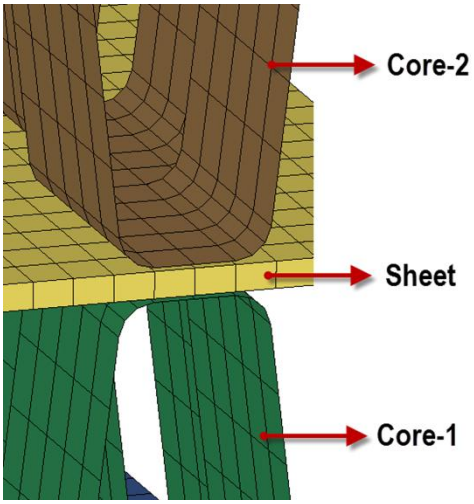

(b)

Figure 6.10. (a) 3 D numerical model of corrugated sandwich panel and (b) contact area between fin layers and interlayer sheet.

The developed full numerical model of drop weight test system with spherical striker tip is shown in Figure 6.11(a). In the model, the striker and top and bottom rings were meshed using quad solid elements. The striker was modeled using three different mesh sizes in order to reduce the element processing. The contact area was meshed using small elements (0.65 mm) and the length section using coarse elements (7 and 20 mm), as seen in Figure 6.11(a). Total 74304, 5400 and 4200 solid elements were used to model striker and top and bottom rings, respectively. In the models with flat and conical striker tips, above-mentioned model parameters were kept the same and only the striker geometries were altered (Figures 6.11(b) and (c)). The striker and rings were modeled using MAT_RIGID material model, material type 20. The density of the striker was proportionally increased to an impact mass of 15.775 kg. The density (ρ) of the striker and rings are 90000 kg m^{-3} and 7800 kg m^{-3}, respectively. Elastic modulus and Poisson's ratio are 210 GPa and 0.3, respectively. The motion of the top and bottom rings in x, y and z-direction and the rotations in all directions were constrained, while the striker motion was only allowed in the z-direction. The clamp force was attained to the top ring by defining LOAD_SET_SEGMENT option in the LS-DYNA. The contacts were assumed to be perfectly bonded and a TIED_NODES_TO_SURFACE contact algorithm was attained between core, interlayer sheets and face sheets. ERODING_SINGLE_SURFACE contact definition was selected in order to take into account self-contacting interfaces. ERODING_SURFACE_TO_SURFACE contact was defined between striker and sandwich panel. The contact between the rigid rings and sandwich panel was defined with AUTOMATIC_SURFACE_TO_SURFACE algorithm. The static and dynamic friction coefficients were set to 0.3 and 0.2, respectively. CONTROL_SHELL card was also defined to include shell thickness in the contact algorithms. Since the total CPU time for the solution was determined to be relatively long (800 CPU hours), resulting from the element processing and intricate contact definitions, the mass scaling was applied by defining CONTROL_TIMESTEP card in the LSDYNA.

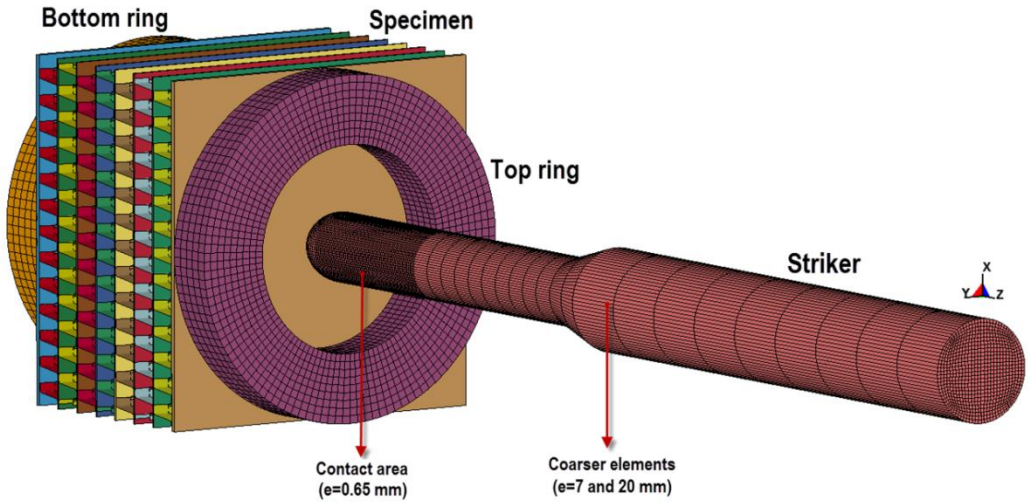

(a)

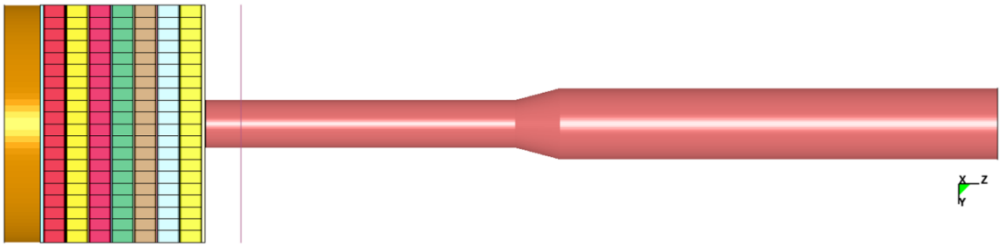

(b)

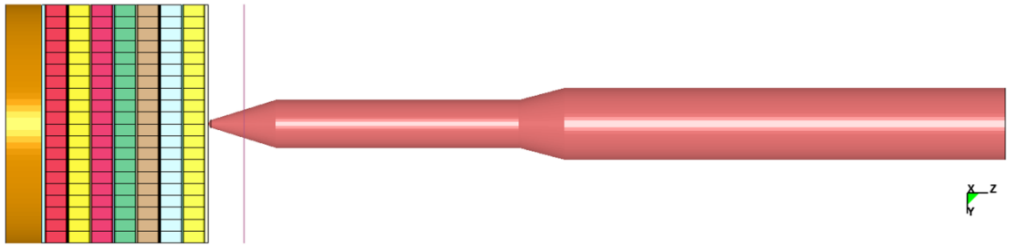

(c)

Figure 6.11. The numerical models of drop weight indentation test system with (a) spherical, (b) flat and (b) conical striker tip.

6.6. Numerical Models of Homogenized Multi-layer Corrugated Sandwiches

In the solid models, the fin layers in single and multi-layer samples were represented by the solid model as shown in Figures 6.12(a-d). The solid fin layers were meshed using quad-constant solid elements. Honeycomb material model, Mat26, was used to model solid fin layers. The boding between cores, interlayers and face sheets

were assumed to be prefect and touching nodes on the contact surfaces were merged by using dup-node function in LS-DYNA.

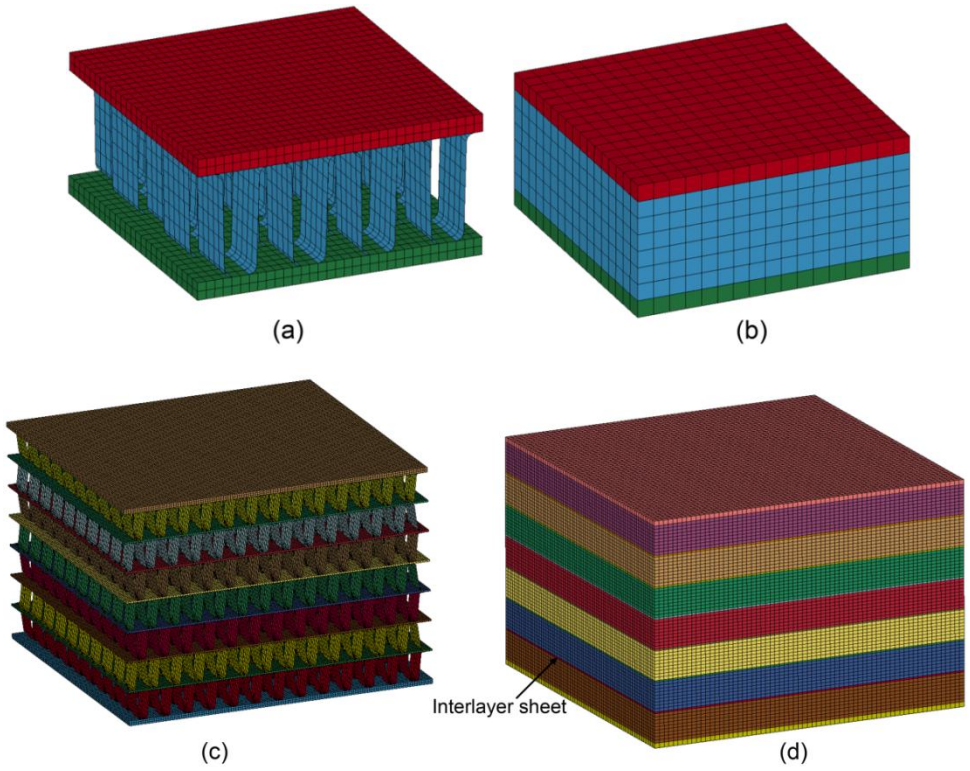

Figure 6.12. 3 D numerical model of full model: (a) single and (c) multi-layer and solid model: (b) single and (d) multi-layer.

6.6.1. Homogenized Numerical Models of Quasi-static Crushing of Single layer of Zig-zag Trapezoidal Corrugated Fin Layer

Figures 6.13(a-c) show the numerical model of the quasi-static compression on single fin layer along three different loading axes (x-aa axis, y-bb axis and z-cc axis). The models consisted of top and bottom platens and a layer of corrugated fins with 50 mm in width and length and 9 mm in height. Each compression platen consisted of 19200 constant solid elements and both platens were assumed to be rigid. The fin layer was compromised of 9800 shell elements. The motion was defined to top platen while the bottom platen was kept stationary. The compression speed at the strain rate of 10^{-1} s^{-1} was defined by using DEFINE_CURVE card in LS-DYNA. The contact between platens and fin layer was defined using AUTOMATIC_SURFACE_TO_SURFACE contact algorithm with 0.3 and 0.2 static and dynamic friction coefficients. In contact

definitions, the thickness of shell elements was also included by defining CONTROL_CONTACT card. Since the time steps in explicit simulations are relatively small, mass scaling method was applied in quasi-static simulations by defining a positive constant time step value. The stress-strain curves obtained from these simulations were used as honeycomb model input curves in following simulations.

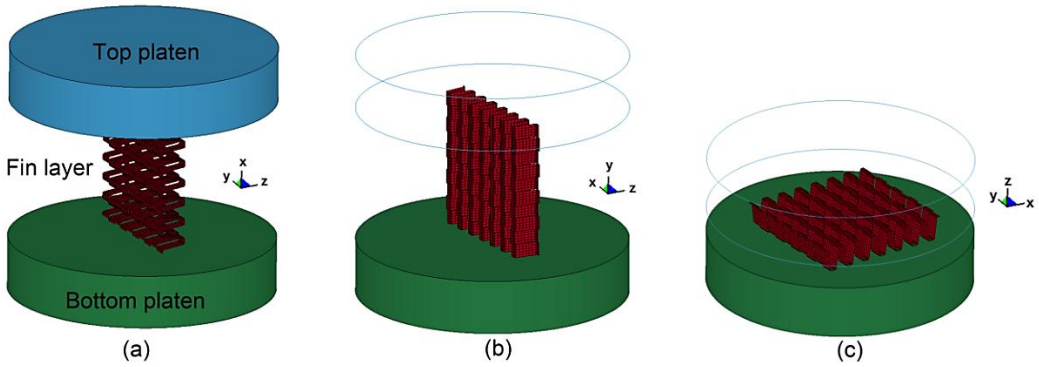

Figure 6.13. The numerical model of quasi-static compression on single fin layer along; (a) x-axis, (b) y-axis and (c) z-axis.

6.6.2. Homogenized Numerical Models of Direct Impact SHPB Tests of Single-layer Corrugated Sandwiches

The FE model of direct SHPB test set-up is shown in Figure 6.14. The model consisted of the striker and incident bars and the single-layer sandwich specimen. The bars were modeled with MAT-01 elastic material model (E=71.7 GPa and μ =0.33). The striker and incident bar compromised of 23660 and 33800 constant stress solid elements, respectively. The single-layer sandwich specimen was meshed with 320 constant solid elements (3 mm in size), called coarse mesh homogenized model, and 2312 constant solid elements (1.5 mm in size), called fine mesh homogenized model. The contact between the bars and specimen was defined by the automatic surface to surface contact algorithm. The striker bar was impacted to the specimen at a velocity of 18 m s^{-1}, the same as the experiments. The stress on the incident bar in the model was determined at an element which had the same distance to the specimen as the strain gages on the incident bar.

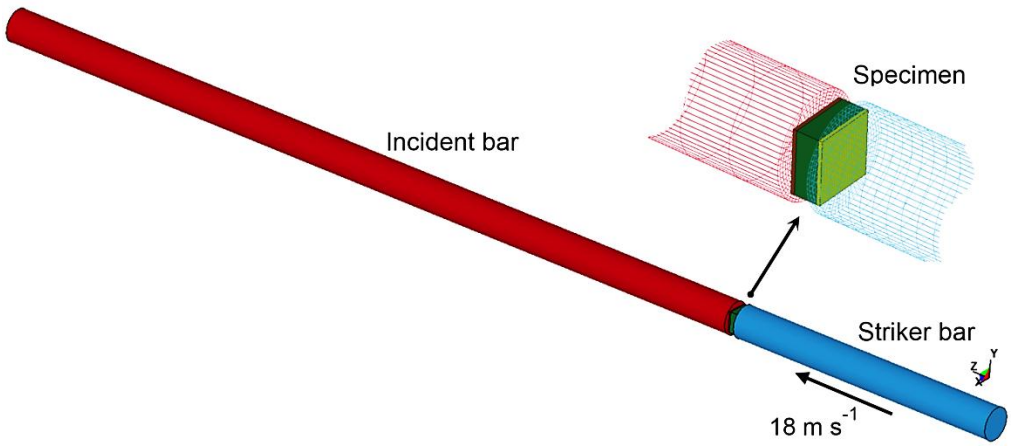

Figure 6.14. The numerical model of direct impact test using solid model corrugated sandwich specimen.

6.6.3. Homogenized Numerical Models of Drop Weight Compression/Indentation Tests of Multi-layer Corrugated Sandwiches

Figures 6.15(a) and (b) show the FE of drop weight indentation and compression (crushing) test, respectively. The indentation test model consisted of spherical-end striker, rings and specimen (Figure 6.15(a)). The striker and rings were assumed rigid and modeled using 73304 and 5400 constant solid elements, respectively. The indentation test specimen was meshed using 318719 constant solid elements. The compression test model consisted of a flat-end striker, bottom platen and specimen (Figure 6.15(b)). The striker and platen were assumed rigid and comprised of 106192 and 5000 constant solid elements, respectively. The compression test specimen was modeled using 119573 constant solid elements and only allowed to extent in the z-axis (constraint test). The contact between specimen and striker was defined by eroding surface to surface algorithm. The dynamic and static friction coefficients were selected as 0.3 and 0.2 for both contact type.

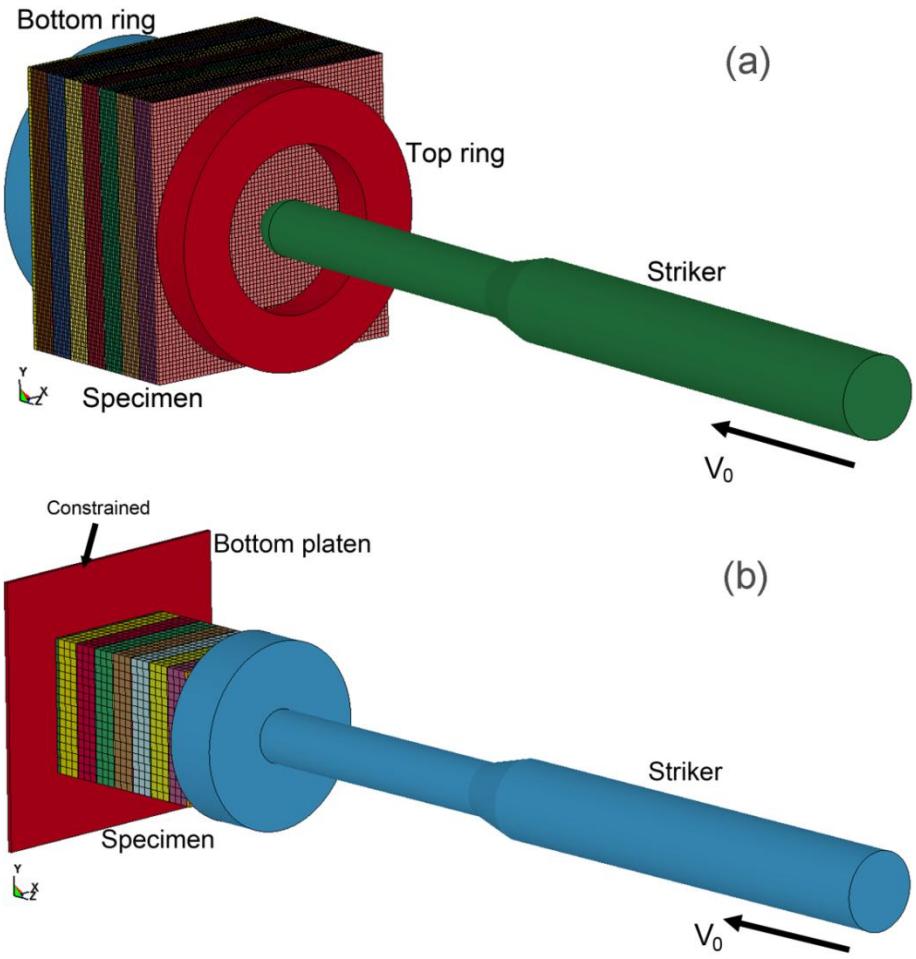

Figure 6.15. The numerical model of drop weight test using solid model corrugated sandwich specimen; (a) indentation and (b) compression.

6.6.4. Homogenized Numerical Models of Projectile Impact Tests of Multi-layer Corrugated Sandwiches

Figure 6.16(a) and (b) shows full model and solid model of projectile impact test. The models consisted of top-bottom frames, projectile and sandwich specimen. The frames were considered to be rigid and each frame compromised of 11232 solid elements. Projectile was also modeled with rigid material model (E=210 GPa) with an impact velocity, 150 m s^{-1}. Solid model sandwich specimen includes 132124 constant solid elements while full model compromised of 362880 shell elements and 260160 solid elements. In the actual test, sandwich specimen is placed between frames and compressed by bolts. The generated compression force due to screwing, ~500 N, was

attained in the model to the top frame by defining LOAD_SEGMENT_SET card in LS-DYNA.

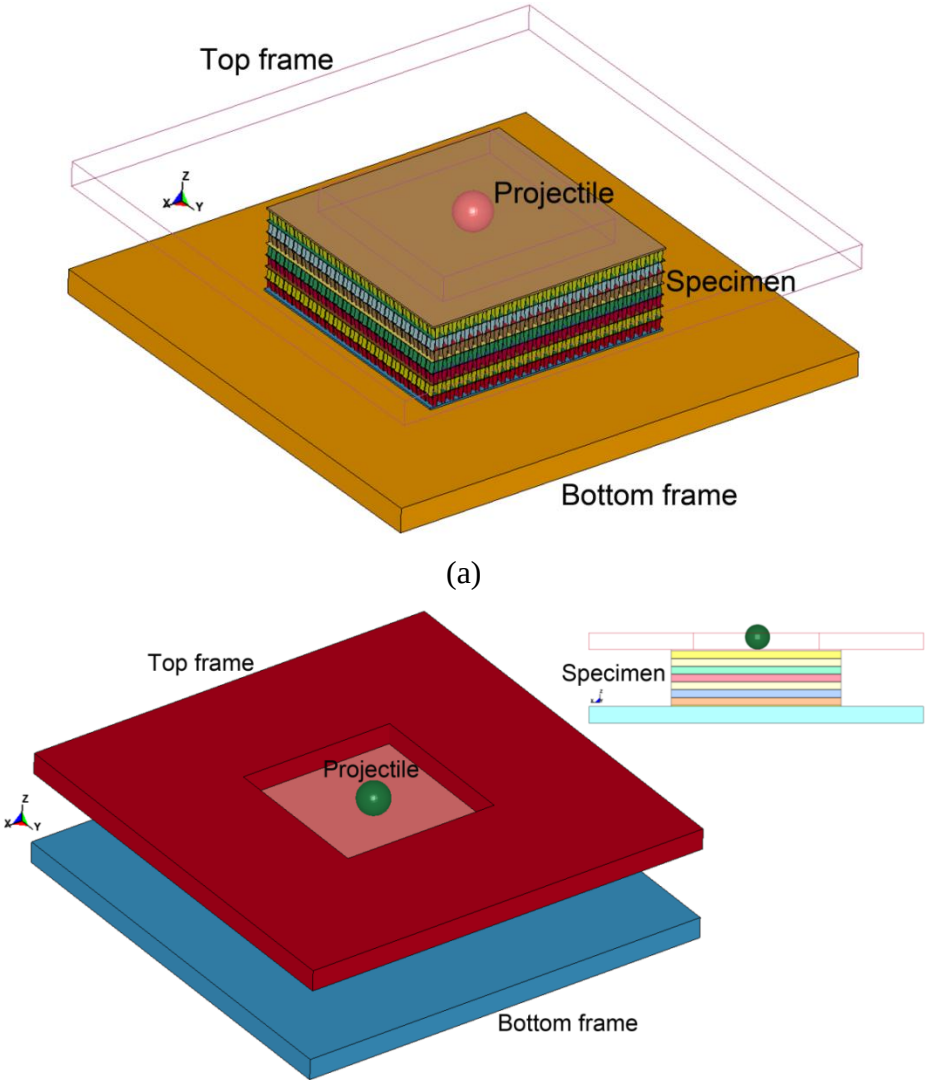

Figure 6.16. The numerical model of projectile impact test; (a) full model and (b) solid model.

CHAPTER 7

DETERMINATION OF JOHNSON-COOK FLOW STRESS MODEL PARAMETERS

7.1. Tension Stress-strain Curves of Standard and Heat-treated 1050 H14 and 3003 Al Alloys

The true stress-true strain curves of standard and heat-treated 1050 H14 and 3003 aluminum alloys are shown in Figures 7.1(a-d). Average stress-strain curves are determined for each alloy. The yield stress of 1050 H14 and 3003 alloys are 102 MPa and 57 MPa, respectively. The yield strength of heat-treated 1050 and 3003 alloys are 24 MPa and 28 MPa, respectively. The elastic modulus of 1050 H14 and 3003 Al alloys were determined as 70 GPa and 69 GPa, respectively.

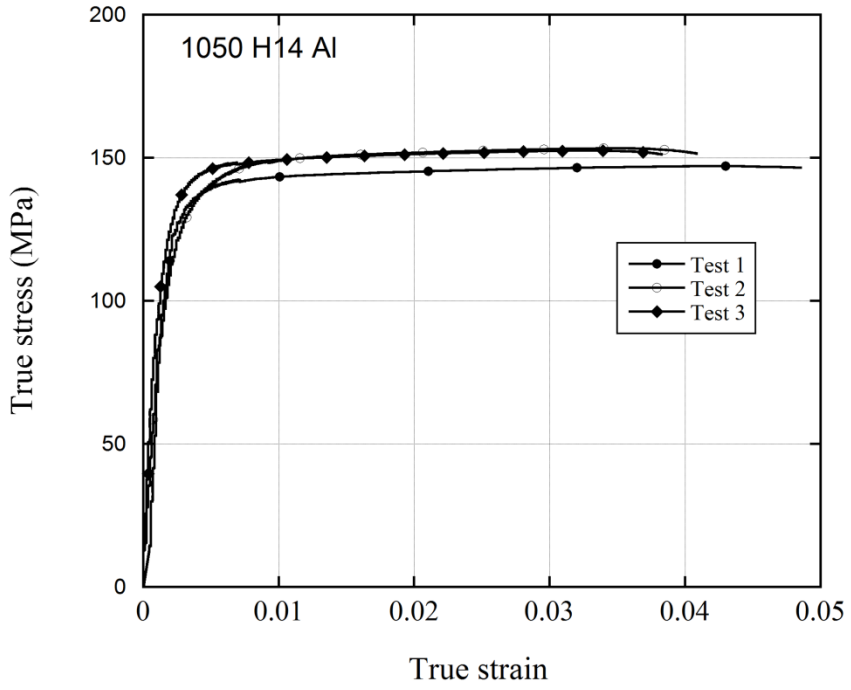

(a)

Figure 7.1. True stress-true strain curves of (a) 1050 H14 Al, (b) heat-treated 1050 H14 Al, (c) 3003 Al and (d) heat-treated 3003 Al.

(cont. on next page)

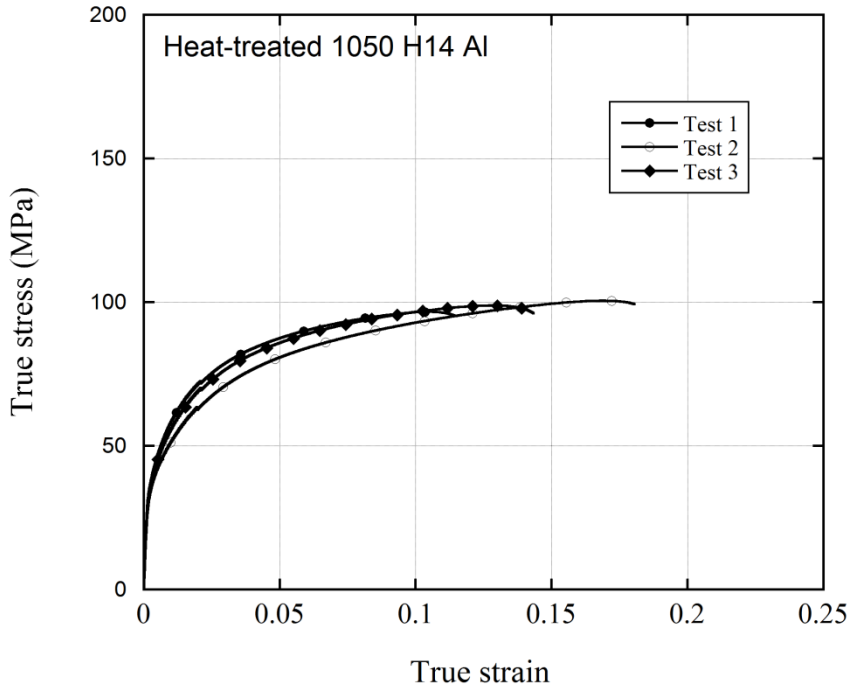

(b)

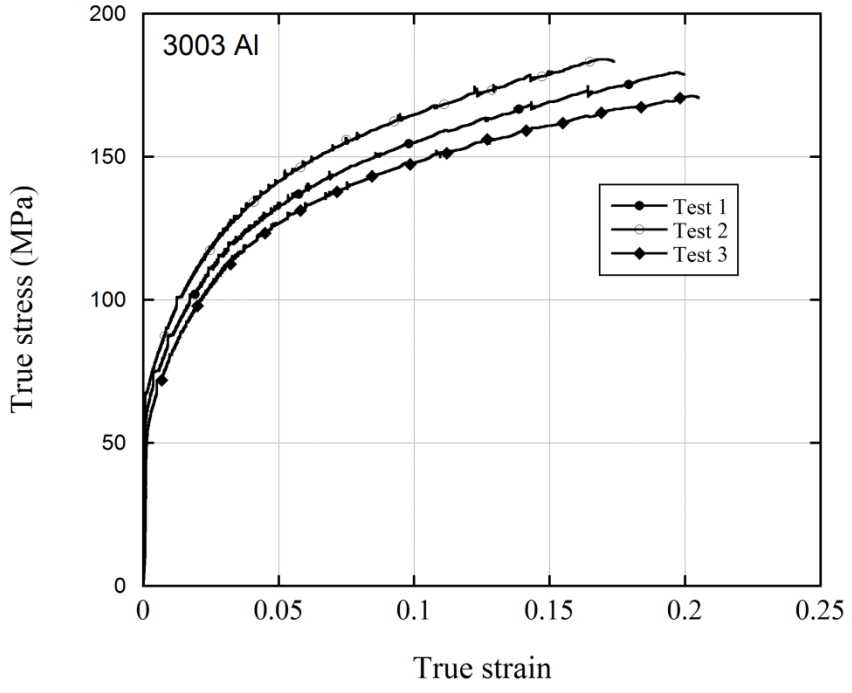

(c)

Figure 7.1 (cont.)

(cont. on next page)

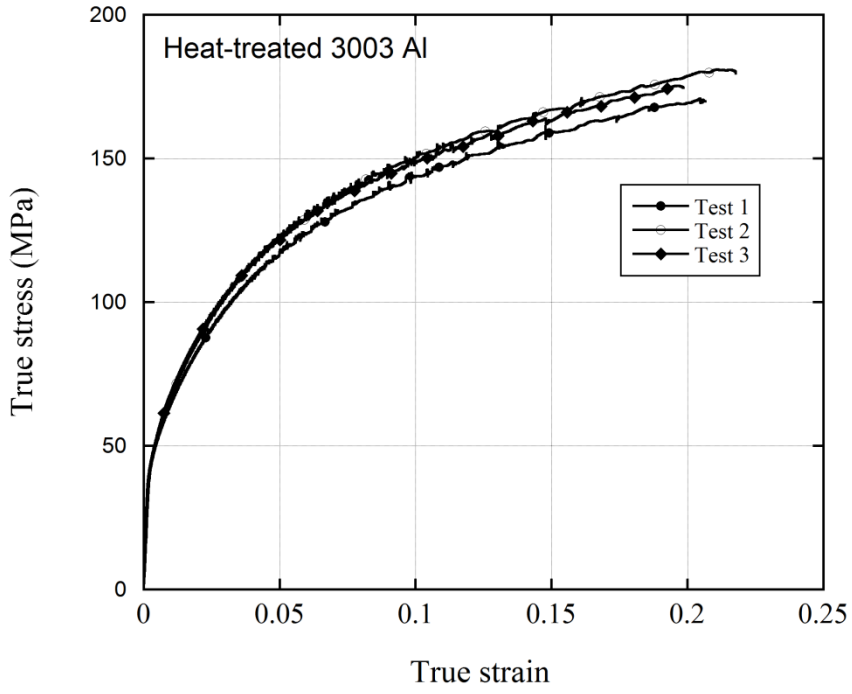

(d)

Figure 7.1 (cont.)

7.2. Johnson-Cook Flow Stress Model Parameters of Standard and Heat-treated 1050 H14 and 3003 Al Alloys

The JC flow stress model parameters of standard and heat-treated 1050 H14 and 3003 Al alloy were determined by fitting the first bracket of Eqn. (6.1) with the experimental true stress-true plastic strain curves. Figures 7.2(a) and (b) show the fit of the JC equation to true stress-true plastic strain of standard and heat-treated 1050 H14 Al alloys. The determined JC model parameters are tabulated in Table 7.1.

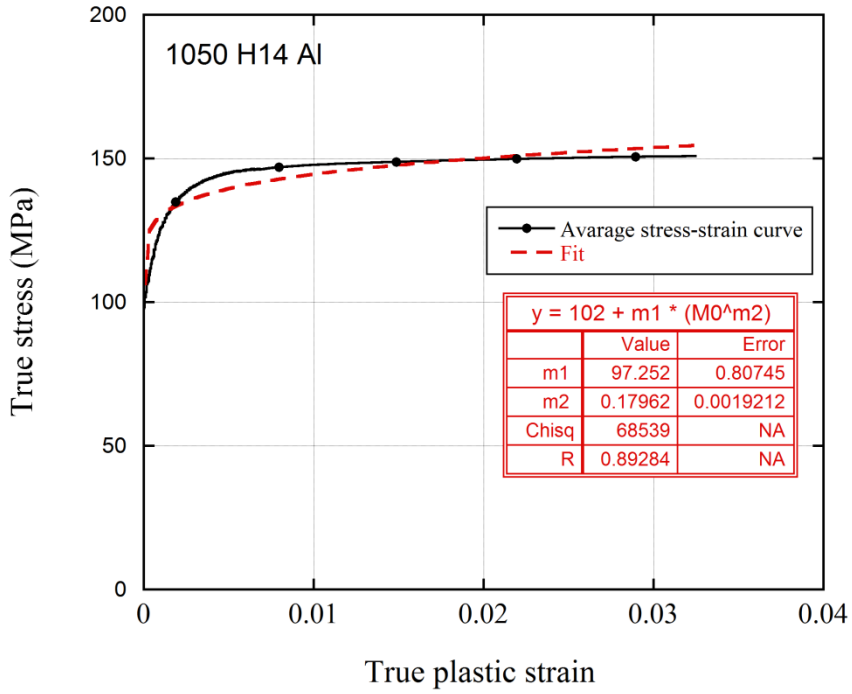

(a)

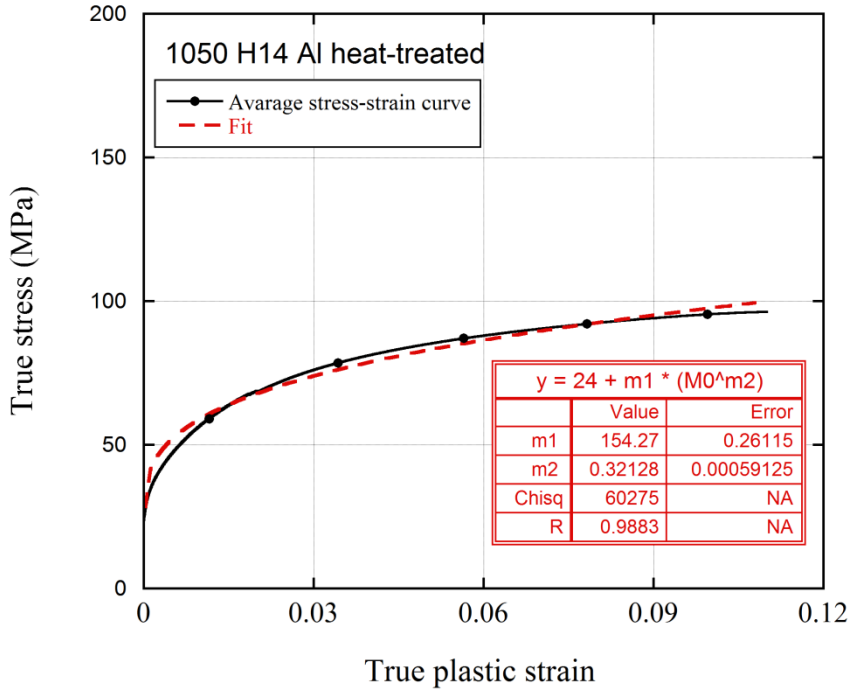

(b)

Figure 7.2. Fitting the JC equation with the true stress-true plastic strain curve of (a) 1050 H14 and (b) heat-treated 1050 H14 Al alloys.

Table 7.1. JC model parameters of standard and heat-treated 1050 H14 Al alloys.

Material	A (MPa)	B (MPa)	n	ε_f
1050 H14 Al	102	97.252	0.18	0.62
Heat-treated 1050 H14 Al	24	154.27	0.321	0.865

The JC equation fitting results of the true stress-true plastic strain curve of standard and heat-treated 3003 Al alloys are shown in Figures 7.3(a) and (b). The JC model parameters of standard and heat-treated 3003 Al are further tabulated in Table 7.2.

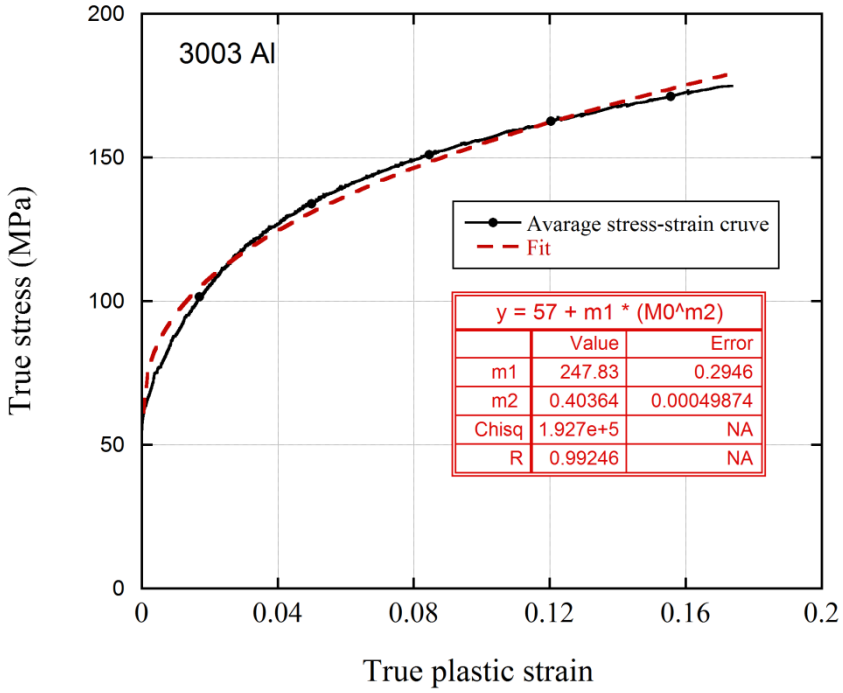

(a)

Figure 7.3. Fitting the JC equation with the true stress-true plastic strain curve of (a) 3003 and (b) heat-treated 3003 Al alloys.

(cont. on next page)

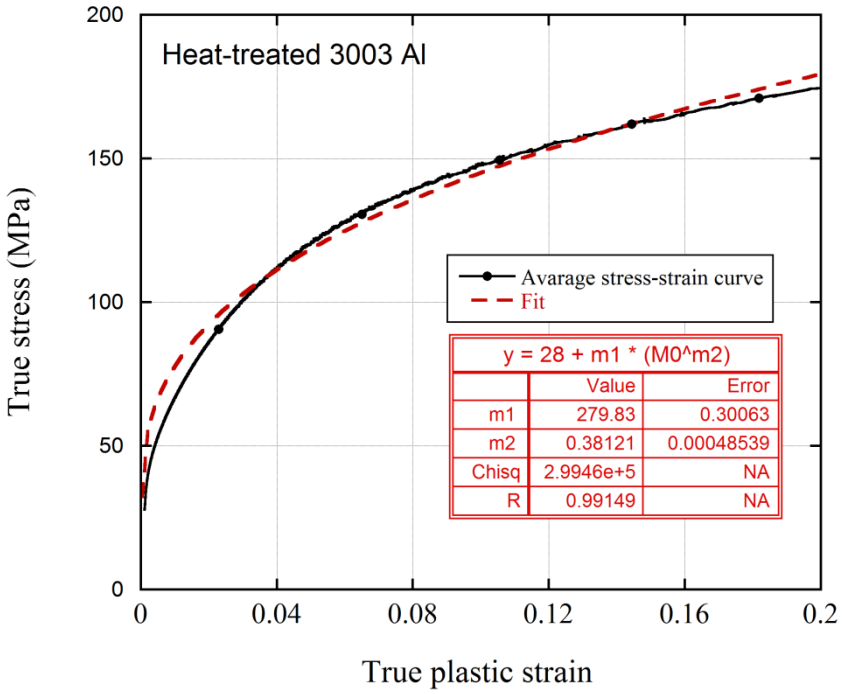

(b)

Figure 7.3 (cont.)

Table 7.2. JC model parameters of standard and heat-treated 3003 Al alloys.

Material	**A (MPa)**	**B (MPa)**	**n**	**ε_f**
3003 Al	57	247.83	0.4	0.397
Heat-treated 3003 Al	28	275.14	0.371	0.4085

CHAPTER 8

QUASI-STATIC AND DYNAMIC COMPRESSION OF SINGLE AND DOUBLE-LAYER CORRUGATED SANDWICHES

Initial modeling efforts focused on the simulation of the quasi-static (10^{-1} s^{-1}) stress-strain behavior of single-layer sandwich structure using the medium mesh size perfect and imperfect core models with and without polyurethane adhesive layers. Figure 8.1(a) shows the early deformation region of the experimental and simulation stress-strain curves of single-layer sandwich structure. As shown in Figure 8.1(a), the initial peak or buckling stresses of three tests vary between 0.73 and 0.91 MPa. However, the simulation with the perfect model results in a higher peak stress (1.25 MPa) and a higher elastic modulus than the experiment. The perfect and imperfect models with polyurethane layer result in relatively lower elastic moduli. The imperfect model, on the other side, gives a peak stress of 0.84 MPa and an elastic modulus comparable with that of the experiment. The post-buckling stresses of the perfect model without and with polyurethane layer are also higher than those of the experiments, while the simulation post-buckling stresses of the imperfect models are comparable with those of the experiments (Figure 8.1(b)). Since the imperfect model with polyurethane layer yields relatively lower elastic modulus, the numerical simulations were continued with the imperfect model. Above results indicated that the compression stresses of single-layer sandwich structure are imperfection sensitive (bending type imperfection) at quasi-static strain rates, as similar with the diamond lattice cores reported previously by Cote et al. [54].

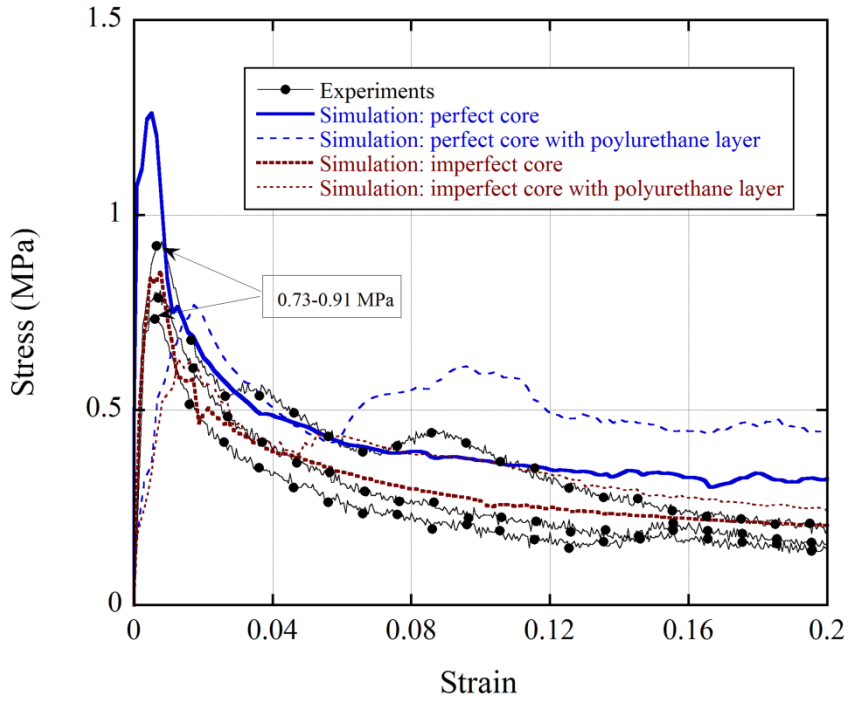

(a)

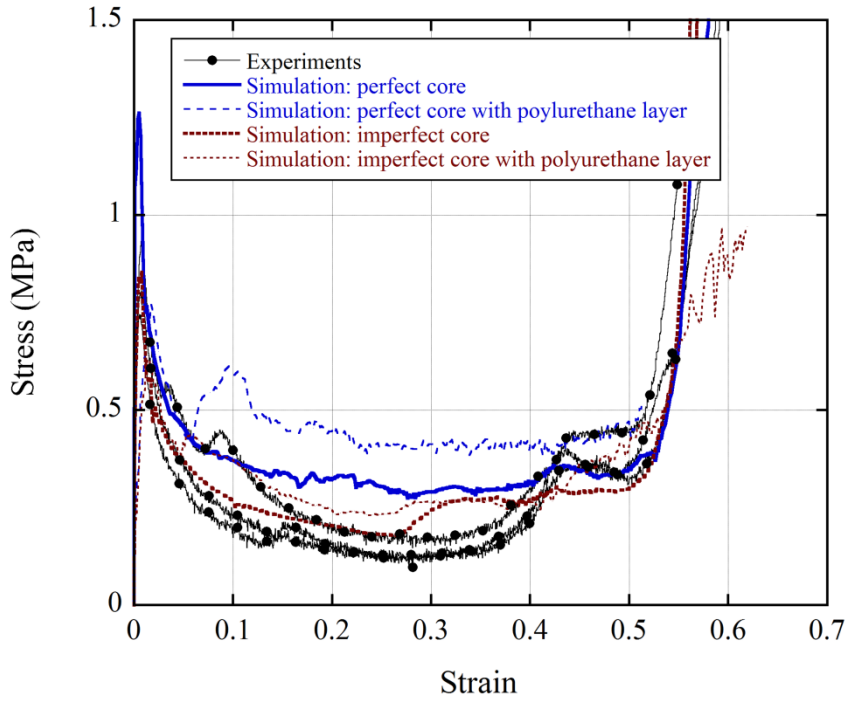

(b)

Figure 8.1. (a) and (b) the experimental and perfect and imperfect model stress-strain curves of single-layer sandwich (10^{-1} s^{-1}).

Figure 8.2(a) shows the experimental and simulation (imperfect model simulations of three different mesh size) high strain rate SHPB (~1500 s^{-1}) stress-strain curves of single-layer sandwich. The experimental buckling stress (shown by an arrow)

in the high strain rate experimental stress-strain curve is well approximated using the coarse and medium mesh size models, while the post-buckling stresses using the medium and fine mesh size models. Therefore, further simulations were implemented using the medium mesh size models. Figure 8.2(b) shows the variations of striker and face sheet velocity with time in SHPB test. The striker velocity remains almost constant (~18 m s^{-1}) during the course of deformation, while the velocity of face sheet increases over that of the striker at beginning of the striker impact and then it reduces to the velocity of striker velocity. Therefore, the crushing velocity of sandwiches during the course deformation was taken constant. It was also seen that the velocity of core is lower than the velocity of striker and face sheet due to lateral movement of fin walls during buckling.

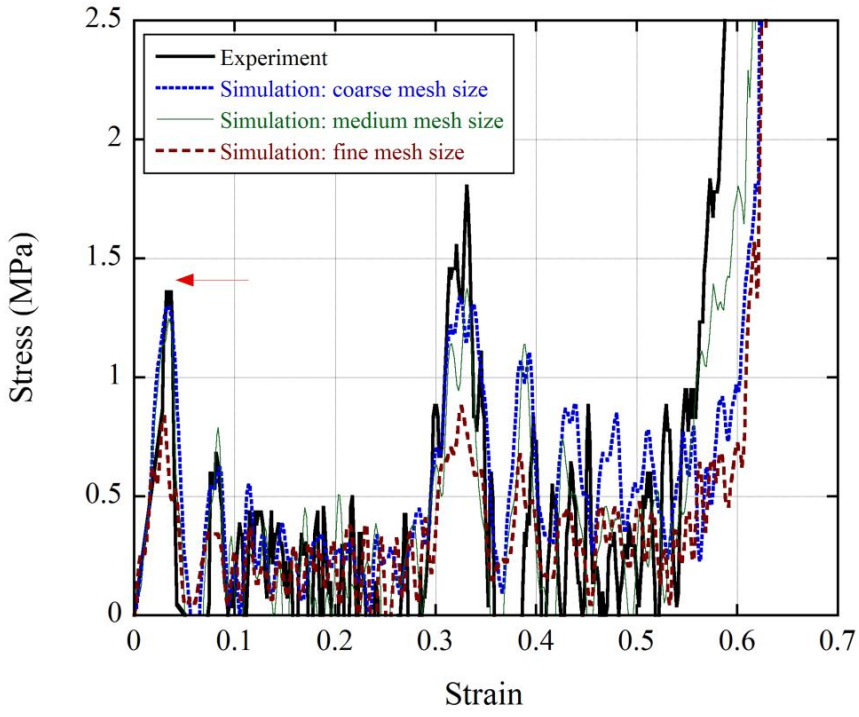

(a)

Figure 8.2. The experimental and simulation of SHPB tests (~1500 s^{-1}) stress-strain curves with three diffrent mesh sizes and (b) the variation of the striker, face sheet and core velocity with time in SHPB test.

(cont. on next page)

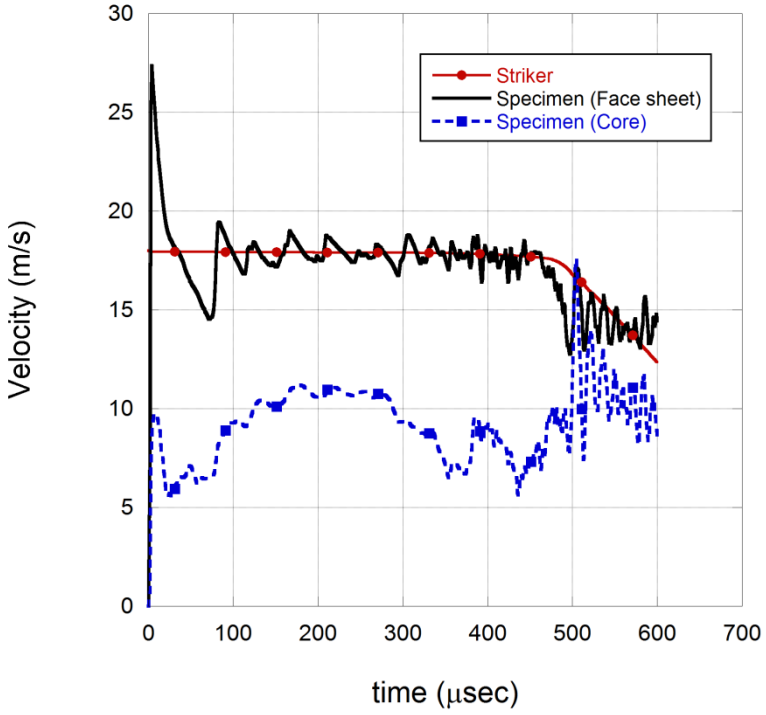

(b)

Figure 8.2 (cont.)

The quasi-static (10^{-3}-10^{-1} s^{-1}) and high strain rate (1500 s^{-1}) experimental and simulation compression stress-strain curves of single-layer sandwich are shown in Figure 8.3(a) for comparison. The quasi-static and high strain rate compression of single-layer specimen exhibits typical strut like structure behavior: after an initial peak stress resulting from the buckling instability of fin walls, the stress values decrease steeply. The increasing strain rate from 10^{-1} s^{-1} ($9x10^{-4}$ m s^{-1}) to 1500 s^{-1} (13.5 m s^{-1}) increases the buckling stress from 0.95 MPa to 1.35 MPa, showing a velocity dependent initial crushing stress behavior of single-layer sandwich. Figures 8.3(b) and (c) show the experimental and numerical deformed pictures of the quasi-statically (10^{-1} s^{-1}) and dynamically (1500 s^{-1}) tested single-layer specimens at different strains, respectively. The buckling mode of the fin wall deformation at quasi-static strain rate is a mixed mode: the adjacent fin walls (normal to the sandwich front face) buckle numerically and experimentally in the opposite directions (shown by arrows in Figure 8.3(b)). While, in dynamically tested single-layer sandwich, the buckling of the adjacent fin walls occurs in the same direction as depicted in Figure 8.3(c). The fin buckling at quasi-static strain rate occurs at the center of fin wall by forming three plastic hinges, two at the face sheets and one at the center of the wall. While, the fin walls at high strain rate buckle

initially near the impact side of the sandwich (striker bar side) and then at the lower section by forming nearly an S-shape deformation with at least four plastic hinges as shown in Figure 8.3(c). The second instability occurs at a strain of 0.3 in dynamically tested samples, leading to the formation of a post-peak stress in the stress-strain curve. The increased stress levels at relatively high strains (>0.5) in Figure 8.3(a) are due to the compression of the folded fin walls, similar to the densification region in foam metal deformation [103]. As a summary, at the quasi-static strain rate, the fin buckling associates with relatively high buckling wavelength comparable with the size of the imperfection leading to reduced buckling stress and post-buckling stress values, while the buckling mode of the dynamically tested samples occurs more axially with relatively smaller wavelength leading to increased buckling stress.

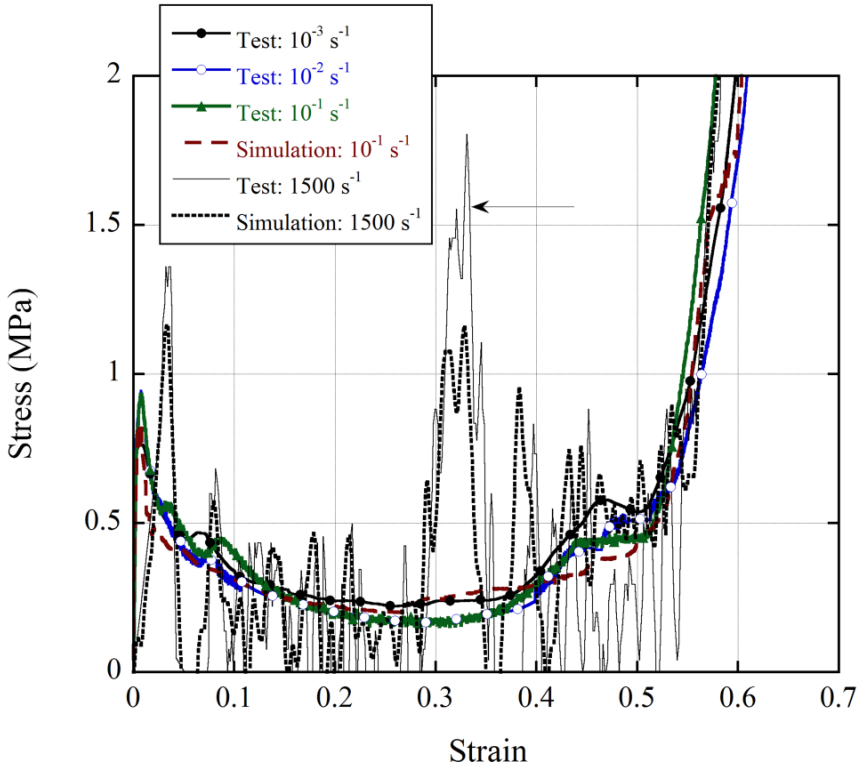

(a)

Figure 8.3. (a) The experimental and numerical stress-strain curves of single-layer sandwich at quasi-static and high strain rates and the deformed pictures at (b) 10^{-1} and (c) 1500 s^{-1}.

(cont. on next page)

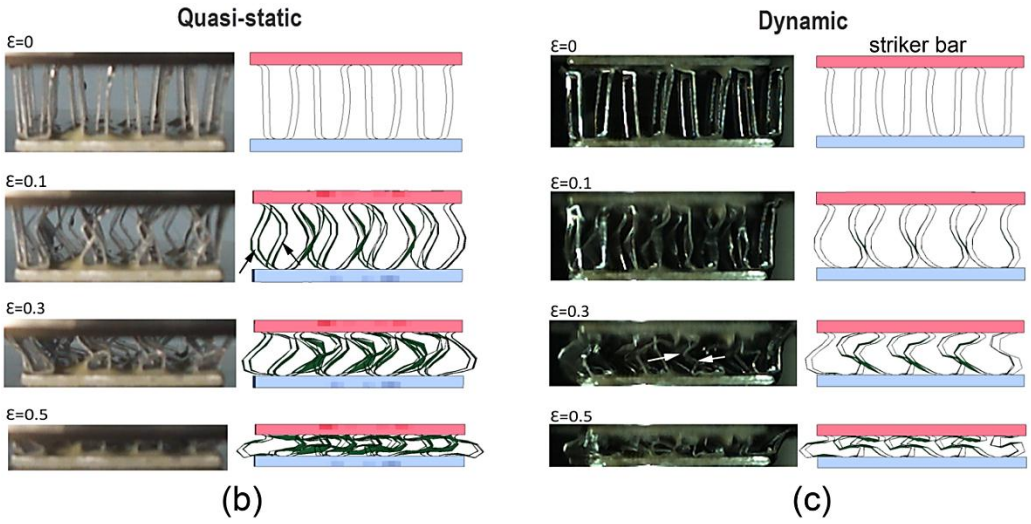

Figure 8.3 (cont.)

The experimental and numerical compression stress-strain curves of double-layer specimens tested at quasi-static (10^{-3}-10^{-1} s^{-1}) and high strain rate (~800 s^{-1}) are shown in Figure 8.4(a). The stress-strain curves of double-layer specimen show very similar trends with those of single-layer specimen; however, the buckling stress (0.50-0.65 MPa) and post-buckling stress values are smaller than those of single-layer specimen. At quasi-static strain rates, 10^{-3}-10^{-1} s^{-1}, the post-buckling region of the stress-strain curve remains smooth due to the shearing of the interlayer sheet as seen in Figure 8.4(b). However, at high strain rate, 800 s^{-1}, the fin wall buckling becomes dominant over the interlayer sheet shearing, leading to increased buckling and post-buckling stresses. At high strain rate, the deformation localized on the top fin layer until about 0.3 strains; thereafter, the bottom fin layer starts to collapse. As with single-layer specimen, the stress values of double-layer specimen increase from 0.50-0.65 MPa at quasi-static strain rates (10^{-3}-10^{-1} s^{-1}) to 1.2 MPa at high strain rate (800 s^{-1}). The peak stresses observed in the plateau region of the dynamically tested samples are due to complex buckling mechanisms of the fin layers. As with single-layer sandwich, double-layer sandwich shows velocity depending crushing stress, simply arising from the change of the deformation mode of the fin walls from buckling and shearing to merely buckling at high strain rate. Double-layer specimens show lower buckling and post buckling stresses than single-layer specimens at both quasi-static and high strain rates, although the difference is more pronounced at quasi-static strain rates.

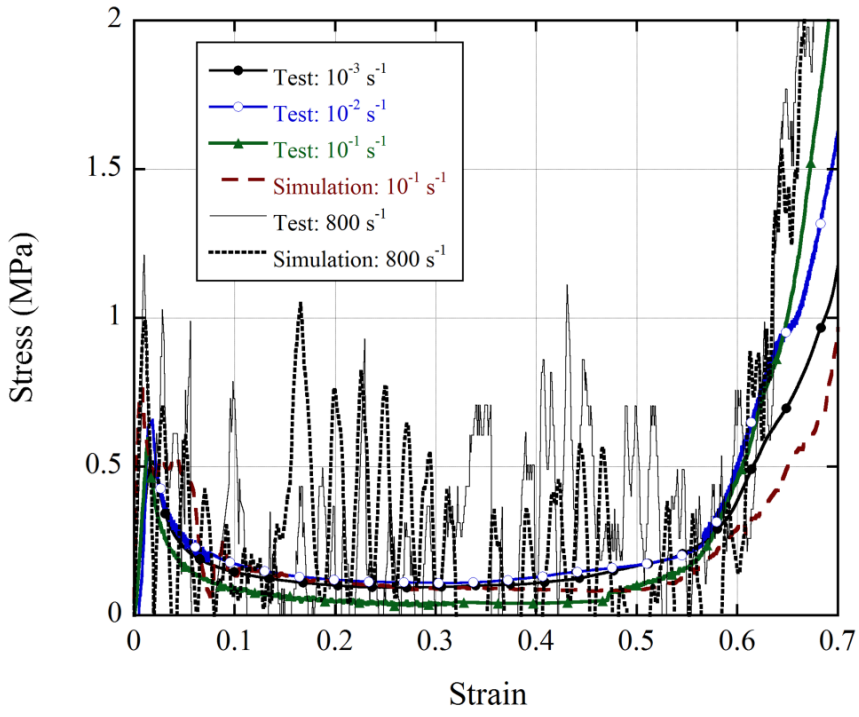

(a)

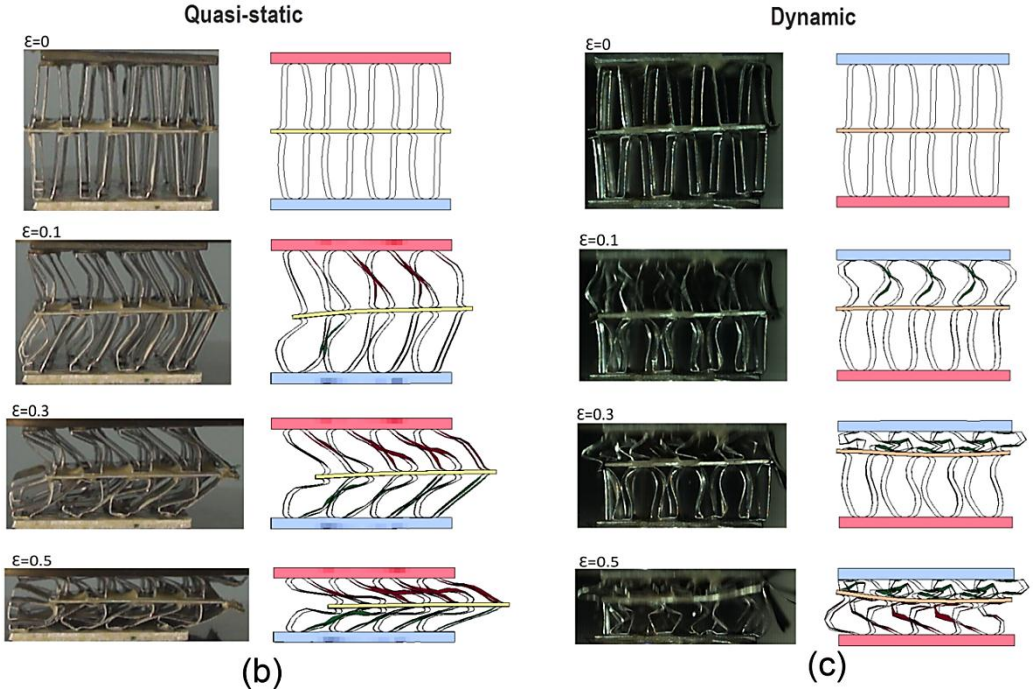

Figure 8.4. (a) The experimental and numerical stress-strain curves of double-layer sandwich at quasi-static and high strain rates and the deformed pictures at (b) 10^{-1} and (c) 800 s^{-1}.

Figure 8.5(a) shows the high strain rate (1500 and 3000 s^{-1}) stress-strain curves of perfect and imperfect models together with that of the quasi-static perfect model for comparison. The perfect and imperfect models give nearly the same buckling and post-

buckling stresses at the strain rate of 1500 s^{-1}. The imperfection insensitive dynamic crushing behavior was also found previously in a corrugated core [74]. The perfect quasi-static model is also noted to have the similar buckling stress with the perfect model at 1500 s^{-1}. When the strain rate numerically increases to 3000 s^{-1}, three effects are seen: the buckling stress increases over the perfect high strain rate and quasi-static models; the perfect model shows slightly higher buckling stress than imperfect model and a stress maximum appears at 0.2 strain. At quasi-static strain rates, the imperfection sensitivity arises since the buckling wavelength is comparable with the size of the imperfection (9 mm), while at high strain rate, the buckling wavelength (~4.5 mm) gets smaller than the imperfection size; hence, the structure becomes imperfection insensitive. The detected increase in the buckling stress at 3000 s^{-1} is due to the micro-inertial effect. When the imperfection size decreases from 9 mm to 1.5 mm (bulge type imperfection), the structure becomes imperfection sensitive at both quasi-static and high strain rates as depicted in Figure 8.5(b). In this case, the buckling wavelength for both quasi-static and high strain rate becomes larger than that of the imperfection size.

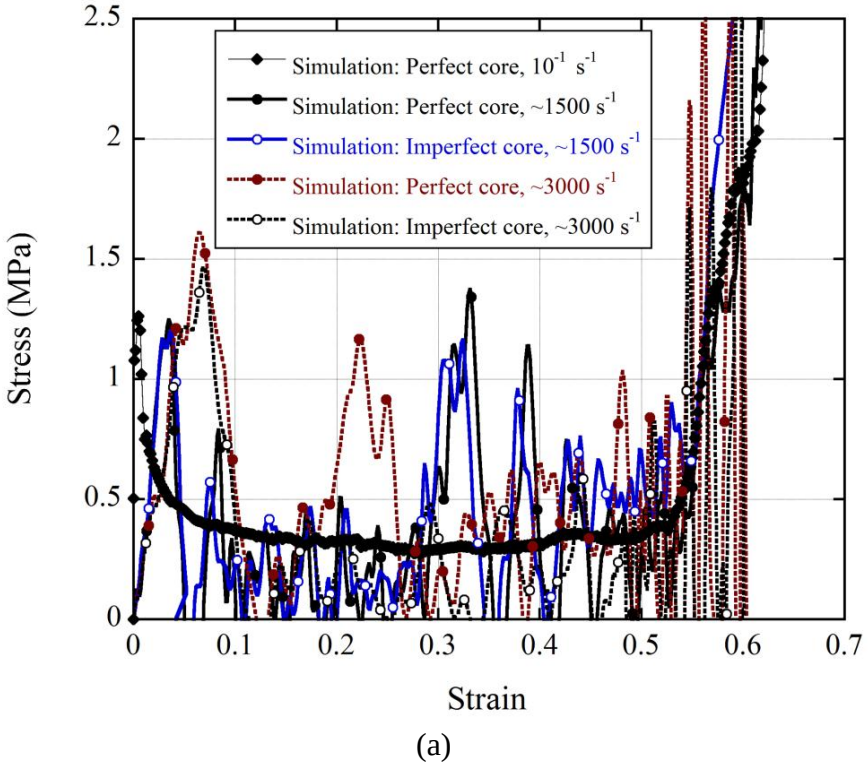

(a)

Figure 8.5. (a) The effect of strain rate on the perfect and imperfect model stress-strain curves and (b) perfect and bulge type imperfect stress-strain curves of single-layer sandwich.

(cont. on next page)

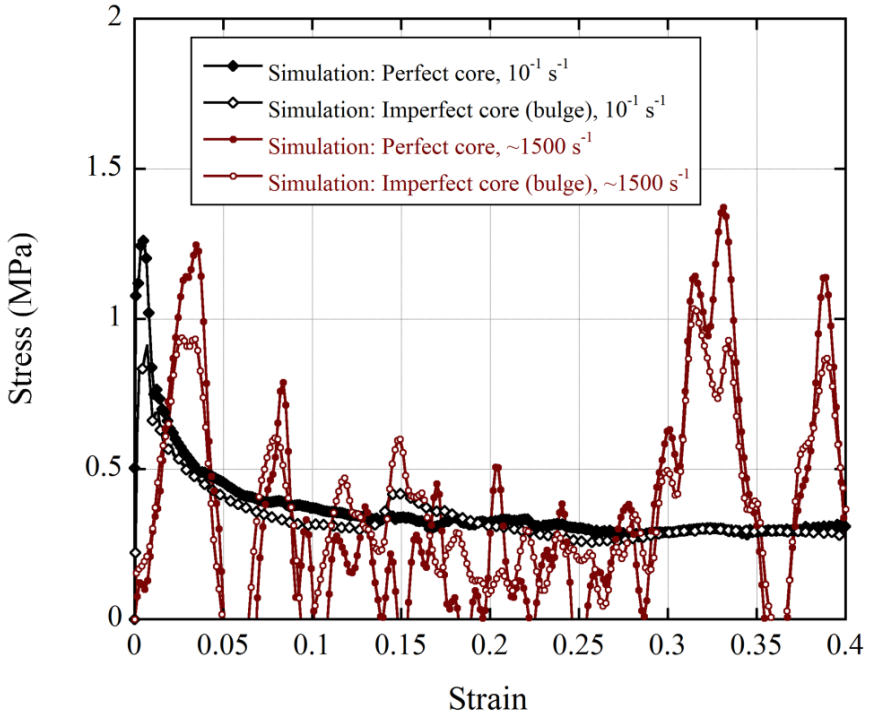

(b)

Figure 8.5 (cont.)

The numerical quasi-static compression stress-strain curves of the perfect zig-zag and straight trapezoidal and triangular corrugated core single-layer sandwiches and the corresponding deformation pictures at different strains are shown in Figure 8.6(a) and (b), respectively. The buckling stresses of the zig-zag (1.25) and straight (1.30 MPa) corrugated core structures are very much similar, showing an insignificant effect of the zig-zag form on the buckling stress. Among three corrugations, the triangular form exhibits the lowest buckling stress (1.04 MPa). As seen in Figure 8.6(b), the deformation modes of the corrugated single-layer sandwich samples are very much similar: the fin wall buckling, while the fin wall buckling in the zig-zag corrugated core sample is a mixed mode (Figure 8.6(b)).

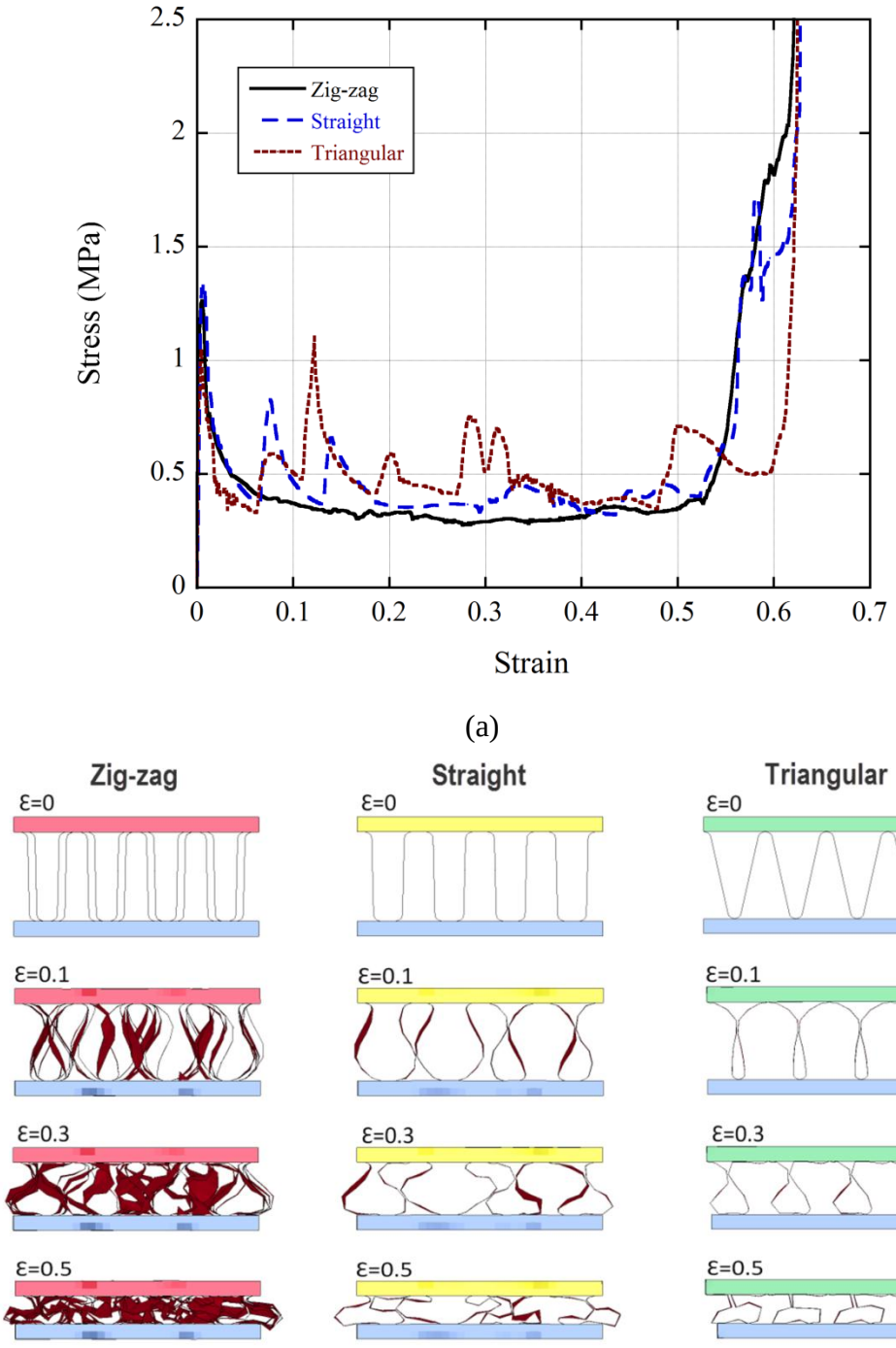

Figure 8.6. (a) The numerical stress-strain curves and (b) deformation pictures of single-layer zig-zag, straight and triangular corrugated core sandwiches at the strain rate of 10^{-1} s^{-1}.

The buckling stresses of zig-zag (1.25 MPa) and straight trapezoidal (1.29 MPa) core single-layer sandwiches almost remain to be the same when the strain rate increases to 1500 s^{-1} (Figure 8.7(a)). However, the buckling stress of the triangular corrugated core single-layer sandwich increases to 1.40 MPa. The buckling mode of the

zig-zag corrugated fin walls switches from mixed mode at quasi-static strain rate to single mode at high strain rate as seen in Figure 8.7(b).

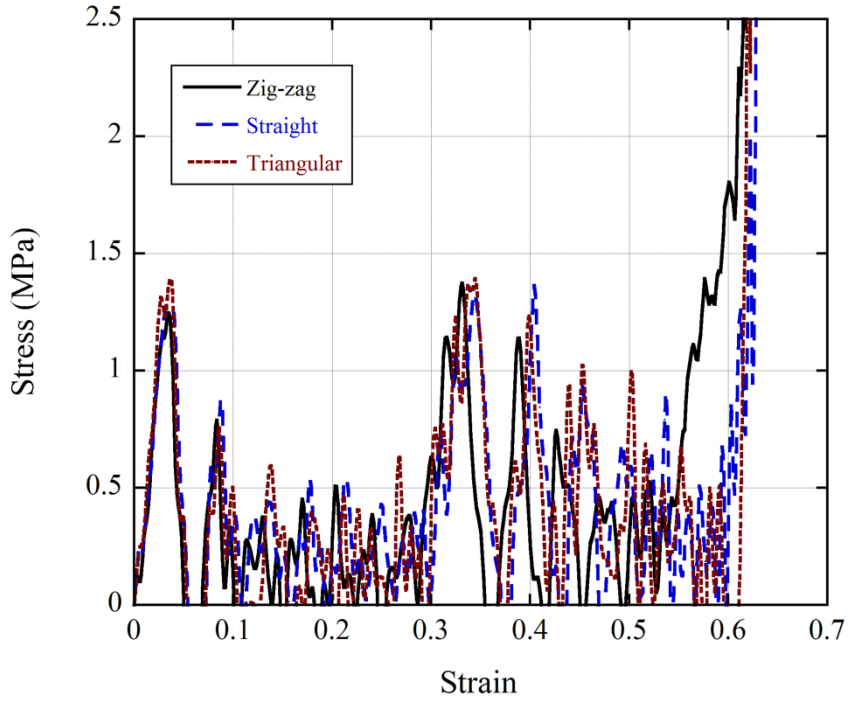

(a)

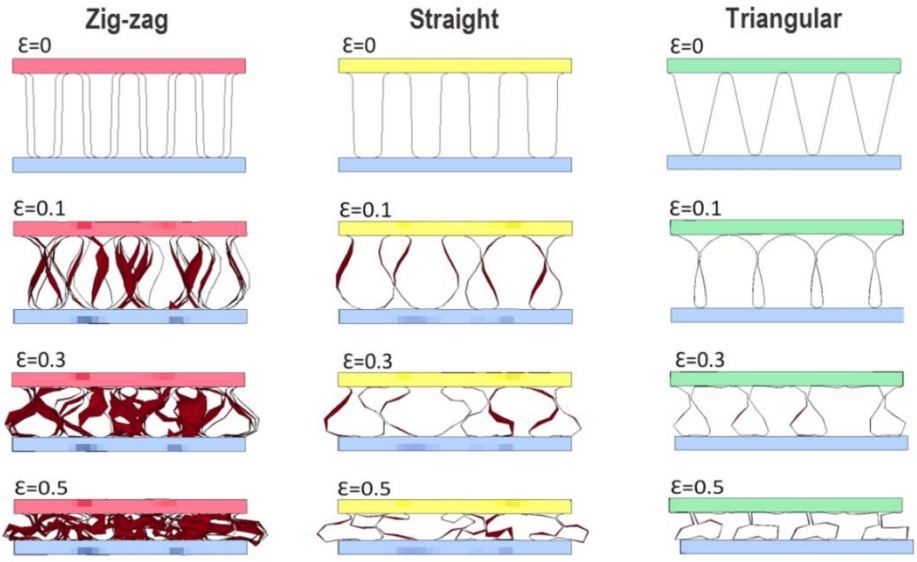

(b)

Figure 8.7. The numerical stress-strain curves and (b) deformation pictures of single- layer zig-zag, straight and triangular corrugated core sandwiches at the strain rate of 1500 s^{-1}.

When the strain rate increases to 3000 s^{-1}, the buckling stresses of the triangular and zig-zag and straight trapezoidal corrugated cores increase sequentially to 1.67, 1.61

and 1.57 MPa (Figure 8.8(a)). The unit fins of zig-zag and straight trapezoidal and triangular corrugated core deform much the same at 3000 s^{-1}, exhibiting peak stresses in the plateau region at 0.2 strains. The deformation at increasing strain rates proceeds with higher order buckling mode and the stabbing and the buckling of the fin wall occur (Figure 8.8(b)). It is noted in Figure 8.8(b) that the buckling length decreases when the strain rate increases to 3000 s^{-1}. The differences in both the initial loading and plateau regions between three corrugations get smaller at 3000 s^{-1} (Figure 8.8(a)). This is directly resulted from the similar deformation behavior of the core layers under dynamic loading; initial buckling and continual crushing of the fin walls (Figure 8.8(b)). The triangular form of the corrugation shows higher and earlier micro inertial effect than trapezoidal corrugated core.

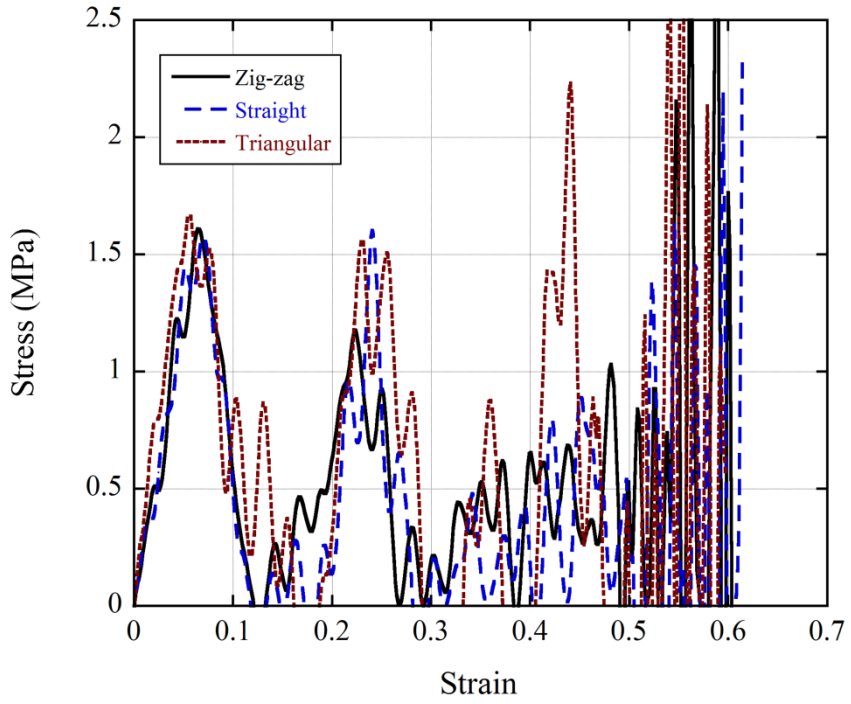

(a)

Figure 8.8. The numerical stress-strain curves and (b) deformation pictures of single- layer zig-zag, straight and triangular corrugated core sandwiches at 3000 s^{-1}.

(cont. on next page)

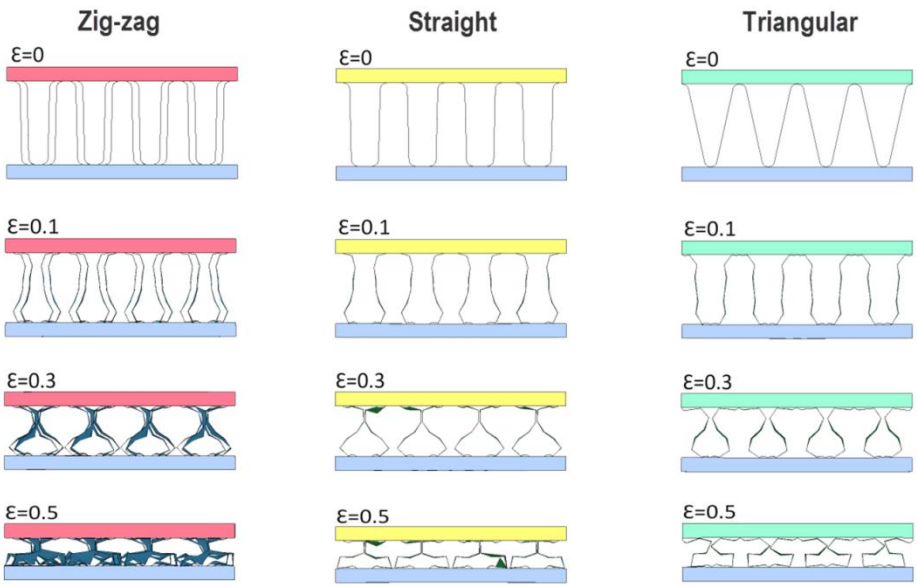

(b)

Figure 8.8 (cont.)

CHAPTER 9

QUASI-STATIC AND DYNAMIC COMPRESSION OF MULTI-LAYER CORRUGATED SANDWICHES

The stress-strain curves of single- and multi-layer specimens (50x50x70 mm) tested at 10^{-3} s^{-1} and the multi-layer specimens tested at 10^{-1} s^{-1} and 40 s^{-1} are shown in Figure 9.1 (a). The deformation sequence pictures of multi-layer sandwiches tested at 10^{-3} s^{-1} and 40 s^{-1} are further shown at various strain levels in Figures 9.1(b) and (c), respectively. The buckling stresses of three tests of single-layer specimens at 10^{-3} s^{-1} varied between 0.73 and 0.91 MPa. The bucking stress (initial peak stress) of the multi-layer samples tested at quasi-static strain rates vary between 0.45 and 0.6 MPa. Multi-layering; therefore, decreases the buckling stress below that of single-layer. The stress-strain behavior of the multi-layer samples tested at 40 s^{-1}; however, shows increased buckling stress (~0.75 MPa), while the post-buckling stress levels are very much similar with those of the quasi-statically tested multi-layer samples. The collapse begins with the buckling of the fin layer at one of the ends of the specimen accompanied by the interlayer sheet shearing (Figures 9.1(b) and (c)). The prescribed deformation mode is progressive until all layers collapse (0.7 strains). The densification strain is noted to increase from ~0.6 in single-layer to ~0.7 in multi-layer configuration. Since, there are seven corrugated layers; the seven peak stresses in the stress-strain curves will correspond to the collapse of individual layers. The missing peak stresses in the curves of Figure 9.1(a) are attributed to the collapse of two or more corrugated layers concurrently. As noted in Figure 7.12(a), after the densification strain of ~0.7, the deformation proceeds with the compression of folded layers and face sheets altogether, leading to abrupt increase in stress values. This deformation type is analogous to elastic-plastic metal foam deformation in the densification region [22].

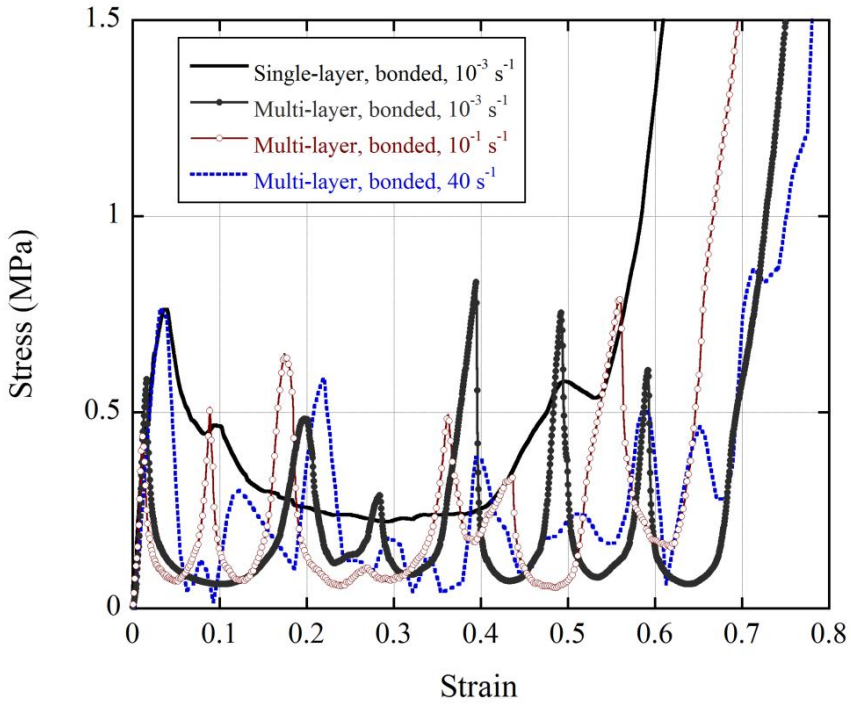

(a)

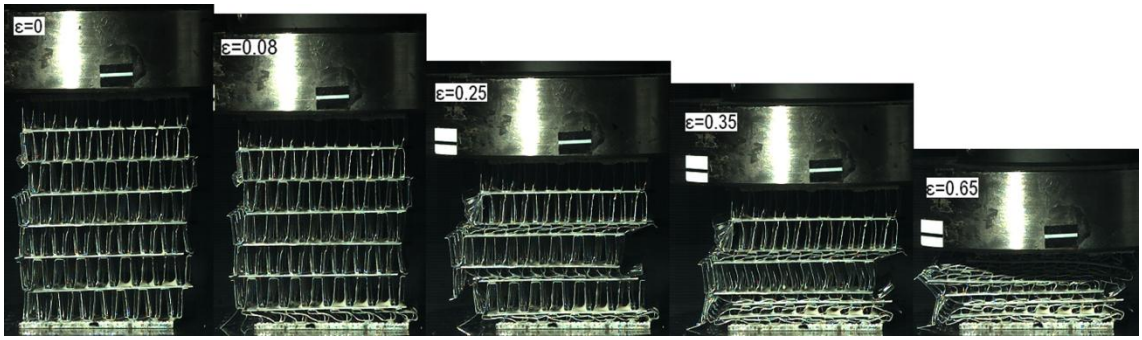

(b)

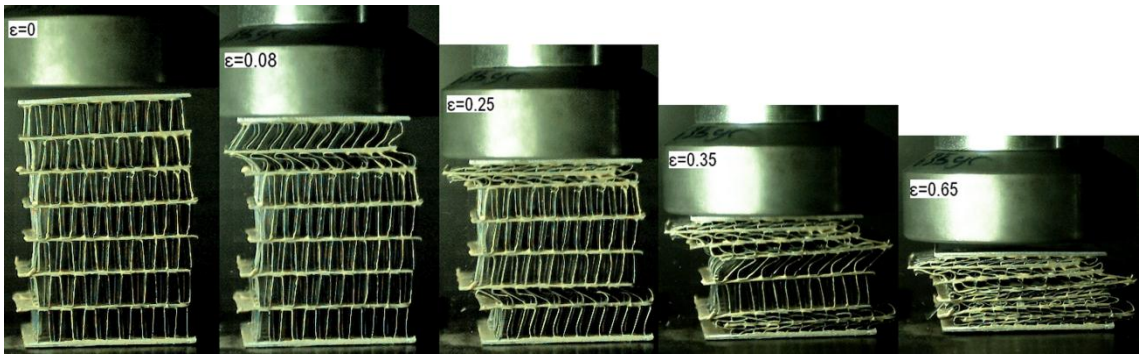

(c)

Figure 9.1. (a) Stress-strain curves of single- and multi-layer specimens tested at 10^{-3} s^{-1} and multi-layer specimens tested at 10^{-3}, 10^{-1} and 40 s^{-1} and the deformation steps of bonded multi-layer specimens at (b) 10^{-3} s^{-1} and (c) 40 s^{-1}.

The deformation modes of brazed corrugated multi-layer samples are pretty much similar with those of bonded samples, but the crushing stresses are 3-4 times lower at the same strain rates (Figure 9.2). As similar with the bonded samples, the brazed samples show an increased buckling stress (0.2 MPa) at 40 s^{-1} as compared with quasi-static test (0.16 MPa) as seen in Figure 9.2. A higher number of the occurrences of the concurrent collapse of corrugated layers were also observed in the brazed samples. This behavior is also reflected in the stress-strain curves of Figure 9.2 with the higher number of missing peak stresses.

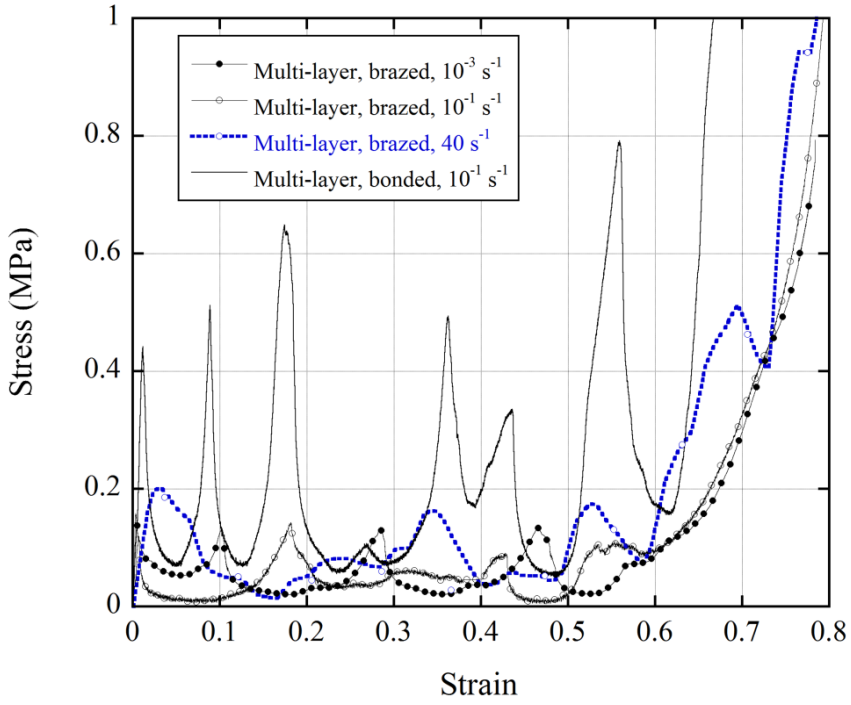

Figure 9.2. Stress-strain curves of bonded multi-layer specimens tested at 10^{-3} and 40 s^{-1} and brazed multi-layer specimens tested at 10^{-3}, 10^{-1} and 40 s^{-1}.

The experimental and simulation unconstraint and constraint tests stress-strain curves of bonded samples at 10^{-1} s^{-1} are shown in Figures 9.3(a) and (b), respectively. In the same figures, the corresponding average stresses are also drawn for comparison. The simulation unconstraint test yields higher crushing stresses than the experiment until about 0.2 strains; but the difference vanishes at increasing strain levels. The experimental buckling and average stresses for unconstraint tests are 0.45 and 0.16 MPa, respectively. Both the experimental and simulation deformation modes of unconstraint samples are very much similar, consisting of fin wall buckling and interlayer sheet shearing (the inset of Figure 9.3(a)). The sheared layers are squashed to

the sides of the sample after the deformation. Both, the simulation and experimental buckling and post bucking stresses increase in constraint tests as shown in Figure 9.3(b). The buckling and average stresses of constraint samples are 0.62 and 0.38 MPa, respectively. If one considers the post-buckling stress as the plateau stress, it may be concluded that the constraining reduces the differences between buckling and plateau stress. The deformation in constraint tests also proceeds more homogeneously: 7 peak stresses occur at the beginning of the buckling of each corrugated layer. The constraint specimen is noted to experience merely fin wall folding and shows no squash through sides (the inset of Figure 9.3(b)). It is concluded that the major effect of constraining occurs on the post-buckling stresses (average stress); while the buckling stress is less affected by constraining.

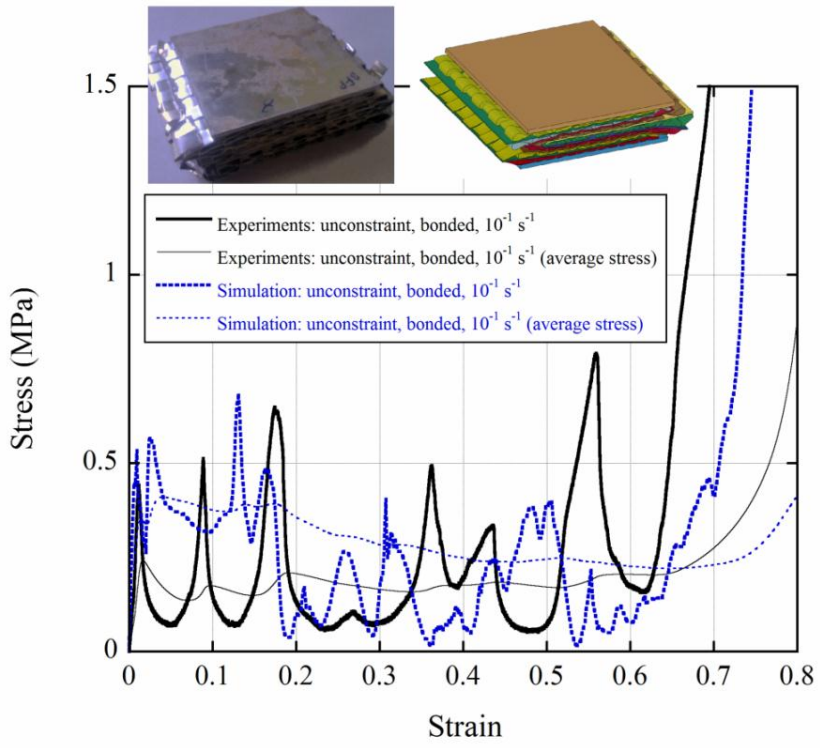

(a)

Figure 9.3. Simulation and experimental stress-strain curves and final deformed shapes of bonded multi-layer sandwiches tested at 10^{-1} s^{-1}: (a) unconstraint and (b) constraint tests.

(cont. on next page)

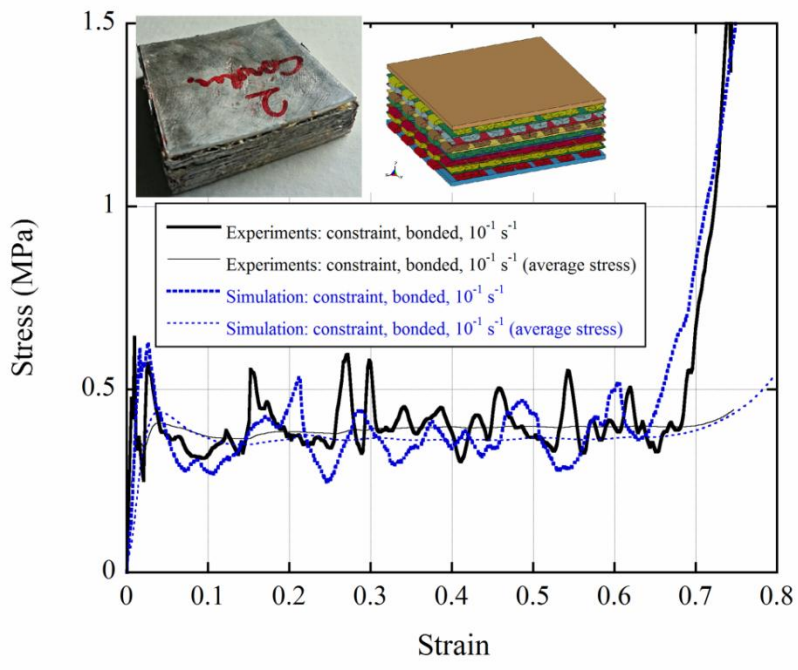

(b)

Figure 9.3 (cont.)

The compression experimental and simulation stress-strain curves of unconstraint bonded and brazed samples at 40 s^{-1} are shown together in Figure 9.4(a). The simulation buckling and post buckling stresses are very similar with the experimental buckling and post buckling stresses; while bonded samples show higher crushing stresses than brazed samples at 40 s^{-1}, as similar with the quasi-static loading. The numerical dynamic buckling stresses of bonded and brazed samples are sequentially 0.68 and 0.25 MPa and the corresponding experimental values are 0.75 and 0.2 MPa, respectively. The dynamic constraint tests stress-strain curves of bonded and brazed samples are shown in Figure 9.4(b). In the same figure, the quasi-static stress-strain curve of bonded samples is also shown for comparison. The constraint tests at dynamic strain rate show the similar buckling stresses with the unconstraint tests but again the post buckling stresses increase with constraining. The average crushing stress is ~0.38 MPa for bonded and ~0.18 MPa for brazed samples. It is also noted that increasing strain rate has no significant effect on the buckling and post buckling stresses of bonded constraint samples. The deformation sequences of the unconstraint test simulation and experiment show close resemblances as depicted in Figure 9.4(c) and proceed with fin wall buckling and interlayer sheet shearing.

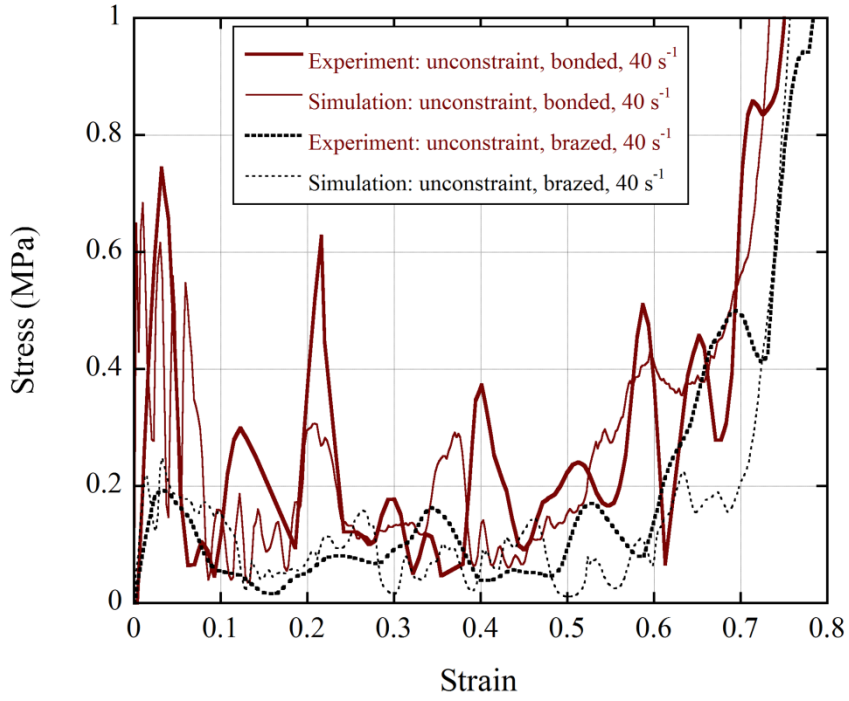

(a)

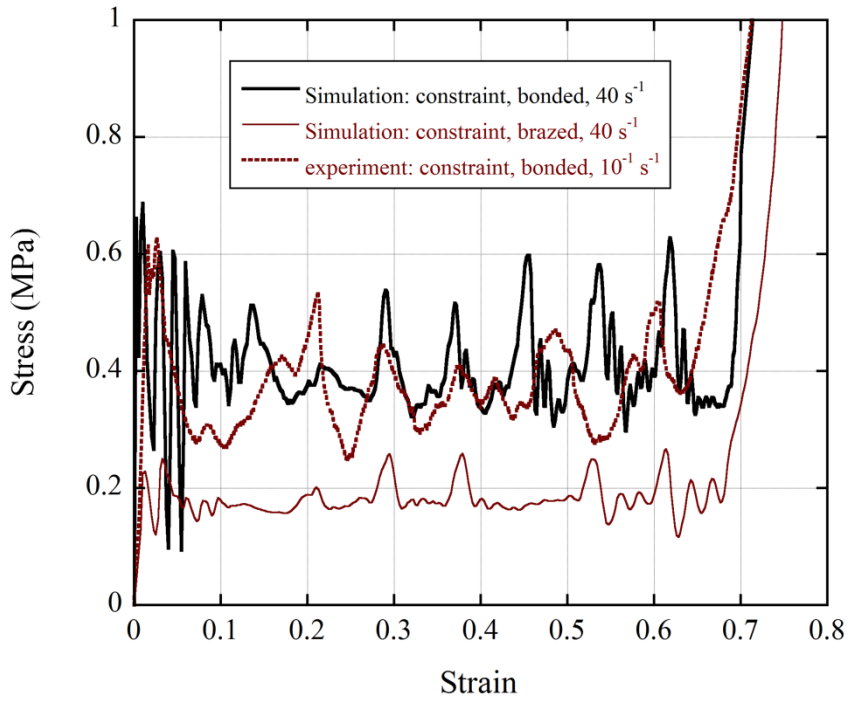

(b)

Figure 9.4. Simulation and experimental stress-strain curves of multi-layer sandwiches tested at 40 s^{-1}: (a) unconstraint and (b) constraint tests and (c) the experimental and simulation deformation pictures of bonded multi-layer samples.

(cont. on next page)

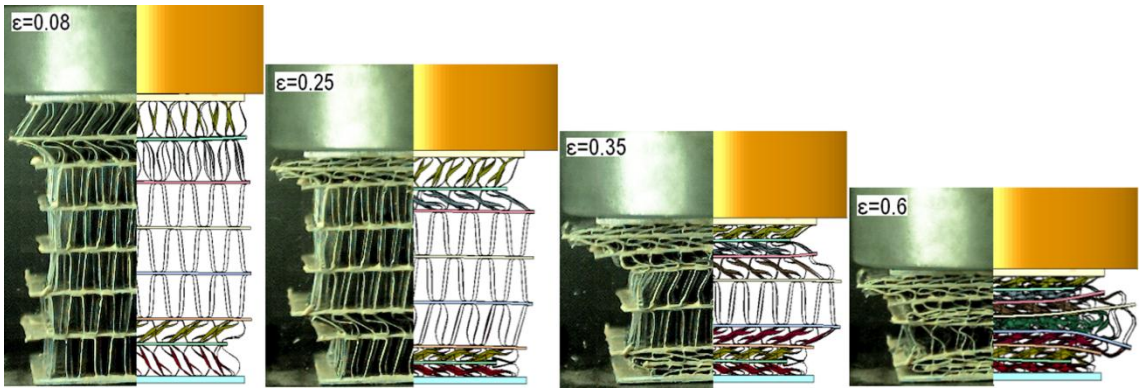

(c)

Figure 9.4 (cont.)

The effect of corrugation layer orientation (0°/0° and 0°/90°) on the stress-strain and average stress-strain curves of bonded multi-layer sandwich samples are shown in Figure 9.5. The samples with 0°/90° core orientation show higher buckling stress than the samples with 0°/0° core orientation. However, the core orientation has almost no effect on the average stress of bonded sandwich samples.

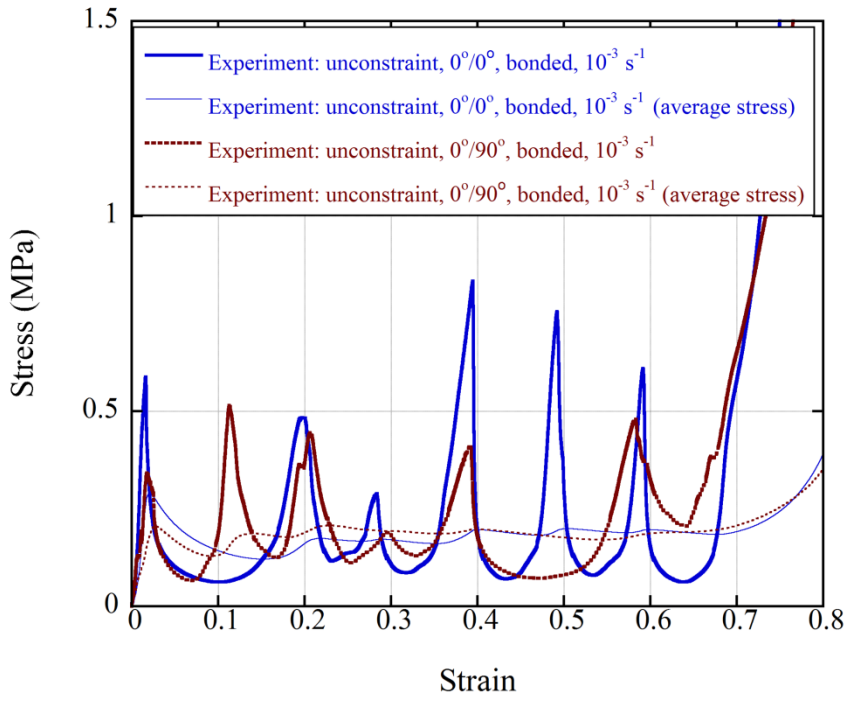

Figure 9.5. Stress-strain curves of 0°/0° and 0°/90° core oriented multi-layer specimens tested at 10^{-3} s^{-1}.

The experimental and simulation compression stress-strain curves and deformation pictures of bonded 0°/0° and 0°/90° core oriented multi-layer specimens

without interlayer sheets at 10^{-1} s^{-1} are shown in Figures 9.6(a) and (b), respectively. As seen in Figure 9.6(a), in the absence of interlayer sheets, the fins open laterally, leading to shearing type non-progressive localized deformation in 0°/0° core oriented sample. This naturally decreases the post buckling stress values. The simulation buckling stress increases significantly at 40 s^{-1}, showing a high strain rate sensitive buckling stress; while, the post buckling stress levels are not affected with increasing strain rate. The presence of interlayer sheets in 0°/0° core oriented sample is noted to induce more stable and progressive collapse of the core layers. A completely different deformation mode is detected in 0°/90° core oriented multi-layer specimens, depicted in Figure 9.6(b). In this orientation, the deformation is localized in individual core layers, which is very a similar deformation mode with that of multi-layer samples with interlayer sheets. A progressive deformation mode is clearly seen both in experiments and numerical simulations (Figure 9.6(b)). Therefore, the stress values of 0°/90° core oriented multi-layer specimens are higher than those of 0°/0° core oriented multi-layer specimens without interlayer sheets. The simulation buckling stress at 40 s^{-1} and 10^{-1} s^{-1} are very much similar, showing insignificant strain rate effect on the buckling stress in this direction.

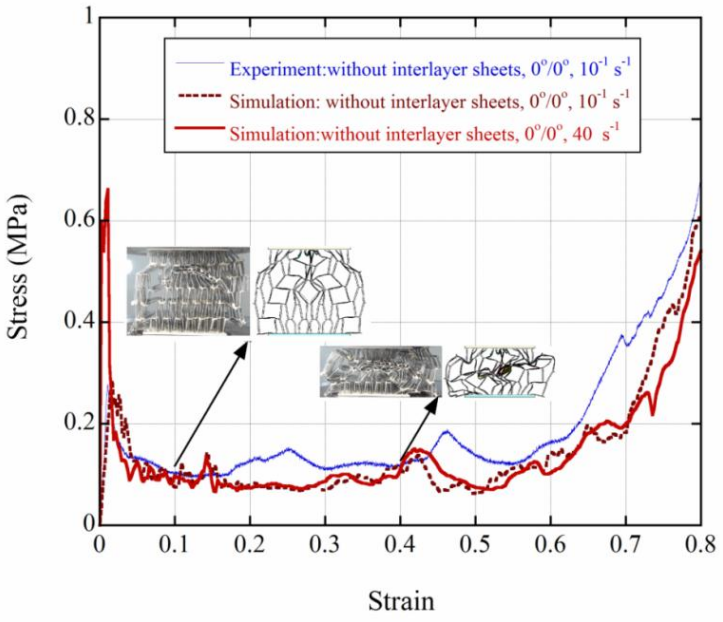

(a)

Figure 9.6. The experimental and simulation stress-strain curves of (a) 0°/0° and (b) 0°/90° core orientated sandwiches without interlayer sheets.

(cont. on next page)

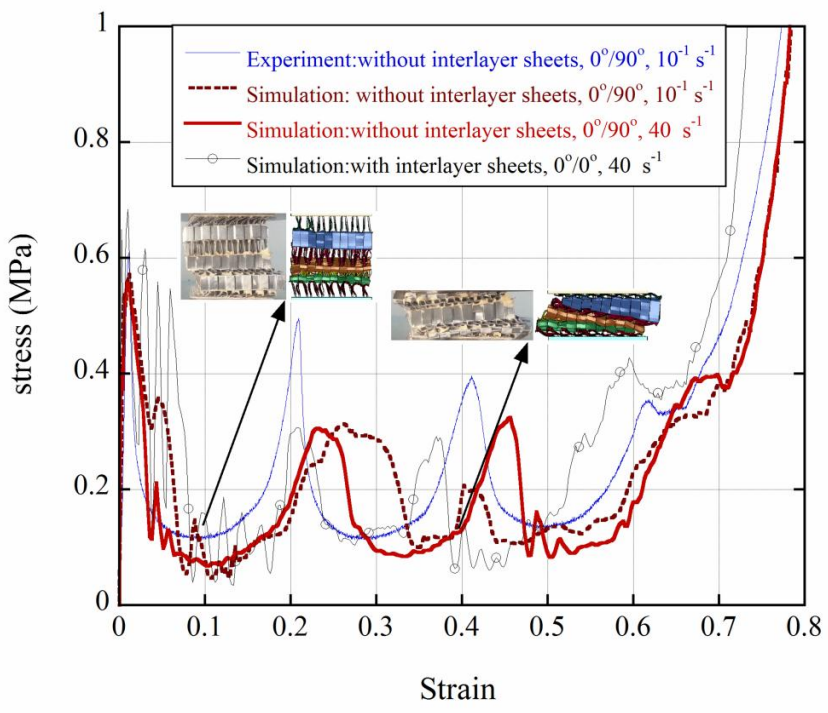

(b)

Figure 9.6 (cont.)

The use of interlayer sheets is advantageous when the separation of corrugated layers is required or perquisite. The presence of interlayer sheets, which induces more homogenous and progressive deformation of the individual layers, increases the indentation resistance in the expense of reduced specific energy absorption as depicted in Figure 9.7. The preference of interlayer sheets is certainly dependent on the type of application. In the applications involving localized type of impact, the presence of interlayer sheets certainly increases the perforation resistance. The corrugated structures without interlayer sheets become advantageous when the impact pulse is distributed over a relatively larger area.

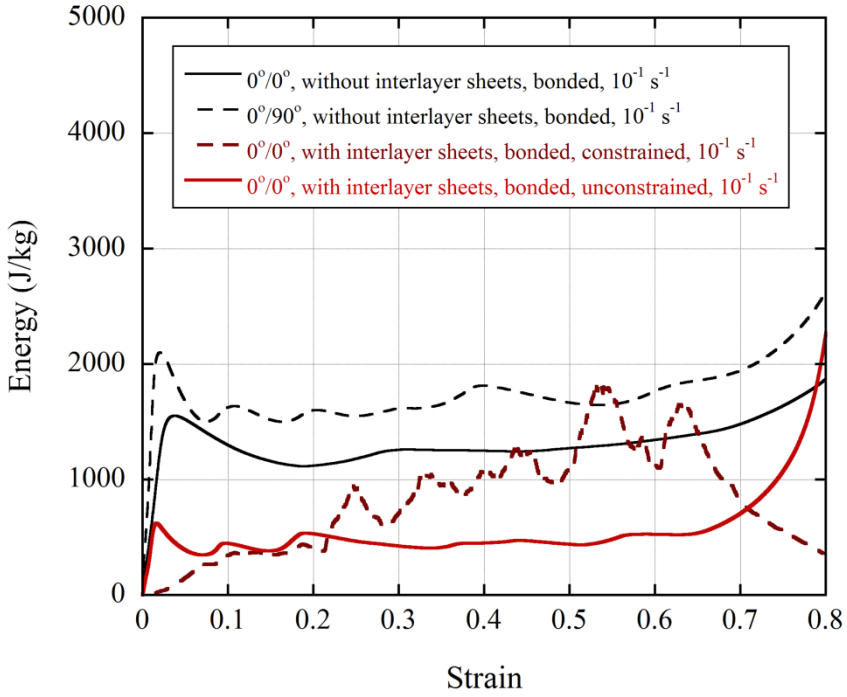

Figure 9.7. Energy absorption vs. strain curves of multi-layer samples with and without interlayer sheet layers.

CHAPTER 10

INDENTATION OF MULTI-LAYER CORRUGATED SANDWICHES

The isometric and back face pictures of brazed samples with 3003 alloy face sheets tested at 3 and 6 m s^{-1} using spherical striker tip are sequentially shown in Figures 10.1(a-d), respectively. The corrugated core and face sheets are seen to be excessively deformed; the fin layers are heavily crushed and the interlayer sheets are bent particularly at the striker impact zone. The main failure mechanism of corrugated layer is the fin wall bending/folding as seen in Figures 10.1(a) and (c). It is also noted that a chequered surface is formed at the front face sheet due to localized plastic deformation. This effect is much more evident in the panels tested at 6 m s^{-1} (Figure 10.1(c)). The back face deflections are 3 and 9 mm at 3 and 6 m s^{-1} impact velocities, respectively.

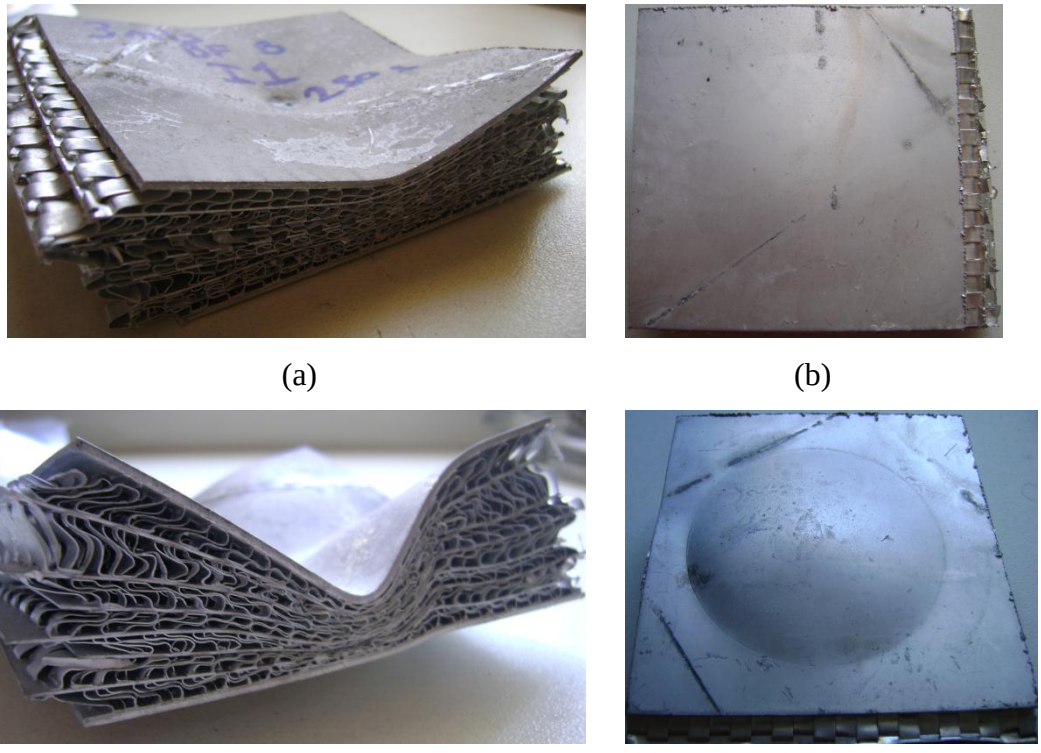

(a) (b)

(c) (d)

Figure 10.1. (a) The isometric and (b) back face sheet pictures of brazed sandwich panels tested at 3 m s^{-1} and (c) the isometric and (d) back face sheet pictures of brazed sandwich panels tested at 6 m s^{-1}.

The isometric and back face pictures of adhesively bonded panels with 3003 alloy face sheets tested at 3 and 6 m s^{-1} are sequentially shown in Figures 10.2(a-d), respectively. The progressive deformation of the panel tested at 3 m s^{-1} is seen in Figure 10.2(a); the first 4-5 fin layers are crushed via fin wall bending. The same deformation mechanism of fin wall bending is also observed in the panels tested at 6 m s^{-1} (Figure 10.2(c)). No back face deflection is detected in the samples test at 3 m s^{-1} (Figure 10.2(b)), while the back face deflection at 6 m s^{-1} is about 3 mm (Figure 10.2(d)), which is less than that of brazed panels tested at the same impact velocity.

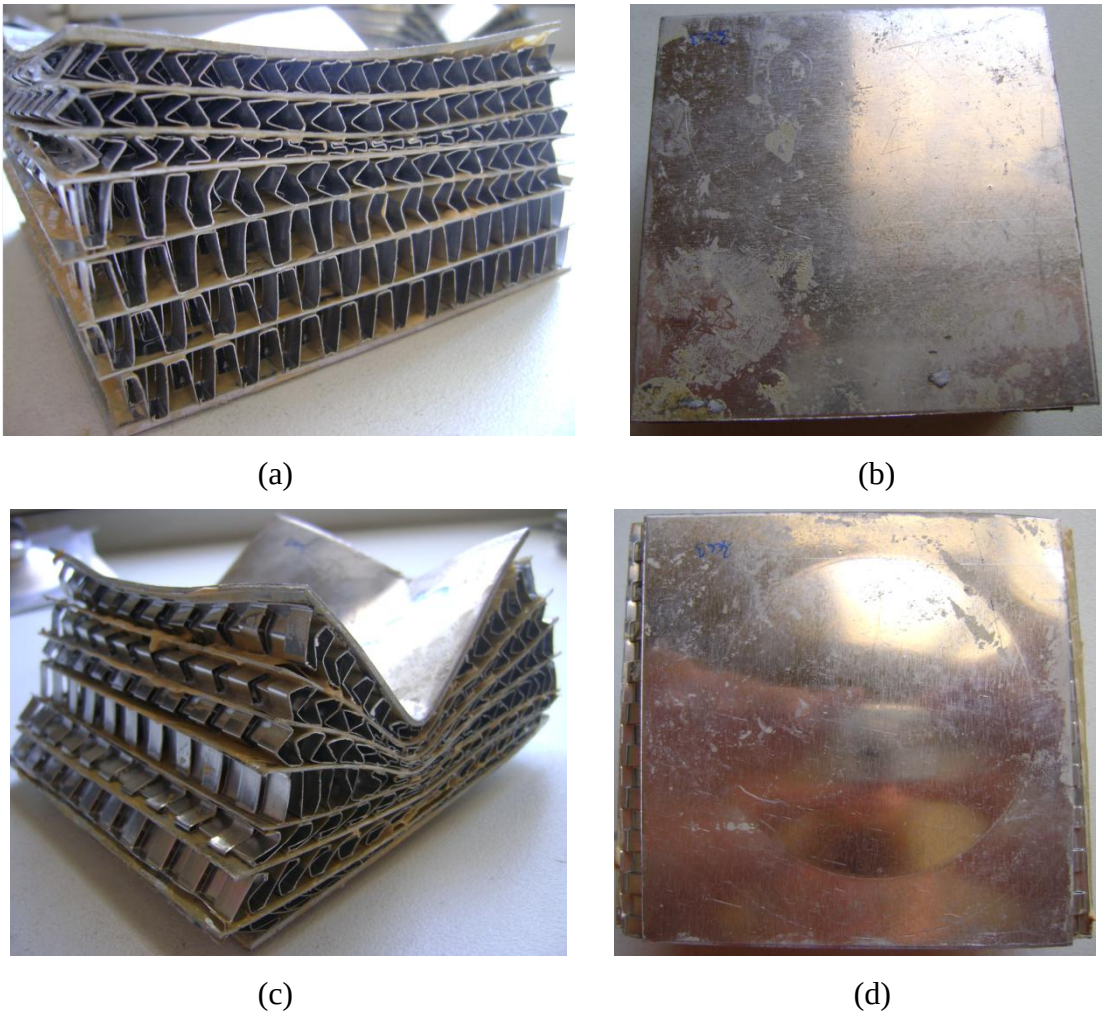

(a) (b)

(c) (d)

Figure 10.2. (a) The isometric and (a) back face sheet pictures of adhesively bonded sandwich panels tested at 3 m $s^{-1}$and (c) the isometric and (d) back face sheet pictures of adhesively bonded sandwich panels tested at 6 m s^{-1}.

The force-displacement and energy-displacement curves of brazed and adhesively bonded panels tested at 3 and 6 m s^{-1} are shown in Figures 10.3(a) and (b), respectively. Load instabilities are detected after the initial peak load in the plateau

region (Figure 10.3(a)). These post-buckling load fluctuations are due to the bending/buckling of the fin layers. Load instabilities were also detected in the corrugated and pyramidal cores under axial compressive loads [51, 54 , 61, 69, 104]. Bonded panels exhibit about two times higher deformation forces than brazed panels at both impact velocities as depicted in Figure 10.3(a). The deformation of the corrugated layers in both panels is progressive fin wall buckling, starting from the impact zone. At large displacements, the deformation proceeds with the compression of folded layers and bent interlayer and face sheets altogether, leading to increased force values. This deformation type is analogous to the ductile metal foam deformation in the densification region [105, 106]. The progressive core layer deformation was also reported in a multilayered pyramidal lattice structure with interlayer sheets under axial compressive loading [69]. The layer wise deformation continued until all layers were completely compacted. It is also seen that bonded panels absorb more energy than brazed panels (Figure 10.3(b)). This is because of the lower flow stresses of aluminum alloys in the brazed sandwich panels. With the applied heat treatment, the flow stress of 1050 H14 alloy is reduced from 150 MPa to 68 MPa at 0.2 strain (Figures 7.1(a) and (b)). The use of low strength core however comes with several advantages in the applications involving impact and blast loading. Low strength core in sandwich plates distributes the load more efficiently, reducing the strain concentration near the point of the impact [48]. It also reduces the forces transmitted to back surface, providing more effective protections for the structures [71, 107]. In accord with this, it is noted that low strength brazed panels (Figures 10.1(a) and (c)) spread the deformation to a larger area compared to high strength bonded panels (Figures 10.2(a) and (c)).

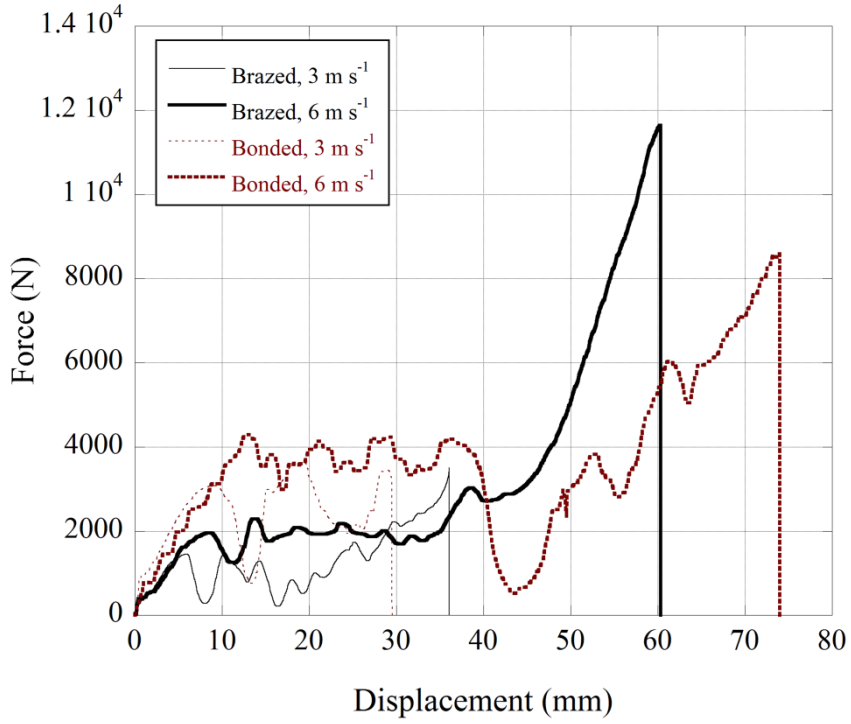

(a)

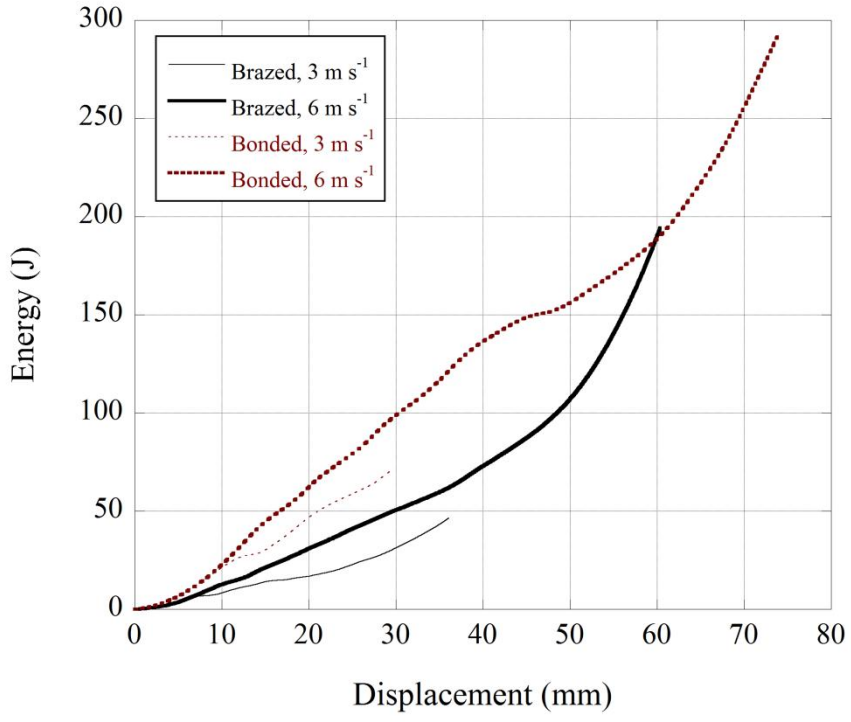

(b)

Figure 10.3. (a) Force-displacement and (b) energy-displacement history of brazed and adhesively bonded panels tested at 3 and 6 m s^{-1}.

Figures 10.4(a) and (b) show the experimental and numerical (fine and coarse mesh) force-displacement and energy-displacement curves of 0°/0° fin layer orientated

panels tested at 6 m s^{-1} using spherical striker tip. The experimental force and energy absorption values are well approximated using a fine mesh model than a coarse mesh model, because the coarse mesh model cannot capture the experimental force values above 30 mm displacements. The experimental back face deflection (3.2 mm) is also well approximated using a fine mesh model (3.5 mm), while numerical model with coarse mesh gives a back face deflection of 2 mm. Therefore, further simulation studies were continued using fine mesh model.

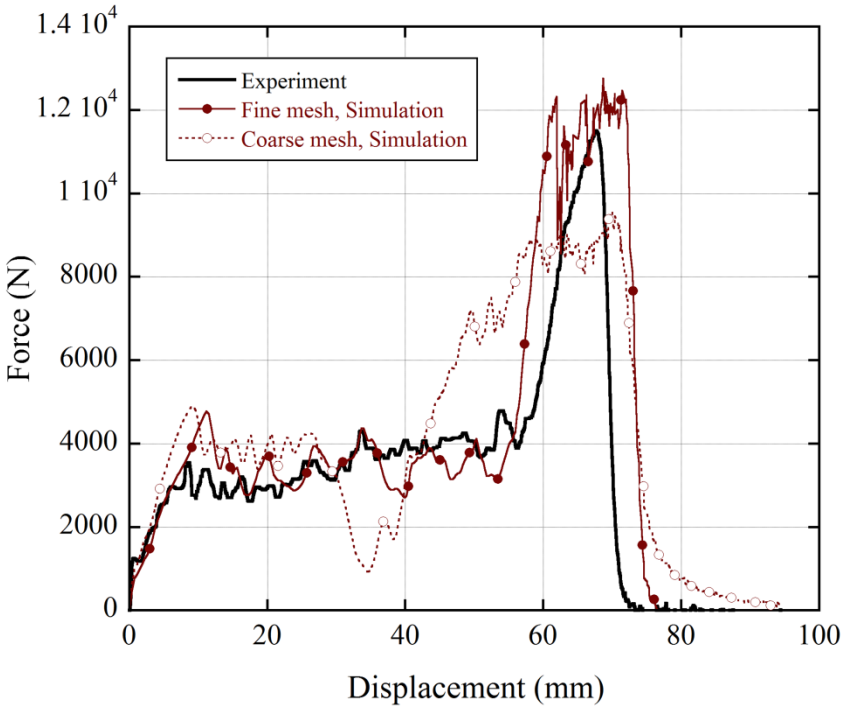

(a)

Figure 10.4. Simulation and experimental (a) force-displacement and (b) energy- displacement curves of 0°/0° adhesively bonded panels tested at 6 m s^{-1}.

(cont. on next page)

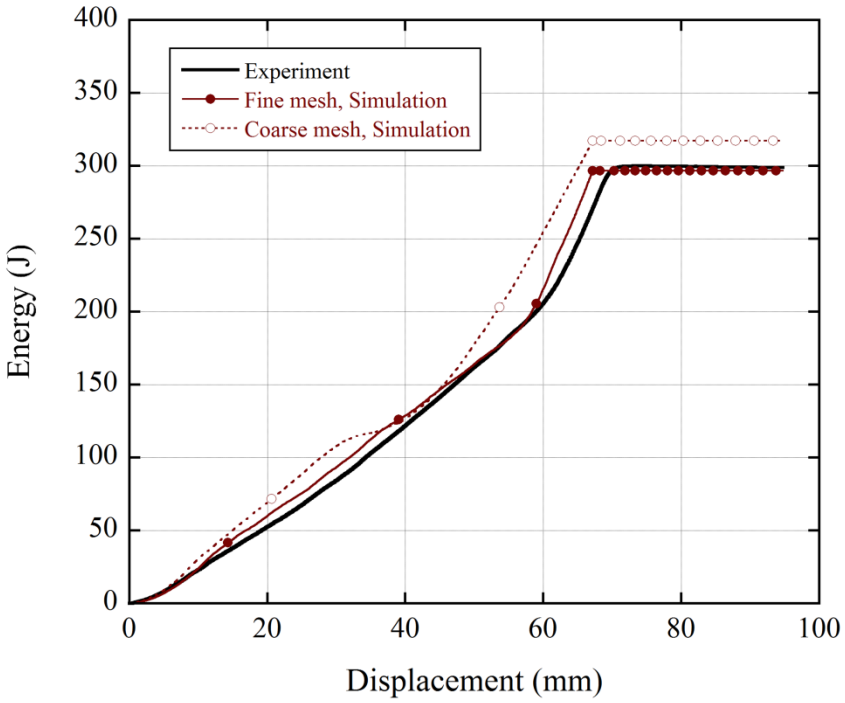

(b)

Figure 10.4 (cont.)

Typical experimental force-displacement curve of 0°/0° and 0°/90° and numerical force-displacement curve of 0°/0° fin layer orientated panels tested at 6 m s^{-1} using spherical striker tip are shown in Figure 10.5(a). It is noted in the same figure that 0°/90° fin layer orientated panel experiences higher loads than 0°/0° fin layer orientated panel at the large extent of deformation. The numerical model load-displacement curve is noted to well agree with the experimental curve in terms of crushing load values and force-displacement curve trends, showing the validity of used material models. The pictures of 0°/90° and 0°/0° fin layer orientated panels tested using spherical tip are sequentially shown in Figures 10.5(b) and (c). The final deformation shapes of the panels are very much similar in both orientations, but a higher lateral compression of the specimen is seen in 0°/90° fin layer orientated panels. The striker tip excessively deforms the face sheets at the contact region without penetration into interior layers. The experimentally measured back face deflection of 0°/90° fin layer oriented panel is 2 mm, which less than that of 0°/0° fin layer oriented panel (3.2 mm). The corresponding numerical model final deformed shape of 0°/0° fin layer orientated panel is shown in Figure 10.5(d) for comparison. The experimental and model final deformed final shapes of the panels are broadly similar. In the striker tip contact region, the ductile

deformation and cracking of the face sheet are observed experimentally; however, the elements in the numerical model in the same region are deleted as the plastic strain criterion is reached; therefore, the layer under the face sheet is seen in numerical model in Figure 10.5(d).

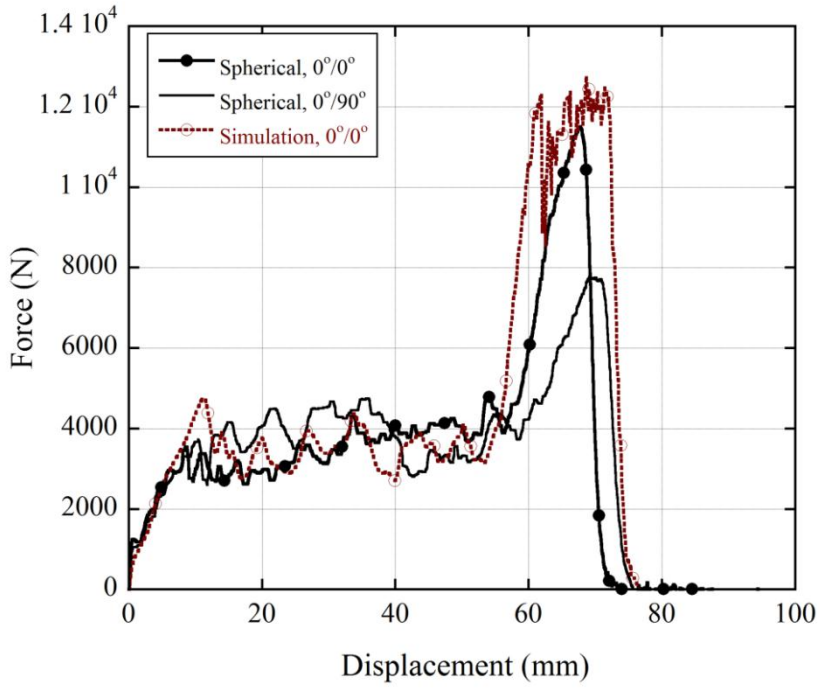

(a)

(b)

(c)

Figure 10.5. (a) Typical experimental force-displacements curves of 0°/0° and 0°/90° oriented panels and simulation force-displacement curve of 0°/90° oriented panel; the pictures of tested (b) 0°/90° and (c) 0°/0° oriented panels and (d) the simulation picture of tested 0°/0° oriented panel (spherical striker tip, the impact velocity is 6 m s-1).

(cont. on next page)

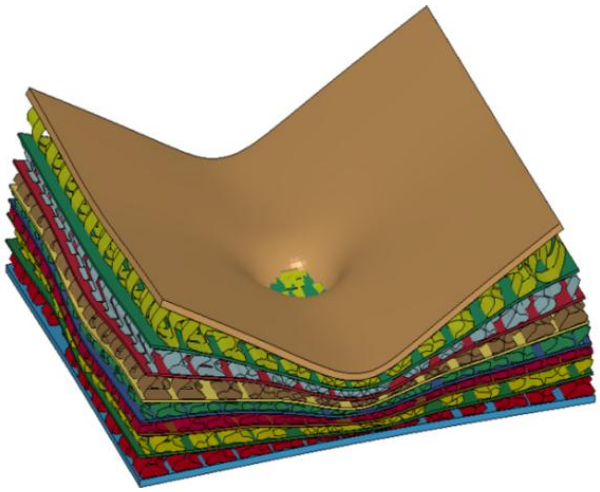

(d)

Figure 10.5 (cont.)

In accord with the experiments, the fin buckling/folding of the corrugated layers and bending of the face and interlayer sheets are the main deformation mechanisms for the numerically tested panels. The fin folding is also noted to be progressive; when the panel is initially loaded by the striker, the fins in the first layer start to buckle (Figures 10.6(a-c)) and with the completion of the fin folding of the first layer, the fins in the next layer start to buckle with the bending of the face sheet (Figure 10.6(d)).

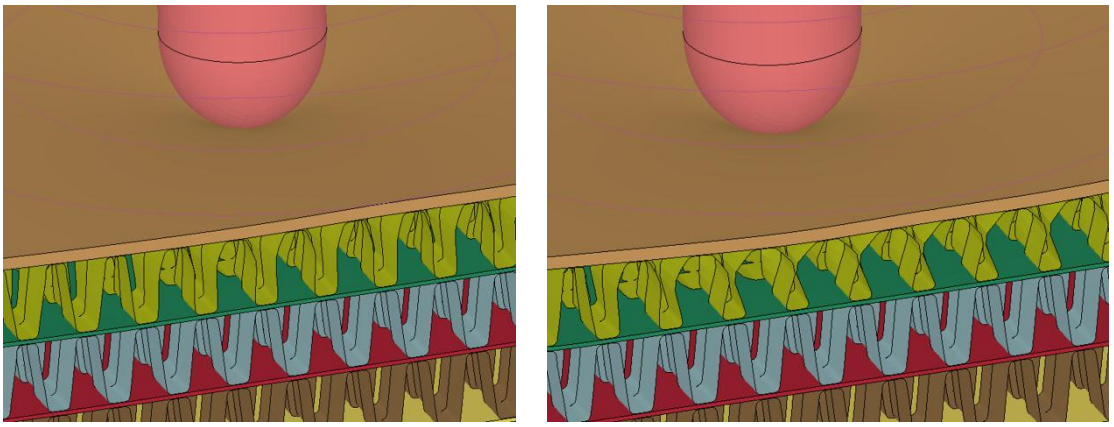

(a) (b)

Figure 10.6. The model deformation pictures of the impact-side first few core layers of $0^o/0^o$ oriented bonded panel tested at 6 m s^{-1} using spherical striker tip: (a) t=0.0015, (b) t=0.00174, (c) t=0.021 and (d) t=0.024 s.

(cont. on next page)

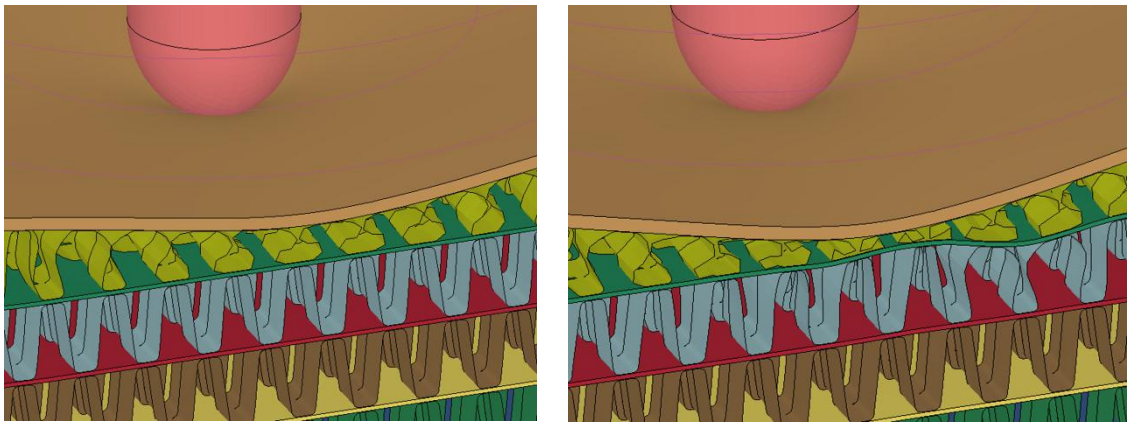

(c) (d)

Figure 10.6 (cont.)

Typical experimental force-displacement curve of 0°/0° and 0°/90° and numerical force-displacement curve of 0°/0° fin layer orientated panels tested at 6 m s^{-1} using flat striker tip are shown in Figure 10.7(a). Again, 0°/90° fin layer orientated panel experiences higher crushing loads than 0°/0° fin layer orientated panel. The numerical model loads also well approximate the experimental loads in 0°/0° fin layer orientation, except the loads in the densification region. The pictures of 0°/90° and 0°/0° fin layer orientated panels tested with flat striker tip are sequentially shown in Figures 10.7(b) and (c). As noted in Figures 10.7(b) and (c), the final deformation shapes and displacements of the panels are similar in both orientations. Similar with spherical indenter tip, flat intender tip deforms excessively the face sheets without penetration and induces a higher lateral deformation in 0°/90° fin layer orientated panels. The experimental back face deflections are 2 mm for 0°/0° and 1 mm for 0°/90° fin layer orientation. The back face deflections are noted to be smaller than those of the panels tested using spherical striker tip. The numerical model final deformed shape of a 0°/0° fin layer orientated panel shown in Figure 10.7(d) simulates well the experimental deformed shape.

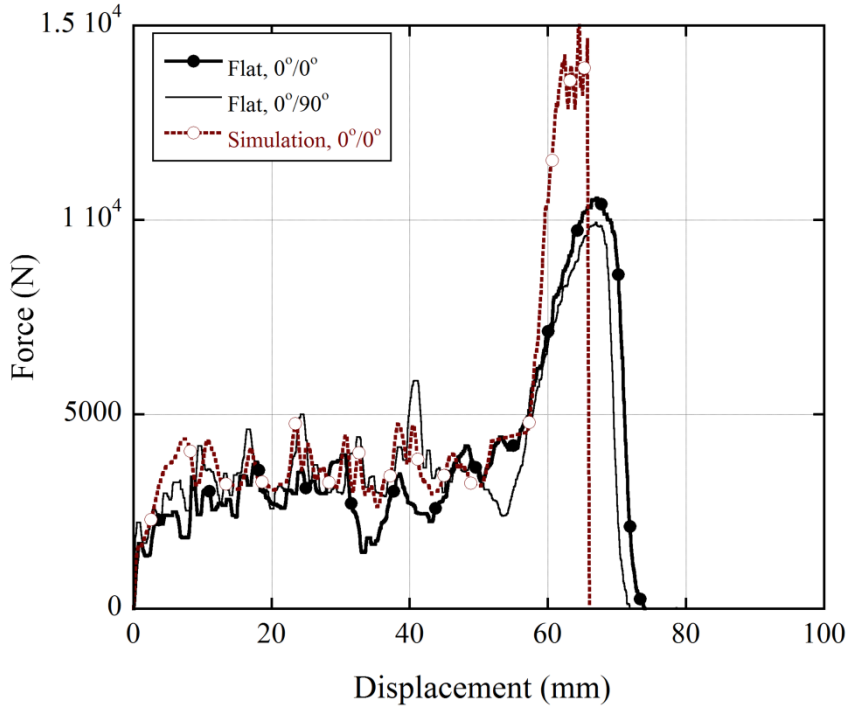

(a)

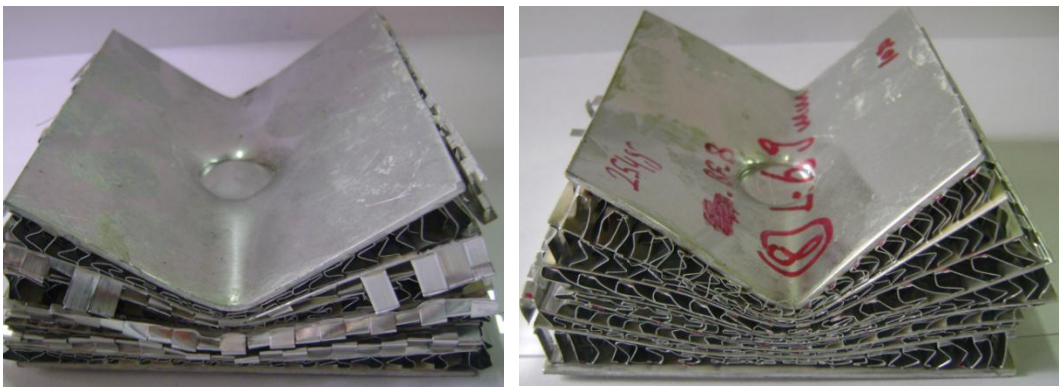

(b) (c)

Figure 10.7. (a) Typical experimental force-displacements curves of 0°/0° and 0°/90° oriented panels and simulation force-displacement curve of 0°/90° oriented panel; the pictures of tested (b) 0°/90° and (c) 0°/0° oriented panels and (d) the simulation picture of tested 0°/0° oriented panel (flat striker tip, the impact velocity is 6 m s-1).

(cont. on next page)

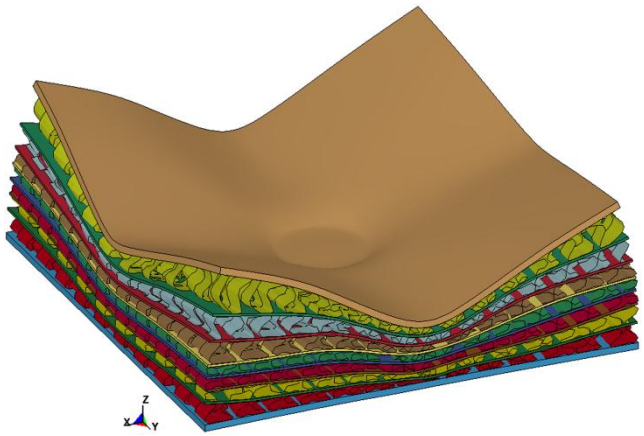

(d)

Figure 10.7 (cont.)

Typical experimental force-displacement curve of 0°/0° and 0°/90° and numerical force-displacement curve of 0°/0° fin layer orientated panels tested at 6 m s^{-1} using conical striker tip are shown in Figure 10.8(a).The corresponding pictures of the tested 0°/90° and 0°/0° fin layer orientated panels using conical striker tip are sequentially shown in Figures 10.8(b) and (c). The conical striker tip partially penetrates through inter layers of 0°/0° fin layer oriented panel (Figures 10.8(c)), while it perforates 0°/90° fin layer oriented panel (Figure 10.8 (b)). No back face deflection is observed in 0°/0° fin layer oriented panel, while the back face deflection of perforated 0°/90° panel is 5 mm. The panel force-displacement responses to conical striker tip are also quite different from those to spherical and flat striker tips. The force exerted by the conical tip in both 0°/0° and 0°/90° fin layer orientated panels increases linearly until about 40 mm (Figure 10.8(a)), as the striker tip penetrates the panel. Above 40 mm displacement, 0°/90° fin layer orientated panel force level decreases due to the delamination of the panel layers. The numerical force values and final deformed shape (Figure 10.8(d)) show close similarities with experimental force values and deformation shape. While, a departure from experimental force values are seen in the force-displacement curve of the model after 70 mm displacement (Figure 10.8 (a)). This result is likely due to small differences in the tip radius of conical striker between model and experiment.

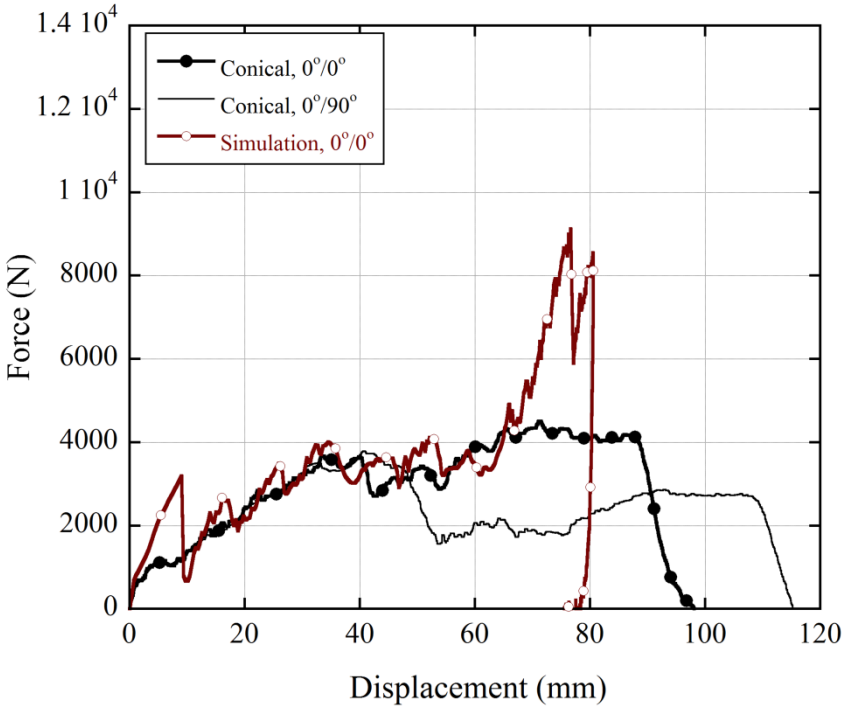

(a)

(b)

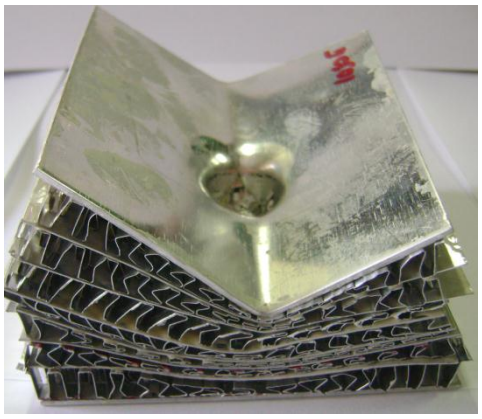

(c)

Figure 10.8. (a) Typical experimental force-displacements curves of 0°/0° and 0°/90° oriented panels and simulation force-displacement curve of 0°/90° oriented panel; the pictures of tested (b) 0°/90° and (c) 0°/0° oriented panels and (d) the simulation picture of tested 0°/0° oriented panel (conical striker tip, the impact velocity is 6 m s-1).

(cont. on next page)

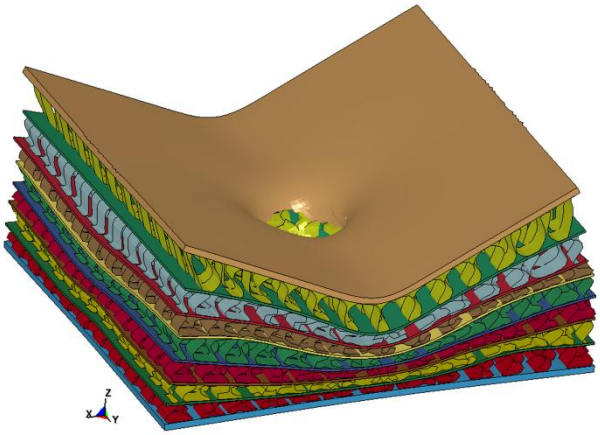

(d)

Figure 10.8 (cont.)

The energy absorbing capacities of the panels as function of displacement are shown in Figure 10.9. The energy absorption of the panels tested using conical striker tip is comparably smaller especially in 0°/90° fin layer orientation (Figure 10.9). The energy absorptions of the panels tested using flat striker tip are further higher than those of the panels tested using spherical striker tip. The panels show higher energy absorption in 0°/90° fin layer orientation than 0°/0° fin layer orientation. As stated earlier, 0°/90° fin layer orientated panels distribute the load laterally more evenly when tested with spherical and flat striker tips. This also proves a higher potentials 0°/90° fin layer orientation in distributing the incident impact laterally; hence improving energy absorption capacity of the tested panels.

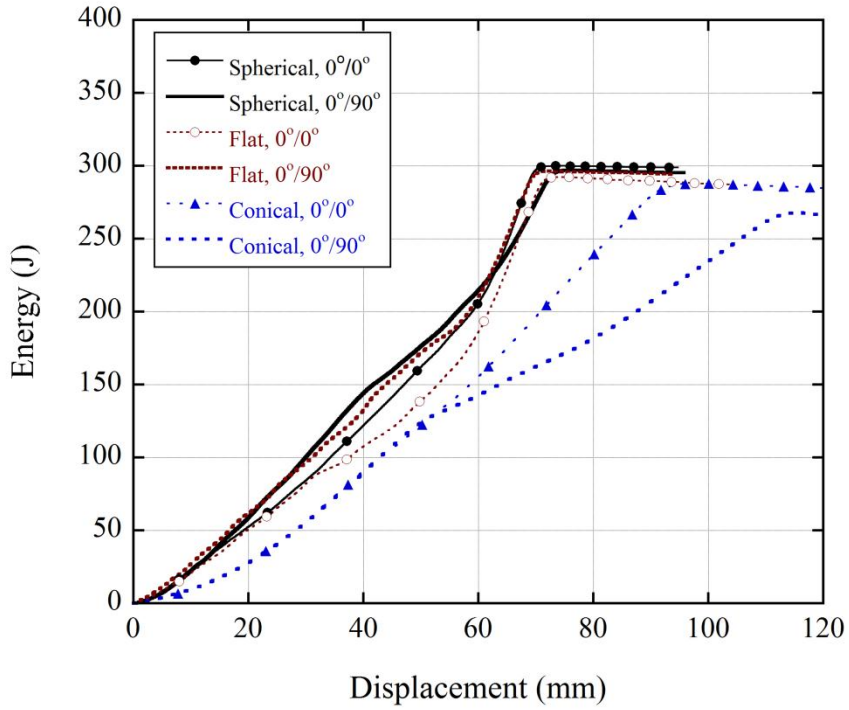

Figure 10.9. Energy-displacement history of 0°/0° and 0°/90° oriented panels tested with spherical, flat and conical striker tips at 6 m s^{-1}.

Typical force-displacement curves of dynamic (6 m s^{-1}) and quasi-static ($7x10^{-5}$ m s^{-1}) indentation tests using spherical striker tip and indenter are shown in Figure 10.10(a). The panel tested dynamically experiences about 1.4 times higher impact loads than quasi-statically tested panel. The effect of drop weight tower impact velocity on the numerical force displacement curve of $0^o/0^o$ fin layer orientated panel is shown in Figure 10.10(b). As the velocity increases the deformation force values increase; the increase being higher in the region of initial peak load of the curve; although, a rate insensitive material model is used in the simulations.

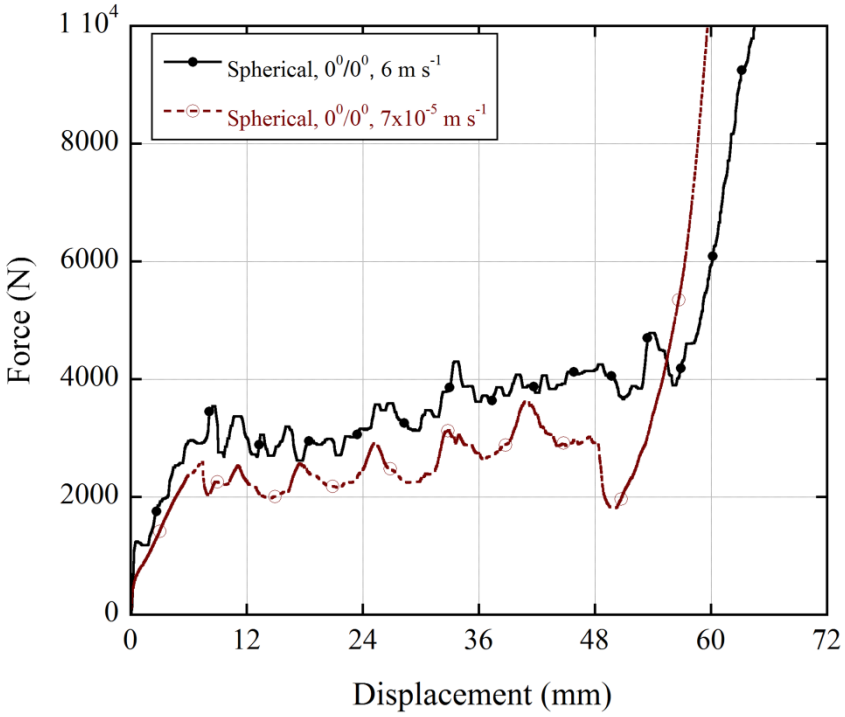

(a)

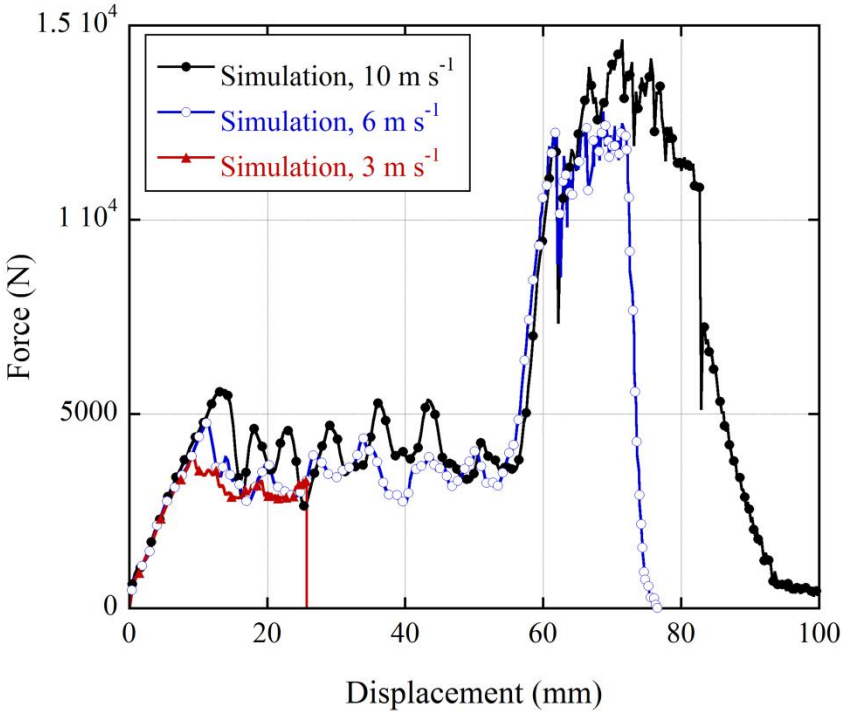

(b)

Figure 10.10. (a) Quasi-static and dynamic force-displacement curves of 0°/0° oriented bonded panels and (b) simulation force displacement curves of 0°/0° oriented bonded panels tested at 3, 6 and 10 m s^{-1}

.

CHAPTER 11

NUMERICAL HOMOGENIZATION OF MULTI-LAYER CORRUGATED SANDWICHES

Figures 11.1(a-c) show the test and simulation compression stress-strain curves of the single core layer tested in the x-, y- and z-axis at 10^{-1} s^{-1}, respectively. The corresponding simulation undeformed and deformed (ε =0.2 and 0.4) and experimental deformed (ε =0.2 and 0.4) test specimen pictures of the single core layer tested in the x-, y- and z-axis are shown in Figures 11.2(a-c), respectively. The single core layer tested in the x-axis deforms elastically under relatively low stresses until about 0.6 strains (Figure 11.1(a)). The deformation proceeds with the compression of horizontal fin walls as similar with the elastic compression of an accordion. Above 0.6 strains, the fin wall flat sections however bend both experimentally and numerically over each other under almost a constant stress, 0.2-0.3 MPa (Figure 11.1(a) and Figure 11.2(a)). At the strains above 0.95, the bent fin walls overlap over each other, resulting in abrupt increase in stress values. The full model simulation stresses are however slightly higher than the experimental stresses as depicted in Figure 11.1(a). The single core layer tested in the y- and z-axis deform both numerically and experimentally through fin wall buckling (Figures 11.2(b) and (c)), exhibiting Type II structure deformation behavior, a classification made by Calladine and English for the inertia sensitive structures [76]. In Type II structure, following the initial peak force, the crushing forces decline gradually as the displacement increases. This is also valid for the single core layer specimen tested in the y- and z-axis (Figures 11.1(b) and (c)). The simulation and experimental initial peak stresses in the y- and z-axis are 0.84 MPa and 0.7 MPa and 0.94 MPa and 0.54 MPa, respectively (Figures 11.1(b) and (c)). Although, simulation and experimental stress-strain curves in the y- and z-axis differ from each other in stress values, the trends of the simulation and experimental stress-strain curves are nearly the same as seen in Figures 11.1(b) and (c). The differences between the simulation and experimental stresses may arise from several factors. The imperfections on the fin walls tend to decrease the experimental crushing stresses. The imperfection sensitivity (bending type imperfection) was previously detected in a diamond lattice core at the quasi-static strain

rates [54]. The misalignment of test specimen during testing expectedly affects the experimental stresses. Nevertheless, the effect of above artifacts of the single core layer are included in the simulation of the multi-layer sandwich test specimens by developing MAT-26 material model based on the single fin layer experimental stress-strain curves. The elastic moduli in the y- and z-axis are measured as 133.8 MPa and 34.35 MPa, respectively, showing highly anisotropic behavior of the tested single core layer.

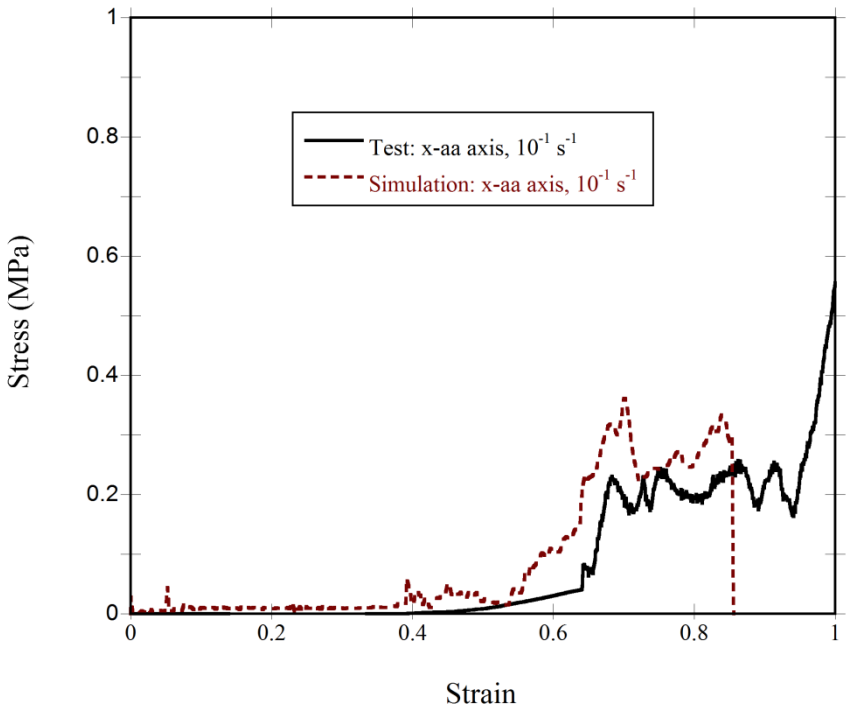

(a)

Figure 11.1. The experimental and simulation compression strain-stress curves of the single core layer at 10^{-1} s^{-1} in (a) x-aa, (b) y-bb and (c) z-cc axis.

(cont. on next page)

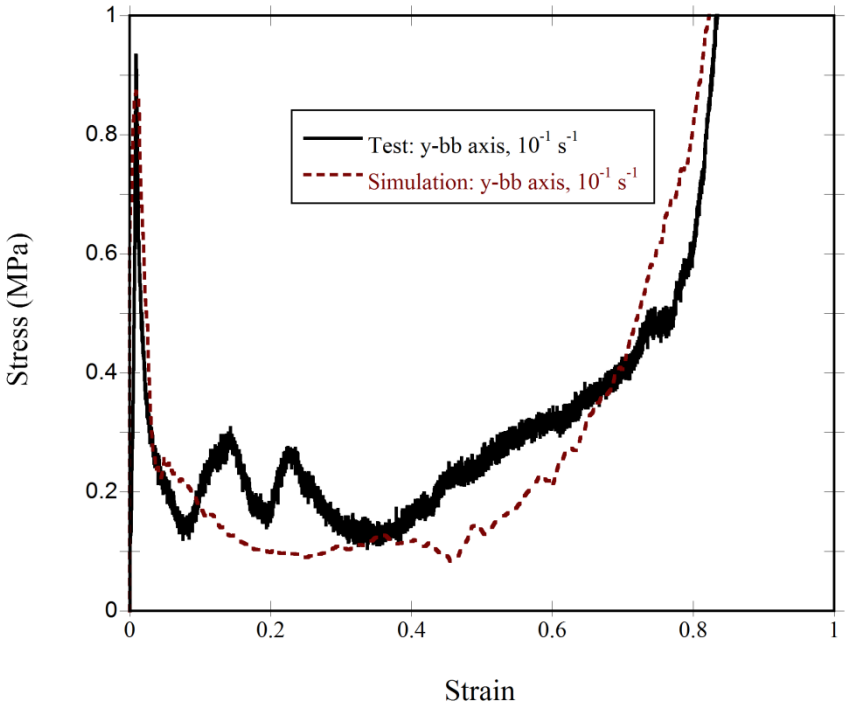

(b)

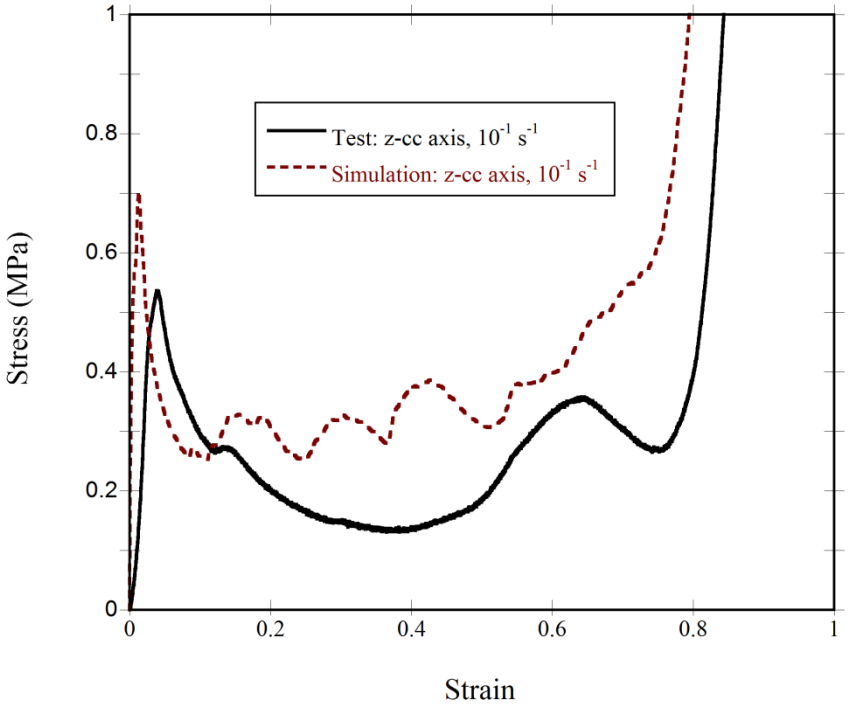

(c)

Figure 11.1 (cont.)

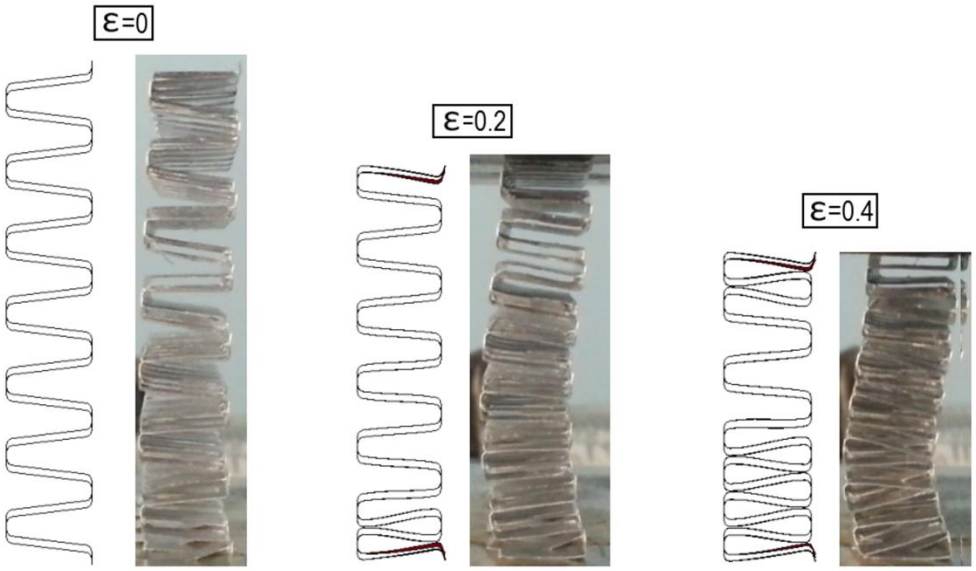

(a)

Figure 11.2. The simulation undeformed and simulation and experimental deformed pictures of the single core layer tested at 10^{-1} s^{-1} in the (a) x-aa, (b) y-bb and (c) z-cc axis.

(cont. on next page)

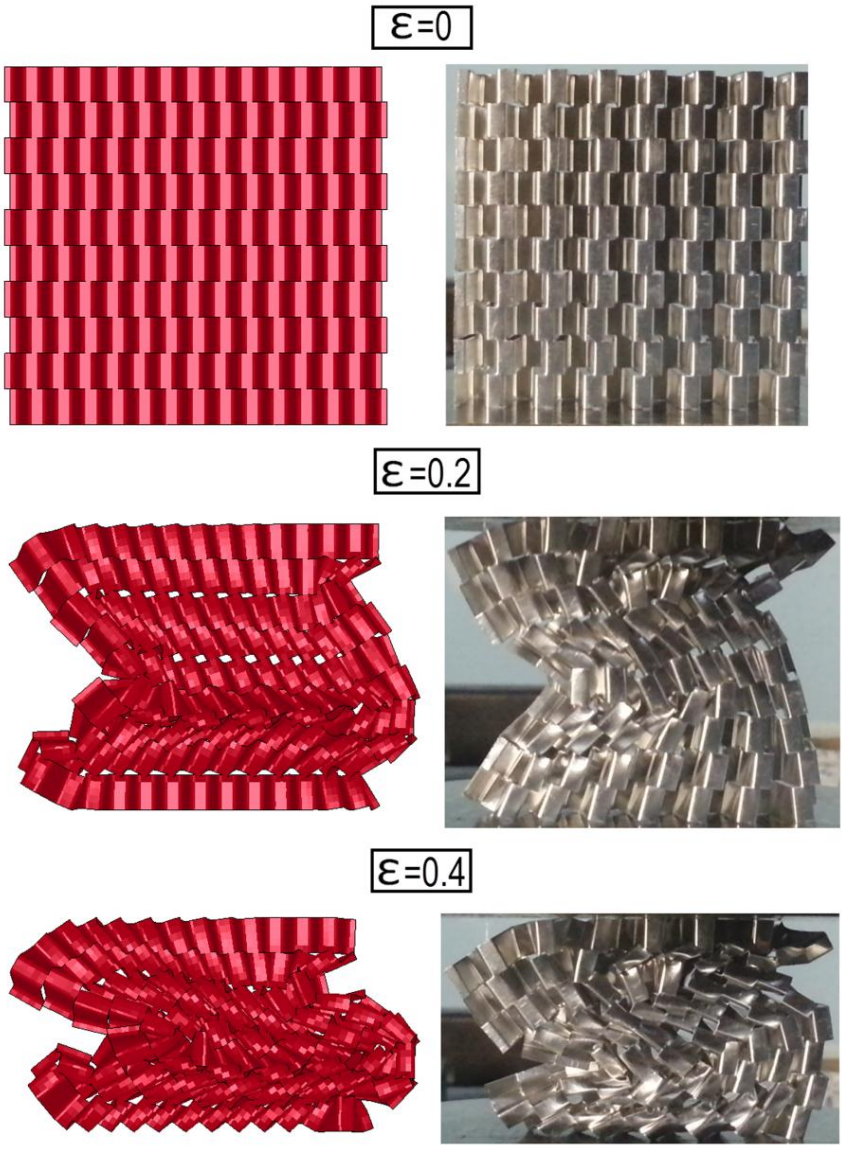

(b)

Figure 11.2 (cont.)

(cont. on next page)

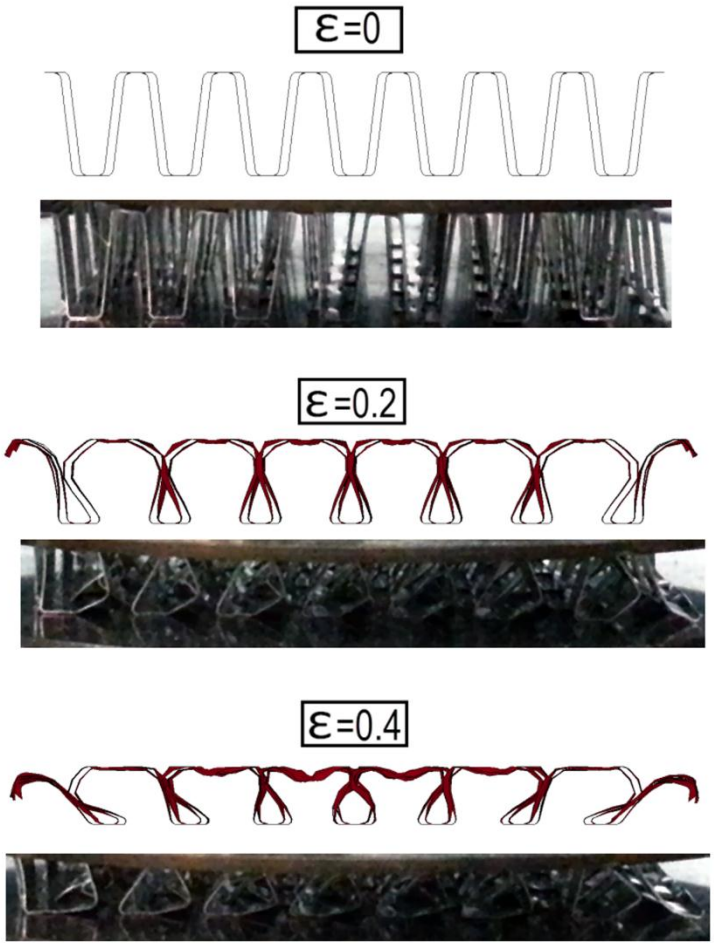

(c)

Figure 11.2 (cont.)

Figure 11.3(a) shows the experimental high strain rate SHPB compression front stress- $\frac{v_o t}{H}$ and quasi-static stress-strain curves of the single-layer sandwich together with those of the full and homogenized coarse mesh numerical models. The simulation initial peak stresses of the homogenized coarse mesh model (1.35 MPa) is the same with that of experiment, while the full model results in slightly lower peak stress (1.16 MPa) as seen in Figure 11.3(a). It is noted that the full model results in similar crushing stresses with the experiment, while the homogenized coarse mesh model gives higher crushing stresses than the experiment in the post-peak stress region until about the densification strain. The increased peak stress of the single-layer sandwich in SHPB test as compared with the quasi-static strain rate test shown in Figure 11.3(a) is due to the inertial effects (Type II structure) which were also previously reported for the similar cellular structures including honeycombs through out of plane [79], metallic columns [80], aluminum foams [79, 81] and balsa wood in the axial direction [82]. The fine mesh

homogenized model and fine mesh homogenized model based on the experimental stress-strain curve of the single core layer result in lower crushing stresses as compared with the homogenized coarse mesh model and yield comparable crushing stresses with the experiments in the post-peak stress region as shown in Figure 11.3(b). They decrease the initial peak stress of the single-layer sandwich to the level of the quasi-static initial peak stress value, 0.75 MPa. These results show that the element size has a significant effect on the initial peak and post-peak stress values of the homogenized models. In the fine mesh homogenized models, the absence of inertial effects is reflected as the reduced initial peak stresses. The reduced initial peak stress was also reported previously in the macro modeling of a hexagonal honeycomb structure [90].

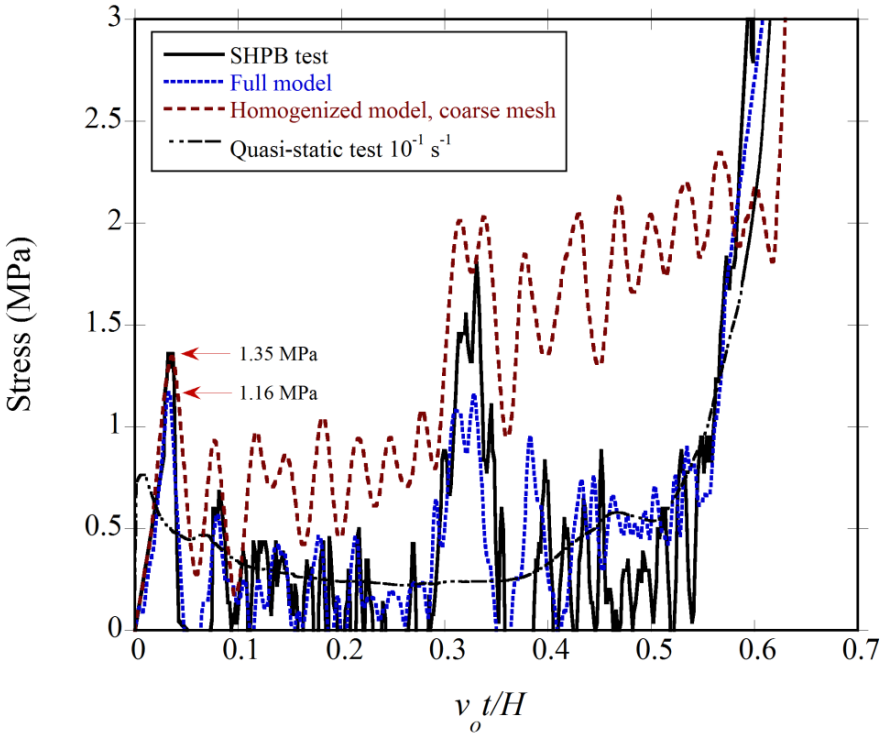

(a)

Figure 11.3. The experimental and simulation stress-strain curves of single-layer sandwich specimen tested in SHPB; (a) test and full and coarse mesh homogenized models with quasi-static stress-strain curve and (b) test and fine mesh homogenized model and fine mesh homogenized model based on the experimental stress-strain curves of the single core layer.

(cont. on next page)

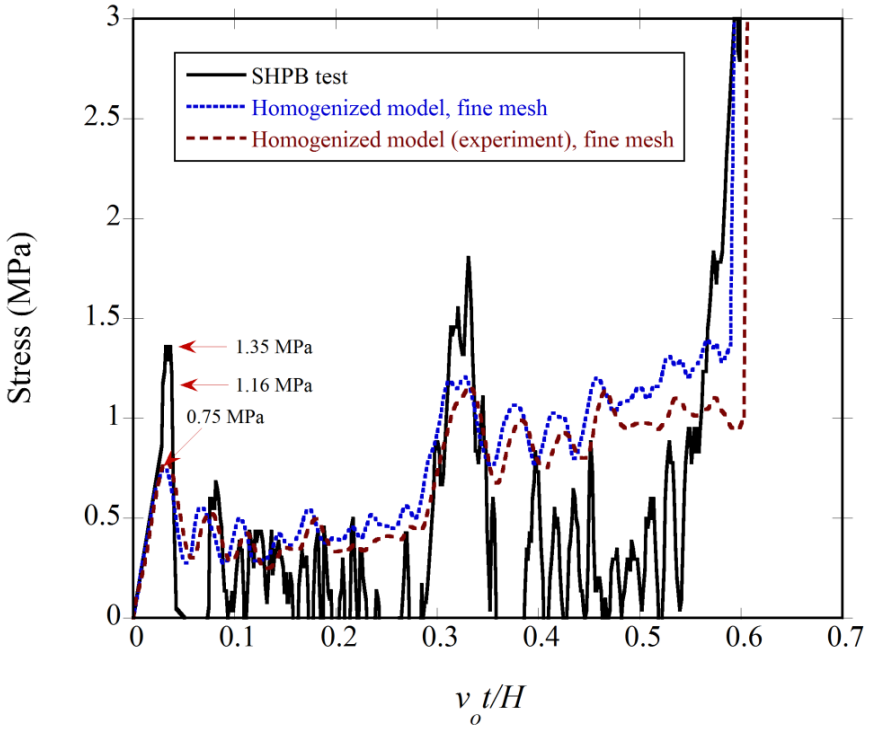

(b)

Figure 11.3 (cont.)

The constraint experimental and numerical compression stress-strain curves of the multi-layer specimens tested in drop weight tower are shown in Figure 11.4. As seen in Figure 11.4, the peak stresses and the post-peak stresses of the full model and the fine mesh homogenized model based on the experimental stress-strain curves of the single core layer show close agreements with the experiments, while the crushing stresses of the fine mesh homogenized model are higher than those of the experiment. Both experimental and numerical models densification strains (~0.68) closely match to each other, except the fine mesh homogenized model based on experimental stress-strain curves of the single core layer gives slightly higher densification strains (~0.7). The experimental and numerical deformed pictures of the compression tested multi-layer sandwiches are shown Figures 11.5(a-d), respectively. The tested specimen shown in Figure 11.5(a) is compressed into the densification region, while the numerically deformed specimens shown in Figures 11.5(b-d) are compressed until about 0.4 strains in the plateau region of the stress-strain curves. In the full model shown in Figure 11.5(b), the fin walls of all corrugated layers are seen to be elastically bent, but only the fin walls of the first top three layers are plastically collapsed via fin wall buckling. The plastic collapse is progressive, starting from the striker contact region. In the fine mesh

homogenized model and fine mesh homogenized model based on the experimental stress-strain curves of the single core layer although the collapse starts from the first top layer, it switches to the bottom layers as seen in Figures 11.5(c-d). The deformation trends of the full and homogenized models are however very much similar, progression with the sequential collapse of the individual fin layers.

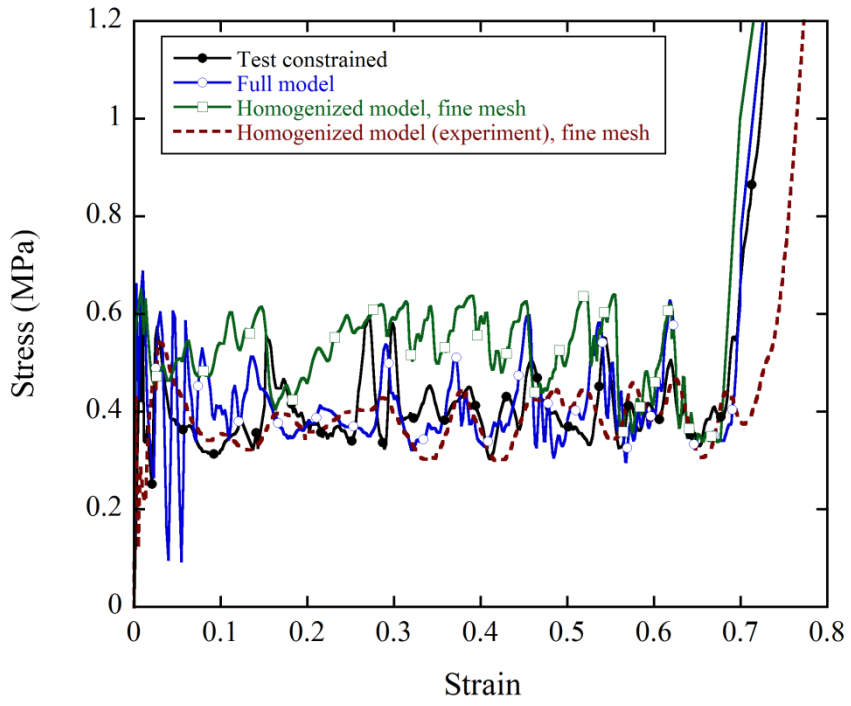

Figure 11.4. The experimental and simulation low velocity compression stress-strain curves of the multi-layer sandwich specimen.

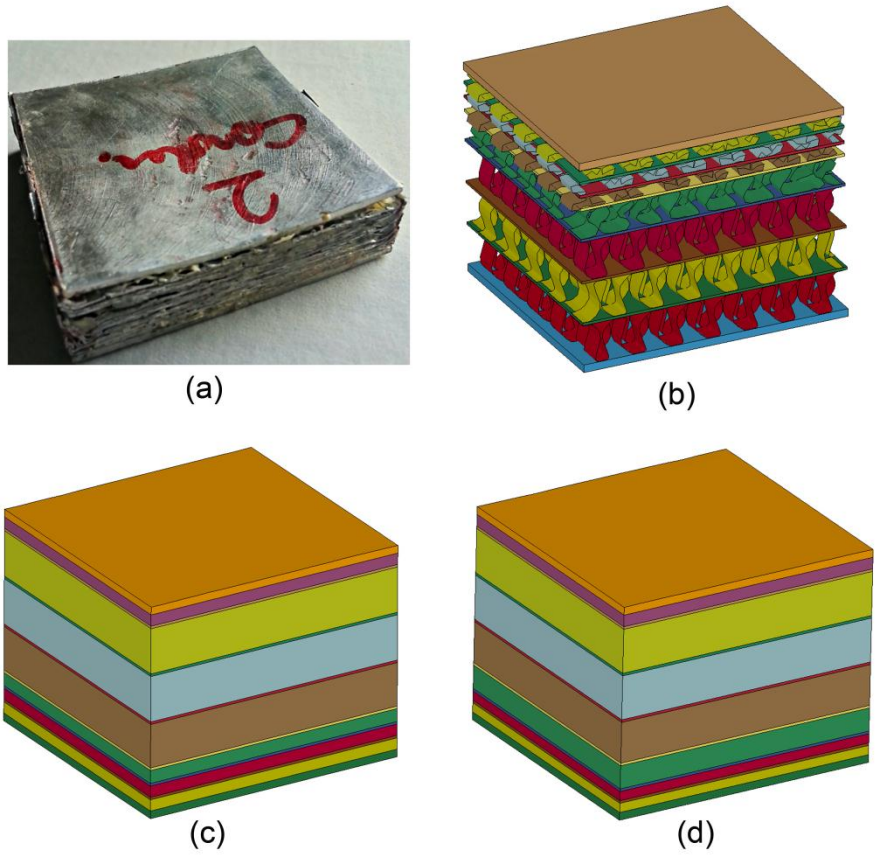

Figure 11.5. The deformation pictures of the low velocity compression tested multi-layer sandwich; (a) experiment, (b) full model, (c) fine mesh homogenized model and (d) fine mesh homogenized model based on the experimental stress-strain curve of the single core layer.

Figure 11.6 shows the experimental and simulation force-displacement curves of the multi-layer sandwich specimens subjected to the low velocity indentation test. The initial linear region of the individual curves is resulted from the elastic deformation of the layers, while the plateau region from the buckling of the fin walls and bending of the face and interlayer sheets. As similar with the low velocity compression test simulations, the full model and fine mesh homogenized model based on the experimental stress-strain curves of the single core layer result in crushing loads comparable with the experiment. Figures 11.7(a-d) show the final deformed shapes of the tested and modeled multi-layer sandwiches. The full model sandwich specimen deformation in Figure 11.7(a) is very similar with the experimental test specimen deformation in Figure 11.7(b) in that the deformation is localized along the striker-specimen contact region. The localized deformation is very anisotropic and proceeds also with the progressive fin wall buckling and interlayer and face sheet bending, starting from the striker-specimen contact region. Although the localized deformation is

clearly seen at the striker-specimen contact region, the left and right edges of the homogenized model test specimens experience larger displacement compared to the full model and experimental test specimen (Figures 11.7(a-d)). This is attributed again to the lack of the inertial effects in the homogenized models.

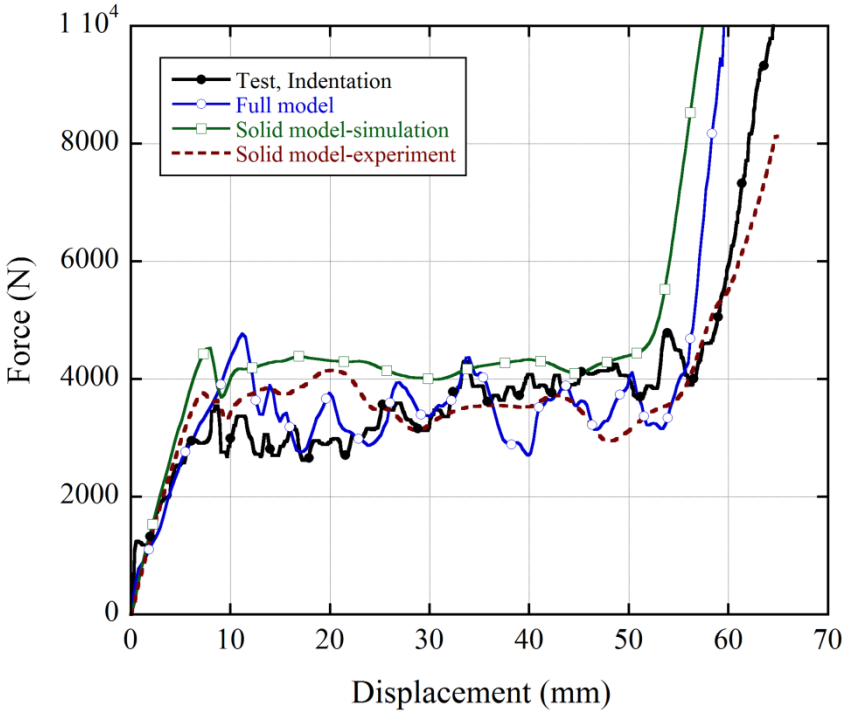

Figure 11.6. The experimental and simulation low velocity indentation force-displacement curves of the multi-layer sandwich specimen.

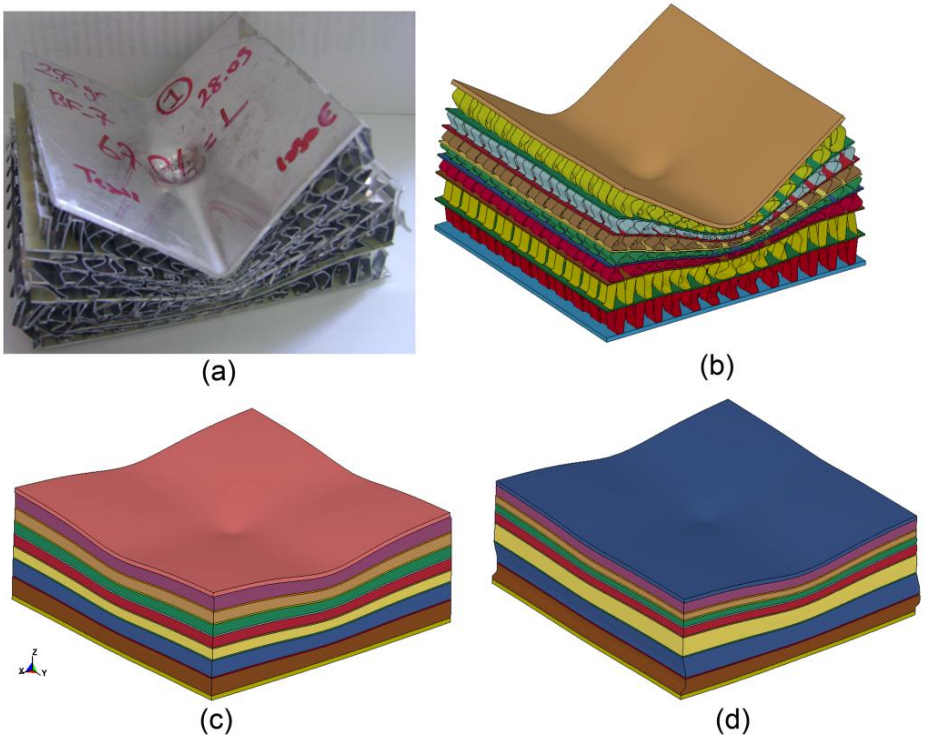

Figure 11.7. The deformation pictures of the low velocity indentation tested multi-layer sandwiches (a) experiment, (b) full model, (c) fine mesh homogenized model and (d) fine mesh homogenized model based on the experimental stress-strain curves of the single core layer.

Figure 11.8 shows the projectile velocity-time curves of the full and homogenized models. The experimental residual projectile velocity (75 m s^{-1}) is also marked in the same figure for comparison. The full model results in the same residual velocity as the experiment, 75 m s^{-1}, while the coarse mesh homogenized model and the coarse mesh homogenized model based on the experimental stress-strain curves of the single core layer predict slightly lower residual velocities, 72.5 and 71 m s^{-1}, than the experiments. Until about 30 mm projectile displacement, the velocity-displacement curves of the full and homogenized models are very similar, thereafter, the full model and homogenized model projectile velocities deviate from each other. The cross-sections of the experimental and full model projectile impact testes specimens show also close resemblances as shown in Figures 11.9(a) and (b). The face and interlayer sheets are seen to bend near the projectile perforated area in both experimental and full model test specimens. The projectile first intends the specimen; thereafter, penetration starts. The deviation between the velocity-displacement curves of the full and homogenized models is therefore presumed to start after about the projectile begins to penetrate the specimen. The higher resistances against the projectile are seen in the

homogenized models than in the full model as the projectile velocity is lower in the homogenized models. The higher resistance of the solid model arises from the higher post-peak stresses of the homogenized models as shown in Figure 11.3. The difference between the residual velocities of the full and homogenized models is about 5%, which lies within the experimental error range.

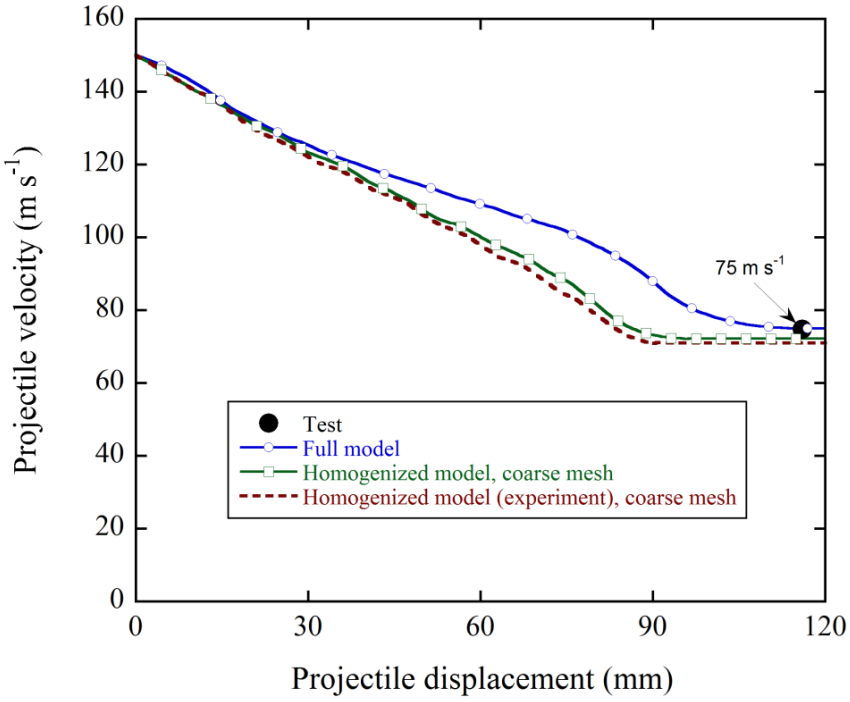

Figure 11.8. Numerical projectile velocity *vs.* projectile displacement curves of the full and homogenized models of the multi-layer sandwich specimen and the experimental projectile residual velocity.

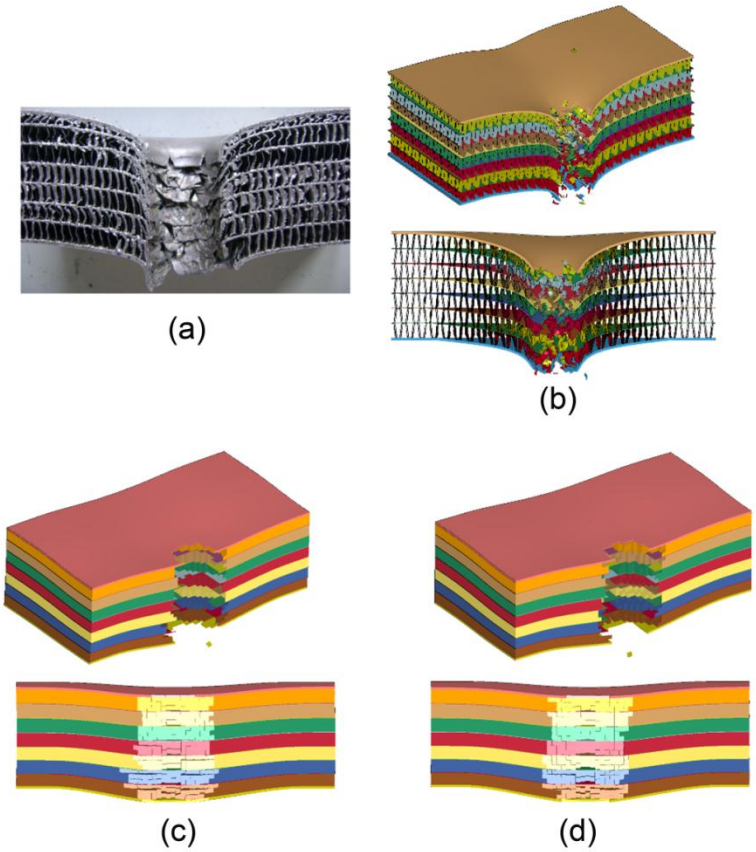

Figure 11.9. The cross-section pictures of sandwiches (a) experiment, (b) full model, (c) coarse mesh homogenized model and (d) coarse mesh homogenized model based on the experimental stress-strain curves of the single core layer.

CHAPTER 12

DISCUSSIONS

12.1. Quasi-static and Dynamic Compression of Single and Double-layer Corrugated Sandwiches

The increased buckling stress of the studied corrugated sandwich structures with increasing strain rate may be considered separately for the imperfection sensitive and insensitive cases. In the former, the increasing strain rate to 1500 s^{-1} changes the deformation mode from bending dominated to stretching dominated for both single- and double layer sandwiches, leading to increased buckling stresses. In a previous study, the peak stress of a unit metallic pyramidal truss core tested in SHPB test was reported to be 60% higher than that in quasi-static test and the increased compressive stress at increasing strain rates was attributed to the strain rate sensitive flow stress of stainless steel and inertial effects [61]. The tested unit core was reported type II structure, showing inertia-induced rate effects [76]. The corrugated structures tested in the present study also show inertia-sensitive type II behavior. The propagation of the plastic wave at high strain rates delays the overall buckling of the member and the member needs to form kinks [108]. The phenomenon of kink formation at high strain rate is also seen in the experimentally tested single- and double layer sandwiches (shown in Figure 6.2(c) by white arrows). The increased buckling stresses were ascribed to micro-inertial effects, which altered the deformation mode of single-layer sandwiches from buckling of three plastic hinges at quasi-static strain rate to higher number of plastic hinge (kink) formations at high strain rate. When the imperfection size is comparably smaller than the buckling wavelength, imperfection insensitive case, the inertial effects appear at higher strain rates, 3000 s^{-1}. The fin wall bending type imperfection model well simulated the experimental quasi-static compression stress-strain curves of the tested sandwiches. The buckling stress at quasi-static strain and high strain rates was shown numerically imperfection sensitive when the imperfection size was reduced below the buckling length, while at larger imperfection size; the structure became imperfection sensitive at quasi-static strain rates. The simulations also showed that the inertial effects

appeared at higher strain rates for the perfect structure or when the imperfection size was smaller than the buckling wavelength. The simulations based on the perfect model at 3000 s^{-1} clearly indicated the inertial sensitive buckling stresses of the single layer sandwiches and higher and earlier micro inertial effect in the triangular form of the corrugation than trapezoidal corrugated cores. The numerical buckling stresses of the zig-zag and straight corrugated core structures were shown to be similar at both quasi-static and high strain rates, implying an insignificant effect of the zig-zag form.

12.2. Quasi-static and Dynamic Compression of Multi-layer Corrugated Sandwiches

The increased deformation forces at increasing strain rates in the compression of aluminum honeycomb structures through out of plane [79], metallic columnar structures [80], aluminum foams [79, 81] and balsa wood in the axial direction [82, 83] were reported to result from the micro-inertial effects. The increased buckling stress of 0°/0° oriented core sandwich is due to micro-inertial effect. The lateral inertia forces lead to increased bending forces at increasing impact velocities. Multi-layering decreased buckling stress and increased the densification strain of corrugated sandwich structure. The deformation modes of bonded and brazed samples were found to be similar; while, bonded specimens experienced higher crushing stresses, resulting from the reduced yield stresses of corrugated, interlayer and face sheets after brazing at elevated temperature. The simulation and experimental results were found to reasonably agree with each at the large extent of deformation and revealed the progressive fin folding of corrugated core layers and shearing the interlayer sheets as the main deformation modes. The unconstraint samples showed increased buckling stress at high strain rate, while constraint sample showed strain rate independent buckling stress. Both, the simulation and experimental post-bucking stresses increased with constraining. The multilayer samples in 0°/90° core orientation showed higher buckling stress than the samples in 0°/0° core orientation. The increased buckling stress of 0°/0° oriented core sandwiches was attributed to the micro-inertial effect which led to increased bending forces at increasing impact velocities. The presence of interlayer sheets induced more homogenous and progressive deformation of individual layers in the expense of reduced specific energy absorption.

12.3. Quasi-static and Dynamic Indentation of Multi-layer Corrugated Sandwiches

The core deformation was shown to be dependent on core density; low density cores deformed by shear and elastic buckling before failure and eventually the core failed by the plastic buckling of the cell walls [109]. These sequences of the deformation also apply to sandwich structure tested in the present study using spherical and flat strikers. It is also noted the low strength brazed fin layers show extensive shearing before fail dominantly by fin wall bending, while the bonded fin layers show more elastic buckling before fail dominantly by fin wall buckling (Figure 7.12(a) and (c) and Figures 7.13 (a) and (c)). For honeycomb structures to be effective to dissipate the energy of a projectile, the diameter of the projectile should be large as compared with the size of cells [110-112]. For the projectile diameters less than the cell size, the projectile penetrates through the core [113]. When the cell size was large compared to the diameter of the projectile, the sandwich panel with a light weight core showed almost the same resistance to projectile penetration as the face sheet alone [62]. This was due to relatively small contribution of the core deformation during penetration. The penetration of the conical striker to the sandwich panel is therefore due to the relatively small tip radius of the striker compared to the fin width (5 mm). However, the penetration of a projector can be reduced when the empty places of the core is filled with a relatively rigid material including polymers and ceramics [62].

The deformation rate sensitive crushing loads of cellular materials may result from the strain rate sensitivity of cell wall material, micro-inertial effects, shock wave propagation and compressed air pressure in the cells [79]. As stated earlier, aluminum and its alloys are known to be rate insensitive. The shock wave propagation was shown to have a significant contribution to the strength of the cellular metallic structures over 50 m s^{-1} [82]; therefore, it could not explain the observed deformation rate sensitivity of the tested panels. Micro-inertial effects arise due to lateral inertia, which increases the buckling loads at increasing strain rates [76]. Lateral inertia causes the buckling of a column under impact compression at a delayed time, so that the critical buckling force is higher than the quasi-static one. Calladine and English [76] classified columnar structures in two groups: Type I structures are characterized with a flat-topped quasi-static load deflection curve, showing limited or no strength enhancement at increasing

deformation velocities and Type II structures are characterized with a strong softening after yielding at quasi-static strain rates and the lateral inertia forces lead to increased bending forces at increasing deformation velocities. The increased deformation forces at increasing strain rates in the compression of aluminum honeycomb structures through out of plane [79], metallic columnar structures [80], aluminum foams [61, 79, 81], sintered stainless steel hollow spheres [114] and balsa wood in the axial direction [82, 83] were reported to result from the micro-inertial effects. The increased peak stresses with increasing impact velocities were also found in periodic cellular metal cores such as Y-frame and corrugated sandwich cores: Y-frame was shown to be less sensitive than corrugated and pyramidal truss cores [49]. The increased initial peak stress of stainless steel pyramidal truss cores [61], textile cellular structures [106] and metallic honeycomb-core sandwich beams [115] at increasing strain rates was reported to be contributed by the inertial effects. In order to differentiate the strain rate hardening and inertial effects, the strain rate parameter of Eqn. (6.1) is taken as zero [61, 114]. However, the simulations were executed in the present study by omitting the strain rate hardening. Based on above, it is concluded that micro inertia effect plays a role on the increased force values of the tested panels at increasing velocities.

The tests in the present study are apparently prone to specimen size end effects; therefore, cannot show the impact behavior of the panels realistically. However, the full geometrical modeling of the panels with larger sizes leads to extremely increased computational times. On the other side, the agreements between simulation and experimental force values and deformation shapes of relatively small size test panels validate the fidelity of the developed material and full geometrical test model. To model larger sizes of the panels, further investigations should therefore focus on the homogenization methods of layered sandwich structure.

The applied brazing process reduced the crushing loads of the corrugated structures due to the reduced yield stresses of the layers. The adhesively bonded panels tested using spherical and flat striker tips were not penetrated and experienced higher deformation forces and energy absorptions in 0°/90° corrugated layer orientation than in 0°/0° orientation. The panels impacted with a conical striker tip were penetrated/perforated and showed comparably smaller deformation forces and energy absorptions, especially in 0°/90° layer orientation. The panels with 0°/90° corrugated layer orientation were shown to have potentials of distributing load laterally more efficiently. The simulation and experimental results were found to reasonably agree

with each at the large extent of striker impact and revealed the progressive fin folding of corrugated core layer and bending of interlayer and face sheets as the main deformation mechanisms. The experimentally and numerically determined impact velocity sensitivity of the tested panels was attributed to the micro inertial effects which increased the critical buckling loads of the fin layers at increasing loading rates.

12.4. Numerical Homogenization of Multi-layer Corrugated Sandwiches

The full model results showed close agreements with the experimental test results. It was shown that the element size had a significant effect on the initial peak and post-peak stress values of the homogenized models. In the homogenized models, the lack of inertial effects was reflected as the reduced initial peak stresses. The homogenized models based on the experimental stress-strain curve of the single core layer was shown to predict the low velocity compression and indentation and projectile impact test results of the multi-layer corrugated sandwiches with an acceptable accuracy. The presented approach reduced the computational time of dynamic deformation models of the multi-layer corrugated sandwich structures significantly

CHAPTER 13

CONCLUSIONS

In this thesis, the quasi-static and dynamic properties of single, double and multi-layer zig-zag 1050 H14 Al trapezoidal corrugated core sandwich structures investigated through experiments at varying impact velocities and numerical simulations conducted in FE code LS-DYNA. The work aims at identifying the deformation characteristics of the corrugated structures at different strain rate regimes; therefore, to increase the level of understanding of the deformation behaviors of such structures.

The axial crushing response of single and double-layer corrugated core sandwich structures were determined experimentally and numerically at quasi-static (10^{-3}-10^{-1} s^{-1}) and dynamic (1500 s^{-1}) strain rates. The buckling stress of the corrugated sandwich structures increased when the strain rate increased from quasi-static to 1500 s^{-1}. The increased buckling stresses were ascribed to micro-inertial effects, which altered the deformation mode of single-layer sandwiches from buckling of three plastic hinges at quasi-static strain rate to higher number of plastic hinge (kink) formations at high strain rate. The buckling stress at quasi-static strain and high strain rates was shown numerically imperfection sensitive when the imperfection size was reduced below the buckling length, while at larger imperfection size; the structure became imperfection sensitive at quasi-static strain rates. The simulations also showed that the inertial effects appeared at higher strain rates for the perfect structure or when the imperfection size was smaller than the buckling wavelength. The simulations based on the perfect model at 3000 s^{-1} clearly indicated the inertial sensitive buckling stresses of the single layer sandwiches and higher and earlier micro inertial effect in the triangular form of the corrugation than trapezoidal corrugated cores. The numerical buckling stresses of the zig-zag and straight corrugated core structures were shown to be similar at both quasi-static and high strain rates, implying an insignificant effect of the zig-zag form.

The axial crushing responses of bonded and brazed multi-layer corrugated core sandwich structures, with and without aluminum interlayer sheets in 0°/0° and 0°/90° core orientations, were both experimentally and numerically investigated at quasi-static

(10^{-3}-10^{-1} s^{-1}) and dynamic (40 s^{-1}) strain rates. Multi-layering decreased buckling stress and increased the densification strain of corrugated sandwich structure. The deformation modes of bonded and brazed samples were found to be similar; while, bonded specimens experienced higher crushing stresses, resulting from the reduced yield stresses of corrugated, interlayer and face sheets after brazing at elevated temperature. The simulation and experimental results were found to reasonably agree with each at the large extent of deformation and revealed the progressive fin folding of corrugated core layers and shearing the interlayer sheets as the main deformation modes. The unconstraint samples showed increased buckling stress at high strain rate, while constraint sample showed strain rate independent buckling stress. Both, the simulation and experimental post-bucking stresses increased with constraining. The multilayer samples in 0°/90° core orientation showed higher buckling stress than the samples in 0°/0° core orientation. The increased buckling stress of 0°/0° oriented core sandwiches was attributed to the micro-inertial effect which led to increased bending forces at increasing impact velocities. The presence of interlayer sheets induced more homogenous and progressive deformation of individual layers in the expense of reduced specific energy absorption. This was due to the increase weight of the sandwiches with the inclusion of the interlayer sheets. A compromise between the interlayer sheet thickness and homogenous and progressive deformation of individual layers is therefore needed to increase the specific energy of the sandwiches with interlayer sheets.

The indentation responses of brazed and adhesively bonded multi-layer corrugated core sandwich panels with 3003 and 1050 H14 Al alloy face sheets in 0°/0° and 0°/90° core orientations were investigated in a drop weight tower tests using spherical, flat and conical end striker tips. The applied brazing process reduced the crushing loads of the corrugated structures due to the reduced yield stresses of the layers. The adhesively bonded panels tested using spherical and flat striker tips were not penetrated and experienced higher deformation forces and energy absorptions in 0°/90° corrugated layer orientation than in 0°/0° orientation. The panels impacted with a conical striker tip were penetrated/perforated and showed comparably smaller deformation forces and energy absorptions, especially in 0°/90° layer orientation. The panels with 0°/90° corrugated layer orientation were shown to have potentials of distributing load laterally more efficiently. The simulation and experimental results were found to reasonably agree with each at the large extent of striker impact and revealed the progressive fin folding of corrugated core layer and bending of interlayer

and face sheets as the main deformation mechanisms. The experimentally and numerically determined impact velocity sensitivity of the tested panels was attributed to the micro inertial effects which increased the critical buckling loads of the fin layers at increasing loading rates.

The full and homogenized numerical models of a single core layer 1050-H14 Al trapezoidal zig-zag multi-layer corrugated sandwiches were developed base on the experimental and numerical compression tests on the single core layer. In the homogenized models, the deformation of the single fin layer was modeled using MAT-26 honeycomb model in LS-DYNA. The differences between the simulation and experimental quasi-static compression stresses of the single fin layer were attributed to the fin wall imperfections and specimen misalignment in the test. The fidelity of the full and homogenized numerical models of multi-layer corrugated sandwiches was checked via direct impact, low velocity compression and indentation and projectile impact tests. In direct impact tests, the full model resulted in similar stresses with the experiment, while the fine mesh homogenized models yielded lower initial peak stresses than the experiments due to lack of inertial effects in the homogenized models. Low velocity compression the stress-strain curves of the of the full model and the fine mesh homogenized model based on the experimental stress-strain curves of the single core layer showed close agreements with each other and with those of the experiments. As similar with compression tests, the simulation of the indentation tests yielded similar force-displacement curves with the experiments. The homogenized models however exhibited higher impact resistances than the full model, which was attributed to higher post-peak stresses of the homogenized models. However, the difference between the projectile residual velocities of the full and homogenized models was found very similar, deviating 5%.

This study clearly revealed the potentials of the use of zig-zag aluminum trapezoidal corrugated sandwich structures as load carriers subjected to impact loadings at low and high strain rates. The optimization of the unit core geometry for specific loadings is recommended as future work.

REFERENCES

[1] P. Compston, M. Styles, and S. Kalyanasundaram, "Low energy impact damage modes in aluminum foam and polymer foam sandwich structures," *Journal of Sandwich Structures & Materials,* vol. 8, pp. 365-379, Sep 2006.

[2] W. H. Hou, F. Zhu, G. X. Lu, and D. N. Fang, "Ballistic impact experiments of metallic sandwich panels with aluminium foam core," *International Journal of Impact Engineering,* vol. 37, pp. 1045-1055, Oct 2010.

[3] H. Kiratisaevee and W. J. Cantwell, "Low-velocity impact response of high-performance aluminum foam sandwich structures," *Journal of Reinforced Plastics and Composites,* vol. 24, pp. 1057-1072, 2005.

[4] K. Mohan, T. H. Yip, S. Idapalapati, and Z. Chen, "Impact response of aluminum foam core sandwich structures," *Materials Science and Engineering a-Structural Materials Properties Microstructure and Processing,* vol. 529, pp. 94-101, Nov 2011.

[5] I. K. Odaci, C. Kilicaslan, A. Tasdemirci, and M. Guden, "Projectile impact testing of glass fiber-reinforced composite and layered corrugated aluminium and aluminium foam core sandwich panels: a comparative study," *International Journal of Crashworthiness,* vol. 17, pp. 508-518, 2012.

[6] S. Pattofatto, H. Zeng, and H. Zhao, "On the piercing force enhancement of aluminum foam sandwich plates under impact loading," *Journal of Sandwich Structures & Materials,* vol. 14, pp. 211-226, Mar 2012.

[7] R. Sriram, U. K. Vaidya, and J. E. Kim, "Blast impact response of aluminum foam sandwich composites," *Journal of Materials Science,* vol. 41, pp. 4023-4039, Jul 2006.

[8] H. Zhao, I. Elnasri, and Y. Girard, "Perforation of aluminium foam core sandwich panels under impact loading - An experimental study," *International Journal of Impact Engineering,* vol. 34, pp. 1246-1257, Jul 2007.

[9] H. Kiratisaevee and W. J. Cantwell, "The impact response of aluminum foam sandwich structures based on a glass fiber-reinforced polypropylene fiber-metal laminate," *Polymer Composites,* vol. 25, pp. 499-509, Oct 2004.

[10] V. Crupi, G. Epasto, and E. Guglielmino, "Collapse modes in aluminium honeycomb sandwich panels under bending and impact loading," *International Journal of Impact Engineering,* vol. 43, pp. 6-15, 2012.

[11] C. C. Foo, G. B. Chai, and L. K. Seah, "Quasi-static and low-velocity impact failure of aluminium honeycomb sandwich panels," *Proceedings of the Institution of Mechanical Engineers Part L-Journal of Materials-Design and Applications*, vol. 220, pp. 53-66, Apr 2006.

[12] C. C. Foo, L. K. Seah, and G. B. Chai, "Low-velocity impact failure of aluminium honeycomb sandwich panels," *Composite Structures*, vol. 85, pp. 20-28, Sep 2008.

[13] A. Francesconi, D. Pavarin, A. Bettella, C. Giacomuzzo, M. Faraud, R. Destefanis, *et al.*, "Generation of transient vibrations on aluminum honeycomb sandwich panels subjected to hypervelocity impacts," *International Journal of Impact Engineering*, vol. 35, pp. 1503-1509, Dec 2008.

[14] M. A. Hazizan and W. J. Cantwell, "The low velocity impact response of an aluminium honeycomb sandwich structure," *Composites Part B-Engineering*, vol. 34, pp. 679-687, 2003.

[15] O. T. Shitta-Bey, J. J. Carruthers, C. Soutis, and M. S. Found, "The localized low-velocity impact response of aluminium honeycombs and sandwich panels for occupant head protection: experimental characterization and analytical modelling," *International Journal of Crashworthiness*, vol. 12, pp. 549-558, 2007.

[16] J. Banhart, "Manufacture, characterisation and application of cellular metals and metal foams," *Progress in Materials Science*, vol. 46, pp. 559-632, // 2001.

[17] J. Banhart, "Aluminium foams for lighter vehicles," *International Journal of Vehicle Design* vol. 37, pp. 114-125, 2005.

[18] J. Banhart, "Manufacturing routes for metallic foams," *Jom-Journal of the Minerals Metals & Materials Society*, vol. 52, pp. 22-27, 2000.

[19] J. Banhart and J. Baumeister, "Production Methods for Metallic Foams," in *MSR Symposium*, 1998, pp. 121-132.

[20] M. F. Ashby, A. G. Evans, N. A. Fleck, L. J. Gibson, J. W. Hutchinson, and H. N. G. Wadley, "Chapter 2 - Making metal foams," in *Metal Foams*, ed Burlington: Butterworth-Heinemann, 2000, pp. 6-23.

[21] S. Yüksel, "The effects of SiC particle addition on the foaming and mechanical behavior of aluminum closed-cell foams produced by foamming of powder compacts," Doctoral, Mechanical Engineering, İzmir Institute of Technology, 2010.

[22] L. J. Gibson, "Mechanical behavior of metallic foams," *Annual Review of Materials Science,* vol. 30, pp. 191-227, 2000.

[23] L. J. Gibson and M. F. Ashby, *Cellular Solids:Structure and Properties*. Oxford: Pergamon Press, 1988.

[24] D. J. Sypeck, "Cellular Truss Core Sandwich Structures," *Applied Composite Materials,* vol. 12, pp. 229-246, 2005.

[25] E. Wu and W.-S. Jiang, "Axial crush of metallic honeycombs," *International Journal of Impact Engineering,* vol. 19, pp. 439-456, 5// 1997.

[26] H. N. Wadley, "Multifunctional periodic cellular metals," *Philos Transact A Math Phys Eng Sci,* vol. 364, pp. 31-68, Jan 15 2006.

[27] L. Aktay, A. F. Johnson, and B.-H. Kröplin, "Numerical modelling of honeycomb core crush behaviour," *Engineering Fracture Mechanics,* vol. 75, pp. 2616-2630, 6// 2008.

[28] T. Wierzbicki, "Crushing analysis of metal honeycombs," *International Journal of Impact Engineering,* vol. 1, pp. 157-174, // 1983.

[29] E. Armentani, F. Caputo, and R. Esposito, "FE Analysis of buckling of corrugated structures," in *4th International Journal of Impact Engineering*, Firenze, 2006.

[30] M. E. Biancolini, "Evaluation of equivalent stiffness properties of corrugated board," *Composite Structures,* vol. 69, pp. 322-328, 2005.

[31] Rahman, A. A.Abubakr, and S. M., "Adhesive in the buckling failure of corrugated fiberboard : a finite element investigation " presented at the Proceedings of the 1998 ANSYS conference : simulating real life : software with no boundaries 1998.

[32] N. Talbi, A. Batti, R. Ayad, and Y. Q. Guo, "An analytical homogenization model for finite element modelling of corrugated cardboard," *Composite Structures,* vol. 88, pp. 280-289, 2009.

[33] Z.-W. Wang and Y.-P. E, "Energy absorption properties of multi-layered corrugated paperboard in various ambient humidities," *Materials & Design,* vol. 32, pp. 3476-3485, 2011.

[34] M. Li, L. Wu, L. Ma, B. Wang, and Z. Guan, "Structural response of all-composite pyramidal truss core sandwich columns in end compression," *Composite Structures,* vol. 93, pp. 1964-1972, 2011.

[35] M. Li, L. Wu, L. Ma, B. Wang, and Z. Guan, "Mechanical Response of All-composite Pyramidal Lattice Truss Core Sandwich Structures," *Journal of Materials Science & Technology*, vol. 27, pp. 570-576, 2011.

[36] A. G. Mamalis, D. E. Manolakos, M. B. Ioannidis, and P. K. Kostazos, "Axial collapse of hybrid square sandwich composite tubular components with corrugated core: Experimental," *International Journal of Crashworthiness*, vol. 5, pp. 315-332, 2000/01/01 2000.

[37] M. R. M. Rejab and W. J. Cantwell, "The mechanical behaviour of corrugated-core sandwich panels," *Composites Part B: Engineering*, vol. 47, pp. 267-277, 2013.

[38] J. Xiong, L. Ma, S. Pan, L. Wu, J. Papadopoulos, and A. Vaziri, "Shear and bending performance of carbon fiber composite sandwich panels with pyramidal truss cores," *Acta Materialia*, vol. 60, pp. 1455-1466, 2012.

[39] J. Xiong, L. Ma, L. Wu, B. Wang, and A. Vaziri, "Fabrication and crushing behavior of low density carbon fiber composite pyramidal truss structures," *Composite Structures*, vol. 92, pp. 2695-2702, 2010.

[40] J. Xiong, A. Vaziri, L. Ma, J. Papadopoulos, and L. Wu, "Compression and impact testing of two-layer composite pyramidal-core sandwich panels," *Composite Structures*, vol. 94, pp. 793-801, 2012.

[41] F. W. Zok, H. J. Rathbun, Z. Wei, and A. G. Evans, "Design of metallic textile core sandwich panels," *International Journal of Solids and Structures*, vol. 40, pp. 5707-5722, 2003.

[42] R. Biagi, J. Y. Lim, and H. Bart-Smith, "In-Plane Compression Response of Extruded Aluminum 6061-T6 Corrugated Core Sandwich Columns," *Journal of the American Ceramic Society*, vol. 94, pp. s76-s84, 2011.

[43] K. P. Dharmasena, D. T. Queheillalt, H. N. G. Wadley, P. Dudt, Y. Chen, D. Knight, *et al.*, "Dynamic compression of metallic sandwich structures during planar impulsive loading in water," *European Journal of Mechanics - A/Solids*, vol. 29, pp. 56-67, 1// 2010.

[44] C. Kılıçaslan, M. Güden, İ. K. Odacı, and A. Taşdemirci, "The impact responses and the finite element modeling of layered trapezoidal corrugated aluminum core and aluminum sheet interlayer sandwich structures," *Materials & Design*, vol. 46, pp. 121-133, 4// 2013.

[45] D. T. Queheillalt and H. N. G. Wadley, "Titanium alloy lattice truss structures," *Materials & Design*, vol. 30, pp. 1966-1975, 2009.

[46] V. Rubino, V. Deshpande, and N. Fleck, "The dynamic response of end-clamped sandwich beams with a Y-frame or corrugated core," *International Journal of Impact Engineering,* vol. 35, pp. 829-844, 2008.

[47] V. Rubino, V. S. Deshpande, and N. A. Fleck, "The dynamic response of clamped rectangular Y-frame and corrugated core sandwich plates," *European Journal of Mechanics - A/Solids,* vol. 28, pp. 14-24, 2009.

[48] V. Rubino, V. S. Deshpande, and N. A. Fleck, "The three-point bending of Y-frame and corrugated core sandwich beams," *International Journal of Mechanical Sciences,* vol. 52, pp. 485-494, 2010.

[49] M. T. Tilbrook, D. D. Radford, V. S. Deshpande, and N. A. Fleck, "Dynamic crushing of sandwich panels with prismatic lattice cores," *International Journal of Solids and Structures,* vol. 44, pp. 6101-6123, 2007.

[50] Y. C. Zhang, S. L. Zhang, and Z. L. Wang, "Crush Behavior of Corrugated Cores Sandwich Panels," *Advanced Materials Research,* vol. 217-218, pp. 1584-1589, 2011.

[51] D. D. Radford, N. A. Fleck, and V. S. Deshpande, "The response of clamped sandwich beams subjected to shock loading," *International Journal of Impact Engineering,* vol. 32, pp. 968-987, 2006.

[52] C.-C. Liang, M.-F. Yang, and P.-W. Wu, "Optimum design of metallic corrugated core sandwich panels subjected to blast loads," *Ocean Engineering,* vol. 28, pp. 825-861, 2001.

[53] Y. Liang, L. Louca, and R. Hobbs, "Corrugated panels under dynamic loads," *International Journal of Impact Engineering,* vol. 34, pp. 1185-1201, 2007.

[54] F. Cote, V. Deshpande, N. Fleck, and A. G. Evans, "The compressive and shear reponses of corrugated and diamond lattice materials," *International Journal of Solids and Structures,* vol. 43, pp. 6220-6242, 2006.

[55] P. Isaksson, A. Krusper, and P. A. Gradin, "Shear correction factors for corrugated core structures," *Composite Structures,* vol. 80, pp. 123-130, 2007.

[56] N. Buannic, P. Cartraud, and T. Quesnel, "Homogenization of corrugated core sandwich panels," *Composite Structures,* vol. 59, pp. 299-312, 2003.

[57] G. W. Kooistra, V. S. Deshpande, and H. N. G. Wadley, "Compressive behavior of age hardenable tetrahedral lattice truss structures made from aluminium," *Acta Materialia,* vol. 52, pp. 4229-4237, 8/16/ 2004.

[58] Y. Sugimura, "Mechanical response of single-layer tetrahedral trusses under shear loading," *Mechanics of Materials,* vol. 36, pp. 715-721, 2004.

[59] J.-H. Lim and K.-J. Kang, "Mechanical behavior of sandwich panels with tetrahedral and Kagome truss cores fabricated from wires," *International Journal of Solids and Structures,* vol. 43, pp. 5228-5246, 2006.

[60] H. J. Rathbun, Z. Wei, M. Y. He, F. W. Zok, A. G. Evans, D. J. Sypeck, *et al.*, "Measurement and Simulation of the Performance of a Lightweight Metallic Sandwich Structure With a Tetrahedral Truss Core," *Journal of Applied Mechanics,* vol. 71, p. 368, 2004.

[61] S. Lee, F. Barthelat, J. W. Hutchinson, and H. D. Espinosa, "Dynamic failure of metallic pyramidal truss core materials - Experiments and modeling," *International Journal of Plasticity,* vol. 22, pp. 2118-2145, 2006.

[62] C. J. Yungwirth, H. N. G. Wadley, J. H. O'Connor, A. J. Zakraysek, and V. S. Deshpande, "Impact response of sandwich plates with a pyramidal lattice core," *International Journal of Impact Engineering,* vol. 35, pp. 920-936, 2008.

[63] S. Hyun, A. M. Karlsson, S. Torquato, and A. G. Evans, "Simulated properties of Kagomé and tetragonal truss core panels," *International Journal of Solids and Structures,* vol. 40, pp. 6989-6998, 2003.

[64] J. Wang, A. G. Evans, K. Dharmasena, and H. N. G. Wadley, "On the performance of truss panels with Kagomé cores," *International Journal of Solids and Structures,* vol. 40, pp. 6981-6988, 2003.

[65] Z. Zhang, S. Liu, and Z. Tang, "Crashworthiness investigation of kagome honeycomb sandwich cylindrical column under axial crushing loads," *Thin-Walled Structures,* vol. 48, pp. 9-18, 2010.

[66] D. T. Queheillalt and H. N. G. Wadley, "Pyramidal lattice truss structures with hollow trusses," *Materials Science and Engineering: A,* vol. 397, pp. 132-137, 2005.

[67] X. Tang, V. Prakash, J. J. Lewandowski, G. W. Kooistra, and H. N. G. Wadley, "Inertial stabilization of buckling at high rates of loading and low test temperatures: Implications for dynamic crush resistance of aluminum-alloy-based sandwich plates with lattice core," *Acta Materialia,* vol. 55, pp. 2829-2840, 2007.

[68] L. F. Mori, S. Lee, Z. Y. Xue, A. Vaziri, D. T. Queheillalt, K. P. Dharmasena, *et al.*, "Deformation and fracture modes of sandwich structures subjected to underwater impulsive loads " *Journal of Mechanics of Materials and Structures,* vol. 2, pp. 1981-2006, 2007.

[69] H. Wadley, K. Dharmasena, Y. Chen, P. Dudt, D. Knight, R. Charette, *et al.*, "Compressive response of multilayered pyramidal lattices during underwater shock loading," *International Journal of Impact Engineering,* vol. 35, pp. 1102-1114, 2008.

[70] W.-c. Jiang, B. Yang, B. Y. Wang, H. Chen, and J. M. Gong, "Experimental and numerical study on the residual stress in a lattice truss sandwich structure: Effect of geometrical dimensions of punching die," *Materials & Design,* vol. 49, pp. 1048-1055, 8// 2013.

[71] K. P. Dharmasena, H. N. G. Wadley, K. Williams, Z. Xue, and J. W. Hutchinson, "Response of metallic pyramidal lattice sandwich panels to high intensity impulsive loading in air," *International Journal of Impact Engineering,* vol. 38, pp. 275-289, 2011.

[72] G. J. McShane, D. D. Radford, V. S. Deshpande, and N. A. Fleck, "The response of clamped sandwich plates with lattice cores subjected to shock loading," *European Journal of Mechanics a-Solids,* vol. 25, pp. 215-229, Mar-Apr 2006.

[73] D. Y. Seong, C. G. Jung, D. Y. Yang, K. J. Moon, and D. G. Ahn, "Quasi-isotropic bending responses of metallic sandwich plates with bi-directionally corrugated cores," *Materials & Design,* vol. 31, pp. 2804-2812, 2010.

[74] G. J. McShane, S. M. Pingle, V. S. Deshpande, and N. A. Fleck, "Dynamic buckling of an inclined strut," *International Journal of Solids and Structures,* vol. 49, pp. 2830-2838, 10/1/ 2012.

[75] S. Hou, S. Zhao, L. Ren, X. Han, and Q. Li, "Crashworthiness optimization of corrugated sandwich panels," *Materials & Design,* vol. 51, pp. 1071-1084, 10// 2013.

[76] C. R. Calladine and R. W. English, "Strain-rate and inertia effects in the collapse of two types of energy-absorbing structure," *International Journal of Mechanical Sciences,* vol. 26, pp. 689-701, 1984.

[77] L. L. Tam and C. R. Calladine, "Inertia and strain-rate effects in a simple plate-structure under impact loading," *International Journal of Impact Engineering,* vol. 11, pp. 349-377, // 1991.

[78] H. Zhao and S. Abdennadher, "On the strength enhancement under impact loading of square tubes made from rate insensitive metals," *International Journal of Solids and Structures,* vol. 41, pp. 6677-6697, 12// 2004.

[79] H. Zhao, I. Elnasri, and S. Abdennadher, "An experimental study on the behaviour under impact loading of metallic cellular materials," *International Journal of Mechanical Sciences,* vol. 47, pp. 757-774, 2005.

[80] M. Langseth and O. S. Hopperstad, "Static and dynamic axial crushing of square thin-walled aluminium extrusions," *International Journal of Impact Engineering,* vol. 18, pp. 949-968, 1996.

[81] A. Paul and U. Ramamurty, "Strain rate sensitivity of a closed-cell aluminum foam," *Materials Science and Engineering A,* vol. 281, pp. 1-7, 2000.

[82] S. R. Reid and C. Peng, "Dynamic uniaxial crushing of wood," *International Journal of Impact Engineering,* vol. 19, pp. 531-570, 1997.

[83] V. L. Tagarielli, V. S. Deshpande, and N. A. Fleck, "The high strain rate response of PVC foams and end-grain balsa wood," *Composites Part B: Engineering,* vol. 39, pp. 83-91, 2008.

[84] P. Feraboli, F. Deleo, B. Wade, M. Rassaian, M. Higgins, A. Byar, *et al.*, "Predictive modeling of an energy-absorbing sandwich structural concept using the building block approach," *Composites Part A: Applied Science and Manufacturing,* vol. 41, pp. 774-786, 6// 2010.

[85] J. Bi, H. Fang, Q. Wang, and X. Ren, "Modeling and optimization of foam-filled thin-walled columns for crashworthiness designs," *Finite Elements in Analysis and Design,* vol. 46, pp. 698-709, 9// 2010.

[86] S. Yang and C. Qi, "Multiobjective optimization for empty and foam-filled square columns under oblique impact loading," *International Journal of Impact Engineering,* vol. 54, pp. 177-191, 4// 2013.

[87] A. K. Toksoy and M. Güden, "Partial Al foam filling of commercial 1050H14 Al crash boxes: The effect of box column thickness and foam relative density on energy absorption," *Thin-Walled Structures,* vol. 48, pp. 482-494, 7// 2010.

[88] A. K. Toksoy and M. Güden, "The optimisation of the energy absorption of partially Al foam-filled commercial 1050H14 and 6061T4 Al crash boxes," *International Journal of Crashworthiness,* vol. 16, pp. 97-109, 2011/04/04 2011.

[89] S. M. H. Hosseini and U. Gabbert, "Numerical simulation of the Lamb wave propagation in honeycomb sandwich panels: A parametric study," *Composite Structures*, vol. 97, pp. 189-201, 3// 2013.

[90] A. J. Lamb, A. K. Pickett, and F. Chaudoye, "Experimental Characterisation and Numerical Modelling of Hexagonal Honeycomb Cellular Solids under Multi-axial Loading," *Strain*, vol. 47, pp. 2-20, 2011.

[91] S. Abrate, "Impact Response of Laminated and Sandwich Composites," in *Impact Engineering of Composite Structures*, ed: Springer Vienna, 2011, pp. 98-107.

[92] H. Kolsky, "An Investigation of the Mechanical Properties of Materials at very High Rates of Loading," *Proceedings of the Physical Society. Section B*, vol. 62, p. 676, 1949.

[93] W. W. Chen and B. Song, "Chapter 1-Conventional Kolsky bars," in *Split Hopkinson (Kolsky) Bar Design, Testing and Applications*, ed: Springer, 2011.

[94] İ. K. Odacı, "The projectile impact responses of the composite faced aluminum foam and corrugated aluminum sandwich structures: a comparative study," Master of Science, Mechanical Engineering, İzmir Institute of Technology, İzmir, 2011.

[95] ASTM Standart E 8M-04 "Standard Specification for Standard Test Methods for Tension Testing of Metallic Materials " ASTM International,West Conshohocken, PA, 2004, www.astm.org. [Online].

[96] W. Johnson and A. G. Mamalis, "A survey of some physical defects arising in metal working processes,in: ," in *Proceedings of the 17th International MTDR Conference*, London, UK, 1977, pp. 607-621.

[97] LSTC, *LS-DYNA Keyword User's Manual* vol. II: Livermore Software Technology Corporation (LSTC), 2007.

[98] K. E. Jackson, "Predicting the Dynamic Crushing Response of a Composite Honeycomb Energy Absorber Using Solid-Element-Based Models in LS-DYNA," presented at the 11th International LS-DYNA® Users Conference, Detroit, 2010.

[99] R. Gumruk and S. Karadeniz, "A numerical study of the influence of bump type triggers on the axial crushing of top hat thin-walled sections," *Thin-Walled Structures*, vol. 46, pp. 1094-1106, 2008.

[100] S. P. Santosa, T. Wierzbicki, A. G. Hanssen, and M. Langseth, "Experimental and numerical studies of foam-filled sections," *International Journal of Impact Engineering,* vol. 24, pp. 509-534, 2000.

[101] H. Zarei and M. Kröger, "Optimum honeycomb filled crash absorber design," *Materials & Design,* vol. 29, pp. 193-204, 2008.

[102] C. T. Lim, V. P. W. Shim, and Y. H. Ng, "Finite-element modeling of the ballistic impact of fabric armor," *International Journal of Impact Engineering,* vol. 28, pp. 13-31, 2003.

[103] L. J. Gibson, *Cellular solids : structure & properties / Lorna J. Gibson, Michael F. Ashby*. Oxford [Oxfordshire] ; New York :: Pergamon Press, 1988.

[104] G. J. McShane, V. S. Deshpande, and N. A. Fleck, "Underwater blast response of free-standing sandwich plates with metallic lattice cores," *International Journal of Impact Engineering,* vol. 37, pp. 1138-1149, 2010.

[105] M. Guden and S. Yüksel, "SiC-particulate aluminum composite foams produced from powder compacts: foaming and compression behavior," *Journal of Materials Science,* vol. 41, pp. 4075-4084, 2006.

[106] S. Lee, F. Barthelat, N. Moldovan, H. D. Espinosa, and H. N. G. Wadley, "Deformation rate effects on failure modes of open-cell Al foams and textile cellular materials," *International Journal of Solids and Structures,* vol. 43, pp. 53-73, 2006.

[107] G. J. McShane, V. Deshpande, and N. Fleck, "The underwater blast resistance of metallic sandwich beams with prismatic lattice cores," *Journal of Applied Mechanics,* vol. 74, pp. 352-364, 2007.

[108] D. G. Vaughn, J. M. Canning, and J. W. Hutchinson, "Coupled plastic wave propagation and column buckling," *Journal of Applied Mechanics-Transactions of the Asme,* vol. 72, pp. 139-146, Jan 2005.

[109] A. Petras and M. P. F. Sutcliffe, "Indentation failure analysis of sandwich beams," *Composite Structures,* vol. 50, pp. 311-318, Nov 2000.

[110] W. Goldsmith and J. L. Sackman, "An experimental study of energy absorption in impact on sandwich plates," *International Journal of Impact Engineering,* vol. 12, pp. 241-262, 1992.

[111] W. Goldsmith and D. L. Louie, "Axial perforation of aluminum honeycombs by projectiles " *International Journal of Solids and Structures,* vol. 32, pp. 1017-1046, 1995.

[112] G. H. Liaghat, A. A. Nia, H. R. Daghyani, and M. Sadighi, "Ballistic limit evaluation for impact of cylindrical projectiles on honeycomb panels," *Thin-Walled Structures,* vol. 48, pp. 55-61, Jan 2010.

[113] M. S. H. Fatt and K. S. Park, "Perforation of honeycomb sandwich plates by projectiles," *Composites Part a-Applied Science and Manufacturing,* vol. 31, pp. 889-899, 2000.

[114] A. Tasdemirci, Ç. Ergönenç, and M. Güden, "Split Hopkinson pressure bar multiple reloading and modeling of a 316 L stainless steel metallic hollow sphere structure," *International Journal of Impact Engineering,* vol. 37, pp. 250-259, 2010.

[115] H. J. Rathbun, D. D. Radford, Z. Xue, M. Y. He, J. Yang, V. Deshpande, *et al.*, "Performance of metallic honeycomb-core sandwich beams under shock loading," *International Journal of Solids and Structures,* vol. 43, pp. 1746-1763, 2006.

VITA

Cenk Kılıçaslan was born in Milas/Muğla/TURKEY in October 10, 1984. He graduated from mechanical engineering department of Uludağ University in 2002. He completed his M.Sc. in 2009 and his Ph.D in 2014 in mechanical engineering department of İzmir Institute of Technology.

Publications

- C. Kılıçaslan, M. Güden, İ. K. Odacı, and A. Taşdemirci, "The impact responses and the finite element modeling of layered trapezoidal corrugated aluminum core and aluminum sheet interlayer sandwich structures," Materials & Design, vol. 46, pp. 121-133, 4//2013.

- M. Çakırcalı, C. Kılıçaslan, M. Güden, E. Kıranlı, V. Shchukin, and V. Petronko,"Cross wedge rolling of a Ti6Al4V (ELI) alloy: the experimental studies and the finite element simulation of the deformation and failure," The International Journal of Advanced Manufacturing Technology, vol. 65, pp. 1273-1287, 2013/04/01 2013.

- İ. K. Odacı, C. Kılıçaslan, A. Taşdemirci, and M. Güden, "Projectile impact testing of glass fiber-reinforced composite and layered corrugated aluminium and aluminium foam core sandwich panels: a comparative study," International Journal of Crashworthiness, vol. 17, pp. 508-518, 2012/10/01 2012.

- C. Kılıçaslan, M. Güden, İ. K. Odacı, A. Taşdemirci, "Experimental testing and full and homogenized numerical models of the low velocity and dynamic deformation of the trapezoidal aluminum corrugated core sandwich", Strain (2014) 50, 236-249, DOI: 10.1111/str.12085, 2014.

- C. Kılıçaslan, M. Güden, İ. K. Odacı, A. Taşdemirci, "Experimental and numerical studies on the quasi-static and dynamic crushing responses of multi-layer trapezoidal aluminum corrugated sandwiches", Journal of Thin-Walled Structures, vol.78, pp.70-78, 2014.